UNIVERSIDAD COMPLUTENSE DE MADRID

FACULTAD DE CIENCIAS FÍSICAS

TESIS DOCTORAL

Measurement of the ^{244}Cm, ^{246}Cm and ^{248}Cm neutron-induced capture cross sections at the CERN n_TOF facility

Medida de las secciones eficaces de captura neutrónica del ^{244}Cm, ^{246}Cm y ^{248}Cm en la instalación n_TOF del CERN

MEMORIA PARA OPTAR AL GRADO DE DOCTOR
PRESENTADA POR

Víctor Alcayne Aicua

Directores

Emilio Mendoza Cembranos
Daniel Cano Ott

UNIVERSIDAD COMPLUTENSE DE MADRID

FACULTAD DE CIENCIAS FÍSICAS
Departamento de Física Teórica
Programa de Doctorado en Física

Measurement of the ^{244}Cm, ^{246}Cm and ^{248}Cm neutron-induced capture cross sections at the CERN n_TOF facility

Medida de las secciones eficaces de captura neutrónica del ^{244}Cm, ^{246}Cm y ^{248}Cm en la instalación n_TOF del CERN

MEMORIA PARA OPTAR AL GRADO DE DOCTOR PRESENTADA POR

Víctor Alcayne Aicua

Directores:

Emilio Mendoza Cembranos

Daniel Cano Ott

Unidad de Innovación Nuclear (CIEMAT)

UNIVERSIDAD COMPLUTENSE MADRID

DECLARACIÓN DE AUTORÍA Y ORIGINALIDAD DE LA TESIS PRESENTADA PARA OBTENER EL TÍTULO DE DOCTOR

D./Dña. Victor Alcayne Aicua,
estudiante en el Programa de Doctorado en Física,
de la Facultad de Ciencias Físicas de la Universidad Complutense de Madrid, como autor/a de la tesis presentada para la obtención del título de Doctor y titulada:

Measurement of the 244Cm, 246Cm and248 Cm neutron-inducedcapture cross sections at the CERN n TOF facility

Medida de las secciones eficaces de captura neutrónica del 244Cm, 246Cm y 248Cm en la instalación n TOF del CERN

y dirigida por: Emilio Mendoza Cembranos y Daniel Cano Ott

DECLARO QUE:

La tesis es una obra original que no infringe los derechos de propiedad intelectual ni los derechos de propiedad industrial u otros, de acuerdo con el ordenamiento jurídico vigente, en particular, la Ley de Propiedad Intelectual (R.D. legislativo 1/1996, de 12 de abril, por el que se aprueba el texto refundido de la Ley de Propiedad Intelectual, modificado por la Ley 2/2019, de 1 de marzo, regularizando, aclarando y armonizando las disposiciones legales vigentes sobre la materia), en particular, las disposiciones referidas al derecho de cita.

Del mismo modo, asumo frente a la Universidad cualquier responsabilidad que pudiera derivarse de la autoría o falta de originalidad del contenido de la tesis presentada de conformidad con el ordenamiento jurídico vigente.

En Madrid, a 20 de noviembre de 2021

Fdo.: 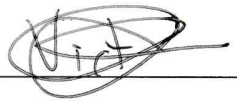

Esta DECLARACIÓN DE AUTORÍA Y ORIGINALIDAD debe ser insertada en la primera página de la tesis presentada para la obtención del título de Doctor.

A todos mis maestros.

Contents

Acknowledgements

First of all, as it has already been mentioned in the first pages, I would like to give my gratitude to all my teachers (*A todos mis maestros*) for always supporting me. In particular, I appreciate those who always supported and encouraged my curiosity.

Of course, the first place on this long list is for my supervisors Emilio and Daniel, for giving me the opportunity to start my research career and for their strong support, enthusiastic passion, great patience, knowledge, and guidance within all the process. I strongly appreciate that they always transmit to me their passion for Science.

This work would not be possible without the Cm samples provided by the Japan Atomic Energy Agency (JAEA). From this institution, I also strongly appreciate the invaluable help of Atsushi Kimura during the experiment at CERN. To all the members of the n_TOF collaboration who helped me a lot during the experiment and my long visits at CERN with special mention to the young members: Alice, Elisso, Jose, Maria, Marta, Massimo, Michi, Simone, Veatriki, Zinovia, and many others. A special thanks to the n_TOF Spanish students capture *team* (Adria, Jorge, Victor, Fran) for becoming a family.

Un agradecimiento especial también a todos mis compañeros del CIEMAT durante todos estos años: Aczel, Adrián, Alberto, Aris, David, Enrique, Javier, Jorge, Julio, Merche, Pablo G., Pablo R., Paco, Soledad, Sonia, Trino y Vicente. Y, por supuesto, también a los que llevan prácticamente toda la vida conmigo, los *Mñns* y los *Niños perdidos* (sois muchos para nombraros a todos). Habéis sido un gran apoyo durante todo este tiempo y es precioso ver como vamos viviendo etapas juntos. Tampoco puedo dejar de agradecer el apoyo de mis vecinas, Cris y Tamara. Gracias por cuidarme siempre. Y gracias, también, a Manolo e Irene, amistades sinceras desde el primer año de carrera.

Al principio de esta tesis hablaba de los maestros y, sin duda, los que más me han enseñado han sido mis padres. Gracias por apoyarme siempre en todo y por darlo todo por mi. Y, por supuesto, gracias también a mi hermana, uno de mis pilares fundamentales durante todos estos años, apoyándome y cuidándome siempre.

Finalmente, quiero dar las gracias a Sílvia por ser mi apoyo más sincero en estos dos últimos años, aguantando todo mi estrés con una sonrisa. Tú, como maestra que también eres, me has enseñado a creer en mí, y eso tiene un valor incalculable. Gracias por compartir tu vida conmigo. Te quiero.

List of Acronyms

ADS Accelerator Driven System 22

BCT Beam Current Transformer 43

BIF Beam Interception Factor 48

BWR Boiling Water Reactor 17

CASTOR CERN Advanced STORage manager 34

CLM Crystal Lattice Model 132

DAQ Data AcQuisition system 34

EAR1 First area of the n_TOF facility 10

EAR2 Second area of the n_TOF facility 10

FGM Free Gas Model 132

FOM Figure Of Merit 62

FWHM Full Width Half Maximum 77

HLW High Level Waste 20

LWR Light Water Reactor 17

MA Minor Actinides 19

P&T Partitioning and transmutation 22

PHWT Pulse Height Weighting Technique 93

PS Proton Synchrotron 31

PSA Pulse Shape Analysis 34

PSF Photon Strength Function 62

PWR Pressurized Water Reactor 17

Abstract

Measurement of the ^{244}Cm, ^{246}Cm and ^{248}Cm neutron-induced capture cross sections at the CERN n_TOF facility

Accurate neutron capture cross section data for minor actinides (MAs) are required to estimate the production and transmutation rates of MAs in light water reactors, critical fast reactors like Gen-IV systems, and other innovative reactor systems such as accelerator driven systems (ADS). In particular, ^{244}Cm, ^{246}Cm and ^{248}Cm (^{244,246,248}Cm) play an important role in the transport, storage and transmutation of the nuclear waste of the actual nuclear reactors, due to the contribution of these isotopes to the radiotoxicity, neutron emission, and decay heat in the spent nuclear fuel. Also, capture reactions in these Cm isotopes open the path for the formation of heavier elements such as Bk and Cf. Recent sensitivity studies have shown that the uncertainties in the evaluations of ^{244,246,248}Cm in the resonance region are too big to obtain the desired uncertainties in the characterisation of the spent fuel of conventional nuclear reactors.

In order to reduce the uncertainties, new measurements of the ^{244,246,248}Cm capture cross sections have been performed at n_TOF. There are only two previous capture measurements of the cross sections of these isotopes. The first measurement was carried out in 1969 by Moore *et al.* using an underground nuclear explosion, and the cross sections were measured between 20 eV and 1 keV. The second measurement was performed in J-PARC by Kimura *et al.* in 2010 with germanium detectors, and the cross sections were measured between 4 and 30 eV.

The measurements at the n_TOF facility have been performed with two different samples, one prepared to measure the cross section of ^{244}Cm and the other to measure the cross sections of ^{246,248}Cm. The two samples were the same as the ones used in the previous Cm capture measurement at J-PARC. The cross section of ^{244}Cm has been measured in the first experimental area of n_TOF (EAR1) located at 185 meters with the Total Absorption Calorimeter (TAC) in the energy range between 7 and 100 eV, and in the second experimental area (EAR2) located at 19 meters with C_6D_6 detectors in the energy range between 7 and 300 eV. The results obtained for the two areas are compatible. In EAR2 the cross sections of ^{246}Cm and ^{248}Cm have also been measured, in the energy range between 4 and 400 eV and between 7 and 100 eV, respectively. In addition, the resonances of ^{240}Pu, present in the samples due to the decay of ^{244}Cm, have been analysed between 20 and 190 eV. The ^{244,246,248}Cm and ^{240}Pu cross sections have been normalised to the first resonance of ^{240}Pu.

In total, 36 resonances of Cm have been fitted, implementing the SAMMY code, and the uncertainties in the resonance parameters are smaller than the uncertainties in the two previous measurements for most of the resonances, improving the status of the nuclear data for these isotopes.

Resumen en español

Medida de las secciones eficaces de captura neutrónica del ^{244}Cm, ^{246}Cm y ^{248}Cm en la instalación n_TOF del CERN

Nuevos datos de las secciones eficaces de captura neutrónica son necesarias para estimar las tasas de producción y transmutación de actínidos minoritarios (MAs) en reactores de agua ligera, reactores rápidos críticos de Gen-IV y otros sistemas de reactores innovadores como los Amplificadores de Energía. En particular, las secciones eficaces del ^{244}Cm, ^{246}Cm y ^{248}Cm (^{244,246,248}Cm) juegan un papel importante en el transporte, almacenamiento y transmutación de los residuos nucleares de los reactores nucleares actuales, debido a la contribución de estos isótopos a la radiotoxicidad, emisión de neutrones y calor de desintegración en el combustible nuclear gastado. Además, las reacciones de captura en estos isótopos de Cm abren el camino para la formación de elementos más pesados como Bk y Cf. Estudios de sensibilidad recientes han demostrado que las incertidumbres en las evaluaciones del ^{244,246,248}Cm en la región de las resonancia resultas son demasiado grandes para obtener las incertidumbres deseadas en la caracterización del combustible gastado de los reactores nucleares convencionales.

Para reducir las incertidumbres, se han realizado nuevas medidas de las secciones eficaces de captura del ^{244,246,248}Cm en n_TOF. Solo existen dos medidas previas de las secciones eficaces de captura de estos isótopos. La primera medida fue realizada en 1969 por Moore *et al.* utilizando una explosión nuclear subterránea y las secciones eficaces se midieron entre 20 eV y 1 keV. La segunda medida fue realizada en J-PARC por Kimura *et al.* en 2010 con detectores de germanio y las secciones eficaces se midieron entre 4 eV y 30 eV.

Las medidas en la instalación n_TOF se han realizado con dos muestras diferentes, una preparada para medir la sección eficaz del ^{244}Cm y la otra para medir las secciones eficaces del ^{246,248}Cm. Las dos muestras eran las mismas que se usaron en la medida de captura de los isótopos del curio en J-PARC. La sección eficaz del ^{244}Cm se ha medido en la primera área experimental de n_TOF (EAR1) ubicada a 185 metros con el Total Absorption Calorimeter (TAC) en el rango de energía entre 7 y 100 eV, y en la segunda área experimental (EAR2) ubicada a 19 metros con detectores C_6D_6 en el rango de energía entre 7 y 300 eV. Los resultados obtenidos para las dos áreas experimentales son compatibles. En el EAR2 también se han medido las secciones eficaces del ^{246}Cm y del ^{248}Cm, en el rango de energía entre 4 y 400 eV y entre 7 y 100 eV, respectivamente. Además, las resonancias del ^{240}Pu, presentes en las muestras debido a la desintegración del ^{244}Cm, se han analizado entre 20 y 190 eV. Las secciones eficaces del ^{244,246,248}Cm y

del ^{240}Pu se han normalizado a la primera resonancia del ^{240}Pu.

En total, se han ajustado 36 resonancias de isótopos del Cm, y las incertidumbres en los parámetros de las resonancias son menores que las incertidumbres en las dos medidas anteriores para la mayoría de las resonancias mejorando el estado de los datos nucleares para estos isótopos.

Chapter 1

Introduction

This work presents the analysis of the measurement of the neutron capture cross sections of ^{244}Cm, ^{246}Cm and ^{248}Cm (hereafter ^{244,246,248}Cm) at the n_TOF facility at CERN. In addition, the cross section of ^{240}Pu is obtained as well from the contaminant of this isotope in the samples. ^{240}Pu is a daughter of ^{244}Cm that has a half-life of 18.11 years. The manuscript is divided into seven chapters:

1. **Introduction.** The motivation of this measurement is presented in Sections 1.1 and 1.2. In Section 1.3, some theoretical aspects related with this work are presented. Finally, the Sections 1.4 and 1.5 are devoted to describe previous measurements and evaluations.

2. **Experimental setup.** This chapter is dedicated to present the experimental setup used in the measurement, which has been performed in the two experimental areas of the n_TOF facility: the first experimental area (EAR1) and the second experimental area (EAR2). In the chapter, the following items are presented: the n_TOF facility (2.1), the detectors used in EAR1 (2.2), the detectors used in EAR2 (2.3), the samples used in the experiment (2.4), and, finally, the properties of the n_TOF neutron beams (2.5).

3. **Monte Carlo simulation of the capture cascades.** For the analysis of both measurements performed in EAR1 and in EAR2 it is necessary to simulate the detector response of the (same) gamma-ray cascades emitted after the capture reactions. Since this is an issue that affects the analysis of data taken in both experimental areas, a dedicated chapter has been devoted to this task.

4. **Procurement of the ^{244}Cm experimental capture yield with the total absorption calorimeter.** This chapter is dedicated to the analysis of the measurement performed in EAR1 with the Total Absorption Calorimeter (TAC).

5. **Procurement of the ^{244,246,248}Cm experimental capture yield with the C_6D_6 detectors.** This chapter is dedicated to the analysis of the measurement performed in EAR2 with the C_6D_6 detectors.

6. **Resonance analysis of the capture yields.** The yields obtained in the previous chapters are analysed to obtain the cross sections, in the form of Resonance Parameters (RP). The results are compared with previous experiments and evaluations.

7. **Summary and conclusions.** A summary and the main conclusions of this manuscript are presented in this chapter.

1.1 Nuclear energy overview

The total energy consumption worldwide has increased continuously since the beginning of industrialization at the end of the nineteenth century. In Figure 1.1, the world total energy supply is presented as an indicator of the total energy consumption, which has been doubled in the last 35 years and tripled in the last 50 [1]. The total energy production by source is presented in the right panel of the figure, which shows that fossil fuels correspond to 81.3% of the total energy production nowadays. This share has been reduced by only 5% in the past 45 years.

The electricity generation worldwide is illustrated in Figure 1.2 for the past 45 years. In this period, the electrical energy production has multiplied by five. Fossil fuels are the main contributor to electricity production (64.2%), even though it has reduced approximately by 10% in the last 45 years, due to the increase of nuclear and renewable electricity production.

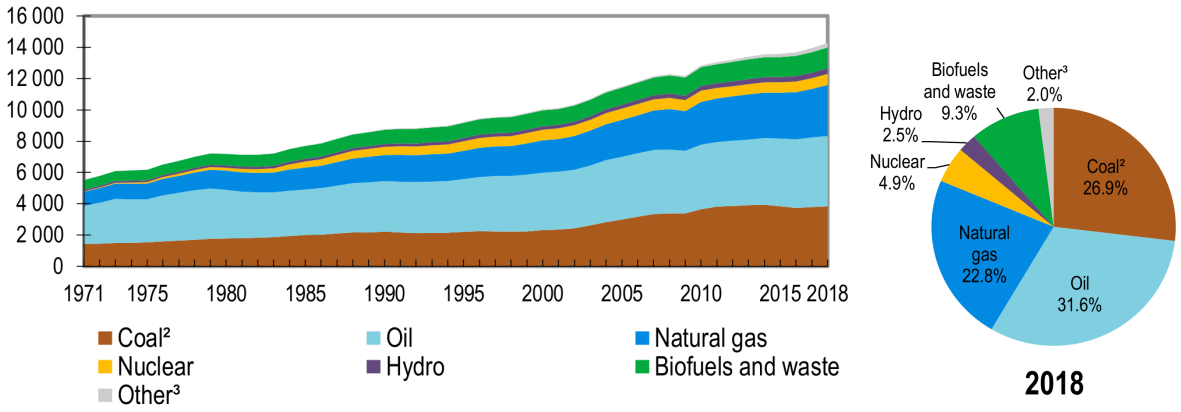

Figure 1.1: World total primary energy supply from 1971 to 2018 by fuel. The Y axis is in million tonnes of oil equivalent (Mtoe). 2) Peat and oil shale are aggregated with coal. 3) Includes geothermal, solar, wind, tide/wave/ocean, heat and other sources [1].

The projections of the International Energy Outlook report from the U. S. Energy Information Administration (2019) [2] for the 'Reference Case' reflects current trends and relationships among supply, demand, and prices in the future. The results for the electricity generation are illustrated in Figure 1.3. In this projection, the electricity generation in the OECD countries increases 1.0% per year until 2050, whereas the non-OECD countries increase 2.3%. In order to achieve the higher demand, renewables will grow 3.6% per year and nuclear 1.0%. By 2025, renewables are expected to overtake coal as the primary source.

Currently, in the world, 10.2% of the total electricity is produced by nuclear power plants [1], 80 years later than the first experimental nuclear chain reaction was done by

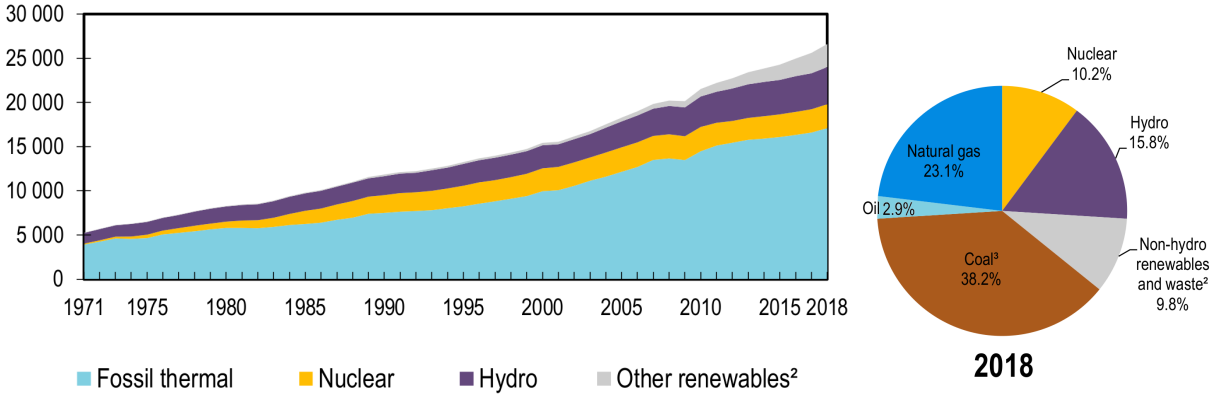

Figure 1.2: World electric generation from 1971 to 2018 by fuel (TWh) [1], excluding electricity generation from pumped storage. 2) includes geothermal, solar, wind, tide/wave/ocean, biofuels, waste, heat and other. 3) peat and oil shale are aggregated with coal [1].

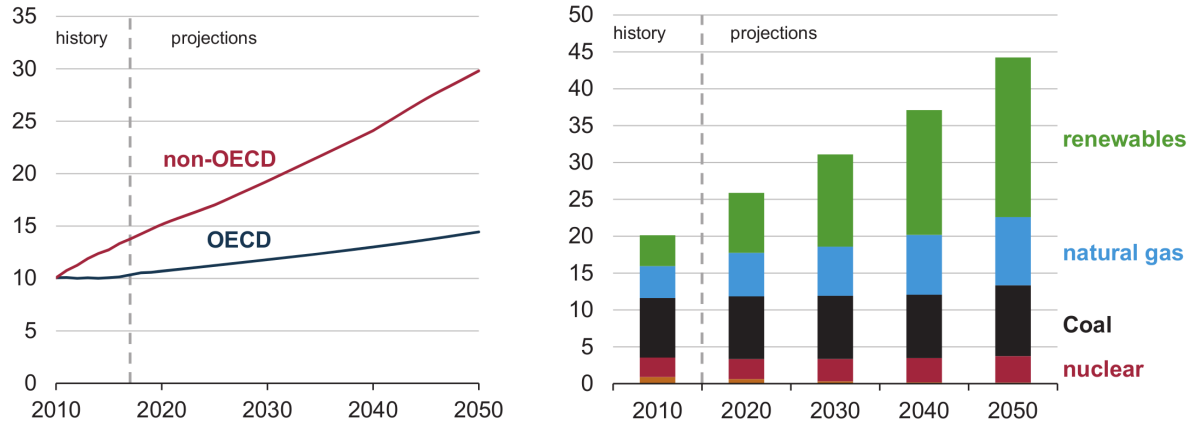

Figure 1.3: Net electricity generation (left) and net electricity generation by fuel (right), worldwide in trillion kilowatthours, according to the 'Reference Case' of the International Energy Outlook report (2019) [2].

Enrico Fermi in 1942 [3]. The first commercial power plants were available at the end of the 1950s, and they started to be a significant fraction of the electricity production in the world from the 1970s. Since then, nuclear energy production has increased continuously till the Fukushima accident occurred in Japan in March 2011, as shown in Figure 1.4. The nuclear energy production has then decreased, due to the reduction of the production in the OECD countries, but is close to reach the level of 2011 mainly due to China. In total, there are in the world 455 operative nuclear reactors, and 54 under construction by June 2020 [4]. Three countries produce 59% of the total nuclear energy: United States (31%), France (14%) and China (13%), as illustrated in Table 1.1.

Regarding Europe, there are 180 nuclear reactors producing 41% of the nuclear en-

ergy worldwide. In 10 European countries, nuclear energy produces more than one-third of the electricity: France (71%), Slovakia (54%), Ukraine (54%), Hungary (49%), Belgium (48%), Bulgaria (37%), Slovenia (37%), Czech Republic (35%), Finland (35%) and Sweden (34%).

As illustrated in Table 1.2, the majority of the nuclear power reactors (83%) use enriched ^{235}U and light water as a moderator. These reactors are known as Light Water Reactor (LWR) and may work with pressurized (PWR) (68%) or boiling water (BWR) (15%). The second most abundant type of nuclear reactor (10%) is the Pressurized Heavy Water Reactor (PHWR), which works with deuterated water and natural or slightly enriched uranium fuel.

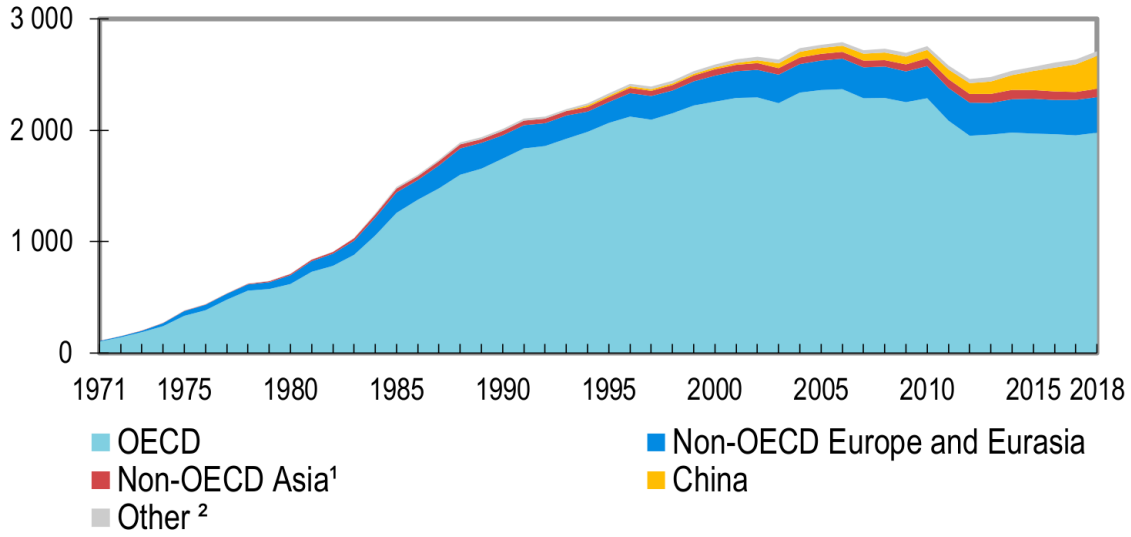

Figure 1.4: World nuclear electricity production from 1971 to 2018 by region (TWh). 1) Non-OECD Asia excludes China. 2) Other includes Africa, Non-OECD Americas and the Middle East [1].

Country	Reactors operational	Reactors under construction	Generated electricity (GWh)	Share of total electricity (%)
United States	95	2	809	19.7
France	56	1	382	70.6
China	49	10	330	4.9
Russia	38	4	196	19.7
South Korea	24	4	139	26.2
Canada	19	0	95	14.9
Ukraine	15	2	78	53.9
Germany	7	0	71	13.8
Japan	33	2	66	7.5
Sweden	7	0	64	34
Spain	7	0	56	21.4
United Kingdom	15	2	51	15.6
India	22	7	41	3.2
Belgium	7	0	41	47.6
Taiwan	4	2	31	13.4
Czech Republic	6	0	29	35.2
Switzerland	4	0	25	23.9
Finland	4	1	23	34.7
Bulgaria	2	0	16	37.5
Hungary	4	0	15	49.2
Brazil	2	1	15	2.7
South Africa	2	0	14	6.7
Slovakia	4	2	14	53.9
Mexico	2	0	11	4.5
Romania	2	0	10	18.5
Pakistan	6	1	9	0
Argentina	3	1	8	5.9
Iran	1	1	6	1.8
Slovenia	1	0	6	37
Netherlands	1	0	4	3.2
Armenia	1	0	2	27.8
United Arab Emirates	1	3	N/A	N/A
Bangladesh	0	2	N/A	N/A
Belarus	0	2	N/A	N/A
Turkey	0	2	N/A	N/A
World total	455	54	2586	

Table 1.1: Overview of all the nuclear reactors in the world for the different countries (at 28 june 2020), ordered by the amount of generated electricity [4].

	Operational reactors	Percentage of total
Pressurised water reactor (PWR)	310	68
Boiling water reactor (BWR)	67	15
Pressurised heavy water reactor (PHWR)	48	11
Advanced gas-cooled reactor (AGR)	14	3
Light water graphite reactor (LWGR)	13	3
Fast neutron reactor (FBR)	3	1
Total	455	100

Table 1.2: Overview of all the nuclear reactors type in the world (at 28 june 2020) [4].

1.2 Nuclear waste and the ^{244,246,248}Cm capture cross sections

The safe and efficient management of nuclear waste from the operation of nuclear reactors is an important issue. In particular, more than 250000 tons of spent fuel from currently operating reactors will require disposal [5].

Radioactive nuclear waste is generated in sizeable amounts due to irradiation with neutrons when operating a nuclear reactor. Figure 1.5 presents the isotopic composition of the spent fuel of a LWR reactor.

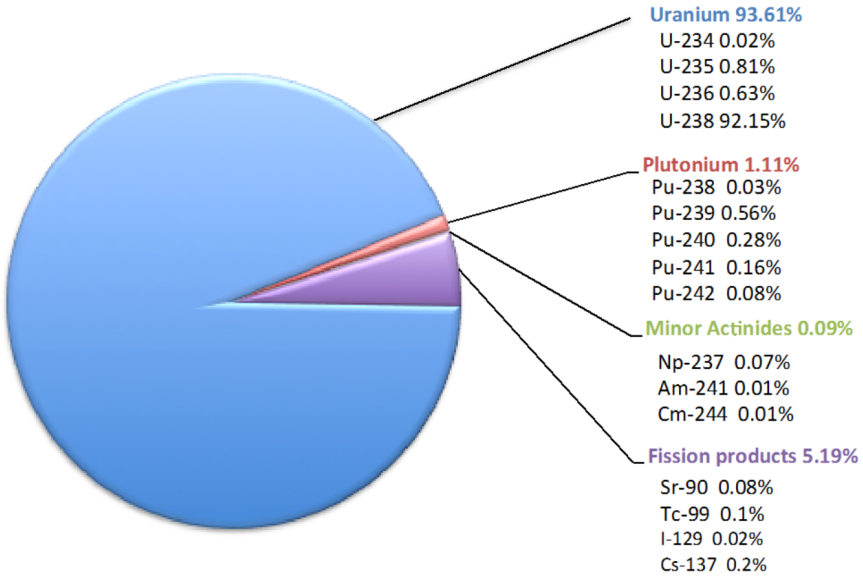

Figure 1.5: Isotopic composition of the burned fuel from a PWR with initial enrichment of 4.5 wt% after a 45 GWd/MTU burnup [6].

Part of the uranium in the fresh fuel has been converted into TRansUranic isotopes (TRU), like Pu and Minor Actinides (MA) (Np, Am, Cm, Bk and Cf), and also in

Fission Products (FP). Transuranic isotopes are produced mainly as a result of neutron capture processes and radioactive decays, as indicated in Figure 1.6. One of the goals of measuring the capture cross sections of ^{244,246,248}Cm is to be able to model with higher accuracy the isotopic composition of the spent fuel in a nuclear reactor. In particular, capture reactions on ^{244,246,248}Cm open the gate to the formation of heavier isotopes such as Bk, Cf or other isotopes of Cm. This was the motivation of some of the previous capture cross section measurements of ^{244,246,248}Cm. In particular, these data were needed in the past to optimise the production of ^{252}Cf in nuclear reactors [7, 8] for commercial uses.

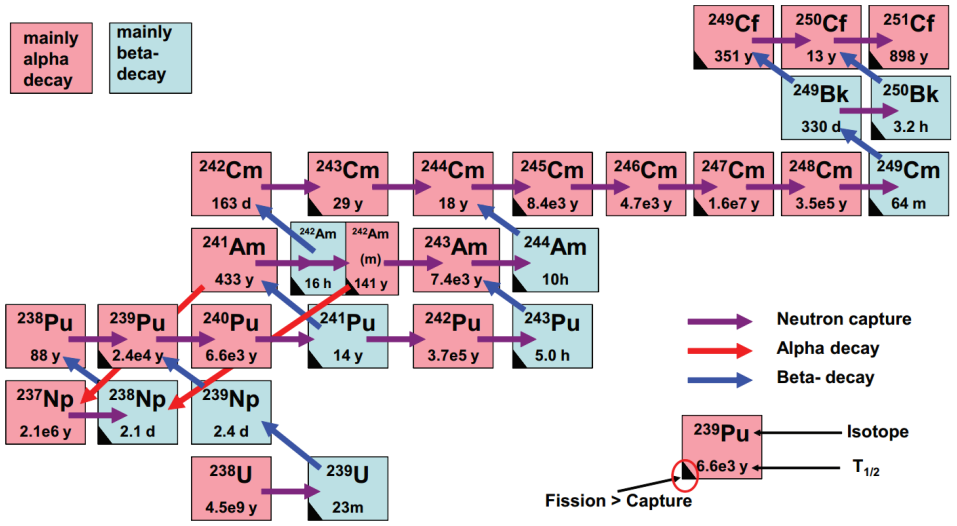

Figure 1.6: Representation of the creation of transuranic isotopes in a nuclear reactor from successive neutron captures and decays [9].

According to the International Atomic Energy Agency (IAEA), the radioactive waste can be classified into six groups [10]. The High Level Waste (HLW), which corresponds mainly to the spent fuel, is the one with the highest activity, and has to be disposed in deep and stable geological formations making use of the surrounding medium as a barrier to prevent the leakage of radioactive isotopes into the environment [11]. The radiotoxicity, decay heat and neutron emission are the properties of the spent fuel that are crucial for transport and storage. The contribution of ^{244,246,248}Cm isotopes to these magnitudes for a spent fuel coming from a PWR are the following:

- **Radiotoxicity** is a magnitude used to measure the hazard of radioactive waste. Figure 1.7 shows the partial contributions of various isotopes to the total radiotoxicity by inhalation as defined by the International Commission on Radiological Protection (ICRP) [12]. The Cm isotopes are responsible for ∼10% of the radiotoxicity in the first 15-20 years, and then is contribution becomes smaller due to the 18.11 years half-life of ^{244}Cm.

- **Neutron emission** is an essential parameter for the spent fuel characterisation, because the protection from these emitted neutrons is a primary objective in the transportation, processing, and storage of the spent fuel. As illustrated in panel (b) of Figure 1.7, the leading neutron emitter by a substantial difference in the first

hundred years is ^{244}Cm. In addition, between 500 and 10000 years ^{246}Cm produce more than 50% of the neutrons emitted.

- **Decay heat** in the spent fuel, which is produced as an effect of radiation on materials: the energy of the alpha, beta or gamma radiation is converted into the thermal movement of atoms. At the moment of a reactor shutdown, the decay heat is still ∼6% of the previous power of the reactor and is reduced to ∼0.2% in a week. To dissipate this heat, the spent fuel is stored in the reactor pool. In panel (c) of Figure 1.7 the decay heat is presented as a function of time, for the same PWR reactor. Cm isotopes produce ∼10% of the total decay heat in the first fifteen years and ∼40% of the actinide decay heat, mainly due to the contribution of ^{244}Cm.

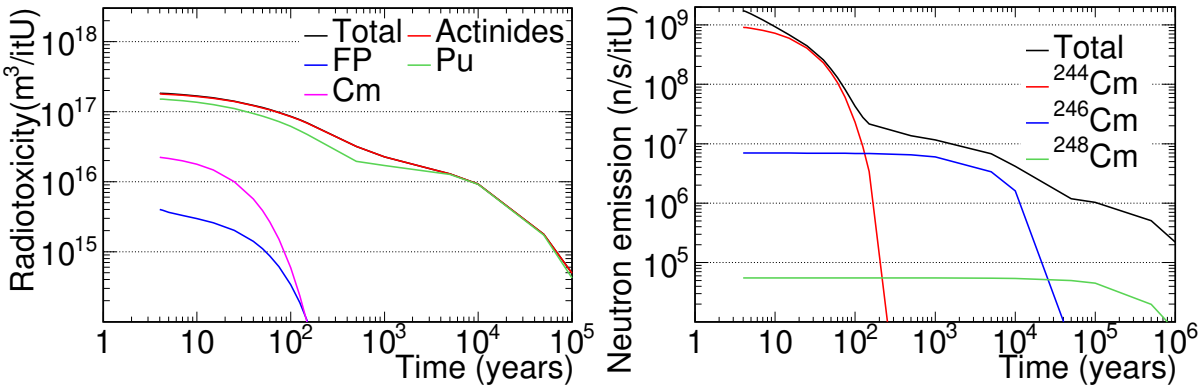

(a) Radiotoxicity

(b) Neutron emission

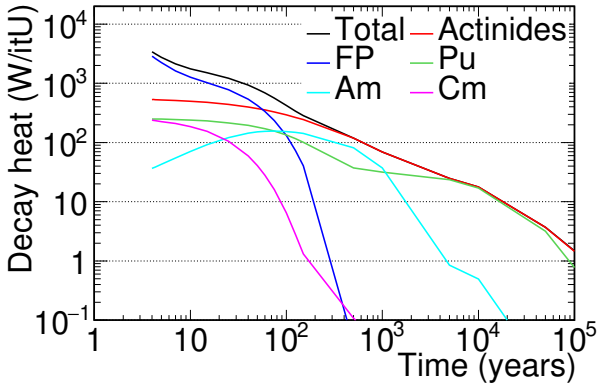

(c) Decay heat

Figure 1.7: Radiotoxicity, neutron emission and decay heat of the spent fuel per initial ton of uranium. The calculations have been done with ORIGEN2 [13] for a PWR with a 50 GWd/tU burnup after four years in the spent fuel pool.

^{244,246,248}Cm isotopes do not play an essential role in the operation of the actual LWR, but they contribute substantially to the radiotoxicity, neutron emission and decay heat of the nuclear waste. Sensitivity analyses have been made to estimate how the present cross section uncertainties affect the accuracy of these macroscopic parameters. One of

the most detailed analyses has been done by G. Aliberti *et al.* [14]. In this study they calculate how the uncertainties in the different reaction cross section need to be improved to reach some target accuracies. For the capture cross section of ^{244}Cm the resulting target accuracies for PWR are 25.7% between thermal and 0.54 eV, 4.1% between 4 to 22.6 eV, and 14.4% between 22.6 and 454 eV.

As previously mentioned, the only possible solution for the spent fuel from currently operating reactors is the disposal in geological repositories [5]. However, some of the isotopes in the spent fuel can be converted into nuclides with significantly lower radiotoxicity, decay heat or neutron emission by partitioning and transmutation (P&T) technologies. The process of P&T consists of separating the long-lived isotopes and 'burning' them with nuclear reactions, especially fission. Although the final disposal of the nuclear waste in geological repositories is unavoidable, the amount of high level waste could be strongly reduced with P&T technologies.

The transmutation of the nuclear waste is mainly done by fission reactions, but, capture processes occur unavoidably at the same time. The transuranic isotopes with an odd number of neutrons have fission cross sections which dominate over capture in the thermal range. In the even isotopes, it is the opposite. However, the fission cross section of these isotopes increases considerably at higher energies (close to 1 MeV). Since it is better to avoid capture to not produce new actinides, transmutation in thermal reactors is not the best option. The best option for the transmutation of actinides is to burn them in fast spectrum technologies, which are apparatuses with high energy neutron fluxes (tens of eV up to tens of MeV). There are two primary types of technologies considered for the transmutation: Accelerator Driven System (ADS) [15, 16] and Generation IV fast reactors [17, 18].

An ADS is a subcritical nuclear reactor core combined with an accelerator coupled to a spallation target which serves as an external neutron source. These systems have higher fuel flexibility allowing to load fuels with a larger concentration of TRU or MA than critical reactors. The Multipurpose hYbrid Research Reactor for High-tech Applications (MYRRHA) [19] is one of the demonstrators of the technology currently under construction in Belgium.

The primary goals of the Gen-IV [17, 18] reactors are to improve safety, sustainability, efficiency, and cost. In addition, some of the Gen-IV fast reactors can be loaded with a small content of TRU and/or MA from the nuclear waste produced in thermal reactors in order to eliminate part of the existing nuclear waste.

Improving the uncertainties in the capture cross sections of ^{244,246,248}Cm allows to perform a better design of the new nuclear devices (ADS and Gen-IV reactors), a better design of the fuel cycles, and a better treatment of the spent fuel.

1.3 Introduction to neutron cross section theory

This section is dedicated to present a brief overview of the theoretical basis relevant for this work. In Section 1.3.1 the neutron cross sections are introduced, whereas in Section 1.3.2 the compound nucleus and the R-matrix theories are presented.

1.3.1 Neutron cross sections

Cross sections (σ) are described as the effective area of an object, that quantifies the probability of a certain interaction between an incident projectile and a target. Focusing in nuclear reactions, cross sections are related with the probability that a certain nuclear reaction occurs, and is expressed in units of surface, typically in barn (b) ($1\text{b} = 10^{-28}\text{m}^2$). Supposing a beam of neutrons with intensity (neutrons per unit time) $I(\text{E}_\text{n})$ incident on a very narrow plate of a given element, density of nuclei N and thickness Δx, then the reaction rate $\text{R}(\text{E}_\text{n})$ is proportional to the number of target nuclei per unit area ($N \cdot \Delta x$) and the intensity of the neutron beam ($\text{I}(\text{E}_\text{n})$). The constant of proportionality is then the total cross section, (σ_{tot}):

$$R = \sigma_{tot} \cdot I \cdot N \cdot \Delta x \tag{1.1}$$

There are a large variety of nuclear processes (elastic scattering, capture, fission ...), and the total interaction probability, σ_{tot}, can be decomposed in the partial contributions for all the reaction channels:

$$\sigma_{tot} = \sigma_n + \sigma_\gamma + \sigma_f ... \tag{1.2}$$

where σ_n, σ_γ and σ_f are the elastic, capture and fission cross sections.

The capture, fission and elastic scattering reactions are non-threshold reactions in most of the actinides. In Figure 1.8 the non-threshold cross sections of ^{244}Cm from JENDL-4.0 [20] are presented. In the rest of actinides the cross sections have similar structures, and can be divided in four regions:

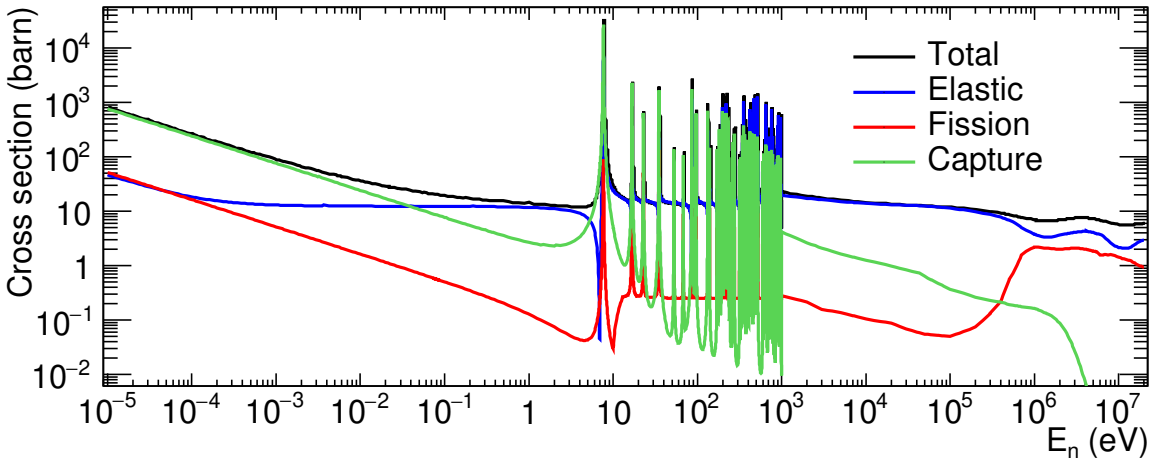

Figure 1.8: ^{244}Cm total and partial neutron cross sections (elastic scattering, fission and capture) in JENDL-4.0 [20].

- **Thermal and epithermal:** between 25.3 meV (thermal point) and the first resonance. The cross sections are smooth and inversely proportional to the velocity of the neutron ($\sigma \sim 1/\sqrt{E_n} \sim 1/v$) in this region.

- **Resolved Resonance Region (RRR):** between the first resonance in the eV region for actinides up to certain neutron energy, typically in the keV region for actinides. A resonant structure is present in this region, with significant variations between peaks and valleys. The resonances of the different reaction channels appear at the same energy.

- **Unresolved Resonance Region (URR):** at higher energies, experimental data are usually not good enough to perform resonance analysis. Resonances are still present, but are unknown. Average values such as the average distance between resonances or average strengths are provided in the libraries.

- **High energy region:** the distance between resonances becomes smaller than their intrinsic widths as the neutron energy increases and the resonant structures disappear.

1.3.2 The compound nucleus and the R-matrix theory

The resonant structure of neutron cross sections is described by using the compound nucleus theory originally proposed by Niels Bohr [21]. The base idea of the theory is that neutron reactions take place in two steps:

- In the first step, the neutron and the target form a nucleus with an excitation energy $E^* \approx S_n + E_n \cdot A/(A+1)$. Where S_n is the neutron separation energy, typically in the 4-10 MeV range, A is the mass number of the target nucleus and E_n is the kinetic energy of the neutron.

- In the second step, the compound nucleus in the quasi-stationary level decays. The decay path is supposed to be independent of how the compound nucleus was created, and each decay path corresponds to a reaction channel. If the compound nucleus decays to the ground or an isomeric state emits γ-rays, it is a capture reaction. If, on the contrary, the neutron and the target nucleus in the ground state are emitted, then it is an elastic scattering reaction. Finally, if a fission occurs, it is a fission reaction.

The decay probability of a decay reaction i is equal to the branching ratio Γ_i/Γ. Γ_i is the width related to the decay reaction i, and Γ is the total width equal to the sum of all the partial widths.

The R-matrix formalism describes accurately the resonance structure of the neutron cross sections with Resonance Parameters (RP). The formalism was introduced by Wigner and Eisenbud [22], and gives a better foundation of the theory proposed by Breit and Wigner for the capture of slow neutrons [23]. In the next paragraphs a brief introduction of the theory is presented, focused in the capture process. An extensive overview of the theory are presented in the work done by Lane and Thomas [24] and more recently in the

work done by Fröner [25].

The total cross section is related to the probability for the compound nucleus to occur, and if the resonance is far from other resonances the cross section can be well described with the Breit-Wigner formula:

$$\sigma_{c^*} = g\frac{\pi\Gamma\Gamma_n}{k_n^2((E_n - E_o)^2 + (\Gamma/2)^2)} \tag{1.3}$$

where E_o is the energy of the resonance, $g = (2J+1)/((2s+1)(2I+1))$ is the statistical spin factor and J, s and I are the spin of the compound nucleus, the neutron and the target nucleus, respectively. Finally, $k_n = 2.196771 \cdot 10^{-3} \cdot \sqrt{E_n} \cdot A/(A+1)$. In this experiment all the analysed nuclei are even-even with spin=0 and thus, since all the observed resonances are s-wave, the spin factor (g) is the unity. The probability to decay by the capture channel is Γ_γ/Γ, so the radiative capture cross section is:

$$\sigma_\gamma = \sigma_{c^*}\frac{\Gamma_\gamma}{\Gamma} = g\frac{\pi\Gamma_\gamma\Gamma_n}{k_n^2((E_n - E_o)^2 + (\Gamma/2)^2)} \tag{1.4}$$

The radiative area (A_r) of a resonance can be defined as the integral of equation 1.4 between $E_o - \Gamma/2$ and $E_o + \Gamma/2$:

$$A_r = g\frac{2\pi^2\Gamma_\gamma\Gamma_n}{k_o^2\Gamma} = \frac{4.09 \cdot 10^6 R_K}{E_o}\left(\frac{A+1}{A}\right)^2 \tag{1.5}$$

where $R_K = g \cdot \Gamma_n \cdot \Gamma_\gamma/\Gamma$ is the radiative kernel, that is proportional to the area of the resonance (A_r). In some cases the resonance width is dominated by a given channel and the radiative kernel (and thus the cross section) becomes proportional to one of the partial widths:

$$\begin{aligned} If\ \ \Gamma_n \gg \Gamma_\gamma + \Gamma_f : R_K \approx g\Gamma_\gamma \\ If\ \ \Gamma_\gamma \gg \Gamma_n + \Gamma_f : R_K \approx g\Gamma_n \end{aligned} \tag{1.6}$$

1.4 Previous ^{244,246,248}Cm measurements

All the time-of-flight capture, fission and transmission measurements of the RRR of ^{244,246,248}Cm available in EXFOR [26, 27, 28] are presented in Table 1.3. Many of the experiments measure at the same time various of the Cm isotopes with a combination of different samples. When capture dominates over elastic scattering and fission, which is the case for most of the resonances in ^{244,246,248}Cm, the capture cross section is quite proportional to the Γ_n parameter of the resonance. In Figure 1.9 the uncertainties of the Γ_n parameter, i.e. in the capture cross section, obtained in each of the previous measurements are illustrated. The uncertainties for ^{244}Cm are significantly larger than the required target accuracy for PWR reactors reported in [14].

Experiment	Type of measurement	Energy range		
		^{244}Cm	^{246}Cm	^{248}Cm
Cote (1964) [29]	Transmission	7-280 eV	4-27 eV	-
Berreth (1972) [8]	Transmission	7-100 eV	4-16 eV	-
Benjamin (1972) [7]	Transmission	-	4-160 eV	7-3000 eV
Belanova (1975) [30]	Transmission	7-180 eV	4-160 eV	7-100 eV
Moore (1971) [31]	Capture	22-1000 eV	80-380 eV	26 eV
Kimura (2010) [32]	Capture	7-23 eV	4-16 eV	7-27 eV
Kawase (2021) [33]	Capture	7-420 eV	4-550 eV	7-100 eV
Moore (1971) [31]	Fission	22-1000 eV	80-380 eV	26-100 eV
Maguire (1985) [34]	Fission	7-35 eV	4-160 eV	7-76 eV
Alekseev (2010) [35, 36, 37]	Fission	7-100 eV	4-160 eV	7-100 eV

Table 1.3: Time-of-flight transmission, capture and fission ^{244,246,248}Cm measurements available in EXFOR in the RRR. Some of the measured yields extend up to higher energies, but the RP are only reported up to the energies presented in the table.

The measurements reported in Table 1.3 are briefly summarised in the following list. The words between brackets are used in the rest of the document to refer to each of these measurements:

- **Transmission measurement from Cote *et al.* in 1964 [29] (Cote).** The first transmission measurement was performed with the Argonne fast chopper [38] and a mass of 46 mg of ^{244}Cm and 1.5 mg of ^{246}Cm. The Γ_γ of the three first resonances of ^{244}Cm and the first of ^{246}Cm were obtained. Also fifteen resonances of ^{244}Cm were fitted with a fixed value of the radiative width of 37 meV and the resonance at 26.9 eV of ^{246}Cm was fitted with a radiative width of 35 meV.

- **Capture and fission measurement from Moore *et al.* in 1971 [31, 39] (Moore).** The first capture and fission measurement was performed with Physics 8 event at Los Alamos [40], using a nuclear explosion to make a one-pulse experiment. 32 samples of various isotopes were used in this experiment including five high purity monoisotopic samples to measure the fission cross sections of ^{244,245,246,247,248}Cm, and one sample containing several Cm isotopes to measure the capture cross sections. The measurement of the five fission Cm samples was performed with a Si p-n junction detector [41], and the position of the resonances found in fission were used for the analysis of the capture sample. The capture measurement was performed with a 387 mg sample containing 79% ^{244}Cm and 16% ^{246}Cm, and using Moxon-Rae detectors [42]. A total of 69 resonances of ^{244}Cm were fitted in the energy range between 20 and 1000 eV, with a fixed radiative width of 37 meV. A total of eight resonances of ^{246}Cm were fitted in the energy range between 80 and 400 eV, with the same value of 37 meV of the radiative width. Also the resonance of ^{248}Cm at 26 eV was fitted.

- **Transmission measurement from Berreth *et al.* in 1972 [8] (Berreth).** The second transmission measurement was performed at the Materials Testing Reactor

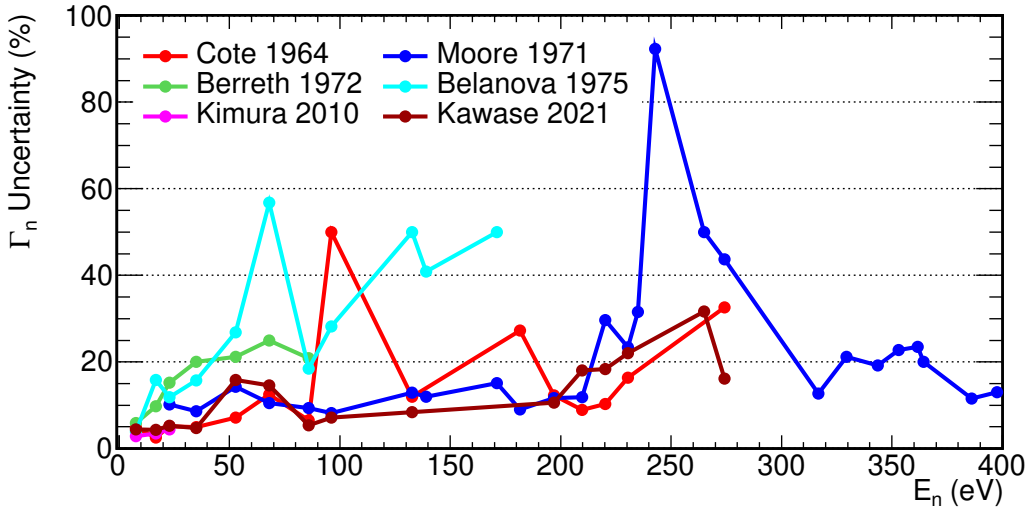

(a) ^{244}Cm

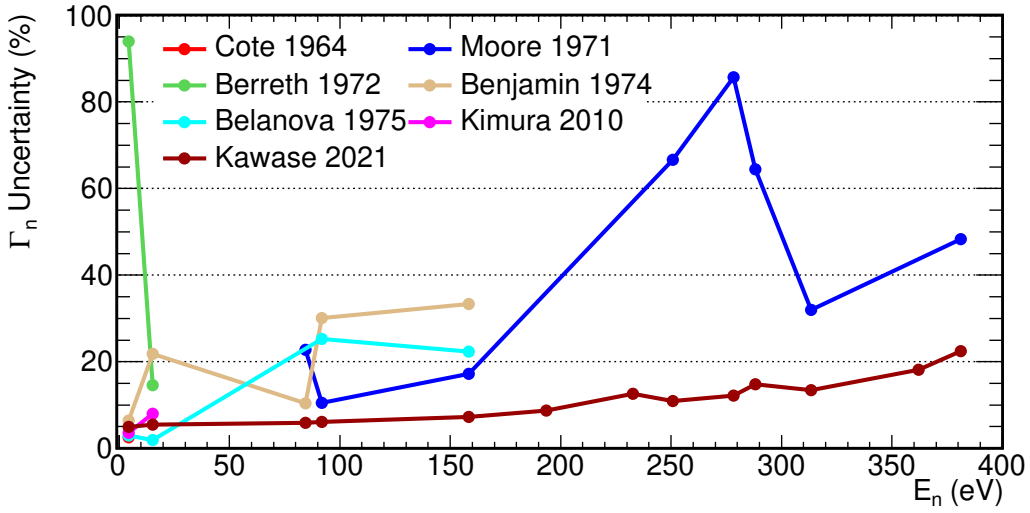

(b) ^{246}Cm

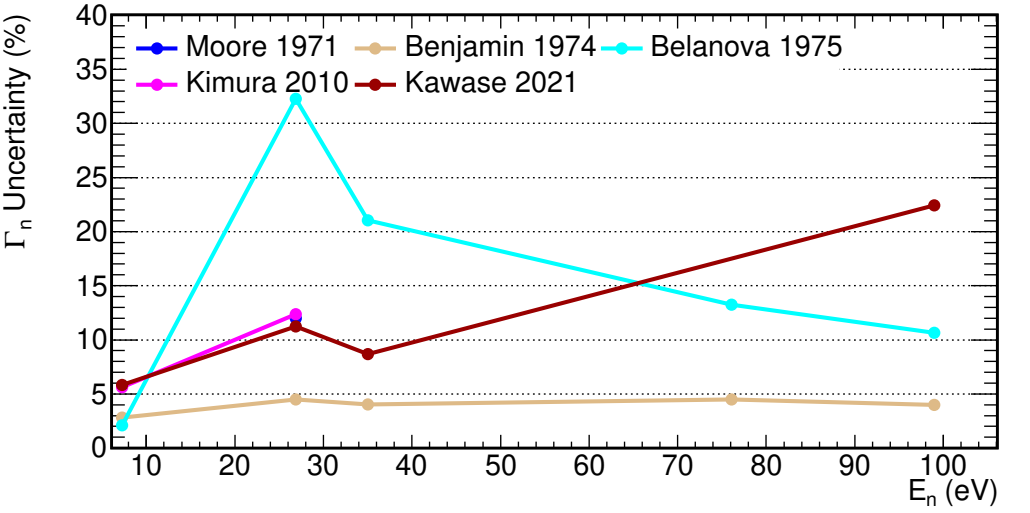

(c) ^{248}Cm

Figure 1.9: Uncertainty in the determination of the Γ_n reported in previous measurements of ^{244,246,248}Cm in the energy range between 0 and 400 eV.

(MTR) [43] with BF_3 counters. Three different samples were used in the measurement with ∼1.7 g of curium oxide each. These samples contain approximately 93% ^{244}Cm and from 0.1% to 4% ^{246}Cm. The resonance parameters of the first seven resonances of ^{244}Cm and the two first of ^{246}Cm were obtained.

- **Transmission measurement from Benjamin *et al.* in 1972 [7] (Benjamin).** This measurement was focussed on ^{248}Cm, for this reason a sample of ∼15 mg with 96.8% ^{248}Cm and 3.1% ^{246}Cm was used. The transmission measurement was performed with the Oak Ridge electron linear accelerator (ORELA) [44] and ^{6}Li detectors. A total of fifty resonances of ^{248}Cm and five resonances of ^{246}Cm were fitted from 7 eV to 3 keV.

- **Transmission measurement from Belanova *et al.* in 1975 [30] (Belanova).** The measurement was performed at the ITEhF and NIIAR reactors [45]. The samples used for the ^{244}Cm, ^{246}Cm and ^{248}Cm measurements contained, respectively, 73, 60 and 8 mg. The first eleven resonances of ^{244}Cm and the five resonances of ^{246}Cm were fitted with a constant radiative width of 37 meV. Also five resonances of ^{248}Cm were fitted with a radiative width of 40 meV.

- **Fission measurement from Maguire *et al.* in 1985 [34] (Maguire).** The second fission measurement was performed at the Rensselaer Intense Neutron Spectrometer (RINS) [46] with fission chambers. The samples had a purity higher than 97% and masses from 5 to 31 μg. The energy of the resonances and the Γ_f parameters were calculated for the first four resonances of ^{244}Cm, the first three of ^{246}Cm, and the first three of ^{248}Cm.

- **Capture measurement from Kimura *et al.* in 2010 [32] (Kimura).** The second capture measurement was performed at J-PARC [47] with an array of large germanium detectors (ANNRI) [48]. The samples measured in the experiment are the same as the one presented in this manuscript. The size of the dead-time corrections and the 'double-bunch mode' allowed to obtain the RP only up to 30 eV, even tough the cross sections were reported to EXFOR until almost 300 eV. Three resonances of ^{244}Cm, two resonances of ^{246}Cm, and two resonances of ^{248}Cm were fitted.

- **Fission measurement from Alekseev *et al.* in 2010 [35, 36, 37] (Alekseev).** The third fission measurement was performed at the neutron lead slowing-down spectrometer (LSDS-100) of the Institute for Nuclear Research (INR, Russian Academy of Sciences, Moscow) [49]. The measurements were performed with samples of 4.5 μg (^{244}Cm), 8.4 μg (^{246}Cm) and 3.6 μg (^{248}Cm) mass, and 8/5/5 resonances of ^{244}Cm/^{246}Cm/^{248}Cm were fitted.

- **Capture measurement from Kawase *et al.* in 2018 [33] (Kawase).** The experiment was performed in 2018, one year after the measurement described in this manuscript. The results of the analysis are presented in a recent publication [33], although the RP of the measurement are not uploaded to EXFOR yet. The measurement was performed at J-PARC [47] with an array of large germanium detectors (ANNRI) [48] with the same samples used in the Kimura and n_TOF

measurements. In this new experiment, the use of the 'single bunch mode' and the new high-speed DAQ system [50] has made it possible to extend the measurement range with respect to the measurement done by Kimura. The RP were calculated for the first sixteen resonances of ^{244}Cm, the first thirty of ^{246}Cm, and the first four of ^{248}Cm.

1.5 Evaluated resonance parameters

Two different evaluations of ^{244,246,248}Cm are present in the most recent data libraries: the one in JENDL-4.0 [20], which has been adopted by JEFF-3.3 [51] and ENDF/B-VIII.0 [52], and the one in BROND-3.1 [53]. The CENDL-3.2 [54] library does not contain Cm isotopes. The evaluations of ^{244,246,248}Cm are described in the following list:

- Evaluations of ^{244}Cm:
  - JENDL-4.0. The RP are taken from the evaluation of T. Nakagawa [55], already included in JENDL-3.2 library [56], considering the measurements of Moore, Benjamin and Maguire. JENDL-4.0 takes these RP and modifies the negative and first resonances to reproduce the thermal cross sections and resonance integrals.
  - BROND-3.1. The RP are taken from BROND-2.2 [57], which is based on the evaluation done by A.B. Klepatskij *et al.* [58] using the measurements from Cote, Belanova, Moore and Maguire.
- Evaluations of ^{246}Cm:
  - JENDL-4.0. The RP are taken from the evaluation of V.M. Maslov *et al.* [59], included in JENDL-3.3 [60] considering the measurements of Berreth, Benjamin, Belanova, Cote, Moore and Maguire. JENDL-4.0 takes these RP and modifies the negative and first resonances to reproduce the thermal cross sections and resonance integrals.
  - BROND-3.1. The RP are taken from the evaluation done by V.M. Maslov *et al.*, i.e. this evaluation is the same as the one in JENDL-3.3.
- The evaluations of ^{248}Cm:
  - JENDL-4.0. The RP are taken from the evaluation of Y. Kikuchi and T. Nakagawa [61], included in JENDL-3.3, and considering the measurements of Benjamin, Moore and Maguire. JENDL-4.0 takes these RP, adding a negative resonance at -30 eV to reproduce the thermal cross sections.
  - BROND-3.1. The same evaluation as the one in JENDL-4.0 is taken in this case.

Chapter 2

Experimental setup

This chapter is dedicated to describe the general aspects of the measurement. As previously mentioned in Section 1.2, new experimental data on ^{244,246,248}Cm are necessary to reduce and asset the uncertainty in the evaluations of the capture cross sections. For this reason, a new measurement of these isotopes has been performed at n_TOF. The three main elements of any capture cross section measurements are: a sample with the isotope to be measured, a neutron beam, and a setup to detect the capture events. This three elements are described in this chapter.

The measurement has been done at the two areas of the n_TOF facility [62]. The EAR1 [63] has a flight path of 185 m, and the EAR2 [64] has a flight path of 19 m and $\sim$40 times larger neutron fluence. The characteristics of the facility are presented in Section 2.1 and the beam properties in Section 2.5.

There are two samples in this measurement, one prepared to measured the capture cross section of ^{244}Cm (^{244}Cm sample) and the other one prepared to measure the capture cross section of ^{246,248}Cm (^{246}Cm sample), the characteristics of the two are presented in Section 2.4. Both samples contain ^{240}Pu that is also analysed.

Both the ^{244}Cm and ^{246}Cm samples have been measured in EAR2 with C_6D_6 detectors [65]. In addition, the ^{244}Cm sample has been measured also in EAR1 with the Total Absorption Calorimeter (TAC) [66]. The detection systems used in the experiment are described, respectively, in Sections 2.2 and 2.3.

2.1 n_TOF facility at CERN

The n_TOF facility is a pulsed neutron source located at CERN designed in 1998 by C. Rubbia *et al.* [62] to measure neutron cross sections with high energy resolution over a wide range of energy. Extended information about the n_TOF facility can be found in [63, 64, 67, 68] and a brief description is presented in this document.

Neutrons at n_TOF are produced by spallation reactions in a lead target. The Proton Synchrotron (PS) accelerator at CERN delivers to the n_TOF spallation target a total of $\sim 7 \cdot 10^{12}$ protons per pulse in dedicated mode and $\sim 4 \cdot 10^{12}$ in parasitic mode. The

energy of the protons is 20 GeV, and the distribution in time of the pulses has a Root Mean Square (RMS) of 7 ns. There can be up to 0.8 pulses per second at n_TOF. The spallation neutrons produced in the lead target, shown in Figure 2.1, can reach one of the two experimental areas of the facility: the EAR1, located at 185 m from the target in the horizontal direction; and the EAR2, located at 19 m in the vertical direction.

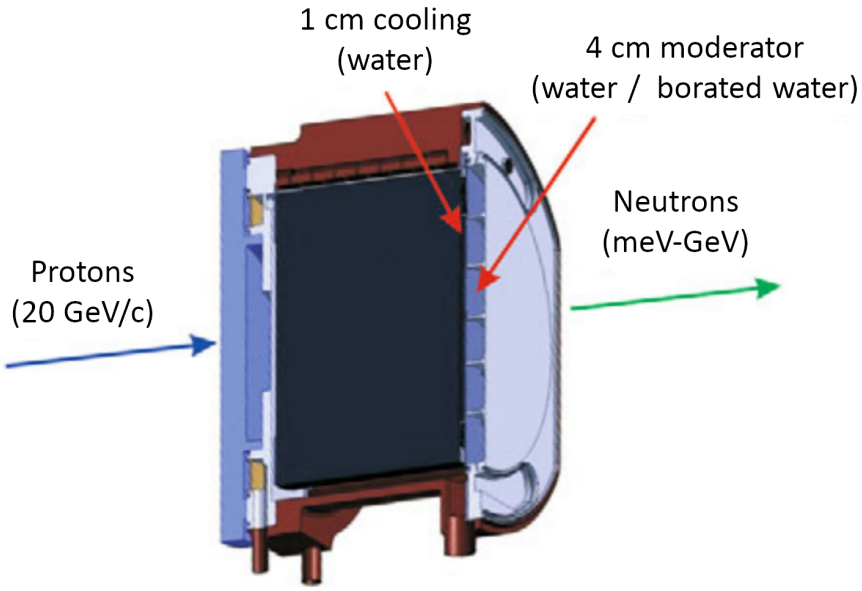

Figure 2.1: Graphical representation of the CERN's n_TOF spallation target [63].

The kinetic energy of the neutrons (E_n) is calculated by means of the Time-Of-Flight (TOF) technique, from the distance covered by the neutrons (L) and the time the neutrons travel (t):

$$E_n = E - m_n c^2 = \sqrt{c^2 p^2 + m_n^2 c^4} - m_n c^2 = m_n c^2 \left(\frac{1}{\sqrt{1 - \frac{v^2}{c^2}}} - 1 \right) \tag{2.1}$$

where c is the speed of light, m_n the mass of the neutron and p the momentum of the neutron. The velocity of the neutron is calculated as $v = L/t$. If the kinetic energy of the neutron is below a few tens of MeV, the classical formula can be used for most practical purposes:

$$E_n = \frac{1}{2} m_n v^2 \tag{2.2}$$

The different constants in equation 2.2 can be grouped:

$$E_n = \left(\frac{72.29 \cdot L}{t} \right)^2 \tag{2.3}$$

where E_n is given in MeV, L in m and t in ns.

The n_TOF facility operation is usually divided into three phases. Phase-1 goes from the beginning of the facility in 2000 up to 2004, and Phase-2 from 2009 up to 2012,

and Phase-3 from 2014 up to 2018. Between Phase-1 and Phase-2 the spallation target changed, and between Phase-2 and Phase-3 the EAR2 was built [64, 69, 70].

Since the beginning of n_TOF, there was a considerable effort to improve the nuclear data for actinides required for nuclear waste management and for the design and operation of innovative nuclear systems. In table 2.1 all the actinides measurements performed at n_TOF are presented.

Detector	C_6D_6	TAC	TAC+FIS	FIC	PPAC	MGAS
Reaction	(n,γ)	(n,γ)	(n,γ)+(n,f)	(n,f)	(n,f)	(n,f)
Phase-1	^{232}Th	^{233,234}U ^{243}Am ^{237}Np ^{240}Pu		^{233,235,238}U ^{241,243}Am	^{232}Th	
Phase-2	^{236,238}U ^{241}Am	^{238}U ^{241}Am	^{235}U		^{232}Th ^{237}Np	^{240,242}Pu
Phase-3	^{241}Am ^{242}Pu ^{244,246,248}Cm ^{238}U	^{244}Cm	^{233}U		^{237}Np ^{241,243}Am	^{230}Th ^{237}Np ^{240}Pu

Table 2.1: Actinides measured at n_TOF, together with the detection system used and the Phase where the measurement took place.

The capture cross section of a total of 14 actinides have been measured with the C_6D_6 detectors [65, 71] or with the TAC [66]. There are some cases, for example, ^{241}Am, that has been measured several times to reduce the systematic uncertainties: the first time at EAR1 with the TAC [72], the second time with the C_6D_6 detectors [73] at EAR1, and recently in 2017 a new measurement in EAR2 was done with the C_6D_6 to profit from the higher instantaneous flux [74].

A total of 11 fission cross sections of actinides have been measured at n_TOF, using FIC [75], PPAC [76], and MGAS [77] detectors. In 2010 (Phase-2), there was a new development at n_TOF to measure the capture and fission cross sections of actinides simultaneously, using the TAC and MGAS detectors in coincidence. The TAC events due to fission reactions are tagged with the MGAS detector to obtain the capture and fission cross sections and the capture to fission cross section ratio (α-ratio) [78, 79].

The EAR2 was built 19 m in the vertical direction from the spallation target. The shortest distance allows to increase the neutron fluence in a factor of $\sim$40 in the region between 10 eV and 100 MeV with respect to the EAR1. The higher instantaneous fluence enables measuring samples with lower mass or/and higher radioactivity. On the other hand, the energy resolution is better in EAR1 (Sections 2.5.2 and 2.5.3). In Figure 2.2 the different components of the beamline are presented. A first collimator reduces the beam halo for both areas, and a second collimator gives the desired shape. The majority of the charged particles are removed from the beam using magnets, also there is the option of insert filters in the beam to suppress neutrons of selected energies.

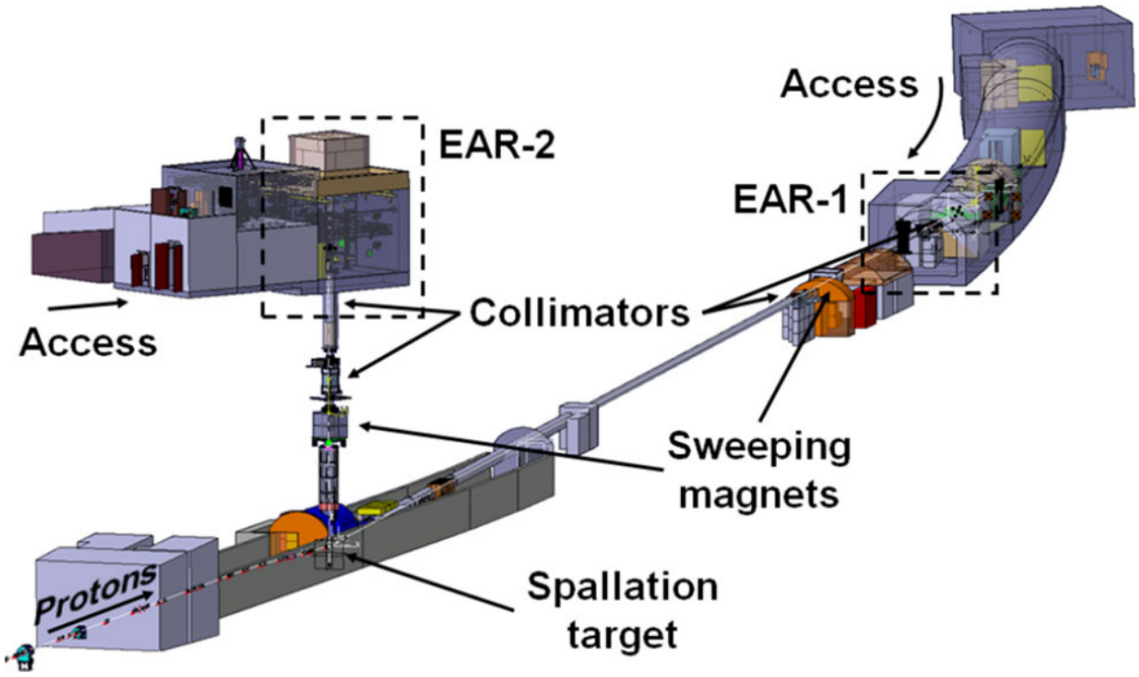

Figure 2.2: Graphical representation of the beam lines of the n_TOF facility [80].

2.1.1 Data Acquisition and the PSA

All the detectors used during the Cm campaign profits from a fully digital Data AcQuisition system (DAQ), described in Ref. [81]. The digitised detector signals are stored in binary files saved in the CERN Advanced STORage manager (CASTOR) [82]. These files are organised in runs; each run has a specific number and corresponds to the data measured between a start and a stop of the DAQ.

One of the advantages of the acquisition system is that it allows to analyse the data offline using different Pulse Shape Analysis (PSA) routines [83]. The read-out of all the detector channels is done via high-performance digitisers, ADQ412 or ADQ414, with 12 or 14 bit resolution respectively, which are operated at 1 GSamples/s maximum [84]. The data acquisition is triggered for each proton pulse by an external signal given by the PS. For each pulse it is possible to record at least 100 ms. This allows the reconstruction of signals above 0.02 eV neutron energy in EAR1 and even lower energies in EAR2. In order to reduce the size of the data, a software threshold algorithm is applied to store only the part of the data containing true detector signals with an amplitude larger than the threshold.

Detailed information concerning the PSA routines used in this work can be found in [85, 86] and in chapter 2.4 of M. Sabate-Gilarte thesis [87]. The pulsed recognition is based on the first derivative calculation in each segment and other user-defined criteria referred to as user input parameters (i.e. minimum and maximum amplitude, width, area to amplitude ratio, etc.). The routine detect signals in the tale of other signals using the

pulse shape fitting [88], i.e. pile-up recognition. This technique consists of comparing each signal with reference pulse shapes characteristic of each detector.

2.2 Detectors in EAR1

Two detectors were used in the EAR1 measurement: the TAC [66], to detect the gamma-rays emitted after the neutron capture; and the silicon flux monitor (SiMon) [89], to monitor the neutron beam and to obtain the energy dependence of the neutron fluence.

2.2.1 n_TOF Total Absorption Calorimeter (TAC)

The cascade detection efficiency depends on the decay scheme of the compound nucleus, in general, which is usually only known at low excitation energies. The γ-rays emitted after the neutron capture are expected to vary not only from one nucleus to another but also, in general, from one resonance to another, within the same nucleus. As a consequence, the efficiency when detecting these cascades could vary as a function of neutron energy, which can make the measurement very difficult or even impossible. One way to overcome this difficulty is to use a calorimeter. By having a very high detection efficiency (the TAC has an efficiency of up to 99%, depending on the analysis cuts), the variations of the efficiency between different resonances will be small.

The TAC is a 4π segmented scintillator array with 40 individual BaF_2 crystals. Twenty-eight crystals have a hexagonal shape, and twelve crystals have a pentagonal shape. Each crystal is encapsulated in a 1 mm thick borated carbon fibre to decrease the neutron sensitivity. The capsules are coupled to Photonics XP4508B photomultipliers and attached to an aluminium holder mounted in a structure that keeps the entire detector shell as shown in Figure 2.3. The whole TAC is divided into two hemispheres that can be opened and closed, as it is shown in the left panel of Figure 2.3. The TAC forms a spherical shell of ∼10 cm inner radius and ∼25 cm outer radius, roughly covering 95% of the total solid angle.

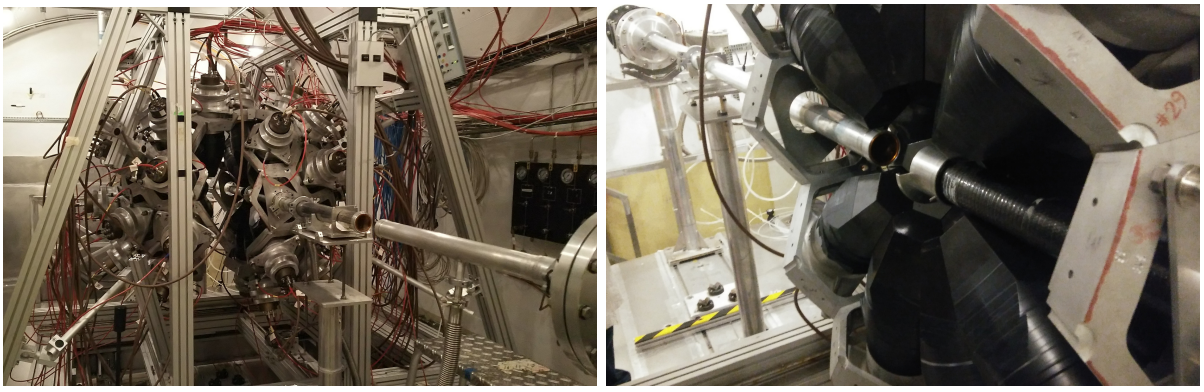

(a) General view of the TAC detector almost closed (b) The TAC opened and the beam pipes and the sample holder inside

Figure 2.3: TAC setup in the experimental EAR1.

The ^{244}Cm sample (Section 2.4) was placed in the center of the TAC using a sample holder designed for the experiment (Figure 2.4).

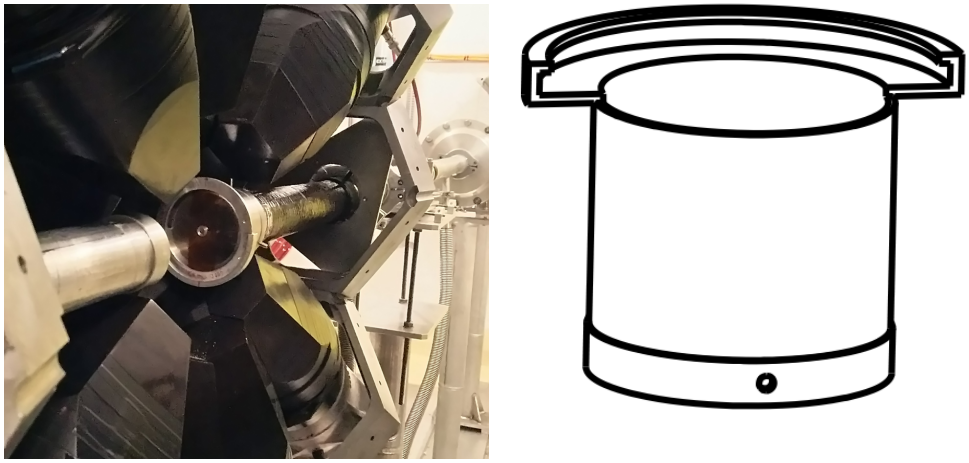

Figure 2.4: On the left panel, the TAC with the sample holder and the ^{244}Cm sample in place. On the right, a drawing of the sample holder.

As previously mentioned, the TAC is operated as a calorimeter. For this purpose, the 40 BaF_2 crystals measure in coincidence. Every time the TAC detects a γ-ray, a coincidence window is opened. The total energy deposited in the TAC during this period (E_{sum}) and the number of crystals (m_{cr}) contributing to the energy deposition are then computed, leading to the creation of events, with a characteristic TOF (neutron energy), E_{sum} and m_{cr}. Conditions (or cuts) applied to E_{sum} and m_{cr} are applied to reduce the signal to background ratio. An example of a digitised TAC signal is shown in Figure 2.5.

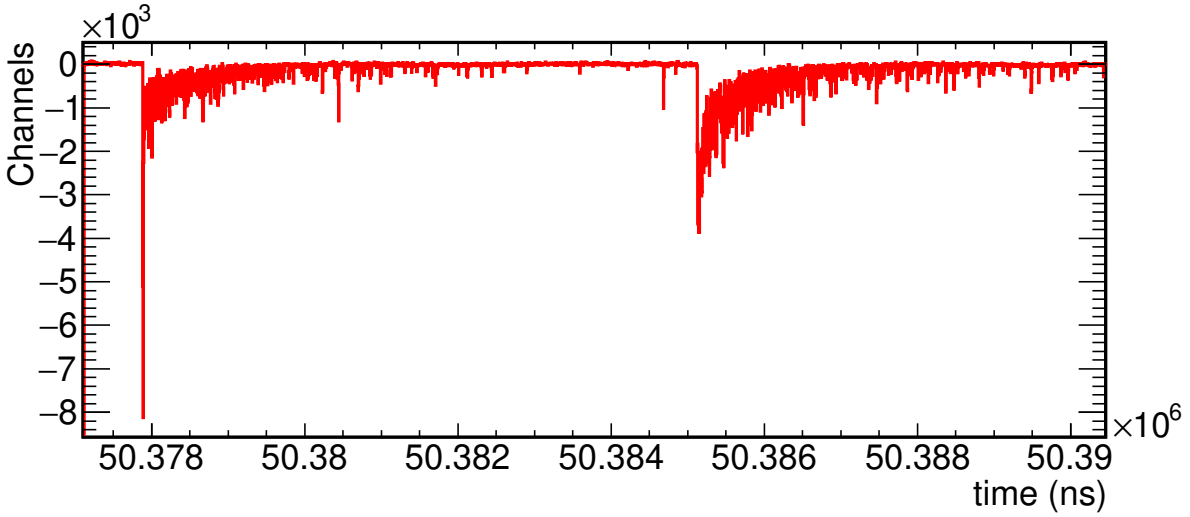

Figure 2.5: Raw buffer digitised from one BaF_2 detector. The signal at the left corresponds to a γ-ray and the one at the right to an α-particle.

2.2.2 SiMon detector

The SiMon detector is constructed to interfere as little as possible with the neutron beam [89]. The setup consists of 4 silicon detectors with a thickness of 300 μm out of the beam as shown in the scheme of the left panel of Figure 2.6. The silicon detectors face a thin Mylar foil with a 600 μg/cm^2 thick deposit of ^{6}LiF placed on the beam. The outgoing particles coming from the ^{6}Li(n,α)t reaction are detected by the silicon detectors. The cross section of this reaction is smooth and a standard below 1 MeV, which allows to perform a precise measurement of the energy dependence of the neutron beam. In the right panel of Figure 2.6 the pulse height spectra of the four silicon detectors are presented. The peak at the right part of the spectra corresponds to the detection of triton particles and is used to monitor the neutron beam.

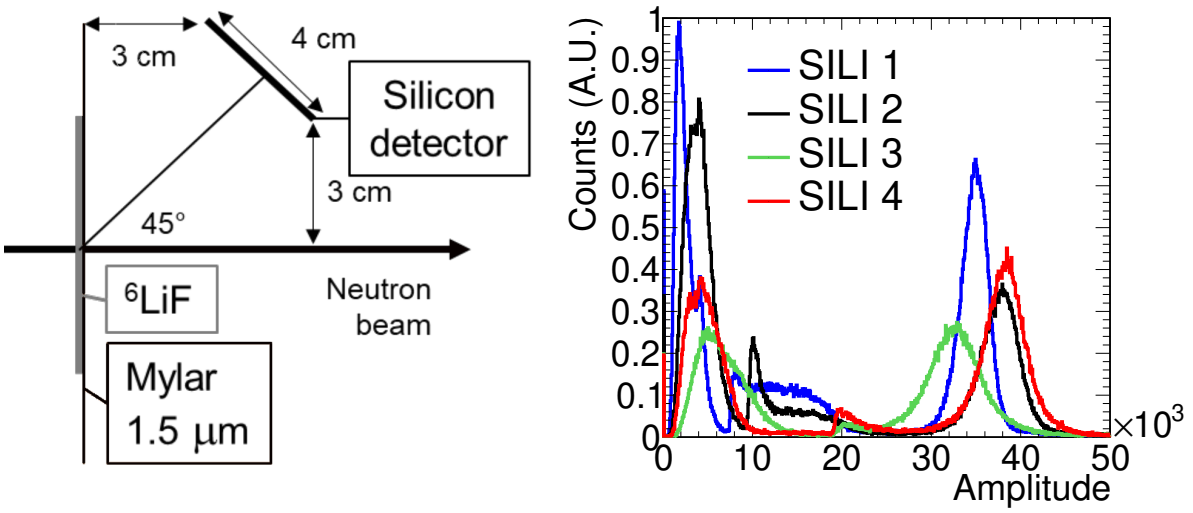

Figure 2.6: On the left panel, a scheme of the SiMon detector [89]. On the right panel, the pulse height spectra measured in the silicon detectors.

2.3 Detectors in EAR2

The measurement of the capture cross sections of ^{244,246,248}Cm and ^{240}Pu have been done at EAR2 with three C_6D_6 detectors. The silicon flux monitor for EAR2 (SiMon2) [90], similarly to the SiMon in EAR1, was used to monitor the beam and to obtain the energy dependence of the neutron fluence.

2.3.1 C_6D_6 detectors

The γ-rays emitted in the (n,γ) cascade have been detected with three commercial BICRON liquid scintillators [71]. They have been placed horizontally at 5 cm from the centre of the sample using a structure to fix the position of the detectors during the three months of the measurement (left panel of Figure 2.7).

Figure 2.7: Left: The three BICRON detectors used to detect the (n,γ) cascades, in the lower part of the picture the chamber with the SiMon2 detector is shown. Right: BICRON C_6D_6 detector.

Each BICRON detector consists of a thin aluminium cell filled with C_6D_6 optimised to reduce the neutron sensitivity. The main action in the optimisation was to replace the borosilicate window of the Photomultiplier Tube (PMT) with a window made of quartz [71]. The PMT used in the measurement is a Photonis XP1208. The C_6D_6 container has a volume of 618 cm^3 and is covered by a Teflon tube coiled around the cell, used for the expansion of the scintillation liquid. A detailed scheme of the detector is given in Appendix A.

The BICRON signals stored in CASTOR are processed with the PSA routine. In the case of the C_6D_6 detectors, the routine provides the amplitude and the time of each signal. The average signals of the three BICRON detectors, used by the PSA routine to make the fit to the measured buffers, are presented in Figure 2.8. The detectors suffer from a systematic reflection at $\sim$800 ns after the original signal. These reflections are small compared with the size of the original signal (approximately 1% in height) but they have been included in the averaged shapes to avoid being detected as additional γ-rays.
In Figure 2.9 the excellent functionality of the PSA routine for the BICRON detectors is presented. The routine uses the tail of the previous signal as the baseline for the next signal and thus correct the possible pile-up effects.

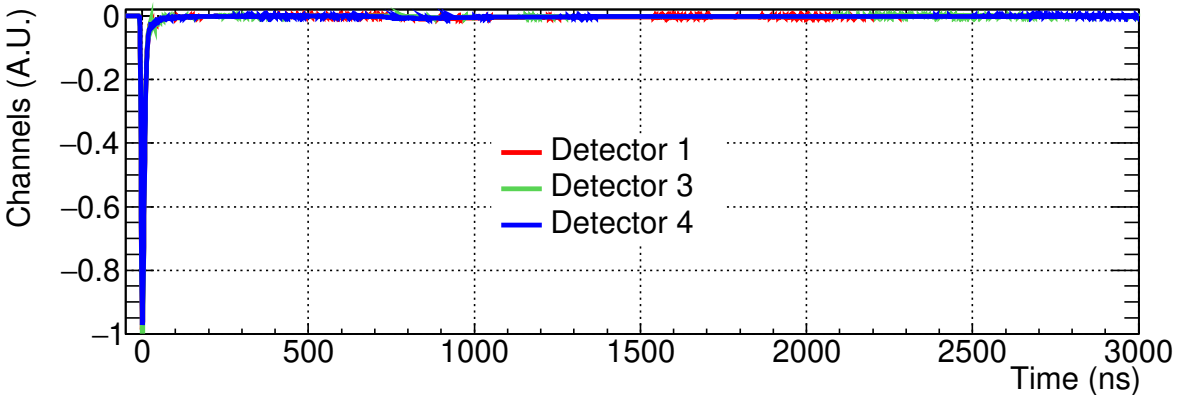

(a) All the range of the signals

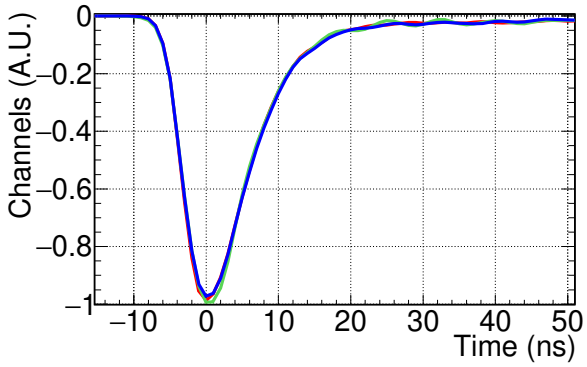

(b) Zoom at low times

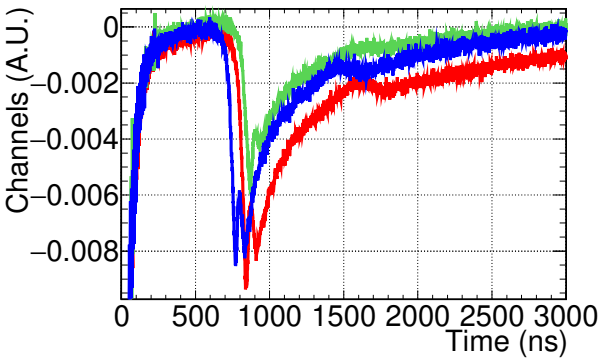

(c) Zoom for reflections

Figure 2.8: Average signals of the three BICRON detectors in subfigure (a). Subfigure (b) is a zoom of subfigure (a) in order to observe the peak of the signals. Subfigure (c) is a zoom of subfigure (a) to observe the reflections of the signals.

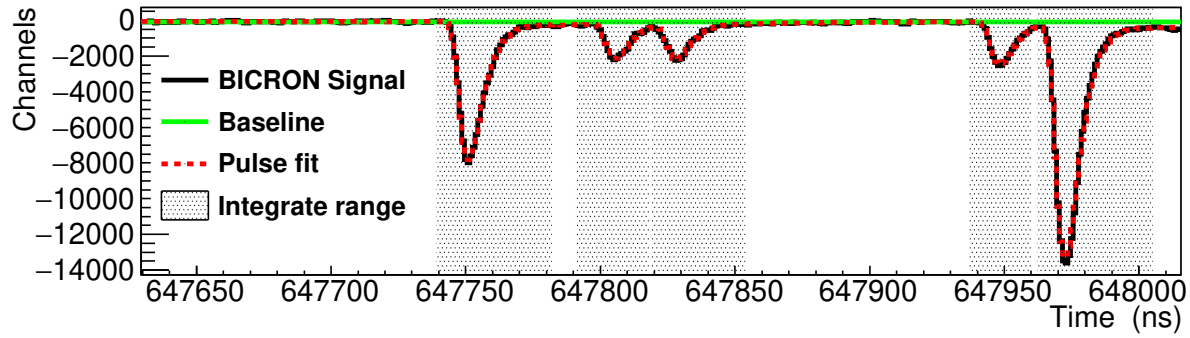

Figure 2.9: Fragment of BICRON digitised signals processed with PSA routine [83].

The samples are kept in the neutron beam's centre with a sample holder designed for the experiment, shown in Figure 2.10.

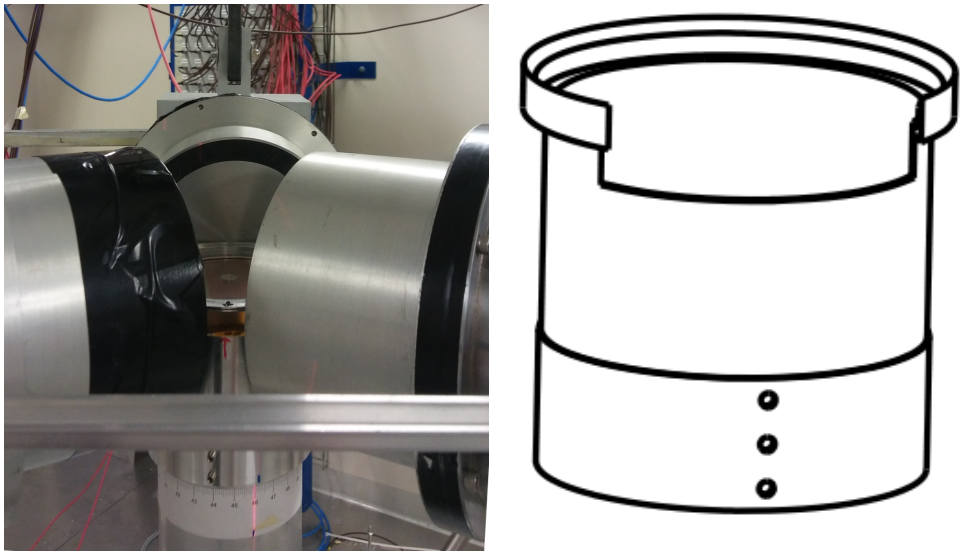

Figure 2.10: The left picture is the sample holder and the three BICRON detectors. The right panel is a drawing of the sample holder used in the experiment.

2.3.2 SiMon2 detector

The SiMon2 detector [90] is an upgrade of the SiMon detector installed in EAR1 (see Section 2.2.2). The new silicon pads have 3x3 cm^2 areal surface and a thickness of 300 μm. The Mylar foil has a 105 $\mu g/cm^2$ thick deposit of ^{6}LiF, which is almost six times thinner than the deposit in EAR1. The chamber with the SiMon2 is presented in the left picture of Figure 2.7. The thinner sample, the improvement in the energy resolution and the electronics with respect to SiMon lead to an excellent separation of the triton and alpha particles, as shown in Figure 2.11. The low level of noise with respect to the signals of the fission fragments is also observed.

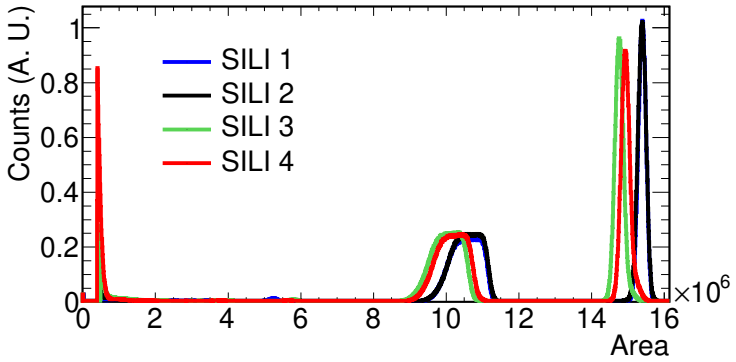

Figure 2.11: Signal area distribution in the SILI detectors. The alpha peaks are located at $\sim 1 \cdot 10^7$ area units and the triton peak are located at $\sim 1.5 \cdot 10^7$ area units.

2.4 Cm samples

The Cm samples were acquired by the JAEA from the Russia Research Institute of Atomic Research, and used in a capture cross section measurement performed at J-PARC (Japan) [32] before the measurement at n_TOF. Two samples were provided for the measurement:

- **^{244}Cm sample**. This sample is prepared to measure the capture cross section of ^{244}Cm. The sample is made with two pellets inside their Al cases, like the ones observed in Figure 2.12 with approximately ∼0.4 mg of ^{244}Cm and ∼0.2 mg of ^{240}Pu in each pellet.

- **^{246}Cm sample**. This sample is prepared to measure the capture cross section of ^{246,248}Cm, although there is also ^{244}Cm. The sample is made with one pellet inside the Al case, that contains ∼0.4 mg of ^{244}Cm, ∼1.1 mg of ^{246}Cm, ∼0.2 mg of ^{248}Cm and ∼0.2 mg of ^{240}Pu.

The three Cm pellets (two for the ^{244}Cm sample and one for the ^{246}Cm sample) with a weight of ∼27 mg each are in the form of oxide, which has been mixed with aluminium powder and pressed to create cylinders of 0.5 mm height and 2.5 mm radius. The pellets were encapsulated in aluminium cases, whose dimensions are presented in Figure 2.12.

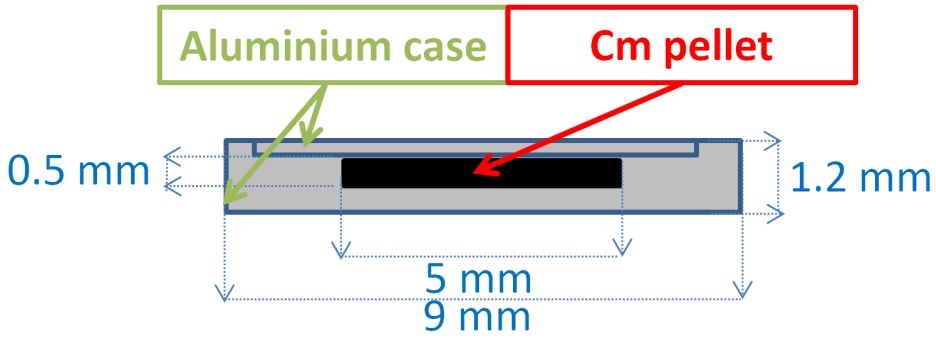

Figure 2.12: Cm pellet inside of the Al case used for the Cm campaign at n_TOF.

The samples contain several Cm isotopes together with ^{240}Pu, which is the daughter of ^{244}Cm ($T_{1/2}$ (^{244}Cm): 18.11 years [91]). Their isotopic composition was measured in June 2010 using a small amount of the same substance used to make the samples. The characterisation was done with a Thermal Ionization Mass Spectrometer (TIMS) to measure the relative abundances of each Cm isotope. The fraction of ^{240}Pu with respect to ^{244}Cm and ^{246}Cm were determined by α-particle spectrometry at KURRI [92]. The isotopic abundances and their uncertainties in August 2017 have been computed from the values reported by Kimura *et al.* [32], and are presented in Table 2.2. Only the relative abundances of the different isotopes were determined with these two measurements, but not the absolute masses in each sample. Therefore, in this work the Cm capture cross sections are normalised to the first resonance of ^{240}Pu in JEFF-3.3 [51]. The ratio ^{240}Pu/^{244}Cm in the ^{244}Cm sample has been increased from 0.151 ± 0.007 in 2010 to 0.515

Isotope	Half-life (years)	^{244}Cm sample	^{246}Cm sample
^{240}Pu	6561	30.8 ± 0.6	9.2 ± 0.2
^{243}Am	7364	0.6 ± 0.1	1.2 ± 0.2
^{244}Cm	18.11	59.9 ± 1.1	20.1 ± 0.4
^{245}Cm	8423	2.4 ± 0.3	1.0 ± 0.3
^{246}Cm	4706	6.3 ± 0.3	57.0 ± 1.2
^{247}Cm	$1.56{\cdot}10^{7}$	-	2.8 ± 0.4
^{248}Cm	$3.48{\cdot}10^{5}$	-	8.7 ± 0.2

Table 2.2: Isotopic abundances (per cent) during the Cm campaign, in August 2017.

± 0.014 in 2017, i.e. its uncertainty has decreased from 4.8% to 2.8%. In the ^{246}Cm sample, the uncertainties in the ^{240}Pu/^{244}Cm, ^{240}Pu/^{246}Cm and ^{240}Pu/^{248}Cm ratios have been decreased, respectively, from 5.0%, 5.2% and 5.4% in 2010 to 2.6%, 2.9% and 3.3% in 2017.

In the resonance analysis, it has been found that the samples contain some small amounts of ^{243}Am, not reported in the TIMS or KURRI measurements. The strongest ^{243}Am resonance at 1.35 eV has been used to determine the amount of this isotope in the samples, by assuming a similar detection efficiency than for other actinides and the JENDL-4.0 RP [20]. The capture to fission ratio for this resonance is less than 0.1%, so the contribution due to fission reactions have been neglected. Figure 2.13 shows the experimental yields in EAR2 in the energy region of the strongest ^{243}Am resonance. The abundance of ^{243}Am obtained in the fit is a 0.6(1)% in the ^{244}Cm sample and a 1.1(1)% in the ^{246}Cm sample. These values are compatible with the ones obtained by Kimura *et al.* [32], 0.63(4)% for ^{244}Cm sample and 1.06(10)% for the ^{246}Cm sample.

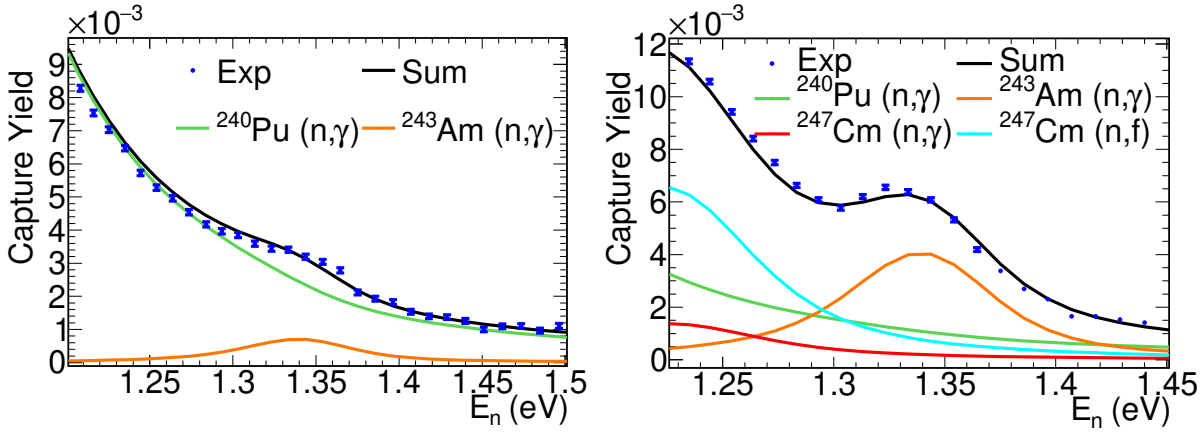

(a) ^{244}Cm sample (b) ^{246}Cm sample

Figure 2.13: Experimental yield (Exp) of the ^{244}Cm (left) and ^{246}Cm (right) samples in the region of the strongest resonance of ^{243}Am. The black line (Sum) is the sum of the contributions of the different isotopes.

The rest of ^{243}Am resonances are much lower than the strongest one, and they do not play a significant role in this measurement.

In order to position the Cm samples in the centre of the n_TOF neutron beam, they were placed between two Mylar foils of 10 μm thickness hold by two aluminium rings located out of the neutron beam. A Kapton foil of 30 μm thick with a hole with the dimensions of the Al cases were used to keep the Cm samples in the centre of the rings. A picture and a schematic view of the rings are presented in Figure 2.14.

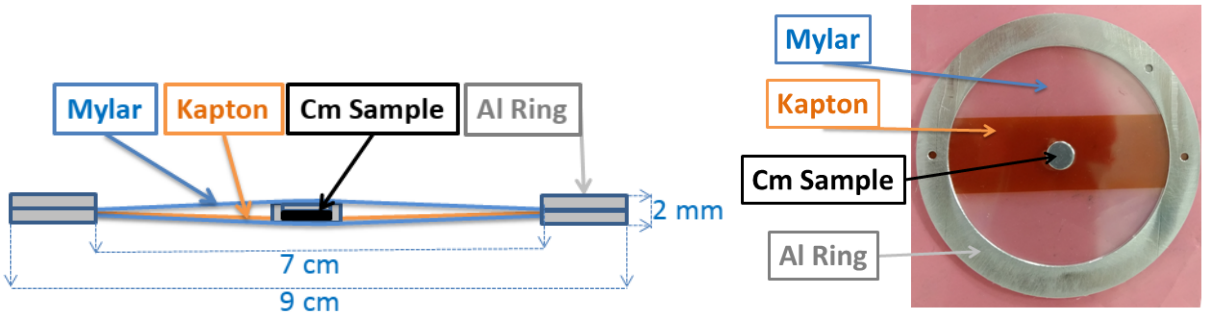

Figure 2.14: Sketch (left) and picture (right) of the Cm samples together with the Kapton and Mylar foils and the Al rings.

Dummy samples were also built to measure the background induced in the detectors by the interaction of the neutron beam with the material of the samples that are not actinides (aluminium, Kapton and Mylar).

2.5 Beam characterisation

This section is devoted to describe the neutron beam in both experimental areas: the monitoring of the beams (2.5.1), the energy dependency and beam profiles (2.5.2 and 2.5.3), and the time-energy distributions of the neutron beams, known as Resolution Function (RF) (2.5.4 and 2.5.5).

2.5.1 Neutron monitoring

The proton beam has been monitored with the Beam Current Transformer (BCT) and PKUP detectors, and the neutron beam with SiMon and SiMon2. These detectors are briefly described in the following list:

- The BCT, designed to get directly the number of protons impinging on the spallation target. The detector is located about 6 meters upstream with respect to the target in the proton beam line providing an absolute measurement of the number of protons.
- The Wall Current Monitor, usually referred to as the PKUP, measures the proton beam intensity in each pulse just after the BCT and provides a signal with an area

proportional to the proton beam intensity. This signal is used to start the data acquisition and is stored in the n_TOF DAQ.

- SiMon, to monitor the neutron beam in EAR1 (Section 2.2.2).
- SiMon2, to monitor the neutron beam in EAR2(Section 2.3.2).

The BCT detector is managed by the PS team, whereas the PKUP is controlled by the n_TOF collaboration. In figure 2.15 the good agreements between both detectors are presented.

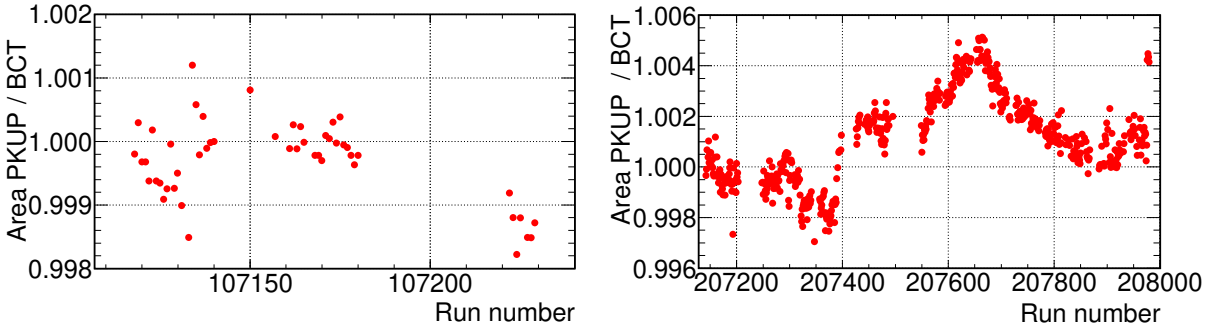

Figure 2.15: Comparison of the area of the PKUP detector with the BCT. In the left (right) panel the comparison for the EAR1 (EAR2) during the Cm campaign. These comparisons shows that the BCT and the PKUP area agree within 0.2% in EAR1 and 0.5% in EAR2.

The evolution of the gains of the SiMon and SiMon2 detectors along the measurements have been characterised by determining the position of the tritium peak for each run. The results, presented in figure 2.16, show that the gains varied less than 4% (SiMon) and 2% (SiMon2). These variations have been taken into account in any case for the integration of the amplitude spectra, which in the case of the SiMon was performed in the tritium peak, and in the case of the SiMon2 in both the alpha and tritium peaks.

The neutron beam is monitored with SiMon and SiMon2 detectors. In Figure 2.17 the ratio between these detectors and the PKUP are illustrated. In EAR1, both the SiMon and the PKUP values are compatible within uncertainties due to counting statistics. On the contrary, in EAR2 the SiMon2 and PKUP values are compatible only at the beginning of the measurement. Then the ratio between the counts registered in both detectors start to decrease, reaching up to 3% less than the initial value. In Figure 2.18, the ratio between the counts in the Simon2 and the C_6D_6 detectors is illustrated for the measurements with the ^{244}Cm sample. The counts in both detectors are proportional to the number of neutrons in the beam and compatible during all the measurement, indicating that the 3% decrease observed in Figure 2.17 is due to a real decrease in the number of neutrons with respect to the proton current provided by the BCT and the PKUP, and not to a problem in the SiMon2. The neutron decrease could be associated with the optics of the proton beam or with a small change on the point where the beam impinges the lead target.

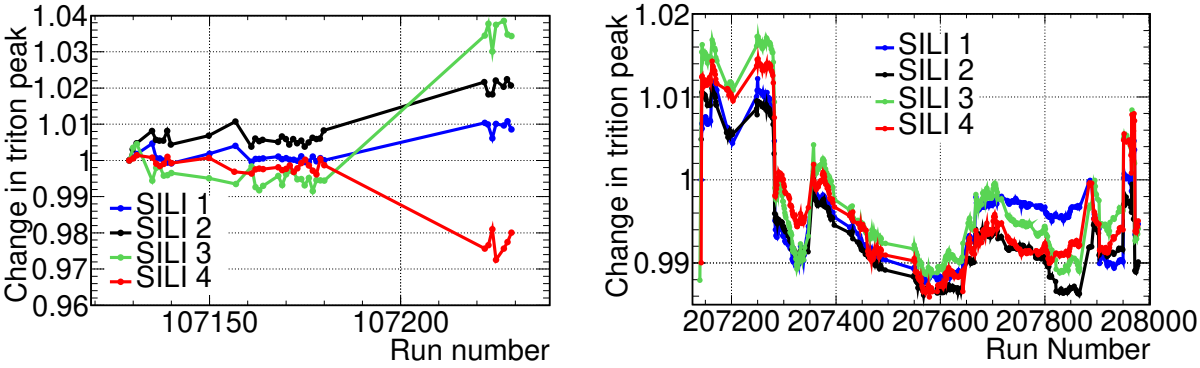

(a) SiMon (EAR1) (b) SiMon2 (EAR2)

Figure 2.16: Evolution of the position of the triton position peaks in the SiMon detector (left) and in the SiMon2 (right) during the Cm campaign in EAR1 and EAR2 respectively.

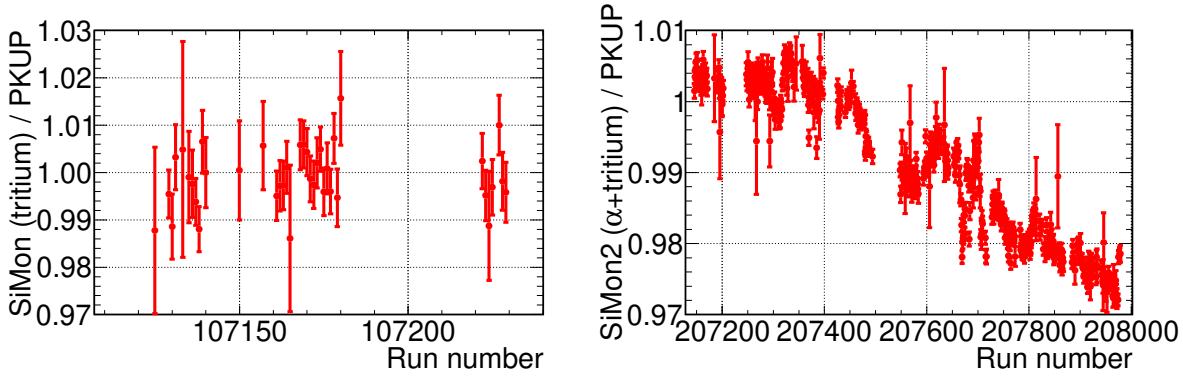

(a) SiMon (EAR1) (b) SiMon2 (EAR2)

Figure 2.17: Ratio (re-scaled) between the number of counts in the SiMon1 (left) and the SiMon2 (right) and the PKUP detector for each run of the Cm campaign for primary pulses.

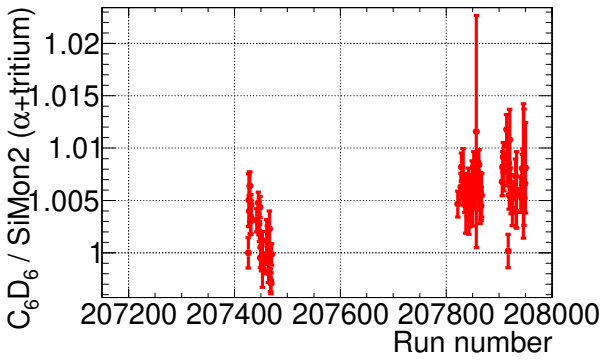

Figure 2.18: Ratio (re-scaled) between the number of counts in C_6D_6 and the SiMon2 for each run measuring the ^{244}Cm sample in EAR2 for primary pulses.

The same consistency studies have been also done for parasitic pulses in EAR1 and EAR2, and similar results have been found with respect to the stability of the measurements. The only difference found was in the ratio between the counts in the SiMon2 and the counts in the PKUP for EAR2. The differences are presented in Figure 2.19. The ratio decreases a 7% in the region close to run 207665. This effect was studied in detail, and the conclusion is that the reduction of the neutron fluence was produced by a shift of the impact position on the lead target of the parasitic proton beam. The accelerator team confirmed this shift. According to previous Monte Carlo simulations, the beam misalignment done by the accelerator team should not affect the neutron beam.

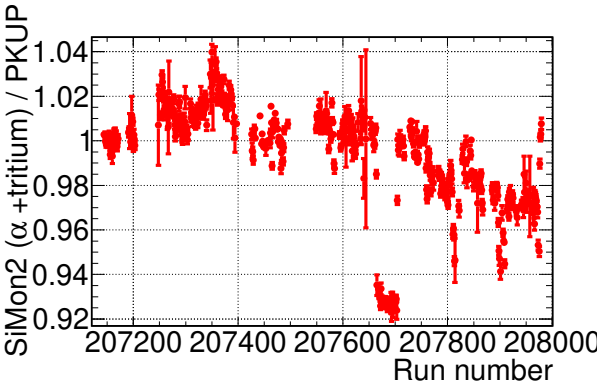

(a) Parasitic pulses

Figure 2.19: Ratio (re-scaled) between the number of counts in the SiMon2 and the PKUP detector for each run of the Cm campaign for parasitic pulses.

After the Cm campaign was finished, different misalignments of the proton beam were studied, and it was found that small misalignments of the proton beam can have a substantial effect on the neutron beam in EAR2. This effect was found thanks to the precise monitoring work done in the Cm campaign and it was considered during the rest of the experiments done in Phase-3.

2.5.2 Neutron fluence and beam profile in EAR1

The energy dependence of the neutron fluence in EAR1 has been obtained from the SiMon detector. Dedicated measurements of the neutron fluence were performed in 2014 with various detectors [93], but there can be small changes in the fluence from one year to another due to changes in the boron content present in the neutron water moderation circuit located just after the spallation target.

The fluence during the Cm campaign is calculated with equation:

$$\phi(E_n) = \frac{C(E_n)}{\varepsilon(E_n)(1 - e^{-n\sigma_t(E_n)})\frac{\sigma_r(E_n)}{\sigma_t(E_n)}} \tag{2.4}$$

where ϕ is the fluence (neutrons per pulse), C are the number of counts in the detector per pulse, ε is the efficiency, n is the areal density (atoms/barn) of the ^{6}Li deposit, and σ_r

and σ_t are, respectively, the reaction and total cross sections. In the energy range of this measurement, between 0.1 and 100 eV, the detection efficiency of the SiMon is constant (9%) [93].

The Cm campaign was two weeks long, so in order to reduce the uncertainty due to counting statistics, the data of the SiMon during the entire year was used. During this time, the SiMon detector was always located in the same position, and no variations on the boron content of the moderator are expected. The fluence evaluated in 2014 is compared with the fluences measured during the Cm campaign and during the entire year 2017 in Figure 2.20. The last two measurements are compatible, and thus the fluence of the year 2017 has been used in this analysis. The differences in Figure 2.20 between the evaluated fluence in 2014 and the fluence in 2017 are ∼4% at 1 eV and ∼1% at 7.5 eV.

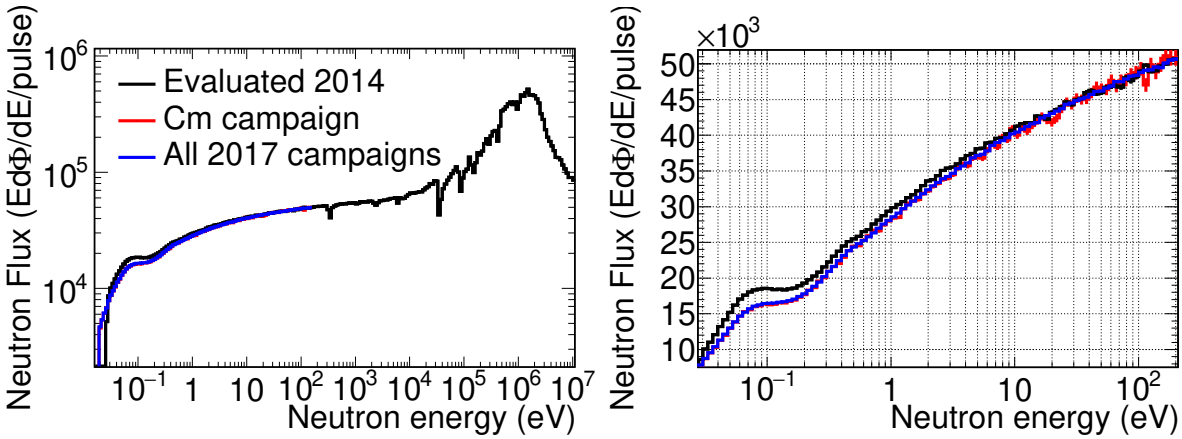

Figure 2.20: Evaluated fluence measured in 2014 from Ref. [93] compared with the fluence measured with the SiMon during the Cm campaign (2 weeks of 2017) and during the entire year 2017. The plot on the right is a zoom of the one on the left.

The experimental fluence calculated with the SiMon detector has been obtained with a ^{6}Li sample covering the full beam, whereas the Cm samples only cover a small fraction of the beam, which according to [63, 94] is ∼6%. Monte Carlo calculations of the n_TOF neutron beam have been used to check that the energy dependence of the neutron fluence is the same in both cases. The comparison has been carried out with the Transport Code of the n_TOF facility (TC) presented in Appendix B. The results, in Figure 2.21, show that the expected differences are very small (∼1% between 1 and 100 eV), which allows to use the energy dependence obtained with the SiMon for the analysis of the Cm cross sections. An additional check has been performed by measuring an Au sample with the same diameter. In Table 2.3 the values obtained in the measurement are compared with evaluated values of the JEFF-3.3 [51] library, indicating the precision of the calculation of the fluence in the energy range of the measurement.

2.5.3 Neutron fluence and beam profile in EAR2

The EAR2 fluence was measured in 2014 by Sabate-Gilarte *et al.* [95] with three different detectors SiMon2 [90], PPAC [76] and MGAS [77] for energies between 0.01 eV and 100

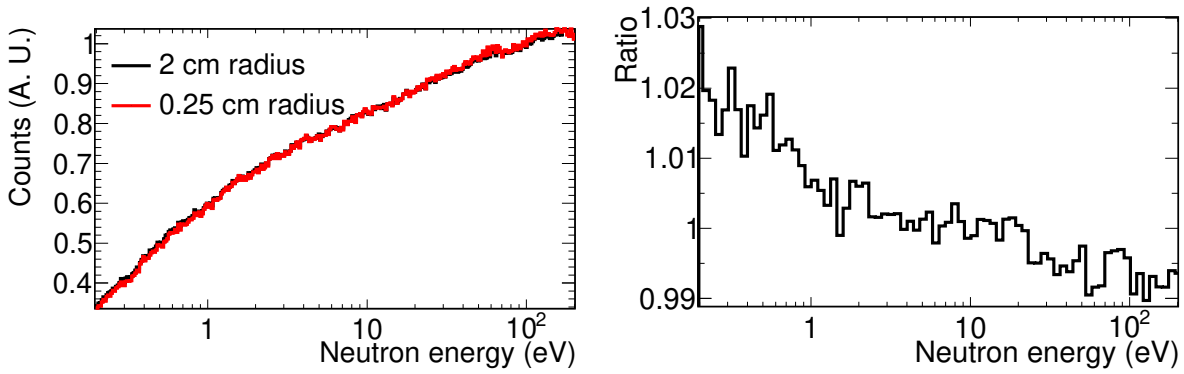

Figure 2.21: Comparison of the energy dependence of the neutron fluence obtained with the TC for a small sample of 2.5 mm radius and the full 2 cm radius beam in EAR1 (left). The ratio of the two fluences is plotted in the right panel.

MeV. The shape of the fluence has also been measured with SiMon2 detector during the Cm campaign, following the same procedure explained in Section 2.5.2 for EAR1 and with the same detection efficiency (∼9%) [95]. Unlike in EAR1, no changes in the fluence between 2014 and 2017 are expected, since there is no boron in the moderation circuit. The RF can affect the calculation of the neutron fluence in EAR2 as explained in [87], but for the energy range between 0.1 eV to 400 eV, the effect is so small that is neglected in the analysis. The fluence measured during the Cm campaign is compared with the fluence evaluated in 2014 in Figure 2.22 and they are compatible within 1%.

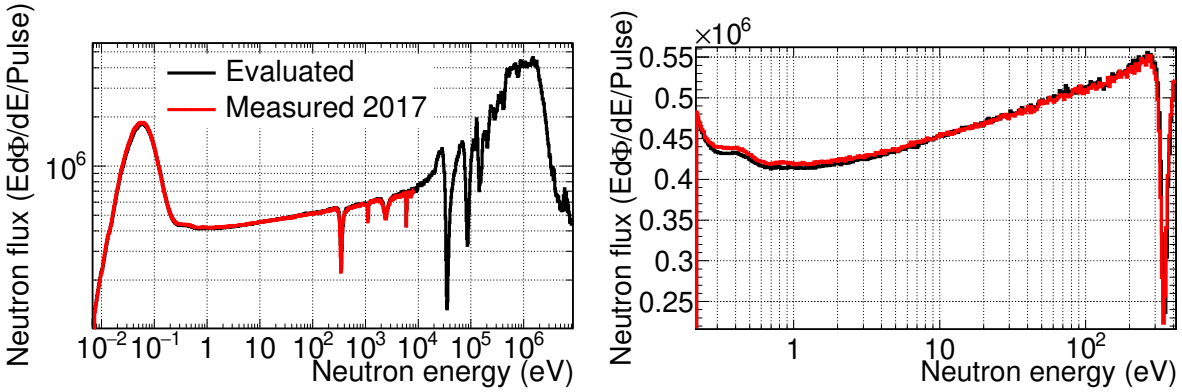

Figure 2.22: Evaluated fluence measured in 2014 from Ref. [95] compare with the fluence measured with the SiMon2 during the Cm campaign for EAR2. The right plot is a zoom of the one at the left.

The beam profile has been obtained with the TC, and it is presented in Figure 2.23. The Beam Interception Factor BIF obtained using these simulations for a sample of 2.5 mm radius placed in the beam centre is ∼3.5%.

The simulated fluence for the ^{6}Li sample and the small sample used in the measurement are compared in Figure 2.24 using the same methodology as in EAR1, showing differences

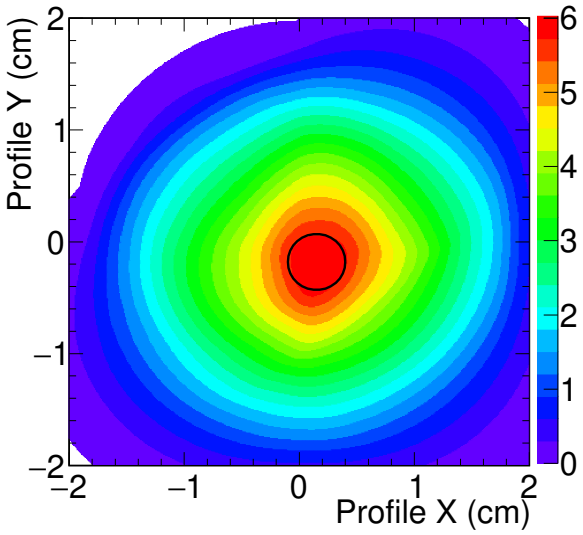

Figure 2.23: Neutron beam profile at a 19.8 m distance from the centre of the spallation target, calculated with the TC. The black circle corresponds to the size of the Cm sample. The fraction of neutrons inside this circle is ∼3.5% of the beam in EAR2.

smaller than 1% in the energy range of this measurement.

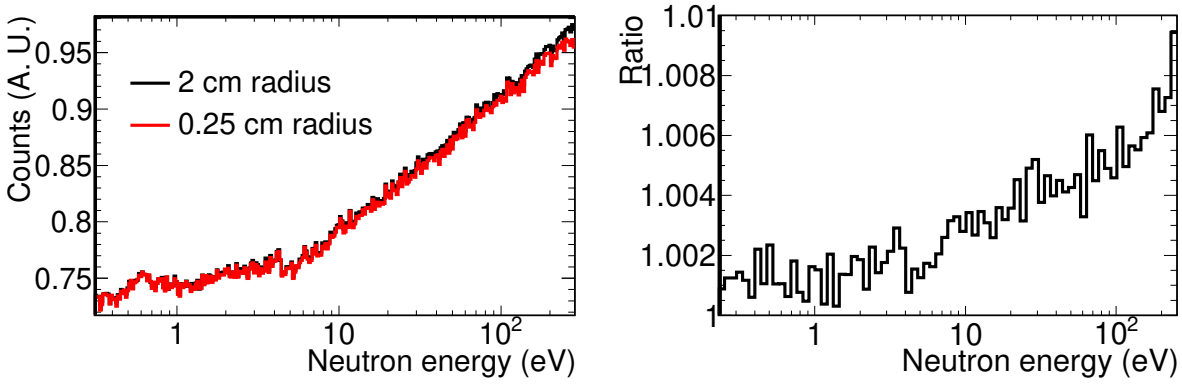

Figure 2.24: Comparison of the energy dependence of the neutron fluence obtained with the TC for a small sample of 2.5 mm radius and the full 2 cm radius beam in EAR2 (left). The ratio of the two fluences is plotted in the right panel.

2.5.4 Resolution function in EAR1

Not all neutrons that reach the experimental area in a given time have the same energy (nor do all neutrons of the same energy reach the experimental area simultaneously). The Energy-TOF probability distribution is referred to as the RF. This distribution is highly non-gaussian and deviates from the ideal case where there is only one time-of-flight for each neutron energy. The deviations are due to different effects:

- Finite duration of the accelerator proton burst. In this case, the RMS of the beam is 7 ns.
- The neutron production mechanism. In particular, there is an effect on the production of neutrons in the target with a non-negligible size.
- The neutron moderation process.

The RF at n_TOF is usually described using an effective flight path distribution, instead of the TOF, which is parametrised as the sum of an average geometrical distance (L_{geo}) plus an equivalent moderation length (λ). The value of L_{geo} is constant, so the RF is provided as a function of λ and E_n.

In EAR1, the broadening effect of the RF is small compared with the Doppler broadening, in the neutron energy range of this measurement (1 to 100 eV) [63, 96, 97]. The EAR1 RF [63] is presented in Figure 2.25.

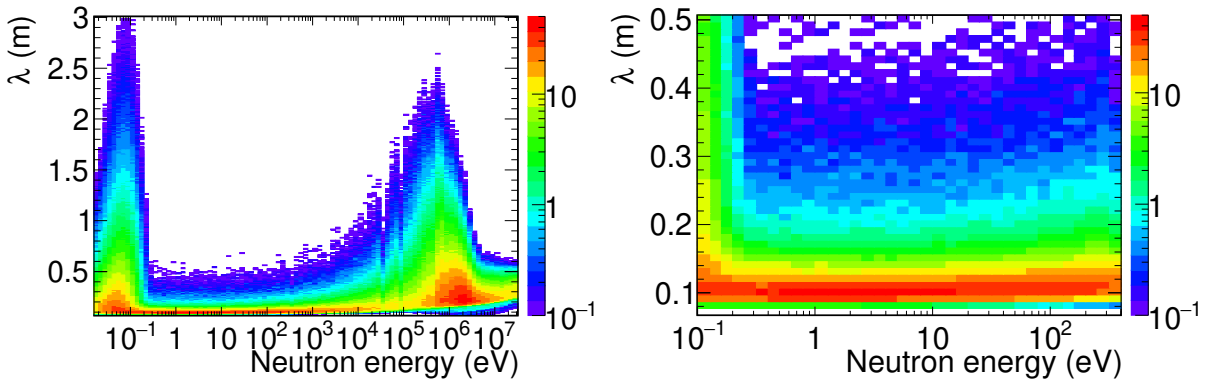

Figure 2.25: Probability distribution of the equivalent moderation length (λ) as a function of neutron energy. The panel on the right is a zoom of the one on the left.

2.5.5 Resolution function in EAR2

The broadening effect of the RF in EAR2 is much more significant than in EAR1. This is because the EAR2 flight path is ∼10 times shorter, and also due to the geometry of the spallation target and the moderation circuit, which was not designed to optimise the RF in EAR2.

The RF has been obtained from Monte Carlo simulations [98], similarly to the EAR1 RF. The simulations have been performed with FLUKA [99] and MCNP [100], and verification calculations have been performed also with Geant4 [101, 102].

The neutrons produced in the simulations are scored in a plane located close to the spallation target. In a second stage, the RF is obtained by transporting these neutrons to the experimental area using the TC (Appendix B). The RF obtained with this procedure is able to reproduce with high accuracy the resolution broadening for samples covering

the full neutron beam. An example is provided in Figure 2.26, where a ^{235}U(n,f) time-of-flight spectrum obtained experimentally is compared with the calculated values, showing an excellent agreement. In this case, the ^{235}U sample covered the entire beam. On the

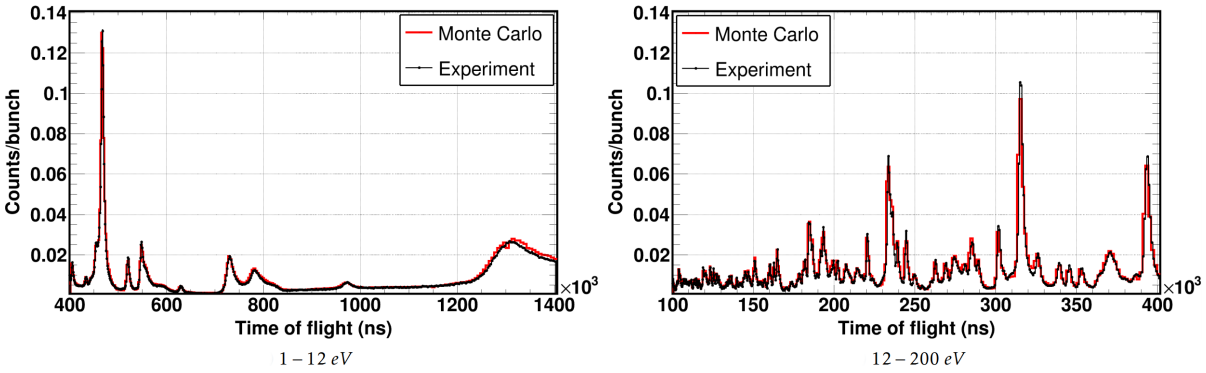

Figure 2.26: Calculated time-of-flight spectrum of ^{235}U(n,f) reaction at a distance of L = 19.5 m from the centre of the lead spallation target compared to the experimental data recorded during the ^{240}Pu(n,f) campaign. Figure extracted from [103].

contrary, the resolution broadening for small samples is not reproduced so well. Figure 2.27 shows a similar comparison, but for a 2.5 mm radius ^{197}Au sample and looking to capture instead of fission. The experimental data are not reproduced when using the same RF as before (Full beam). The situation improves when the RF is computed considering the sample size (TC centred), but still, the obtained results do not reproduce the experimental values with enough accuracy to perform a resonance analysis. Note that both the ^{235}U and ^{197}Au cross sections are known with enough accuracy to attribute the observed differences to the RF.

In summary, the Monte Carlo calculations are able to reproduce the resolution broadening with high accuracy for large radius samples and to predict a significant change in the RF for small radius samples, but the accuracy is significative worse in the second case and needs to be improved.

The situation improves if a small misalignment of the sample with respect to the centre of the beam is considered, but still, it is not precise enough to perform an accurate resonance analysis. The study of the effect of the misalignment has been performed by calculating the RF of the neutron beam in a 2.5 mm radius disk (shape of the Cm samples) located at different positions with respect to the beam's centre. The ^{197}Au(n,γ) yield has been then computed with SAMMY [104] (one of the most standard resonance analysis codes and the one used to analyse the Cm data) using the ^{197}Au cross sections from JEFF-3.3, and compared to the experimental data in the resonance at 78.5 eV, with a time-of-flight distance of 19.425 m. The choice of this resonance is based on having enough statistics and low multiple scattering effects, and the comparison has been performed by computing a reduced-χ^2. The results for different misalignments are shown in Figure 2.28, and the minimum reduced-χ^2 value obtained for a misalignment smaller than 2 mm is obtained in the position -0.15 cm in the x-axis and 0.1 cm in the y-axis. The comparison of the ^{197}Au(n,γ) yield obtained with the RF in the centre of the beam and

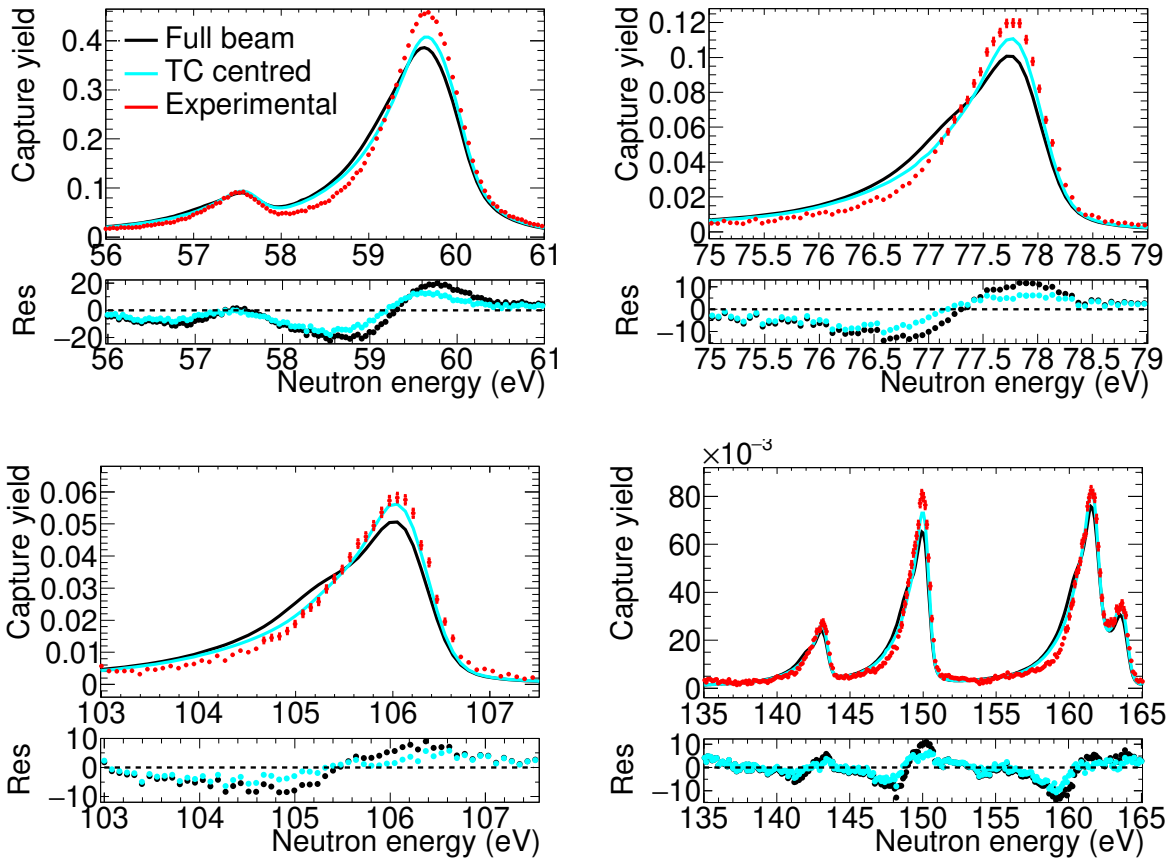

Figure 2.27: Experimental ^{197}Au capture yield for a circular sample with 2.5 mm radius compared with two yields obtained from the cross sections in JEFF-3.3 and two RF obtained from MC calculations (theoretical yields). In one of them the RF corresponds to the full neutron beam (Full beam) and in the other the RF corresponds to the 2.5 mm radius central part of the neutron beam (TC centred). In the bottom panel of each figure the residuals are plotted.

in the position with the best reduced-χ^2 is presented in Figure 2.29. If larger misalignments are considered, smaller reduced-χ^2 values can be achieved, but the situation does not improve significantly. In addition, larger misalignments are excluded from the results of experimental measurements performed during the campaign with the ^{197}Au sample located at different positions of the neutron beam. By comparing the obtained counting rates with the beam profile measured with the PPAC detector [76], it was concluded that the missalignment of the samples used during the Cm experiment with respect of the center of the neutron beam were smaller than 2 mm.

A new method to calculate the RF has been implemented in this work, in order to improve the RF obtained with the n_TOF standard tools. The RF at the (fixed) neutron energies of the ^{197}Au resonances has been fitted to reproduce the experimental ^{197}Au(n,γ) yield. The RF in the entire neutron energy range is then obtained by interpolating the obtained values. The process followed to obtain the final RF is explained in detail in the following paragraphs, and the uncertainties associated are estimated.

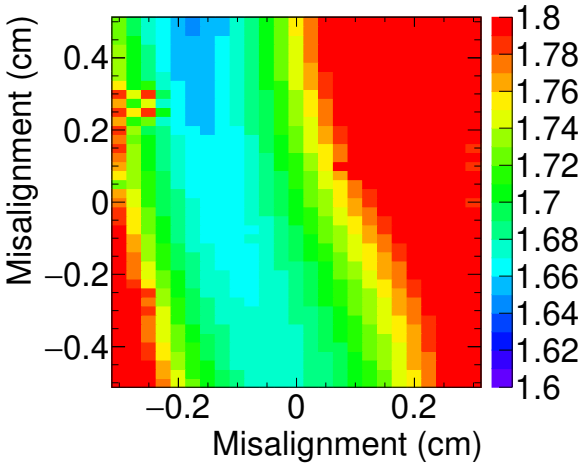

Figure 2.28: Reduced χ^2 obtained when comparing the experimental and theoretical capture yields in the 78.5 eV ^{197}Au resonance (2.5 mm radius sample). Each point has been computed using a RF assuming a misalignment with respect to the centre of the beam given by the X and Y axis.

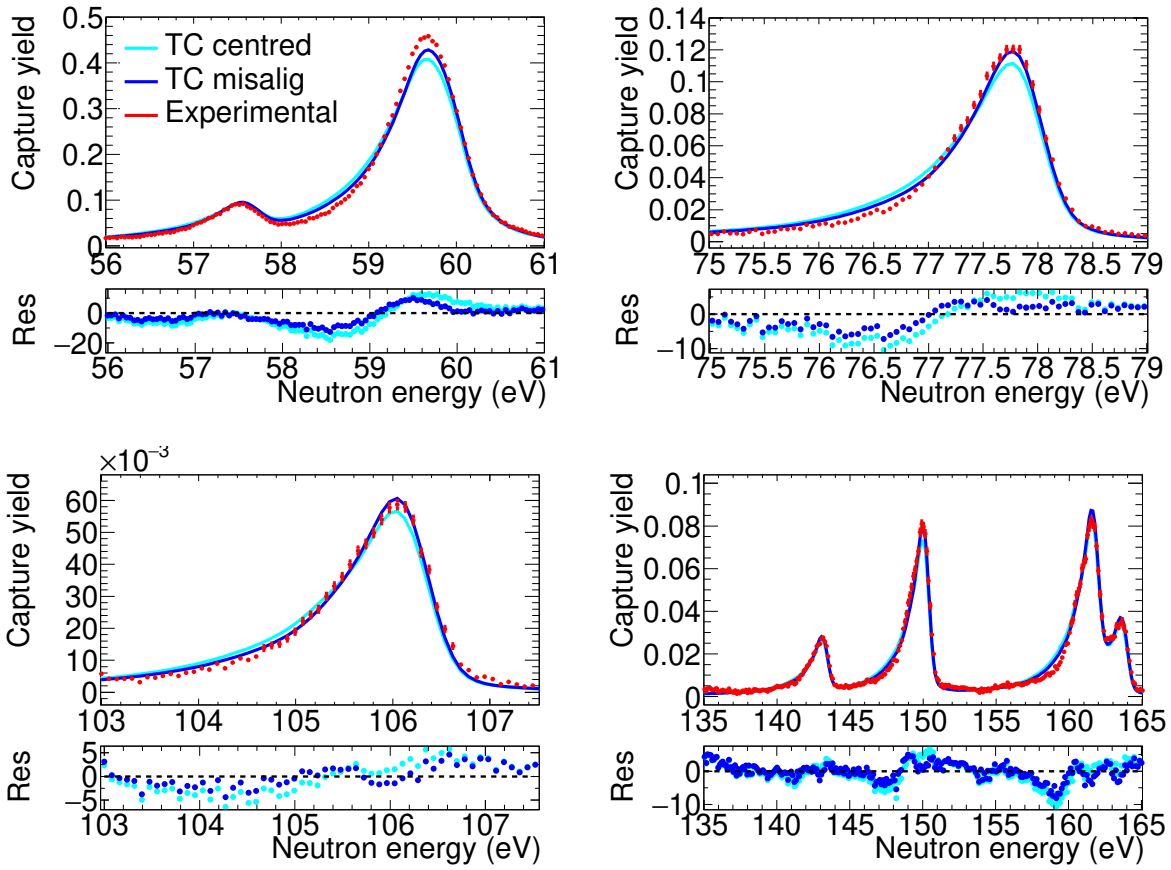

Figure 2.29: Same as Figure 2.27, but including also a RF corresponding to a 2.5 mm sample misaligned by 1.8 mm (TC misalig).

The fitting procedure has been performed as follows. Instead of using the moderator distance (λ) the RF was parametrised as a function of the equivalent moderation time distribution. This is the elapsed time between the protons impinges the target, and the neutrons reach the scoring plane. The moderation time distribution for a given neutron energy, i.e. the RF at a fixed neutron energy, is then parametrised with the linear combination of a Gaussian, a Landau and an Exponential functions. In the right panel of Figure 2.30, the time distributions at 78.5 eV obtained with Monte Carlo simulations + TC (Optical) is compared with the functions used to parametrise.

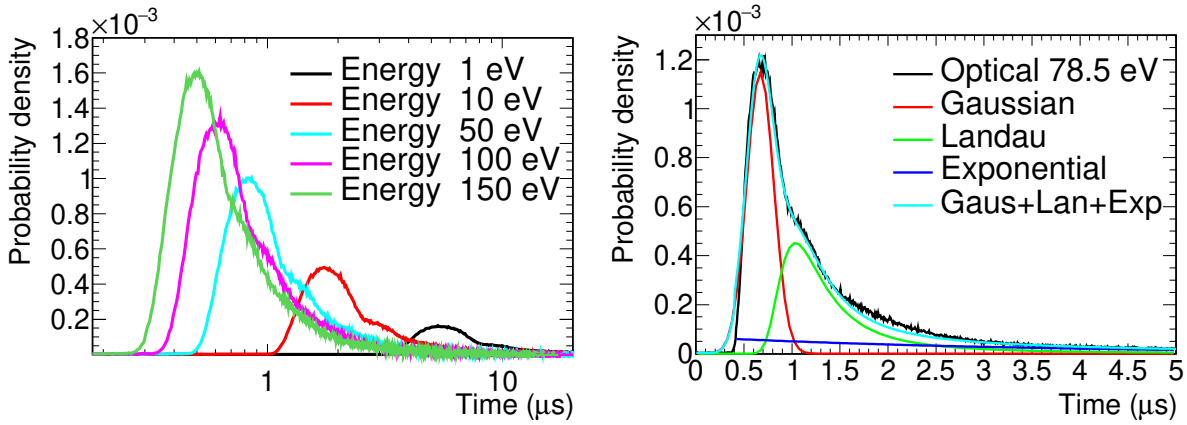

Figure 2.30: RF for various neutron energies as a function of the moderation time distribution (left). The moderation time distribution at 78.5 eV obtained with MC simulations + TC (black) is compared with the functions used in the parametrisation (right).

The fit to the experimental data has been performed by varying the relative weights of the Gaussian, Landau and Exponential functions, i.e. by fitting two parameters. A reduced-χ^2 between the experimental and the calculated yields has been minimised for each of the ^{197}Au resonances. The RF between resonances is calculated by interpolating the fitted parameters.

The first strong resonance of ^{197}Au, located at 4.9 eV has not been used to fit the RF, due to the strong multiple scattering, which affects the shape of the resonance. Since the second resonance of ^{197}Au is located at 58 eV, we have used the first resonance of ^{244}Cm at 7.6 eV to fit the RF. The first resonance of ^{240}Pu has not been used because it is also affected by multiple scattering. The resonance parameters of ^{244}Cm in this resonance used to perform the fit have been obtained from the measurement in EAR1, where the effect of the RF is negligible. The precise reproduction of the experimental yield of these two resonances are illustrated in panels (a) and (b) of Figure 2.31.

The results obtained with the fits are presented in Figure 2.32, the time distributions are plotted in the left panel and the distance distribution (λ) in the right one. The λ curves obtained with the fits are similar to the ones obtained with the Monte Carlo simulations + TC (Figure 2.33). The main difference with respect to the Monte Carlo simulations +

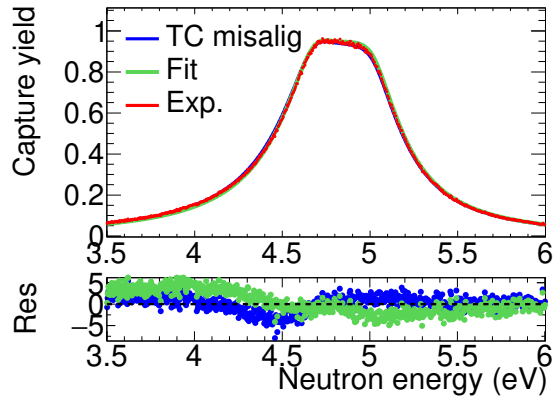

(a) ^{197}Au-4.9 eV

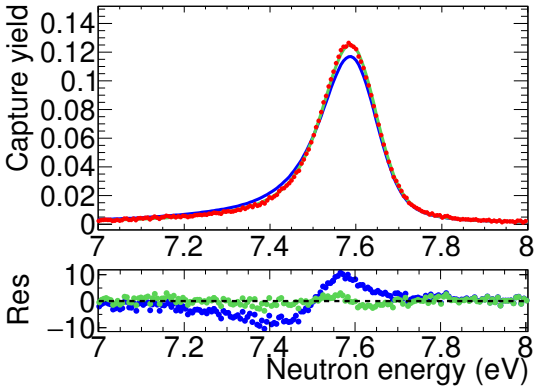

(b) ^{244}Cm-6.7 eV

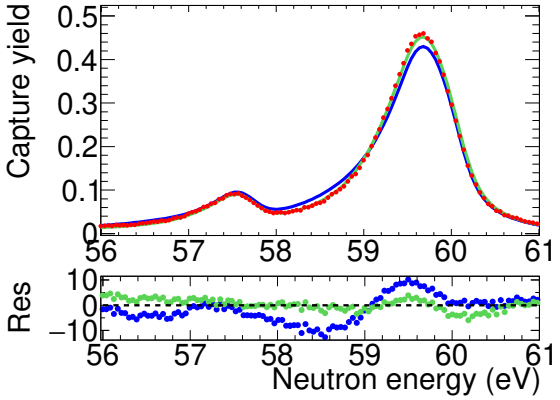

(c) ^{197}Au-58.1 and 60.2 eV

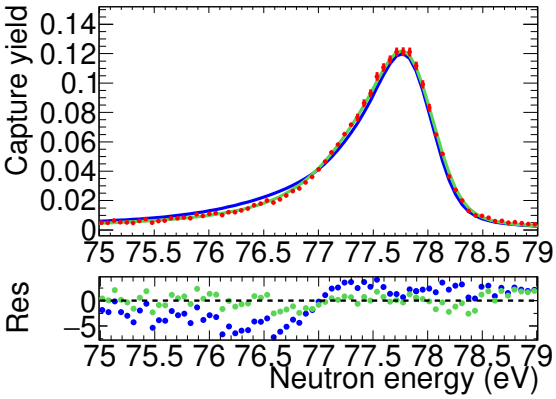

(d) ^{197}Au-78.5 eV

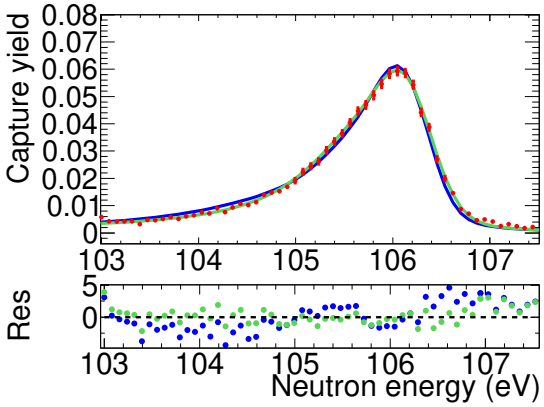

(e) ^{197}Au-107 eV

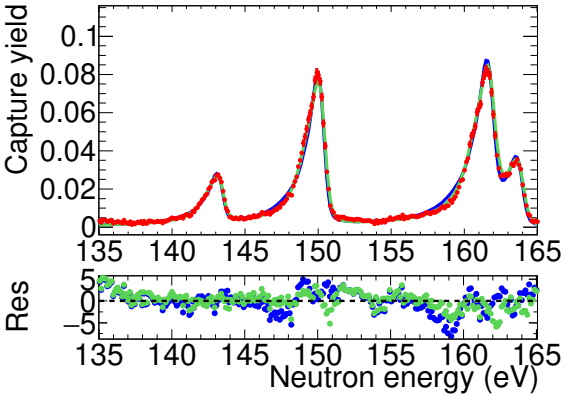

(f) ^{197}Au-144, 151, 163 and 165 eV

Figure 2.31: Experimental ^{197}Au and ^{244}Cm capture yields for a circular sample with 2.5 mm radius compared with two theoretical yields. One uses one of the RF in Figure 2.29 (TC misalig), which is the RF from MC calculations which better reproduces the experimental data, and the other (Fit) uses the RF obtained from the fitting method explained in the body text. In the bottom panel of each figure the residuals are plotted.

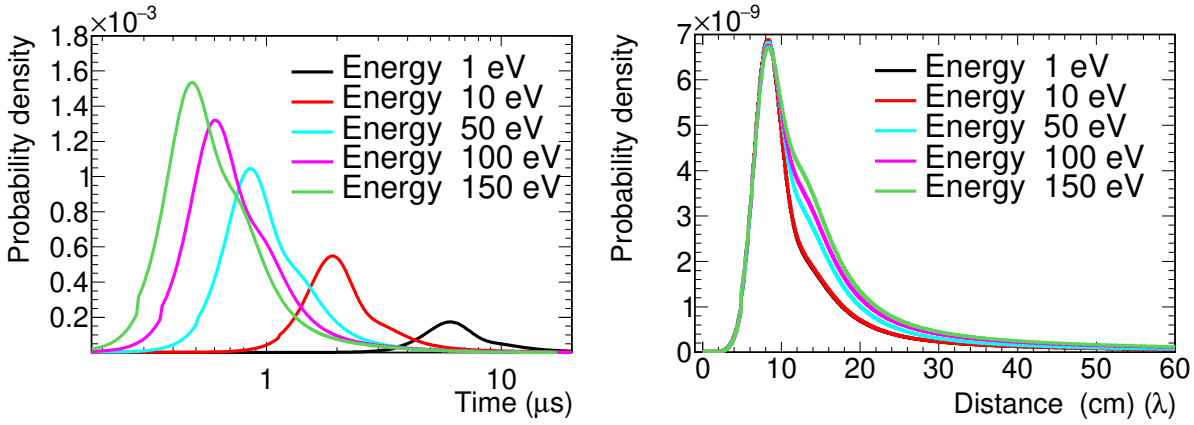

Figure 2.32: Fitted RF at different neutron energies, as a function of the moderation time (left) and as a function of the moderation distance (right).

TC curves is the reduction of the exponential tale in all of the λ distributions.

The performance of this new RF is shown in Figure 2.31, where it is compared with the experimental results and with the RF obtained with the Monte Carlo calculations + TC obtained with a misalignment of 1.8 mm respect to the beam center. The new RF obtained with the fits is also shown in Figure 2.34.

A resonance analysis of the ^{197}Au(n,γ) measurement performed during the Cm campaign has been performed to quantify the impact of using one RF or another. The fits were performed with SAMMY, using the two RF mentioned above: the one obtained from the fit and the one from the Monte Carlo + TC with a misalignment of 1.8 mm.

The results of the analysis with the two RF are presented in Table 2.3 and Figure 2.35, where the fitted resonance parameters are compared to JEFF-3.3. A fit of the ^{197}Au(n,γ) measurement performed in EAR1, where the impact of the RF is negligible, has been performed as well and included in the comparison. The results of this comparison show that the energy of the resonances obtained in the fits are compatible with JEFF-3.3 within 0.05%. The ^{197}Au parameters, which are closely related with the area of the resonance for ^{197}Au, are compatible with JEFF-3.3 in most of the cases, although there are some exceptions, especially with the data fitted with the Monte Carlo+TC RF. Larger discrepancies are found when comparing the Γ_γ values, which for ^{197}Au are closely related with the widths (i.e. the shape) of the resonances. In this case, the RF obtained from the fits to the experimental data gives significantly better results than the ones from the Monte Carlo+TC RF.

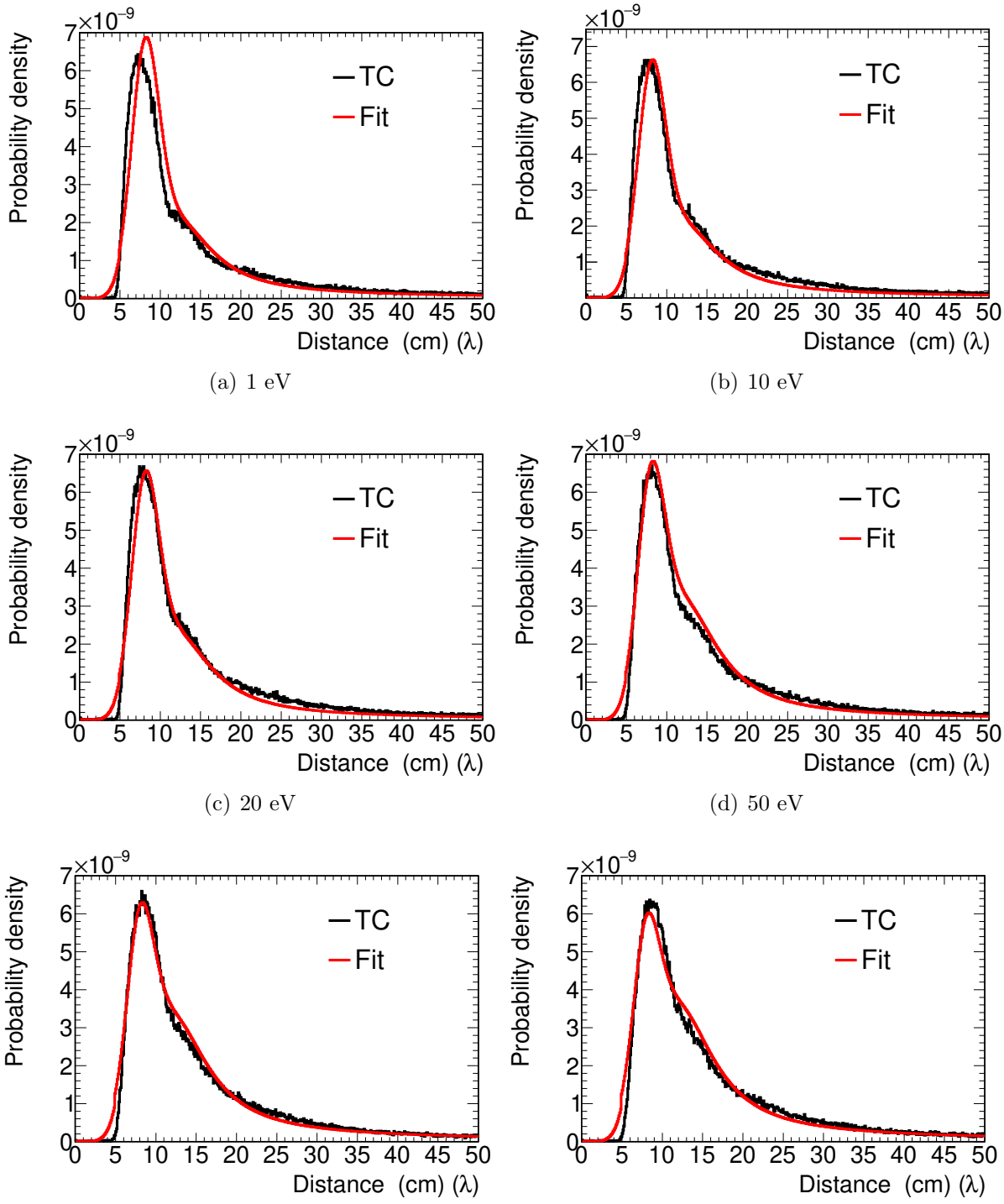

(a) 1 eV

(b) 10 eV

(c) 20 eV

(d) 50 eV

(e) 100 eV

(f) 150 eV

Figure 2.33: Comparison of the RF obtained with the Monte Carlo + TC calculations (TC) and the RF obtained from the fits to the ^{197}Au and ^{244}Cm data (Fit). The RF is presented as a function of the moderator distance (λ), for different neutron energies.

In conclusion, the performance of the RF obtained from the fitting method presented in this section, and developed specifically for this work, is able to reproduce the resolution

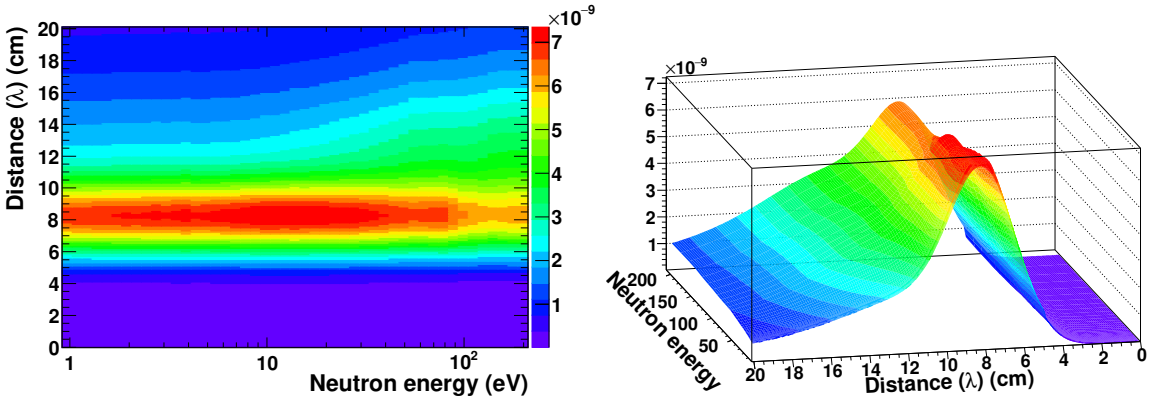

Figure 2.34: The RF obtained from the fits to the ^{197}Au(n,γ) and ^{244}Cm(n,γ) experimental data.

broadening of the capture yield in EAR2 with significantly larger accuracy than the RF obtained from the standard n_TOF analysis tools. This RF has been used to perform the resonance analysis of the Cm data.

E_0				
E_0	Evaluated JEFF-3.3	EAR1	EAR2 MC+TC	EAR2 Fit
58	58.08	58.08 ± 0.01	58.06 ± 0.01	58.06 ± 0.01
60	60.29	60.32 ± 0.01	60.31 ± 0.01	60.30 ± 0.01
79	78.50	78.51 ± 0.01	78.52 ± 0.01	78.50 ± 0.01
107	107.03	107.05 ± 0.01	107.06 ± 0.01	107.03 ± 0.01
151	151.39	151.40 ± 0.01	151.42 ± 0.01	151.37 ± 0.01
163	163.07	163.07 ± 0.01	163.11 ± 0.01	163.03 ± 0.01
165	165.08	165.08 ± 0.01	165.07 ± 0.01	165.05 ± 0.01
190	190.03	190.05 ± 0.01	190.09 ± 0.01	190.01 ± 0.01
241	240.61	240.64 ± 0.01	240.68 ± 0.01	240.52 ± 0.01
262	262.26	262.25 ± 0.01	262.35 ± 0.01	262.14 ± 0.01
274	273.86	273.88 ± 0.04	273.87 ± 0.04	273.68 ± 0.04

Γ_γ				
E_0	Evaluated JEFF-3.3	EAR1	EAR2 MC+TC	EAR2 Fit
58	113	124 ± 8	115 ± 4	143 ± 4
60	118	110 ± 24	123 ± 20	127 ± 20
79	124	114 ± 19	101 ± 1	122 ± 3
107	123	127 ± 21	134 ± 15	120 ± 10
151	121	121 ± 1	94 ± 1	85 ± 1
163	129	106 ± 2	61 ± 3	104 ± 2

165	121	82 ± 16	269 ± 8	126 ± 7
190	121	101 ± 14	190 ± 9	134 ± 7
241	121	119 ± 21	84 ± 28	124 ± 11
262	129	106 ± 23	211 ± 10	126 ± 10
274	121	109 ± 33	120 ± 69	125 ± 42

	Γ_n			
E_0	Evaluated JEFF-3.3	EAR1	EAR2 MC+TC	EAR2 Fit
58	4.3	4.6 ± 0.4	4.6 ± 0.1	4.2 ± 0.1
60	70.7	69.2 ± 0.4	67.3 ± 0.8	68.9 ± 0.1
79	17.0	16.4 ± 4.8	16.6 ± 9.9	15.5 ± 2.8
107	7.8	7.3 ± 5.4	7.9 ± 0.8	7.9 ± 1.3
151	22.3	23.1 ± 0.1	23.9 ± 0.1	24.3 ± 0.1
163	55.2	51.8 ± 2.3	48.3 ± 1.4	54.1 ± 0.2
165	10.0	8.0 ± 0.2	10.0 ± 0.1	9.3 ± 0.1
190	49.1	51.1 ± 0.7	41.7 ± 0.7	45.2 ± 0.7
241	74.2	69.6 ± 0.3	96.8 ± 0.2	62.8 ± 0.1
262	144.0	151 ± 14	79.6 ± 9.8	135.5 ± 3.1
274	4.8	3.9 ± 0.4	4.8 ± 0.1	4.8 ± 0.1

Table 2.3: Resonance parameters of ^{197}Au in JEFF-3.3 compared with the results of the fits performed with SAMMY of the data measured in EAR1 with the TAC and in EAR2 with the C_6D_6 detectors. In the latter, fit has been performed with the two RF mentioned in the text: the one obtained from Monte Carlo simulations + TC (MC+TC) and the one obtained with the fit to the measured data(Fit). Uncertainties are due to counting statistics.

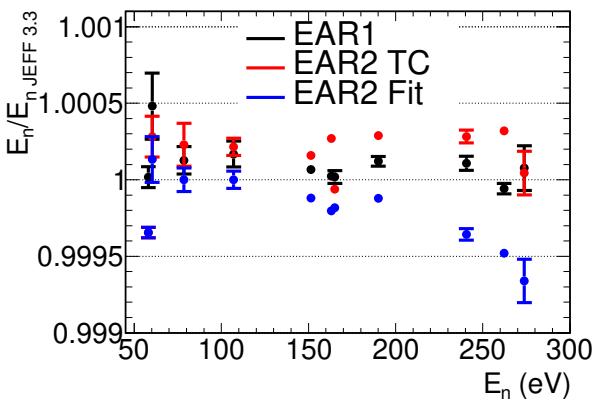

(a) E_R

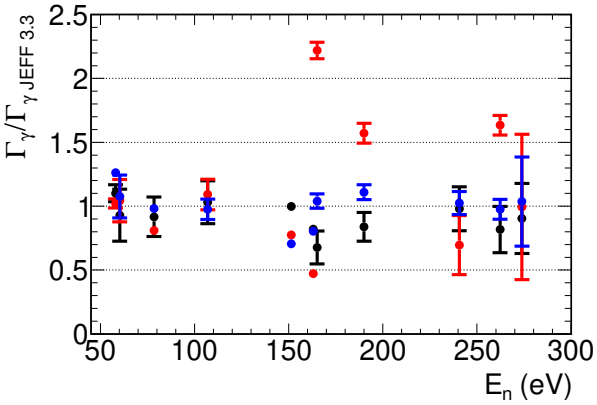

(b) Γ_γ

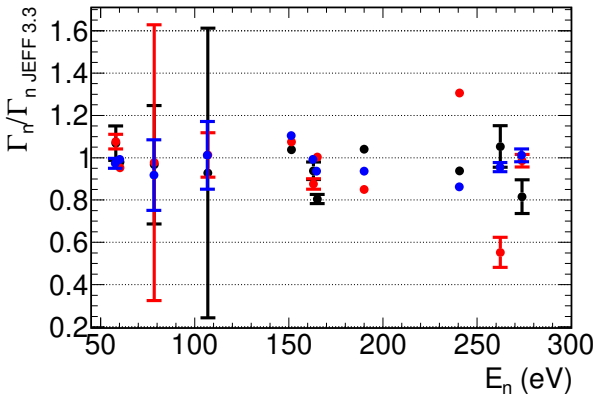

(c) Γ_n

Figure 2.35: Resonance parameters of ^{197}Au obtained in the fits performed with SAMMY of the data measured in EAR1 with the TAC and in EAR2 with the C_6D_6 detectors divided by the JEFF-3.3 values. In the latter, the fit has been performed with the two RF mentioned in the text: the one obtained from Monte Carlo simulations + TC (EAR2 TC) and the one obtained with the fit to the measured data (EAR2 Fit). The only uncertainties considered are the ones due to due to counting statistics.

Chapter 3

Monte Carlo simulations of the capture cascades

Accurate simulations of the detection of the γ-ray cascades emitted after neutron capture are needed to analyse both measurements, the one performed with the TAC and the one with the C_6D_6 detectors. Since this is a common task for both measurements, a dedicated chapter has been devoted to it.

For the TAC, they are needed to calculate the detection efficiency, as has been done in previous measurements [78, 79, 105, 106]. For the C_6D_6, Monte Carlo simulations of the detection of single γ-rays are needed to calculate the so called Weighting Functions (WF, 5.3), and simulations of the detection of the full cascades are needed to calculate the corrections to the PHWT analysis technique (Section 5.3), as has been done in previous measurements [73, 107, 108, 109, 110, 111]. The necessary simulations are performed in three steps:

i) Generation of the electromagnetic cascades.

ii) Transport of the cascades into the geometry modelled with the Geant4 toolkit [101].

iii) Reconstruction of the events recorded in the detectors in the same way as it is done in the real measurement, including experimental effects such as the energy resolution.

The validation of steps 2 and 3 of the simulation process has been performed by simulating the detector response to the decay of several radioactive sources: ^{137}Cs, ^{88}Y, Am-Be and Cm-C for the TAC and ^{133}Ba, ^{137}Cs, ^{60}Co, ^{88}Y, Am-Be and Cm-C for the C_6D_6 detectors. A full comparison showing how well the experimental results are reproduced are presented in Sections 4.2.1 (TAC) and 5.2 (C_6D_6).

In order to generate the capture cascades following the neutron capture, it is, in principle, necessary to know the complete nuclear level scheme, branching ratios, and conversion coefficients below the capture level. This information is only well-known for some light nuclei. The level schemes are only known below certain excitation energy for the general case. Consequently, the generation of the cascades is founded on a model that merges experimental information at low excitation energies and theory-based statistical models at high excitation energies. The model relies on some parameters, which are modified to

reproduce the measured energy spectra. This has been the procedure already followed in previous n_TOF measurements [78, 79, 105, 106] and also in similar analysis performed in other facilities [112, 113, 114]. In this work, the methodology has been improved with respect to previous analysis: instead of modifying *by hand* the parameters to reproduce the experimental results, a differential evolution algorithm has been used to fit these parameters.

The cascades are generated using NuDEX [115], a code developed at CIEMAT which operates in a similar way to DICEBOX [116] or DEGEN [117]. The known part of the level scheme, the known branching ratios and the known electron internal conversion coefficients are taken from RIPL-3 [118]. At higher energies, the levels and transitions probabilities between them are calculated using statistical models [116, 119, 120]. The individual levels are created by sampling the level density distribution given by the Back Shifted Fermi Gas (BSFG) or the Gilbert-Cameron (GC) formulas. The transition probabilities between the levels are calculated only for E1, M1 and E2 transitions, using their associated Photon Strength Function (PSF). The PSF models are usually parameterised as a combination of Standard Lorentzian (SL) or Enhanced Generalized Lorentzian (EGLO) functions. Three parameters describe these functions: the energy E_r, the width Γ_r and the cross section σ_r. By default, NuDEX takes the PSFs from an internal database, constructed mostly from the information provided by IAEA models database [121] and by RIPL-3 [118], but they can be changed by the user at convenience.

In this analysis, the deexcitation cascades of the following compound nuclei are needed: ^{197}Au(n,γ), ^{240}Pu(n,γ) and ^{244,246,248}Cm(n,γ). It has been assumed that these cascades do not vary significantly in the energy range of the measurement because the energy of the incident neutrons are much smaller than the neutron separation energies and the nuclear level densities are very large.

The cascades of ^{197}Au(n,γ) used in this work have been the same used in previous TAC analysis [9, 122]. The cascades of ^{240}Pu(n,γ) and ^{244}Cm(n,γ) have been obtained using an evolution algorithm to fit several experimental deposited energy spectra in the TAC. The cascades of ^{246}Cm(n,γ), which have not been measured with the TAC, have been obtained by adjusting *by hand* some PSF parameters to reproduce the energy deposited spectrum in the C_6D_6. For the ^{248}Cm(n,γ), the default cascades produced by NuDEX have been used, since there is not enough statistics in the measured spectra to perform any adjustment. The highest the information is about the deexcitation cascades, the lowest are the uncertainties in the yields, as presented for example in Section 5.3.2.

The simulated response of the TAC and the C_6D_6 detectors to the detection of ^{197}Au(n,γ) cascades used in previous works [9, 122] are compared with the experimental data in Figure 3.1. The excellent reproduction is a proof of the quality of the data and the accuracy of the Monte Carlo simulations for the Cm campaign.

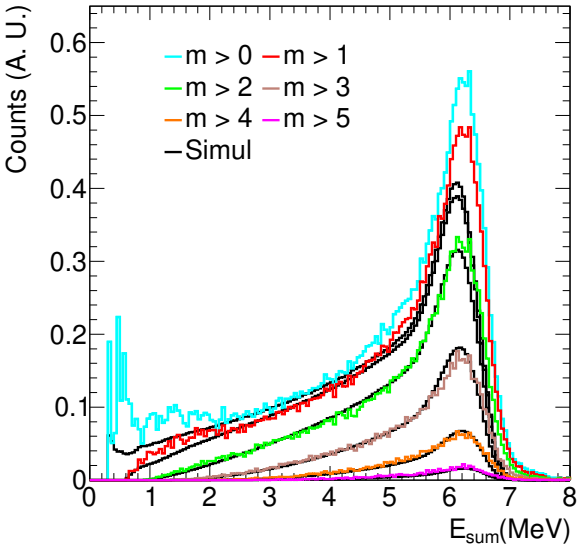

(a) NuDEX default - TAC

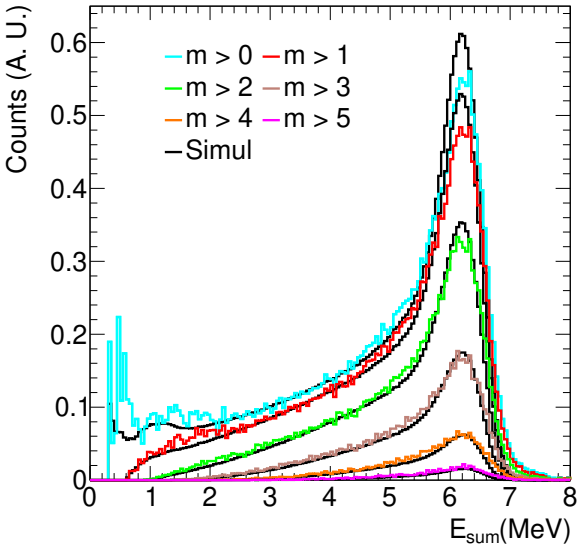

(b) Previous n_TOF analysis - TAC

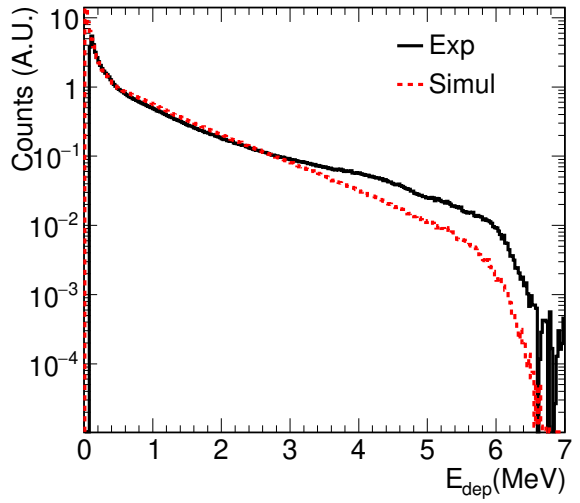

(c) NuDEX default - C_6D_6

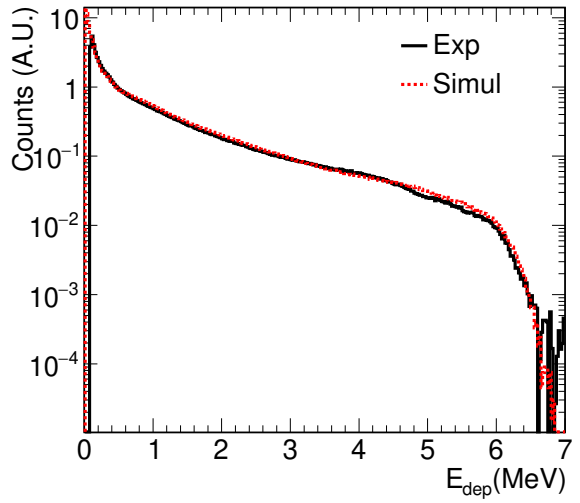

(d) Previous n_TOF analysis - C_6D_6

Figure 3.1: Comparison between experimental and simulated (Simul) deposited energy spectra for ^{197}Au(n,γ) cascades, in the 4.9-5.1 eV neutron energy range. The default cascades produced by NuDEX are used in the left panels, whereas the cascades used in previous n_TOF measurements with the TAC [9, 122] are used in the right panels. The top panels are obtained for the TAC detector for different multiplicities (m) with a threshold of 0.3 MeV in each BaF_2 crystal. The bottom panels are for the C_6D_6 detectors.

3.1 ^{240}Pu(n,γ) and ^{244}Cm(n,γ) cascades

The fitting procedure to obtain the cascades is explained in detail in [123]. The methodology consists in the minimization of a Figure Of Merit (FOM) by modifying the PSF

parameters. The process is based on the repetition of the following steps until the result converges:

i) The cascades are generated with NuDEX, using certain PSF which depend on some parameters.

ii) The response of the TAC to the cascades are simulated with Geant4. The simulated data are reconstructed in the same way as the experimental data, and several deposited energy spectra are created using different conditions on the total energy and the multiplicity of the detected events.

iii) The simulated and experimental spectra are compared using a FOM. In this analysis the FOM has been constructed using a linear combination of reduced chi-square values computed from different spectra.

iv) If the convergence criterium is satisfied, then the program stops. Otherwise, a new set of PSF parameters are created with a differential evolution algorithm [124, 125], and the loop goes to step (i).

There are several ways to paramatrise the PSF. Since E1 and M1 transitions are expected to dominate, the strategy followed to fit the PSFs was to try different models for the E1 PSF (Standard Lorentzian, Generalized Lorentzian, Simplified Modified Lorentzian ...), and with fixed parameters coming from [121]. For each E1 model, a fit of the M1 PSF, defined as the sum of three Standard Lorentizans, was performed. The best spectra resulting from these fits are presented on the right panels of Figures 3.2 and 3.3, together with the spectra obtained from the default NuDEX cascades (on the left). These results show that the default NuDEX cascades seem to reproduce the experimental spectra quite well, but the results from the fits reproduce them significantly better. In order to quantify the impact of the different results on the detection efficiency values (ε_γ), they are presented, for different conditions on the detection multiplicity, in Table 3.1, together with the ratios between the integrals of the experimental and the simulated spectra. While the integrals obtained with the default cascades differ by up to 20-30% with respect to the experimental values, the results from the fit agree within 1% for the ^{240}Pu(n,γ) cascades and within 1.5% for the ^{244}Cm(n,γ) cascades. Also in Figure 3.4, the good agreement between the m_{cr} with cuts $1 < E_{sum}$ (MeV) < 6.0 for the fitted cascades are presented.

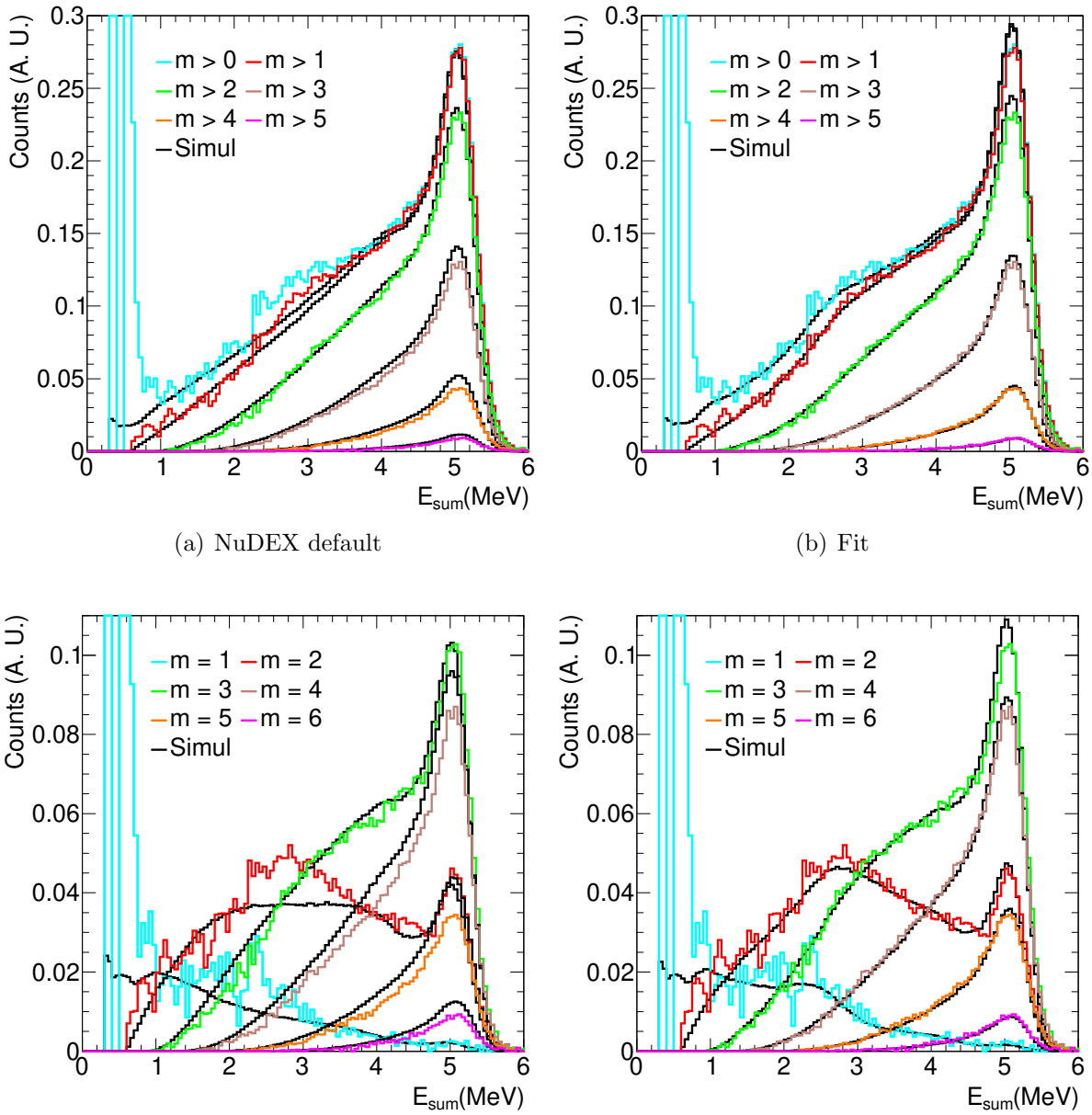

(a) NuDEX default

(b) Fit

(c) NuDEX default

(d) Fit

Figure 3.2: Comparison between experimental and simulated total deposited energy spectra of ^{240}Pu(n,γ) cascades in the TAC, for different conditions on the detected multiplicity (m), in the 0.9-1.1 eV neutron energy range with a threshold of 0.3 MeV in each BaF_2 crystal. The panels on the left correspond to the default NuDEX cascades, whereas the panels of the right to the fitted results.

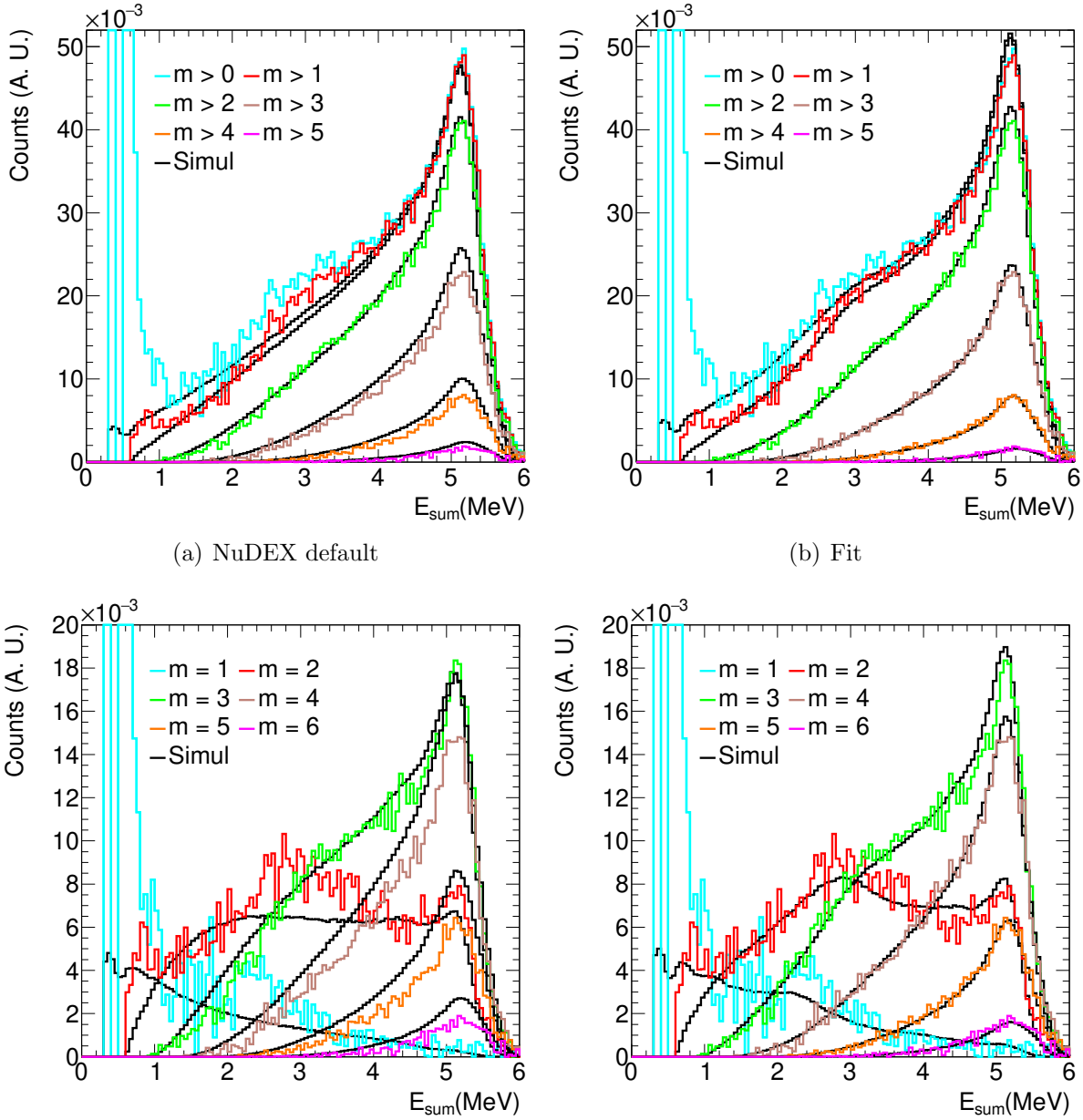

(a) NuDEX default

(b) Fit

(c) NuDEX default

(d) Fit

Figure 3.3: Comparison between experimental and simulated total deposited energy spectra of ^{244}Cm(n,γ) cascades in the TAC, for different conditions on the detected multiplicity (m), in the 7.4-7.8 eV neutron energy range with a threshold of 0.3 MeV in each BaF_2 crystal. The panels on the left correspond to the default NuDEX cascades, whereas the panels of the right to the fitted results.

$m_{cr}>$	^{240}Pu				^{244}Cm			
	$\varepsilon_{\gamma\ Fit}$	$\varepsilon_{\gamma\ def.}$	$C_{Exp}/\varepsilon_{\gamma\ Fit}$	$C_{Exp}/\varepsilon_{\gamma\ def.}$	$\varepsilon_{\gamma\ Fit}$	$\varepsilon_{\gamma\ def.}$	$C_{Exp}/\varepsilon_{\gamma\ Fit}$	$C_{Exp}/\varepsilon_{\gamma\ def.}$
0	0.802 (3)	0.807	1.005 (4)	0.998 (2)	0.805 (2)	0.815	1.005 (5)	0.994 (4)
1	0.777 (4)	0.785	1.001 (6)	0.991 (2)	0.778 (4)	0.794	1.005 (6)	0.985 (4)
2	0.589 (7)	0.618	1.000 (13)	0.947 (2)	0.589 (7)	0.636	1.000 (12)	0.919 (5)
3	0.278 (6)	0.321	1.012 (21)	0.876 (3)	0.282 (6)	0.345	1.004 (21)	0.822 (7)
4	0.080 (2)	0.102	1.020 (29)	0.802 (7)	0.083 (2)	0.117	1.030 (31)	0.729 (13)

Table 3.1: Integrals of the total deposited energy spectra for $2.5 < E_{sum}$ (MeV) < 6.0 for different multiplicity conditions (m_{cr}). The simulated values ($\varepsilon_{\gamma\ Fit}$ and $\varepsilon_{\gamma\ def.}$) normalised to the number of simulated cascades correspond to the capture detection efficiencies. The ratios between the experimental and simulated values ($C_{Exp}/\varepsilon_{\gamma\ Fit}$ and $C_{Exp}/\varepsilon_{\gamma\ def.}$) are presented normalised to the m_{cr} >2 results. The uncertainties in the $\varepsilon_{\gamma\ Fit}$ include only the uncertainties due to the event generator and $C_{Exp}/\varepsilon_{\gamma\ Fit}$ include these uncertainties and the ones due to counting statistics.

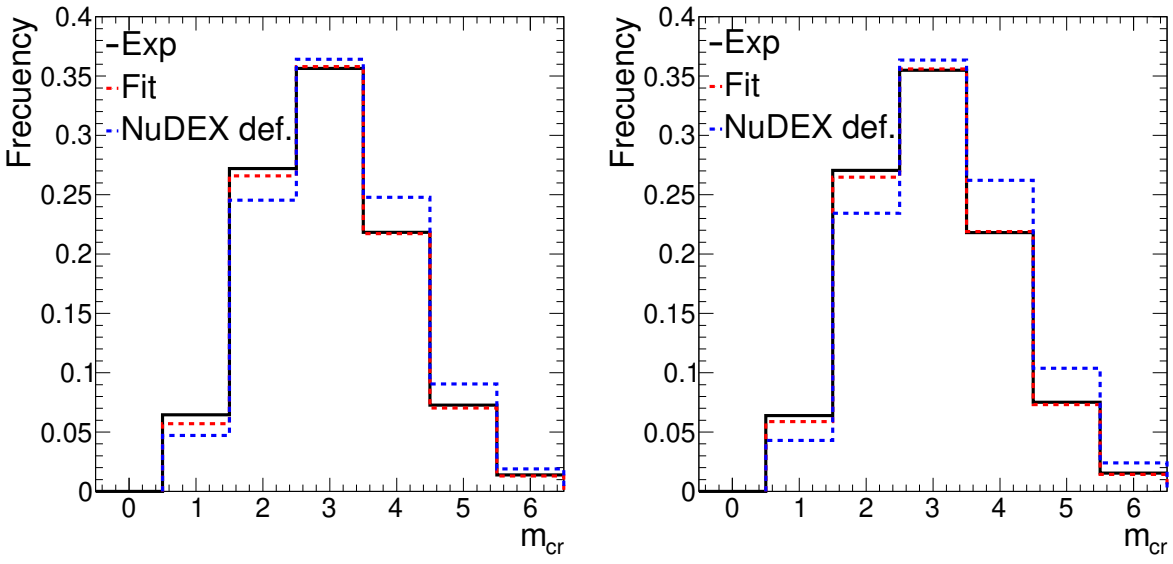

(a) ^{240}Pu(n,γ) (b) ^{244}Cm(n,γ)

Figure 3.4: Distribution of the detected multiplicity in the TAC (m_{cr}) for events with $1<E_{sum}$(MeV)<6, the experimental data are compared with the simulations performed with the default NuDEX PSFs and with the new PSFs obtained from the fit. The ^{240}Pu(n,γ) data are in the left panel and the ^{244}Cm(n,γ) are in the right panel.

Uncertainties in the TAC detection efficiency due to the event generator have been estimated by making several (1000) different cascades with different PSF parameters. For each of these cascades, the same FOM used for the fitting procedure was computed, as well as the detection efficiencies for different conditions in E_{sum} and m_{cr}. In the left panels of Figures 3.5 and 3.6 a scatter plot of these two variables are shown, for $m_{cr} > 2$. The uncertainties due to the event generator were estimated then as the standard deviation

of the efficiencies with a FOM below the red line, i.e. with a FOM close to the minimum value.

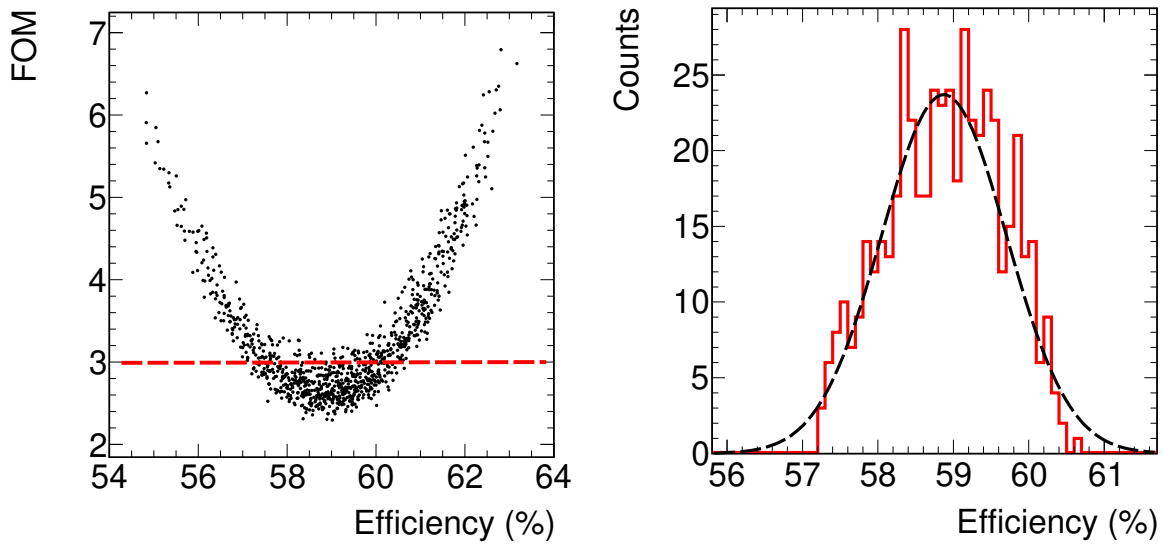

Figure 3.5: FOM and detection efficiency for 2.5<E_{sum}(MeV)<6 and m_{cr} >2 obtained in the simulation of 1000 different ^{240}Pu(n,γ) cascades. On the left panel, a scatter plot of the two values. On the right panel, the values of the efficiency with a FOM <3 are histogramed and fitted with a Gaussian function.

The new PSFs obtained from the fits are shown in Figure 3.7, together with the default PSFs from NuDEX. The fitted M1 PSF seem larger than expected from the results of other works, compared to the E1 PSF, since E1 transitions are expected to dominate. However, the obtained cascades aims to obtain an accurate detection efficiency of the TAC for the capture cascades. It can not be excluded that other PSFs are able to obtain similar cascades. The fitting technique used in this work will be used for further investigation in this topic, since it has a great potential for obtaining valuable nuclear structure information [126, 127, 128, 129, 130, 131].

3.1.1 Simulation of the cascades with the C_6D_6 detectors

The cascades obtained in EAR1 with the TAC have also been validated with the C_6D_6 data measured in EAR2. The agreement of the simulated and experimental cascades measured with a different detection setup and experimental area is a solid proof of the robustness of the methodology. In Figure 3.8, the experimental cascades are compared with the simulated data for the first resonances of ^{240}Pu (0.8-1.3 eV) and ^{244}Cm (7.45-7.65 eV). The experimental spectra are reproduced considerably better with the cascades obtained by fitting the EAR1 data than with the default NuDEX cascades. The propagation of the uncertainty in the normalisation of the EAR2 yields due to the γ-cascades are presented in Section 5.3.2.

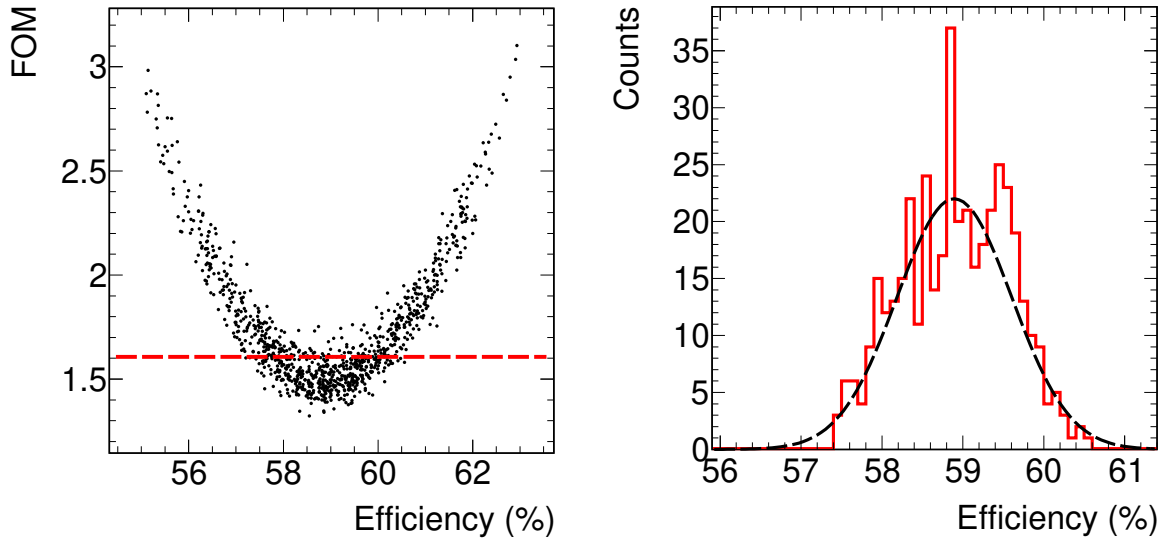

Figure 3.6: FOM and detection efficiency for 2.5<E_{sum}(MeV)<6 and m_{cr} >2 obtained in the simulation of 1000 different ^{244}Cm(n,γ) cascades. On the left panel, a scatter plot of the two values. On the right panel, the values of the efficiency with a FOM <1.6 are histogramed and fitted with a Gaussian function.

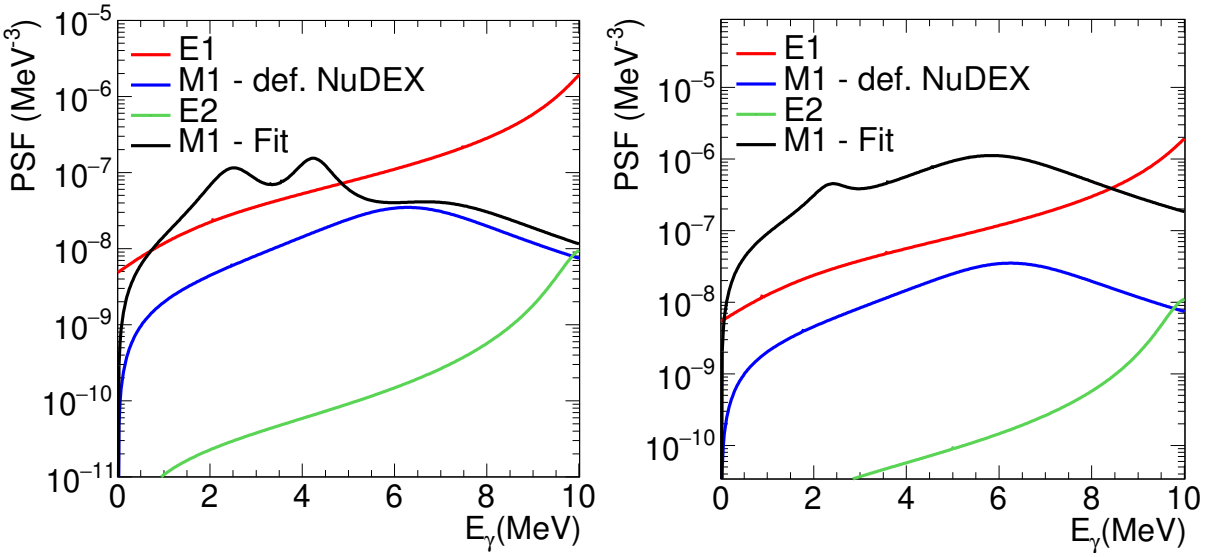

(a) ^{240}Pu(n,γ) (b) ^{244}Cm(n,γ)

Figure 3.7: PSFs used in the calculations presented in the previous figures. The default values of the E1, M1 and E2 PSFs in NuDEX are plotted together with the modified M1 PSFs (M1-Fit) obtained from the fitting procedure.

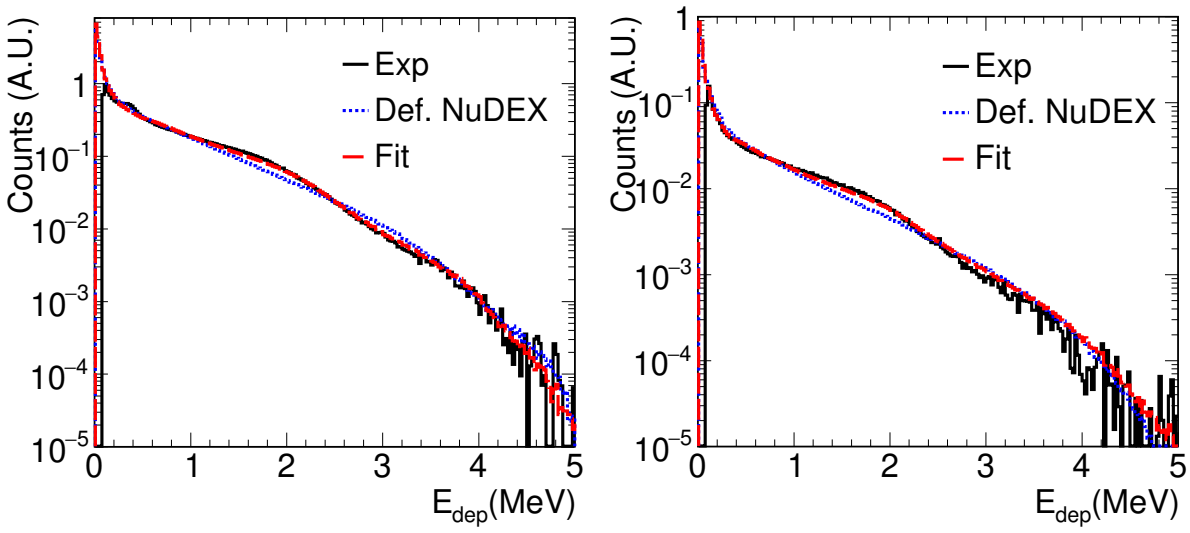

(a) ^{240}Pu(n,γ)

(b) ^{244}Cm(n,γ)

Figure 3.8: Comparison between experimental and simulated deposited energy spectra in the C_6D_6 detectors in EAR2. The experimental data are compared with the simulations performed with the same cascades used for the results presented in figures 3.2 and 3.3, i.e. using the default NuDEX PSFs and the PSFs fitted to reproduce the TAC spectra. The ^{240}Pu(n,γ) data are in the left panel and the ^{244}Cm(n,γ) are in the right panel.

3.2 ^{246}Cm(n,γ) cascades

The ^{246}Cm sample was only measured in EAR2 with the C_6D_6 detectors. No data were obtained in the measurement with the TAC due to limitations in the beam time and the size of the cross section of the first resonance of ^{246}Cm. The cascades were obtained by fitting the experimental data obtained with the C_6D_6 detectors. In this fit, the E1 and E2 PSFs were fixed to the default values in NuDEX, and the M1 PSF, defined with a SLO shape, was adjusted to match the experimental spectra. Only the energy and total size (σ) of the M1-PSF was varied, *by hand*. A reduced χ^2 was calculated for each set of PSF parameters, finding the minimum value.

In the left panel of Figure 3.9, the experimental deposited energy spectrum for the C_6D_6 detectors due to ^{246}Cm(n,γ) cascades is compared with the simulations using the default NuDEX cascades and the fitted ones. It can be observed that the modified PSFs reproduce with high accuracy the data. The propagation of the uncertainty in the normalisation of the EAR2 yields due to the γ-cascades are presented in Section 5.3.2.

The fitted M1 PSF is compared in the right panel of Figure 3.9 to the default NuDEX PSF. The fitted M1 PSF seems to be larger than expected, compared to the E1 PSF, since E1 transitions are assumed to dominate.

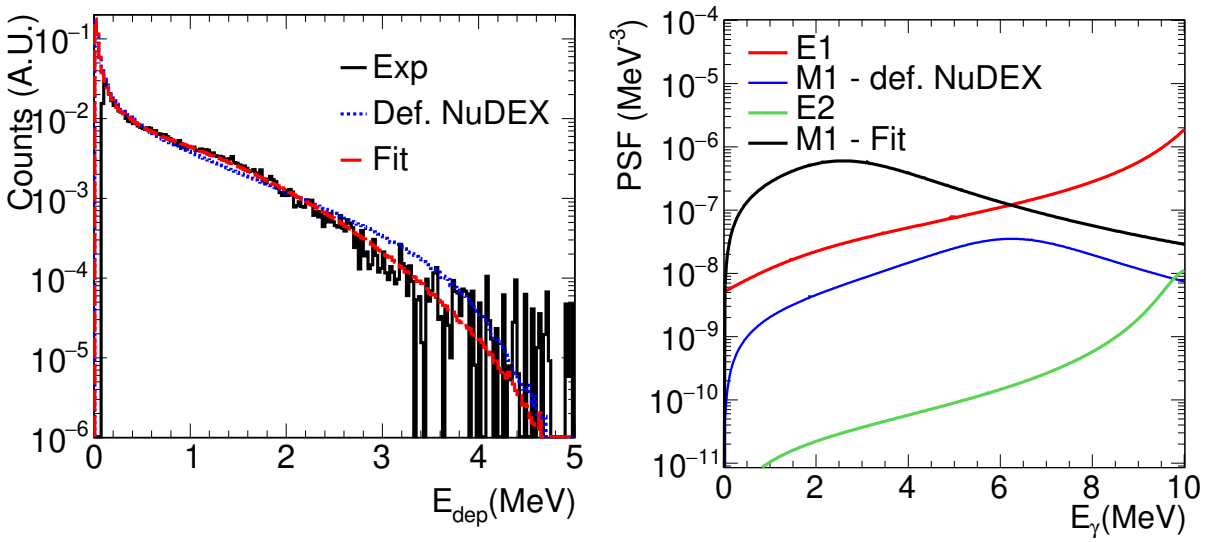

Figure 3.9: On the left panel, the comparison between experimental and simulated deposited energy spectra of ^{246}Cm(n,γ) (4.17-4.32 eV) obtained with the C_6D_6 detectors in EAR2. The experimental data (Exp) are compared with the simulations done with the default NuDEX PSF (Def. NuDEX) and the new adjusted PSF (Fit). On the right panel, PSFs of ^{246}Cm(n,γ) used in the calculations presented in the previous figures. The default values of the E1, M1 and E2 PSFs in NuDEX are plotted together with the modified M1 PSFs (M1 - Fit).

3.3 ^{248}Cm(n,γ) cascades

The default cascades from NuDEX have been used for ^{248}Cm, since there is not enough statistics to perform any fit or adjustment. Consequently, the uncertainties in the corrections associated with this cascade are larger than for the fitted cascades (Section 5.3.2). In Figure 3.10 the simulated response of the C_6D_6 detectors to capture cascades of ^{248}Cm are compared with the cascades of ^{240}Pu, ^{244}Cm and ^{246}Cm.

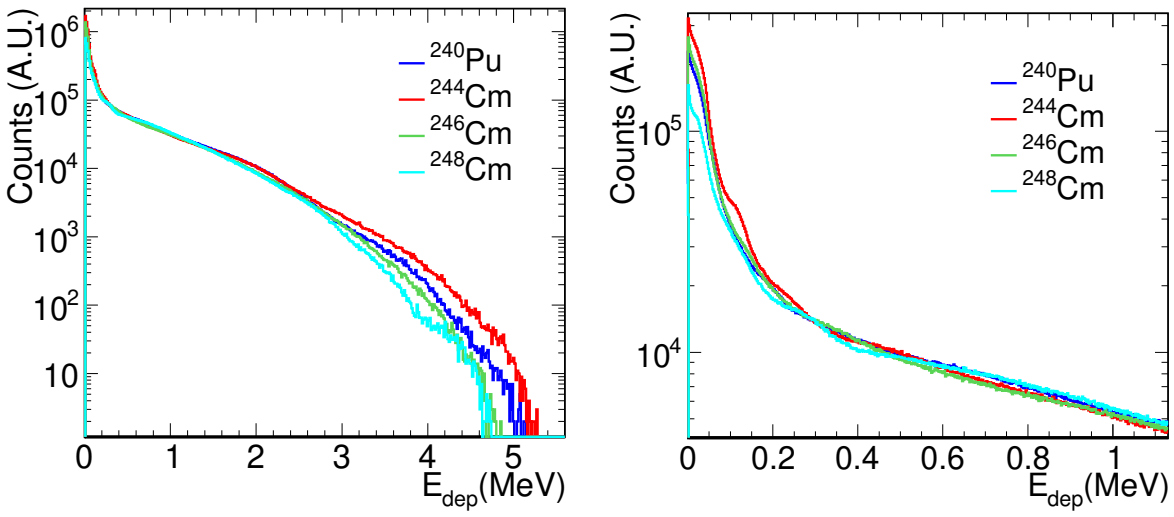

Figure 3.10: Comparison between the simulated deposited energy spectra in the C_6D_6 detectors due to ^{240}Pu, ^{244}Cm, ^{246}Cm and ^{248}Cm capture cascades. The cascades of ^{240}Pu and ^{244}Cm are obtained with the fit to the TAC experimental data, the cascades of ^{246}Cm with the adjustment to the C_6D_6 detectors spectra, and the cascades of ^{248}Cm correspond to the default cascades provided by NuDEX.

o

Chapter 4

Procurement of the ^{244}Cm experimental capture yield with the Total Absorption Calorimeter

The observable quantity in neutron capture cross section measurements is the capture yield. Which is defined for an isotope i as the fraction of neutrons impinging in a sample that undergoes a capture reaction in this isotope. The capture yield ($Y_{\gamma,i}$) is related to the capture cross section ($\sigma_{\gamma,i}(E_n)$) and to the total cross section $\sigma_{tot,i}(E_n)$ according to:

$$Y_{\gamma,i} = F_{ms}(E_n)\left(1 - e^{-n\sigma_{tot,i}(E_n)}\right)\frac{\sigma_{\gamma,i}(E_n)}{\sigma_{tot,i}(E_n)} \tag{4.1}$$

where n is the areal density (at/b) of the sample and $F_{ms}(E_n)$ is a factor to take into account the multiple scattering corrections, and it is described in detail in Section 6.1. Experimentally the capture yield ($Y_{\gamma,exp,i}$) is obtained for a given isotope:

$$Y_{\gamma,exp,i} = \frac{C - B}{\varepsilon_i \cdot \phi_n} \tag{4.2}$$

where C is the total counting rate, and B is the background counting rate, ε_i is the capture detection efficiency for the isotope i and ϕ_n is the number of neutrons impinging in the sample per unit time.

In this chapter, the detailed explanation of the calculation of the different parameters of the previous equation (4.2) are presented. The various steps to precisely obtain the TAC events counting rate (C) from the detector signals are presented in Section 4.1. The efficiency (ε_i) values are presented in Section 4.2. The different background (B) components are described in Section 4.3. The number of neutrons impinging in the sample (ϕ_n) is determined by multiplying the BIF (Section 4.4) with the fluence (Section 2.5.2). In the last section of the chapter, the final yield and the uncertainties are presented.

The Cm campaign in EAR1 lasted ten days, from 12/09/2017 to 21/09/2017. Table 4.1 summarises the type of measurements performed, together with the number of protons and the run identifications numbers (abbreviated as *run*).

	Number of protons	Run number
^{244}Cm sample	$4.0{\cdot}10^{17}$	107136-107140 107161-107165 107168-107180
Dummy ^{244}Cm sample	$1.1{\cdot}10^{17}$	107222-107229
Activity ^{244}Cm sample	-	107141 107151 107156 107166-107167
^{197}Au	$1.0{\cdot}10^{17}$	107129-107135
Calibration sources	-	107185-107214
Total	$6.1{\cdot}10^{17}$	107129-107229

Table 4.1: Different measurements performed in EAR1 in the ^{244}Cm campaign. The number of protons and the corresponding run numbers are given for each measurement.

4.1 Calibration and reduction of the TAC data

This section describes the analysis of the data from the BaF_2 signals to obtain the final TAC events (Section 2.2.1). Many of the tools and procedures needed for this analysis have been developed and used in previous measurements [72, 78, 105, 106].

The first step is the α/γ/noise discrimination (4.1.1). Then, the γ-signals are calibrated in energy, and the energy resolution of each module is obtained (4.1.2). In order to correct for the different gain modifications the gain shifts are calculated for each run (Section 4.1.3). Apart from the detailed energy calibration performed in the two previous sections to create the TAC events is necessary to perform precise time coincidences between all the TAC crystals. For this reason, the time calibration of each module is necessary (4.1.4). Pile-up corrections, which were large in previous measurements [105, 106] are treated in Section 4.1.5. Finally, in order to validate the previous work, the counting rates in the crystals after the analysis are monitored (4.1.6).

The same procedure is followed in the analysis of all the crystals (except in the cases explicitly mentioned in the text). The results obtained for detector 17 are shown as an example in this manuscript.

4.1.1 α/γ/noise discrimination

The BaF_2 crystals have an intrinsic background due to the presence of the isotopes of ^{226,228}Ra, and its progeny [9]. Part of this background corresponds to the detection of α-particles emitted in the radioactive decay, which can be efficiently separated from other signals via pulse shape discrimination. The discrimination between γ-rays and α-particles is based on the direct relationship between the type of ionising particle and the relative contribution of the fast ($\sim$0.7 ns) and slow ($\sim$620 ns) scintillation components [86]. The α-particles show a significantly suppressed fast component.

The signals are fitted with two exponential functions with the slow and fast decay times obtaining the corresponding slow (A_{slow}) and fast (A_{fast}) amplitudes. The ratio between the fast amplitude (A_{fast}) and the total area ($Area$) is calculated to perform the

discrimination between the particles. The small signals detected by the analysis routine that do not correspond to real signals are usually called noise and are removed from the analysis by the comparison of the time width of the detected signal (T_{real}) and the expected real-time of the signal ($T_{expected} \approx 620$ ns).

In Figures 4.1 and 4.2, the cuts implemented to separate the different components are shown. In the left top panel of the figures, the different components (α/γ/noise) are separated after the discrimination. In the rest of the panels the cuts applied to the signals (dashed lines) in the ratios $T_{real}/T_{expected}$ and $A_{fast}/Area$ are presented with cuts in A_{slow}.

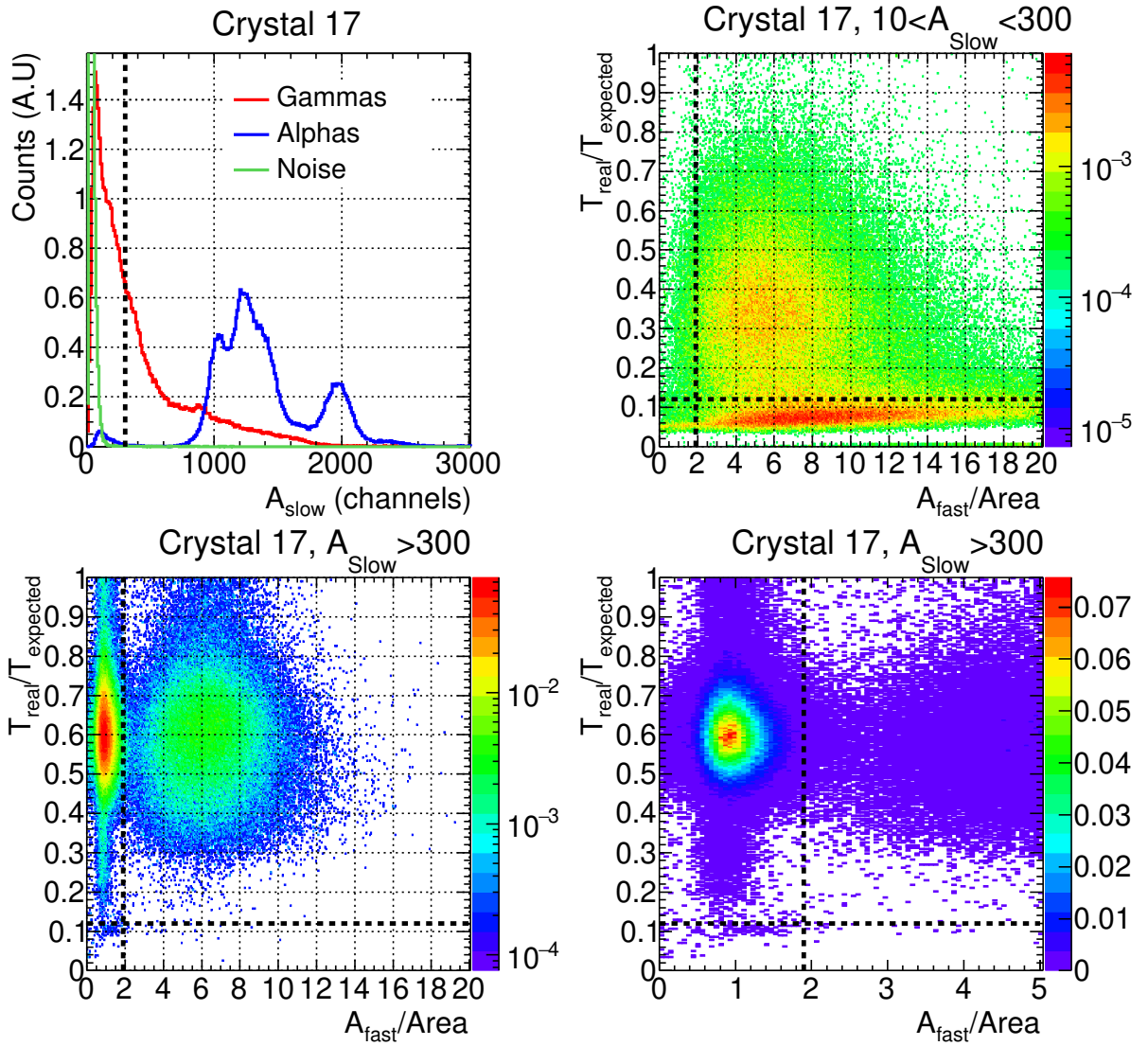

Figure 4.1: Pulse shape discrimination for signals detected in crystal 17 with a measurement performed without beam. The top left panel shows the discrimination of the α-component (blue), the γ-component (red) and the noise (green). The rest of the panels shows the cuts apply to separate the different components with different A_{Slow} conditions for the same run.

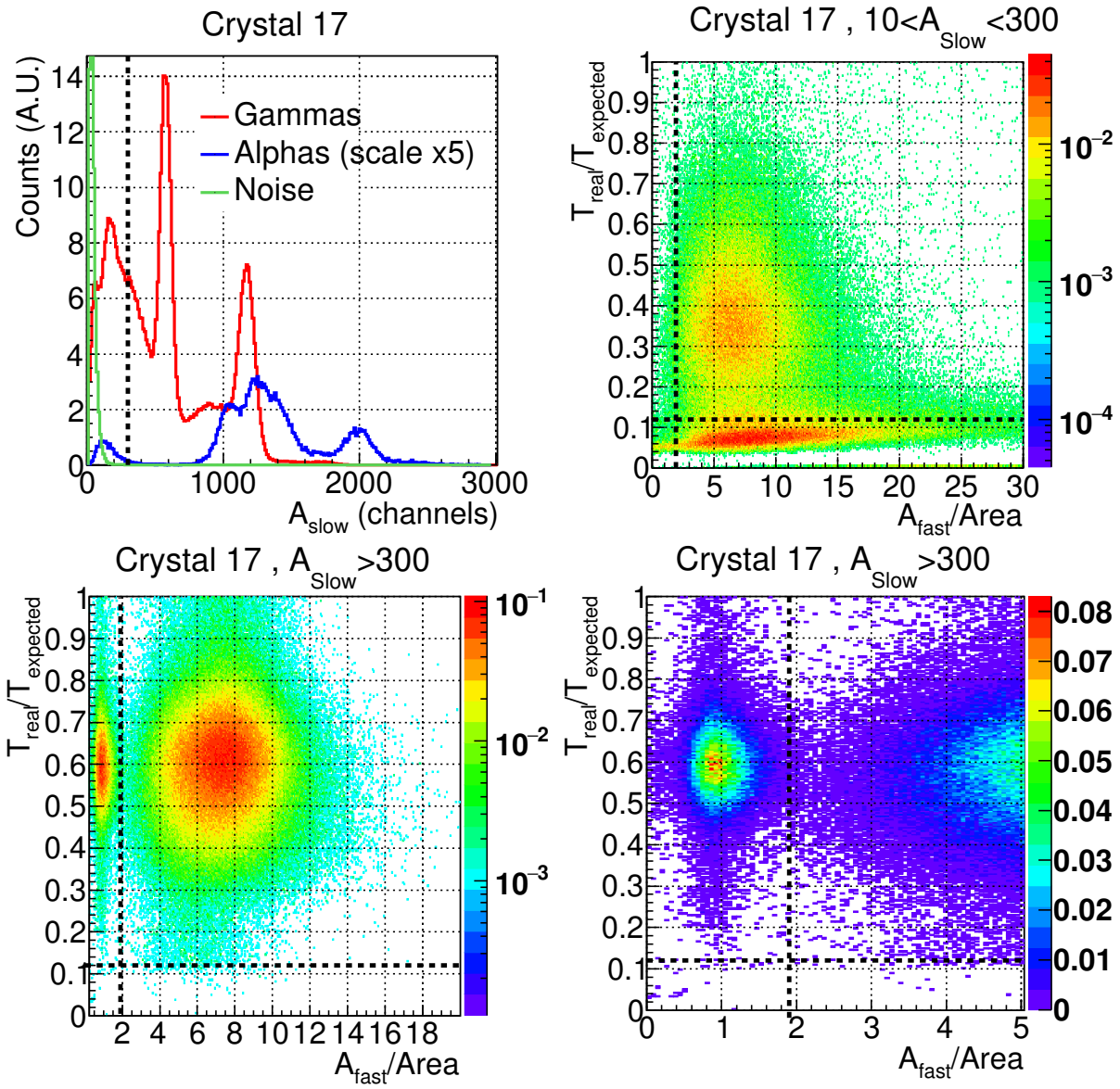

Figure 4.2: Pulse shape discrimination for signals detected in crystal 17 with a ^{88}Y calibration source. The top left panel shows the discrimination of the α-component (blue), the γ-component (red) and the noise (green). The rest of the panels shows the cuts apply to separate the different components with different A_{Slow} conditions for the same run.

The amount of α-particles emitted by all the detectors but detector 6, which does not have an appreciable amount of α-particles contaminants, are similar.

4.1.2 Energy calibration and characterisation of the energy resolution

The energy calibration of the TAC was performed with four standard γ-ray sources, which emit gamma rays covering a wide energy range:

- ^{137}Cs: E_γ= 0.662 MeV.
- ^{88}Y: E_γ=0.898 MeV and E_γ=1.836 MeV.
- Am-Be: E_γ= 4.438 MeV.
- Cm-C: E_γ= 6.130 MeV.

The energy calibration has been done obtaining the correspondence between the A_{slow} component and the energies of the four γ-ray sources [9]. This process has been performed by obtaining the position of the different peaks with Gaussian (+ straight line) fits. The ^{137}Cs peak and the two peaks of ^{88}Y are fitted in the top panel of Figure 4.3. The Am-Be and Cm-C produce a spectrum with two peaks: the full absorption peak at higher energy and the single escape peak at 511 keV below. As observed in the bottom panels of Figure 4.3 the full absorption peak is fitted with a Gaussian curve.

The relation between the energy of the γ-rays and the centroids of the fits are employed to obtain the energy calibration. A parabolic fit, $E_{dep}(A_{slow}) = a_1 + a_2 A_{slow} + a_3 A_{slow}^2$, is used to obtain the energy calibration in Figure 4.4. A linear fit can also be used, but the parabolic fit reproduces the data better, particularly the two points at higher energies.

The energy resolution of the crystals are needed to calculate the response of the TAC by Monte Carlo simulations. It was determined as a function of E_{dep} for each crystal from the detector response to the four γ-ray sources. The resolution at each of the energies was obtained from the widths of the fitted gaussians. The function used to fit this values is FWHM $= \sqrt{(\alpha \cdot E^2 + \beta \cdot E)}$, where the Full Width Half Maximum (FWHM) is calculated in MeV and the resolution is defined as $R(E_{dep})$=FWHM/E_{dep}. For more details on this formula the reader is referred to [132].

In Figure 4.5 the fit is presented for detector 17. The resolution obtained with this detector is 14.3% at 1 MeV and 9.2% at 5 MeV. These values are very similar to those obtained in [133] and [9].

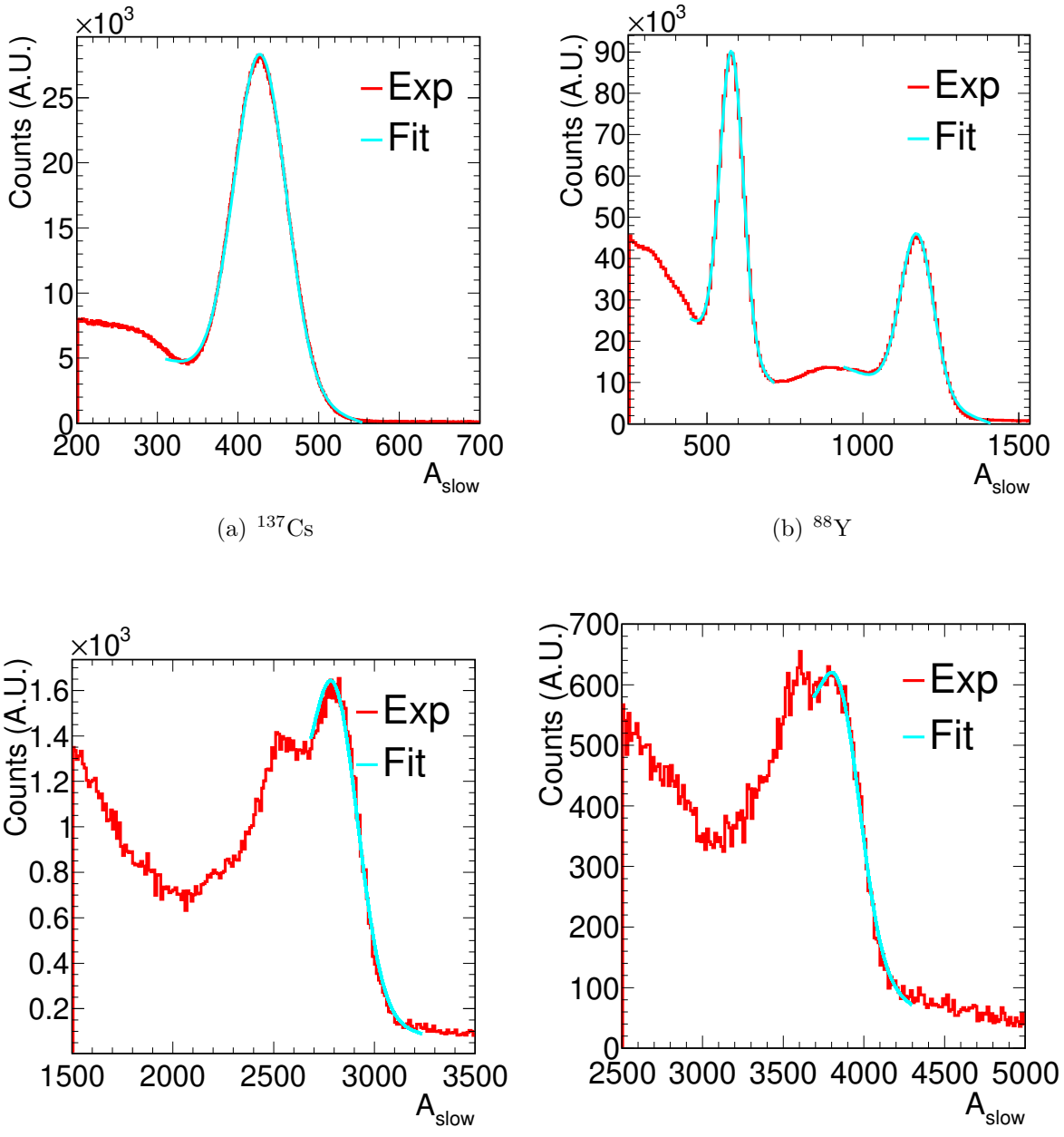

(a) ^{137}Cs

(b) ^{88}Y

(c) Am-Be

(d) Cm-C

Figure 4.3: Response of BaF_2 module 17 to four calibration sources. The cyan lines fit the experimental data, in red, using Gaussian functions mounted on straight lines.

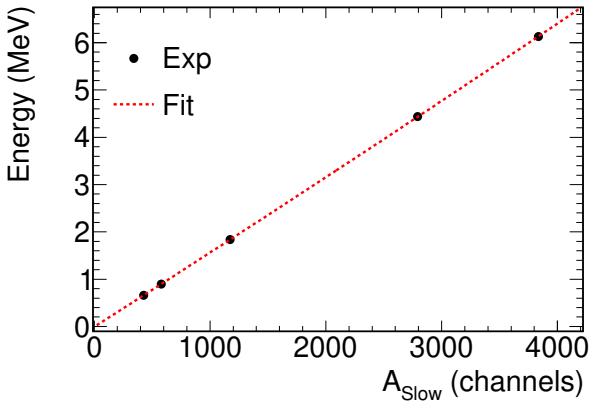

Figure 4.4: Energy calibration for detector 17. The five calibration points of ^{137}Cs, ^{88}Y, Am-Be and Cm-C are fitted with a parabolic ($E_\gamma(A_{slow}) = a_1 + a_2 A_{slow} + a_3 A_{slow}^2$) curve to obtain the relation between the A_{slow} and the energy deposited in the detector.

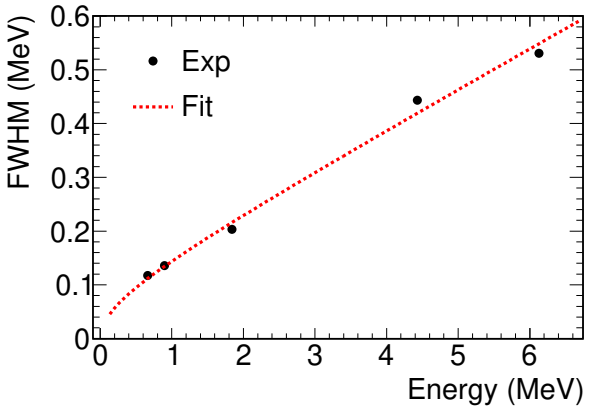

Figure 4.5: FWHM of the photopeaks of detector 17 as a function of the deposited energy obtained with the different calibration sources. The experimental points have been fitted to the function FWHM $= \sqrt{(\alpha \cdot E^2 + \beta \cdot E)}$.

4.1.3 Gain monitoring and correction

The changes of the BaF_2 detector gains along the measurement have been determined from the changes in the α-spectra produced by the ^{226,228}Ra contaminants. The methodology was developed and used in previous measurements [72, 78, 105, 106]. Two different techniques are used to monitor the changes of gain.

In the first technique, the evolution of the centroid of the high energy peak in the α-spectrum (left panel of Figure 4.6) was used to monitor the change in the energy calibration for each run. These changes in gain are calculated with respect to the first run (107118) as a gain factor.

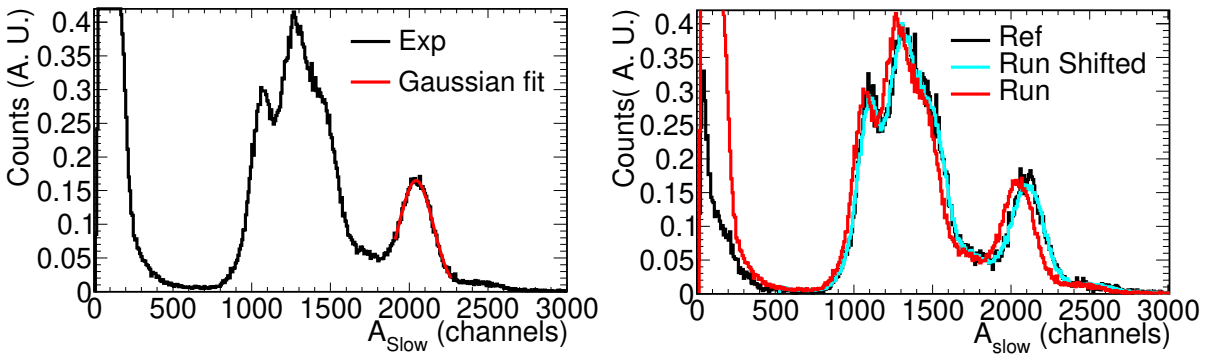

Figure 4.6: Different techniques to calculate the changes in gain for each run. The left panel shows the α-spectrum with the Gaussian fit done in the higher energy peak. The right panel shows the α-spectrum of the reference run (107118) (black) and the one of the run 107162 (red). The cyan line corresponds to the spectrum of the run 107162 multiplied by 1.025 to match the reference α-spectrum. Then the gain factor obtained with this technique is 1/1.025=0.976.

The second technique calculates the gain factor for each run by transforming the run spectrum linearly to match the reference run spectrum (107118), as presented in the right panel of Figure 4.6. The gain factor is the inverse of the value used to match the reference run.

The two different techniques to obtain the gain variations give very similar results (Figure 4.7) and the average of the two values has been used to correct the crystal gain shifts in each run. In addition, in Figure 4.7, two separate tendencies are observed: a steady modification of the gain as a function of the time and a sharp modification of the gain when there is a change of sample or beam conditions.

In the precise calibration process of each detector, it has been observed that detector 25 has a strong and unstable modification of the gain in runs with beam. For this reason, detector 25 was not used in the analysis to obtain the final yield. This effect was also considered in the Geant4 simulations used to calculate the efficiency of the TAC.

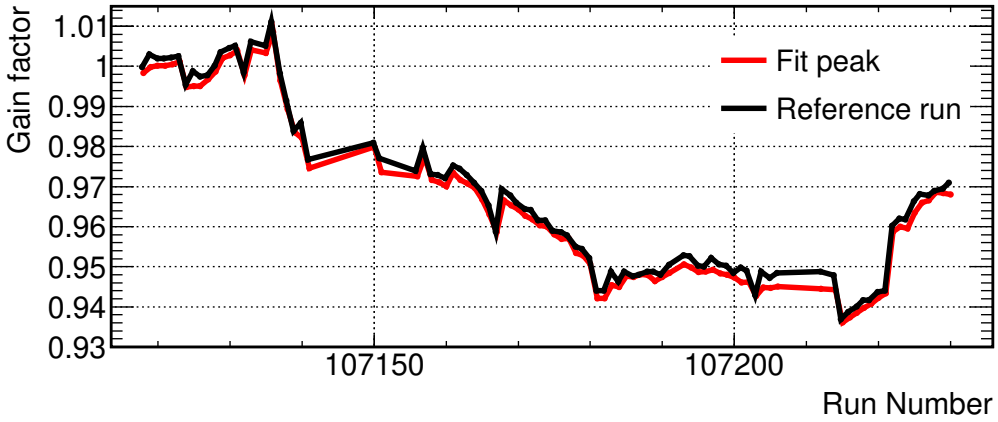

Figure 4.7: Evolution of the gain of detector 17 calculated with two different techniques. The red line is obtained by fitting the highest energy peak of the α-spectra, and the black line is calculated by comparing the shift of the whole α-spectra to a reference run.

4.1.4 Time calibration

The coincidence of the 39 BAF_2 detectors (detector 25 was removed from the analysis) is required to produce the TAC events. The time of each individual detector needs to be synchronised to take into account the effect of the different cable lengths and the different digitiser clocks (one per board). All the detectors are synchronised with respect to a master detector, in this experiment detector 13. This synchronisation is done by adding a different constant time offset to each detector's time, calculated from coincident data measured with an ^{88}Y source.

The time difference between the two γ-rays of ^{88}Y emitted in coincidence and detected in different crystals has been calculated and stored as a function of the buffer time (i.e. time-of-flight in a real measurement). These distributions have been fitted to obtain the time differences between the detectors. The differences between detector 13 (reference detector) and detector 17 are shown in Figure 4.8 together with the fit. The differences in time between detectors are of the order of tens of ns and independent of the TOF.
A time window of 20 ns has been used to make the TAC detectors' coincidences [72, 78, 106].

4.1.5 Pile-up corrections

The BaF_2 crystals are an excellent scintillator material due to its fast timing scintillation component $\tau_{fast} = 0.6$ ns but they also have a slow component ($\tau_{slow} = 620$ ns). The long tail of the decay can cause pile-up: two signals overlap, and there can be a distortion in the reconstruction of one or both.

The DAQ system used at n_TOF is able to record all the signals, even though due to the high counting rate and the slow component of the signals, the Pulse Shape Analysis can have difficulties in fitting the signals (pile-up). In previous measurements with the TAC [72, 78, 105, 106] pile-up corrections were needed due to the high counting rates, and

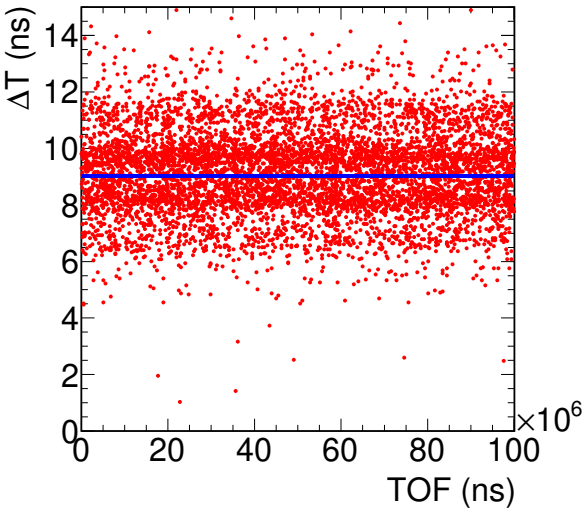

Figure 4.8: Time differences of detector 17 with respect to detector 13 calculated with an ^{88}Y source. The blue line is a constant fit to the data points

new methods were implemented to correct for the pile-up effects [134, 135]. In the Cm campaign, the small mass of the sample resulted in lower counting rates. In particular, for neutron energies below 200 eV there were less than 0.04 counts/μs per detector, as can be seen in Figure 4.9 for detector 17. In reference [9], it was mentioned that no pile-up corrections are needed in the TAC for counting rates below 0.1 counts/μs.

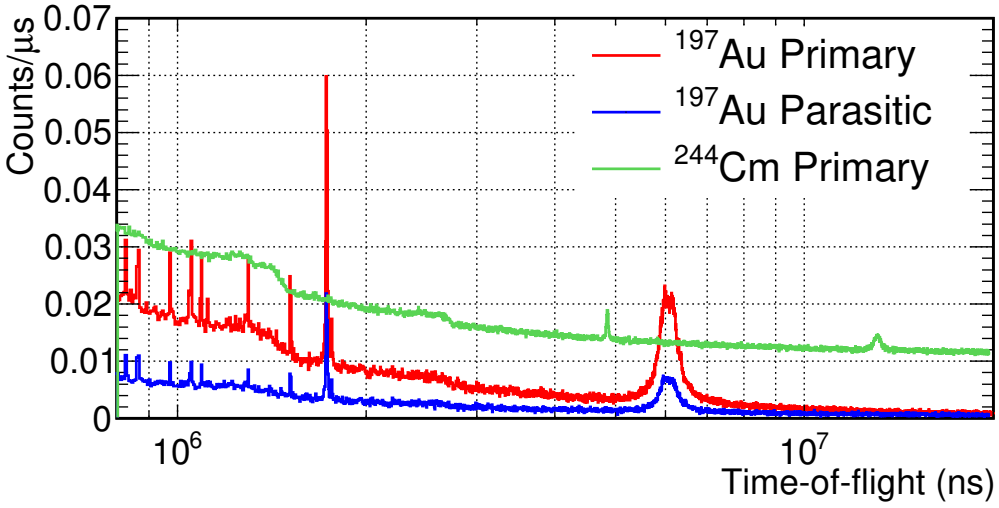

Figure 4.9: Counting rates in detector 17 when measuring the ^{197}Au and ^{244}Cm samples. A TOF of 10^6 ns corresponds in EAR1 to neutrons of approximately 180 eV.

The comparison of the data measured with high intensity (dedicated) and low intensity (parasitic) neutron pulses in Figure 4.10 for the ^{197}Au sample shows no difference in those resonances where there should be if there were pile-up effects. The counting rates for

the ^{244}Cm sample are lower than in the saturated resonance of ^{197}Au (Figure 4.9), so no differences are expected for the ^{244}Cm sample measurement.

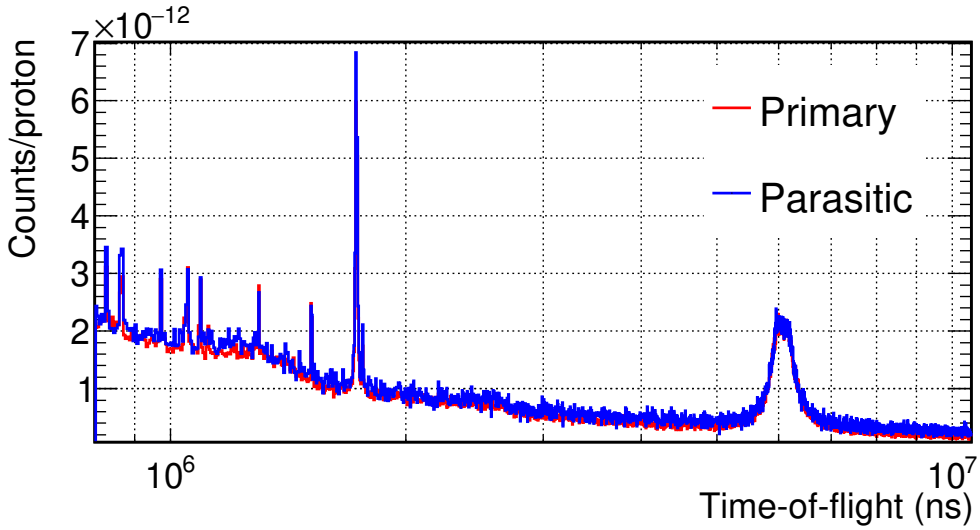

Figure 4.10: Comparison of the shape of the TAC count rate for dedicated and parasitic beam types normalised to the number of protons for the ^{197}Au measurement.

For these reasons, no pile-up corrections are applied in the analysis, which is done only for resonances below 100 eV.

4.1.6 Monitorisation of the counting rate

The possible wrong run assessments, no corrected changes in the gain or other problems with the TAC detector has been assessed by verifying that the counting rates in the TAC crystals after the energy calibration remained constant with respect to the neutron beam intensity, for each type of measurement.

The ratio between the counting rates in the TAC and the SiMon for each run are constant, as presented in Figure 4.11, for all the measurements: ^{244}Cm sample, ^{244}Cm dummy and ^{197}Au sample.

4.2 TAC efficiency calculation

The TAC efficiency is required for the calculation of the experimental yield. In Chapter 3, it is described the general process to obtain the efficiency with simulations and the de-excitation cascades.

The Monte Carlo simulations of the TAC detector are presented together with the reconstruction of this data to produce TAC events in Section 4.2.1. Using these simulations, the efficiency to detect the ^{240}Pu(n,γ) and ^{244}Cm(n,γ) cascades with the analysis cuts are presented with their uncertainties in Section 4.2.2.

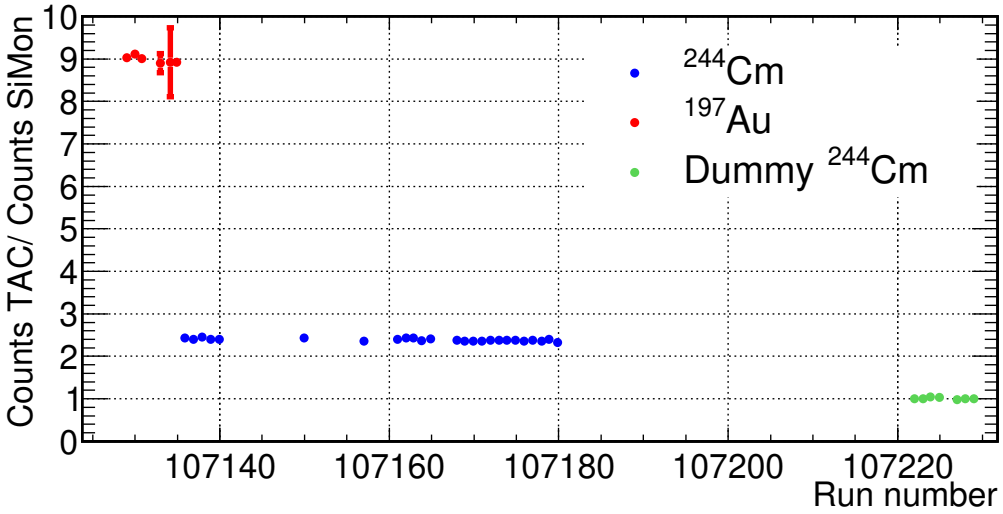

Figure 4.11: Number of events in the TAC with $2.5 < E_{sum}$ (MeV) < 6 cuts divided by the number of counts in the SiMon detector, for each run with beam. All the ratios have been normalised to the value obtained for run 107222.

4.2.1 Geant4 simulations of the TAC

The response of the TAC has been simulated with the Geant4 code version 10.2 [101]. The option 4 of the Standard Electromagnetic Physics Package [136] was used for accurate modelling of the electromagnetic processes. The precise geometry of the TAC used for this measurement (Figure 4.12) has been already used in previous measurements [9, 105, 133, 137, 138]. This geometry includes the crystals with their encapsulation, the photomultipliers, the honeycomb structure supporting the detector array, the Cm sample and the sample holder illustrated in Figure 2.4.

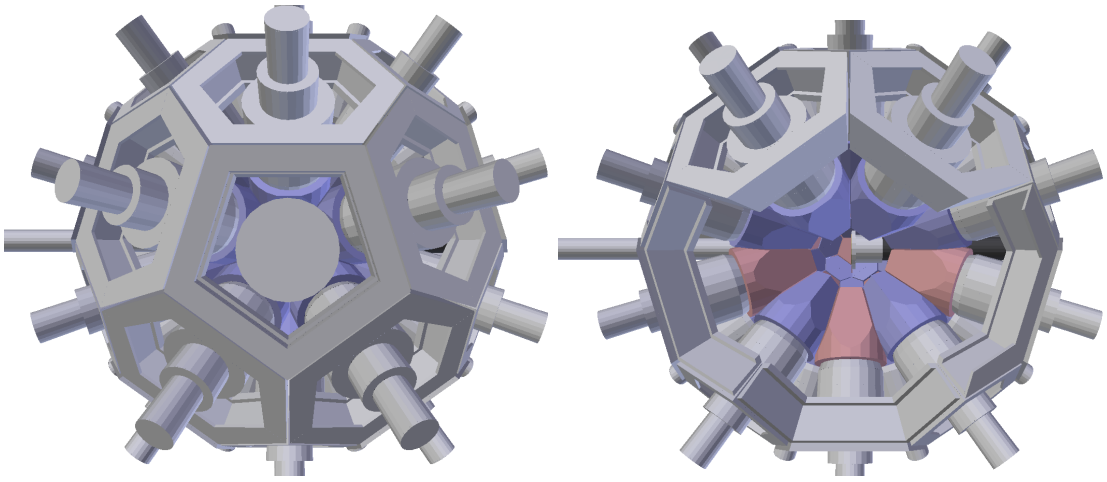

Figure 4.12: View of the TAC as implemented in Geant4 used for the Monte Carlo simulations. The left panel shows all the TAC modules, and the right panel shows the detector removing some modules to see the centre of the TAC.

The outcomes obtained from the simulations are processed with an event reconstruc-

tion software, analogous to the one used for the experimental data, divided into three steps:

- The energy deposition in each crystal in the simulations is folded with the experimental energy resolution.
- A coincidence analysis is performed after setting the experimental threshold in each crystal applying the same time coincidence window as in the experiment.
- The total energy (E_{sum}) and multiplicity (m_{cr}) of the events are obtained.

From the point of view of the uncertainties associated with the Monte Carlo simulations, previous studies [9, 105, 133, 137, 138] have shown that one of the most significant sources of uncertainty is the lack of knowledge of the exact position of the TAC crystals. This effect has been parametrised as the average distance from the crystals to the TAC centre, called the TAC radius. This value is calibrated by comparing simulations and experimental data measured with γ-ray calibration sources. The TAC radius obtained was 10.49(9) cm. As illustrated in Figure 4.13, the simulations reproduce with high accuracy the experimental spectra with this radius and a 0.3 MeV threshold in the crystals. The reproduction of the spectra is worse when lower thresholds are used. Indeed, these comparisons were used to set the energy threshold of the BaF_2 crystals in 0.3 MeV.

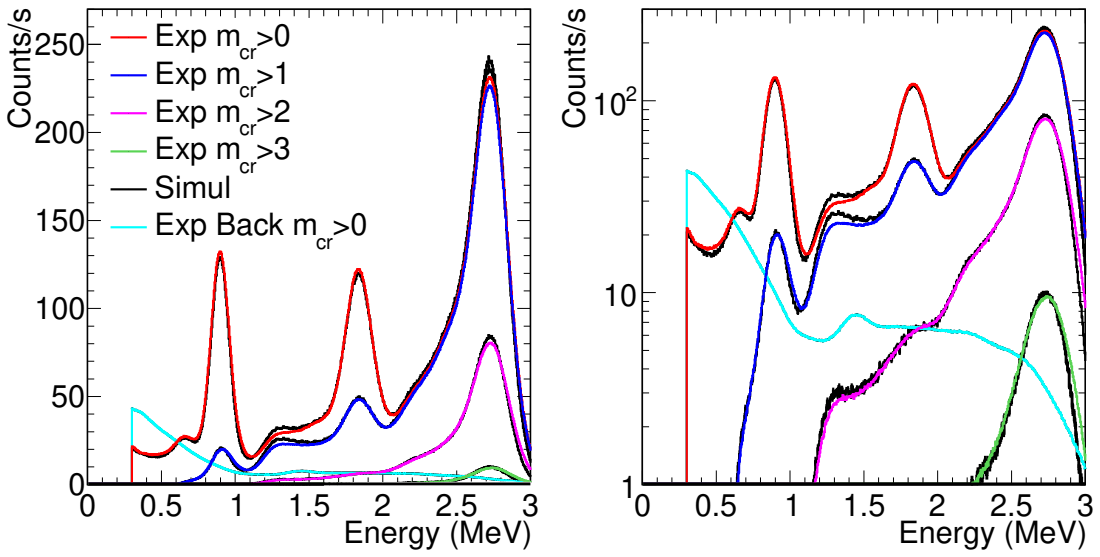

(a) Linear scale

(b) Logarithmic scale

Figure 4.13: Comparison between the experimental data the Monte Carlo results for the standard γ-ray ^{88}Y calibration source in linear and logarithmic scale.

The value obtained for the radius is very similar to the one obtained from the previous measurement with the TAC done in 2016 by M. Bacak, which was 10.56 cm [138]. In the measurement of ^{235}U in 2012, the value obtained was 11.40 cm [133].

The excellent reproduction of the γ-cascade of ^{197}Au(γ,n) in Figure 3.1 with the cascades obtained in previous works is also an indication of the quality of the Monte Carlo simulations and the determination of the inner radius of the TAC.

4.2.2 Final efficiencies and their uncertainties

The efficiencies to detect the ^{240}Pu(n,γ) and ^{244}Cm(n,γ) cascades, from certain cuts in E_{sum} and m_{cr}, are obtained from the results of the simulations (Figures 3.2 and 3.3). The efficiency values are then presented in Table 4.2 for 2.5<E_{sum} (MeV)<6.0 and various m_{cr}.

m_{cr} >	^{240}Pu		^{244}Cm		$\varepsilon_{\gamma\ ^{240}Pu\ Fit}/\varepsilon_{\gamma\ ^{244}Cm\ Fit}$	$\varepsilon_{\gamma\ ^{240}Pu\ def}/\varepsilon_{\gamma\ ^{244}Cm\ def.}$
	$\varepsilon_{\gamma\ Fit}$	$\varepsilon_{\gamma\ def.}$	$\varepsilon_{\gamma\ Fit}$	$\varepsilon_{\gamma\ def.}$		
0	0.802(3)	0.807	0.805(2)	0.815	0.996(4)	0.991
1	0.777(4)	0.785	0.778(4)	0.794	0.999(7)	0.989
2	0.589(7)	0.618	0.589(7)	0.636	1.000(17)	0.97
3	0.278(6)	0.321	0.282(6)	0.345	0.983(28)	0.93
4	0.080(2)	0.102	0.083(2)	0.117	0.964(39)	0.87

Table 4.2: Detection efficiency (ε_γ) for 2.5 < E_{sum} (MeV) < 6.0 and different multiplicities obtained with the default NuDEX ($def.$) and the fitted (Fit) cascades presented in Section 3.1. The uncertainties in the ^{240}Pu and ^{244}Cm efficiencies correspond to the uncertainties in the event generator only, i.e. without considering the contribution of the geometry, and the uncertainties in the efficiencies ratio (second column from the right) correspond to the total uncertainties.

In previous works with the TAC [9, 105, 133, 137, 138], the uncertainty in the efficiency due to the Monte Carlo transport has been estimated in 1-2%, and corresponds to the propagation of the uncertainty in the radius of the TAC to the detection efficiency. In the Cm campaign, the ^{244}Cm cross section has been normalised with respect to the first resonance of ^{240}Pu, and the characteristics of the γ-cascades are very similar. Consequently, when simulations are done with different inner radius, the differences in the ratio $\varepsilon_{\gamma^{240}Pu}/\varepsilon_{\gamma^{244}Cm}$ are less than 0.2 % for variations of the radius of some millimetres. However, the variations of each of the two efficiencies are much larger. For the uncertainties associated with the reconstruction process, the differences in the calculation of $\varepsilon_{\gamma^{240}Pu}/\varepsilon_{\gamma^{244}Cm}$ are also minimal due to the similarity of the two cascades. The most significant contribution to the total uncertainty in this ratio, shown in the second column on the right of Table 4.2, is the uncertainty in the event generator presented in Table 3.1 of Section 3.1.

4.3 Background

The different sources of background in the ^{244}Cm and ^{244}Pu measurements in EAR1 with the TAC detector are:

i) **The environmental background.** This background was estimated from the environmental background dedicated measurement performed with beam-off and without any sample. This contribution is presented in the pink line (Env. background) of Figure 4.14.

ii) **The activity of the Cm sample.** Mainly the γ-rays and neutrons emitted from the decay of the different actinide isotopes in the sample. The activity of the sample is measured in dedicated runs with beam-off. The result obtained is presented in the red line (Activity ^{244}Cm) of Figure 4.14.

iii) **Background induced by the neutron beam, excluding the part related to the interaction with the actinides of the sample.** In order to obtain this background, a dummy sample was created, including the aluminium canings, the Kapton foils, the Mylar foils and the aluminium ring shown in Figure 2.14. All the interactions of the neutron beam were measured in dedicated runs with the dummy sample and are shown in the green line (Dummy ^{244}Cm) of Figure 4.14.

iv) **The interaction of the neutron beam with the actinides in the sample.** The background produced by the capture, fission and elastic scattering in the actinides of the sample, except the capture events in ^{244}Cm and ^{240}Pu. This component has not been determined experimentally but from the corresponding reaction yields and the associated detection efficiencies. The reaction yields were obtained with SAMMY, using the cross sections in JEFF-3.3 (or those adjusted in the resonance analysis) and from the different isotopic abundances (Table 2.2). The calculation of the various efficiencies is discussed below, in section 4.3.1.

In figure 4.14 the different background components explained in the previous list are presented, except the contributions associated with the interaction of neutrons with the actinides that are going to be subtracted in the resonance analysis.

4.3.1 Capture, fission and elastic scattering detection efficiencies of the different actinides in the sample

In the sample of ^{244}Cm, in addition to ^{244}Cm and ^{240}Pu there is ^{246}Cm. Therefore, in order to calculate the background correctly, it is necessary to know, in principle, the capture efficiency of ^{246}Cm and the fission detection and elastic scattering efficiencies of the three isotopes.

- **The capture efficiency (ε_γ).** The capture efficiency of ^{246}Cm has been estimated in 0.60(5). This value has been obtained from Monte Carlo simulations similar to those used for ^{244}Cm and ^{240}Pu, using NuDEX's default cascades. In any case the impact of ^{246}Cm on the results of the analysis is negligible. This is because the amount of ^{246}Cm is very low (10 times less than ^{244}Cm) and the resonances do not overlap with those of ^{244}Cm and ^{240}Pu.

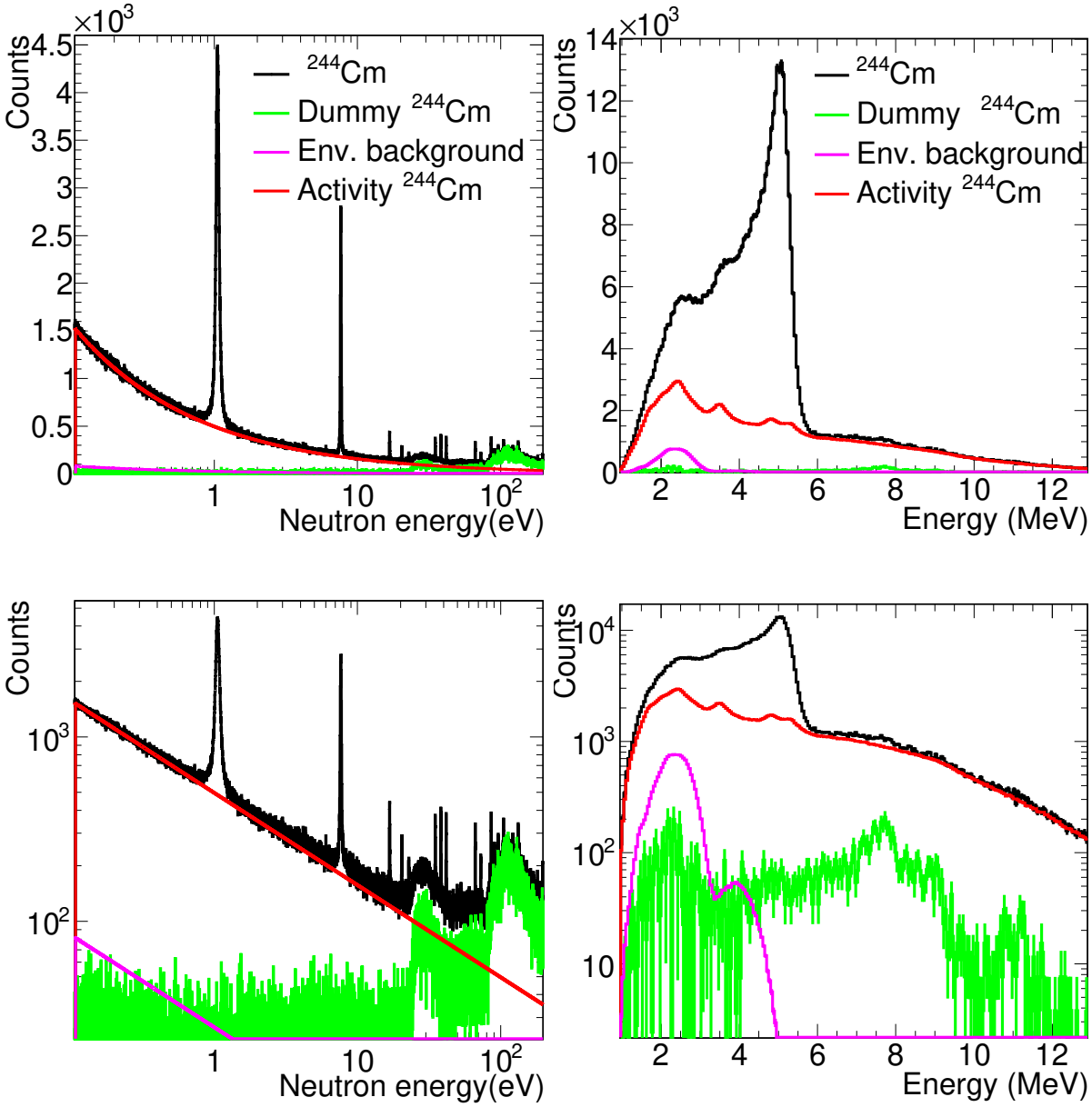

Figure 4.14: ^{244}Cm sample measurement (black) with the different background components of the measurement. A detailed description of the background components can be found in the text. The left panels show the number of counts as a function of the neutron energy with the analysis cuts, 2.5<E_{sum} <6 and m_{cr} >2 in linear and logarithmic scales. The right panels show the E_{sum} spectra contributions for the first ^{240}Pu resonance (0.9<E_n <1.1) with m_{cr}>2.

- **The fission efficiency (ε_f).** The fission efficiency has been assumed to be the same for the different isotopes in the sample. The value has been set to $\varepsilon_f = 0.37 \pm 0.05$, which has been taken from the TAC detection efficiency to ^{235}U(n,f) events reported by J. Balibrea et al. [78]. The uncertainty is large (∼15%) because it considers differences in both the experimental conditions and the fissioning nuclei. The uncertainties in the fission cross section of ^{240}Pu and the even Cm isotopes

are approximately 20%, according to the evaluations. For this reason, the final uncertainty in the fission subtraction is 30%.

- **The elastic scattering efficiency (ε_{elas}).** The efficiency has been calculated by measuring an aluminium sample. By considering the fluence, the size of the sample and the background contributions, the elastic scattering efficiency as a function of the neutron energy has been obtained from the measurement (Figure 4.15).

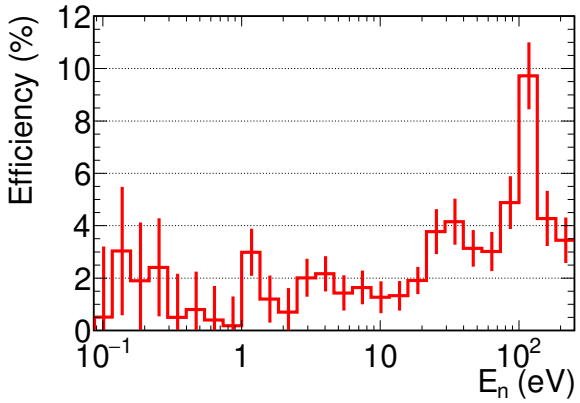

Figure 4.15: Probability of detecting a neutron emitted in the centre of the TAC (elastic scattering efficiency) with a given energy, the analysis cuts used are $m_{cr} > 2$ and $2.5 < E_{sum} < 6.0$.

The efficiency obtained is higher than in previous measurements [122, 133] because the Cm campaign measurement has been done without a neutron absorber.

4.4 Normalisation of the experimental yield

The total amount of ^{240}Pu and ^{244}Cm present in the sample is not known with reasonable accuracy, has been normalised whereas the ratio ^{240}Pu/^{244}Cm is known with a 2.8% uncertainty. Hence the ^{244}Cm(n,γ) cross section has been normalised to the first resonance of ^{240}Pu.

On the other hand, a reasonable estimation of ^{240}Pu and ^{244}Cm masses are necessary to perform the shelf-shielding and multiple scattering corrections in the resonance analysis. The absolute mass of ^{240}Pu has been obtained by normalising the yield to the first resonance at 1.056 eV in JEFF-3.3. The masses of the rest of the isotopes have been calculated with the value obtained for ^{240}Pu and the abundances of Table 2.2. The neutron fluence in the sample, necessary for this calculation, has been obtained by multiplying the neutron fluence of the full beam (Section 2.5.2) with the so called Beam Interception Factor (BIF), which is the fraction of the beam covered by the sample.

In order to precisely determine the BIF, the Saturated Resonance Method [139, 140] has been used. This method uses resonances with large cross-sections. For these resonances, almost all the neutrons passing through the sample interacts and then the BIF

can be obtained with a small dependence on the cross section or samples mass. This is the standard method used at n_TOF to obtain the BIF, used in most of the capture measurements. The method has been applied to the yield obtained for the first strong resonance of ^{197}Au at 4.9 eV, measured using a sample with the same diameter as the ^{244}Cm sample. The efficiency used in the calculation has been determined from Monte Carlo simulations (Figure 3.1), in the same way as for ^{240}Pu and ^{244}Cm, and the value obtained is ε_γ=0.502 ± 0.005. The precise fit to the resonance of ^{197}Au is presented in Figure 4.16 and the BIF obtained in the fit is 0.067 ± 0.001.

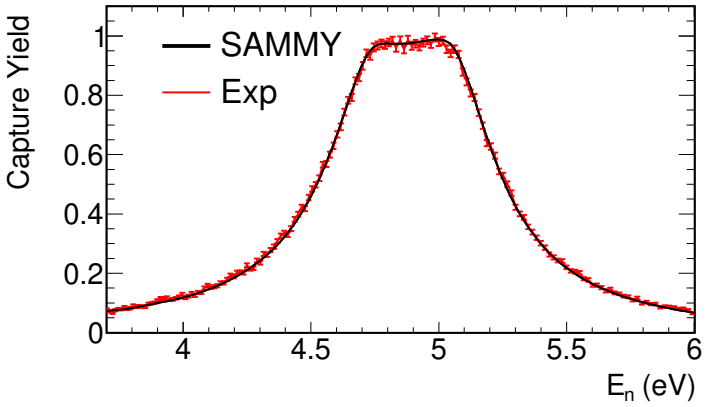

Figure 4.16: Capture yield of the 4.9 eV ^{197}Au saturated resonance, used to determine the fraction of the neutron beam intercepted by the sample.

4.5 Experimental yield with the TAC

In this section, the determination of the ^{240}Pu and ^{244}Cm yields and their uncertainties are presented. The experimental yield for an isotope i is calculated with equation 4.2. The necessary time-of-flight to energy conversion is performed with Equation 2.3 using a time-of-flight distance of 185.6 m. This value has been obtained by adjusting the measured ^{197}Au(n,γ) yield to reproduce the energies of the ^{197}Au resonances in JEFF-3.3.

Different conditions in the detected events are chosen to obtain the capture yield. The more restrictive these conditions are, the better the signal to background ratio is, but the lower the detection efficiency is. A compromise has to be found.

The condition used in the total deposited energy is $2.5 < E_{sum}$ (MeV) < 6. The neutron separation energies of ^{241}Pu and ^{245}Cm are 5.241 MeV and 5.520 MeV, respectively. For this reason, a 6 MeV limit is used. The lower limit is set to 2.5 MeV because as presented in Figure 4.14 the majority of the events detected in the TAC for deposited energies below 2.5 MeV are due to the activity of the ^{244}Cm sample.

It has been verified that the capture yields constructed from different multiplicity conditions of the detected events are equivalent, as it is presented in Figure 4.17 for the 7.67 eV ^{244}Cm resonance. In the right panel of Figure 4.17 the yields, without subtracting

the backgrounds, are calculated for different multiplicities. The background to signal ratio is reduced approximately a factor of 1.5 when comparing the conditions $m_{cr} > 0$ and $m_{cr} > 1$. This factor is 3 when comparing $m_{cr} > 0$ and $m_{cr} > 2$. The signal to background is very similar for the conditions $m_{cr} > 2$ and $m_{cr} > 3$, whereas the efficiency is reduced to the half (Table 4.2). For this reason, the final multiplicity cut used in the analysis are $m_{cr} > 2$ to find a compromise between the signal to noise ratio and the efficiency.

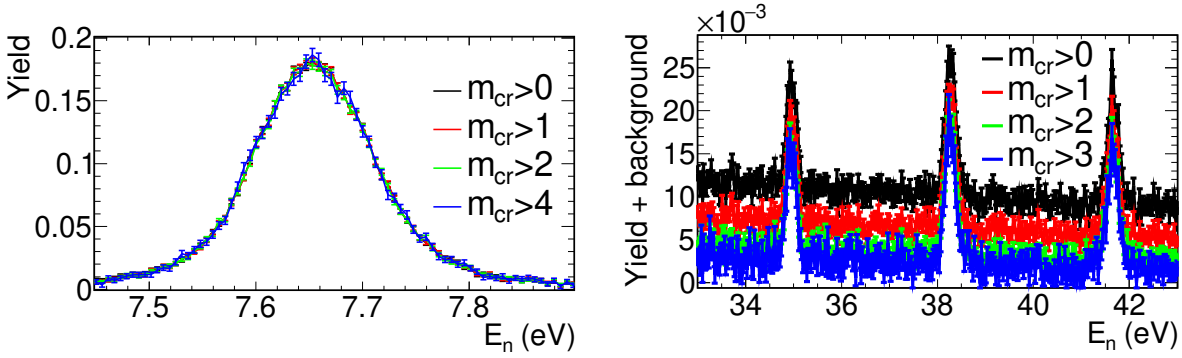

Figure 4.17: Experimental capture yield obtained from 2.5<E_{sum} (MeV)<6 and different multiplicity cuts. The yields with the backgrounds subtracted are compared for the first ^{244}Cm resonance in the left panel. In the right panel, the yields without subtracting the backgrounds are compared for various multiplicities to observe the difference signal to background levels.

Concerning the uncertainties, in addition to those due to counting statistics, the following contributions have been considered:

i) **Uncertainty in the normalisation**. The yields are normalised with respect to the first resonance of ^{240}Pu. The uncertainties associated with this process for the ^{244}Cm yield are:

- Uncertainty in the efficiencies ratio $\varepsilon_{\gamma^{240}Pu}/\varepsilon_{\gamma^{244}Cm}$, which is 1.7% (Section 4.2).
- Uncertainty in the calculation of the ratio between the ^{240}Pu and the ^{244}Cm masses, which is 2.8% (Table 2.2).
- Uncertainty in the capture cross section of the first resonance of ^{240}Pu, which is 2.75% (Section 6.2).

The total uncertainty in the normalisation for ^{244}Cm has been calculated by adding these three uncertainties quadratically, yielding ΔNorm=4.3%. If the uncertainty due to the capture cross section of ^{240}Pu is not taken into account, then ΔNorm=3.3%, which corresponds to the uncertainty in the normalisation of the ^{244}Cm(n,γ) cross section to the ^{240}Pu(n,γ) cross section. Respect to the ^{240}Pu yield, it has been normalised to the first resonance at 1.056 eV, so the only uncertainty is the one to the capture cross section of this resonance (2.75%).

ii) **Uncertainty in the energy dependence of the neutron fluence**. Described in Section 2.5.2, which is 1%.

iii) **Uncertainty in the background subtraction (excluding the background related with the interaction of the neutron beam with the actinides in the sample)**. The uncertainty in the normalisation of this background has been estimated in 1%, including the normalisation between measurements performed with the SiMon detector and the possible small differences in the dummy sample with respect to the real sample.

iv) **Uncertainty in the subtraction of the background related with the interaction of the neutron beam with the actinides in the sample**. This contribution is described in detail in Section 6. It is obtained from the uncertainties in the different detection efficiencies (ε_{fis} is 15% and ε_{elas} is in Figure 4.15) and the uncertainties in the evaluated cross sections.

v) **Uncertainties in the masses**. The ^{244}Cm and ^{240}Pu capture cross sections have been normalised to the first resonance of ^{240}Pu, so the uncertainties in the total values of the different masses, which have been estimated in 5% (Section 6.2) have only a small impact in the calculation of the self shielding and multiple scattering effects.

Chapter 5

Procurement of the ^{244,246,248}Cm experimental capture yield with the C_6D_6 detectors

The observable quantity in the neutron capture cross section measurements is the capture yield. The Total Energy Detection (TED) technique have been applied to the yield analysis to have an efficiency in detecting the cascade equal to his neutron separation energy. In order to apply this technique is necessary that the efficiency to detect a γ-ray is proportional to his energy. To achieve this condition the Pulse Height Weighting Technique (PHWT) has been applied with pulse-height-dependent Weighting Functions (WFs). Then the equation used to calculate the capture yield in EAR2 with the C_6D_6, and this techniques is similar to the one used in EAR1 for the TAC (Equation 4.2):

$$Y_{\gamma,exp,i} = F_{PHWT,i}\frac{C_w - B_w}{S_{n,i}\cdot\phi_n} \tag{5.1}$$

where C_w is the total weighted counting rate, B_w is the background weighted counting rate, $S_{n,i}$ is the neutron separation energy of the isotope i, $F_{PHWT,i}$ is the factor for correcting the deviations from the ideal situation with the PHWT, and ϕ_n are the number of neutrons impinging in the sample per unit time.

Geant4 Monte Carlo simulations have been used in many steps of the analysis, and they are described in Section 5.1. These simulations have been used, for example, in the detector calibration, which is one of the steps of the process to transform the digitised signals of the C_6D_6 detectors to the counting rate (C_w), described in Section 5.2. The work in this section includes many innovations with respect to previous measurements, for example, the calculation of the active volume of the detectors or the precise characterisation of the detector gains. The different background (B_w) components are described in Section 5.4.

The main difference of the C_6D_6 detectors analysis with respect to the TAC measurement is the use of the TED and PHWT techniques, which are described in Section 5.3. In this section, the WFs for the calculation of the weighted counting rates are determined, and also the different corrections of the technique. The calculation of the number

of neutrons impinging in the sample (ϕ_n) is presented in Section 5.5 following the same proceeding as in EAR1.

One disadvantage of the PHWT is that the statistical fluctuations are larger than the *traditional* counting technique, which does not use weights. In order to reduce the uncertainties associated with these fluctuations (uncertainties due to counting statistics), the unweighted yield has also been obtained and normalised to the weighted yield, as explained in Section 5.6. The unweighted yield can be used instead of the weighted one if the detection efficiency does not vary from one resonance to another. Finally, in Section 5.7 the final uncertainties of the yield calculation are presented.

The necessary time-of-flight to neutron energy conversion has been done using Equation 2.3. The time-of-flight distance is adjusted comparing the experimental yield of ^{197}Au with the evaluated yield obtained with JEFF-3.3 [51] in Section 2.5.5, obtaining a value of 19.425 meters.

The Cm campaign in EAR2 lasted more than three months, from 20/05/2017 to 25/08/2017. Table 5.1 summarises the type of measurements performed together with the number of protons and the run identifications numbers.

	Number of protons	Run number
^{244}Cm sample	$1.8{\cdot}10^{18}$	207421-207460 207828-207867 207906-207950
Dummy ^{244}Cm sample	$0.9{\cdot}10^{18}$	207290-207394 207784-207814
Activity ^{244}Cm sample	-	207461-207470 2079151-207960
^{246}Cm sample	$1.8{\cdot}10^{18}$	207471-207495 207549-207584 207594-207630
Dummy ^{246}Cm sample	$0.9{\cdot}10^{18}$	207728-207772 207894-207904
Activity ^{246}Cm sample	-	207497-207515 207538-207546 207636-207636
^{197}Au	$1.5{\cdot}10^{18}$	207282-207287 207660-207665 207697-207703 207820-207821 207885-207890 207951-207964
Dummy ^{197}Au	$0.2{\cdot}10^{18}$	207653-207659
Total	$7.1{\cdot}10^{18}$	207282-207964

Table 5.1: Different measurements performed in EAR2 in the Cm campaign. The number of protons and the corresponding run numbers are given for each measurement.

5.1 Geant4 simulations of the C_6D_6 detectors

As previously mentioned, Monte Carlo simulations are an essential tool in many steps of the analysis. They have been used extensively for:

- The energy calibration (5.2).
- The characterisation of the energy resolution (5.2.1).

- The calculation of the active volume of the detectors (5.2.2).
- The calculation of the WFs and the corrections associated with the technique (5.3).
- The neutron sensitivity (5.4.2).
- The calculation of the de-excitation cascades (3.1.1 and 3.2).

In order to simulate the response of the detectors to different sources, a detailed implementation of the geometry setup has been done. The work performed for this setup is similar to the ones in previous measurements for C_6D_6 detectors in EAR1 [107, 110, 141, 142, 143]. The main components are listed below and can be seen in Figure 5.1:

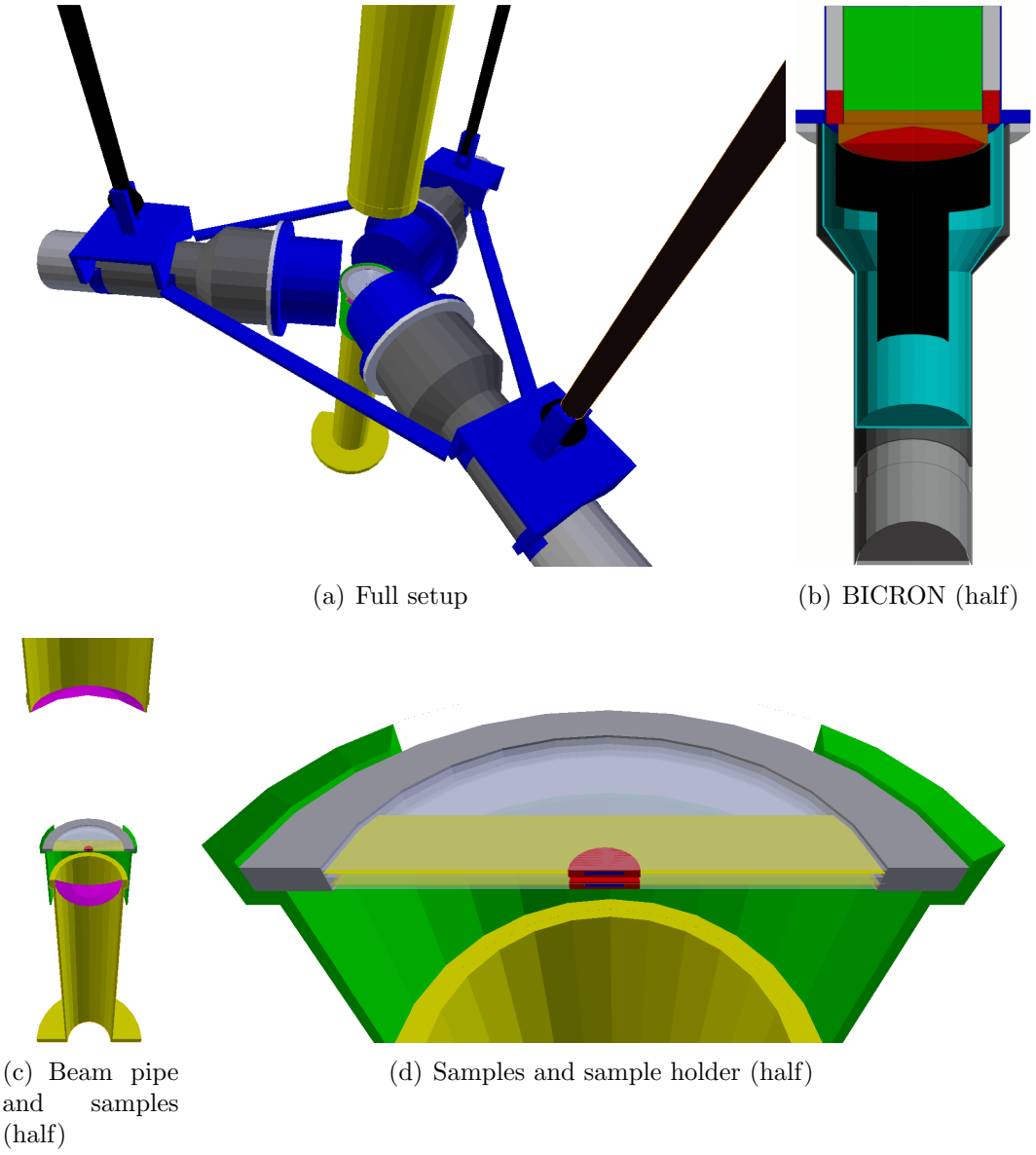

(a) Full setup

(b) BICRON (half)

(c) Beam pipe and samples (half)

(d) Samples and sample holder (half)

Figure 5.1: Geometries implemented in Geant4 to simulate the different setups used in the Cm campaign. The panels (b), (c) and (d) show different parts of the geometry with a transversal cut.

- The detector holders made of aluminium presented in panel (a) of Figure 5.1 (in blue).
- The three BICRON detectors (panel (b) of Figure 5.1) have been simulated directly from the original drawings of Appendix A.
- The beam pipes presented in panel (c) of Figure 5.1.
- The sample holder presented in panels (c) and (d) of Figure 5.1. The sample holder is made of aluminium, and the size has been obtained from the drawing of Figure 2.10.
- The Geant4 program is able to simulate different samples: the ^{244}Cm sample, the ^{246}Cm sample or a calibration source. In the panel (d) of Figure 5.1 the ^{244}Cm sample is simulated.

Different event generators were developed for performing the simulations. The γ-rays or the neutrons may be emitted from the centre or distributed in the volumes of the different samples. The source particles, emitted isotropically, can be taken from an input file created by NuDEX [115], from the decay of known isotopes or can be mono-energetic.

5.2 Calibrations and data reduction

A thorough characterisation of the C_6D_6 detectors and their behaviour during the experiments has been carried out. The different steps of the process are presented in the following sections:

i) In Section 5.2.1, the energy calibrations and the characterisation of the energy resolution of each detector.

ii) In Section 5.2.2, the calculation of the active volume of the C_6D_6 detectors.

iii) In Section 5.2.3, the characterisation of gain changes.

iv) In Section 5.2.4, the time calibrations, and the calculation of the coincidence time window.

v) In Section 5.2.5, the determination of the thresholds in deposited energy.

vi) In Section 5.2.6, the determination of the pile-up.

vii) In Section 5.2.7, the monitoring of the counting rates during all the measurement in the EAR2.

5.2.1 Energy calibrations and characterisation of the energy resolutions

The energy calibration of the C_6D_6 detectors is not a straightforward procedure due to the limited detection efficiency and poor resolution of these liquid scintillators. No full absorption peak is observed in the response to single γ-rays, and thus only the resolution

broadened Compton edge can be used as an energy reference. The method applied in this work consists in comparing the experimental spectra with the simulated spectra obtained with Geant4. The process is divided into five steps:

i) The measurement of six well known γ-ray sources are performed. The energy of the γ-rays emmited by the sources are: ^{133}Ba (E_γ=0.302 MeV, E_γ=0.356 MeV, E_γ=0.383 MeV), ^{137}Cs (E_γ= 0.6616 MeV), ^{60}Co (E_γ=1.173 MeV, E_γ=1.332 MeV), ^{88}Y (E_γ=0.898 MeV, E_γ=1.836 MeV), Am-Be (E_γ= 4.438 MeV) and Cm-C (E_γ= 6.130 MeV).

ii) The response of the setup to these γ-ray sources are simulated with Geant4.

iii) The Geant4 simulations are shifted and broadened to match the experimental spectra. The free parameters of the fit are the coefficients of the energy calibration and the resolution broadening. In Figure 5.2 the fits for the seven peaks are presented.

iv) The final energy calibration is performed with the results provided in the previous step. The linear or quadratic polynomials do not fit the experimental results correctly. So a combination of a second-degree polynomial at low energies and a linear polynomial at higher energies is used to transform the amplitude spectra in deposited energy:

$$f(x) = \begin{cases} ax^2 + bx + c & x > x_0 \\ dx + e & x \leq x_0 \end{cases} \tag{5.2}$$

The function is constructed to be continuous and derivable. In Figure 5.3 the energy calibration for detector 3 is illustrated. In this figure, the comparison between the function used in the analysis and a linear polynomial is also presented.

v) The energy resolution of the detectors are needed to perform precise Monte Carlo simulations. The function used to describe the dependence of the resolution with the deposited energy (E) is FWHM=$\sqrt{(\alpha \cdot E^2 + \beta \cdot E)}$. In Figure 5.4 the fit of this function to the resolution values obtained from the measurements performed with calibration sources for detector 3 is presented. The resolution obtained for this detector is 10.0% at 1 MeV and 6.8% at 5 MeV. These resolutions are very similar to the ones obtained by C. Domingo [144] for the same detectors.

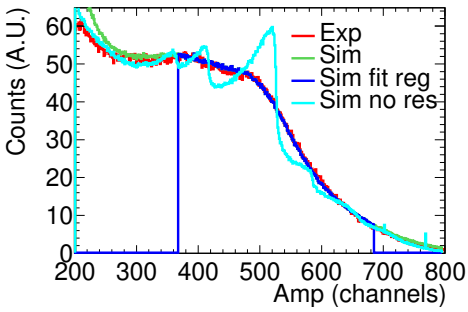

(a) ^{133}Ba

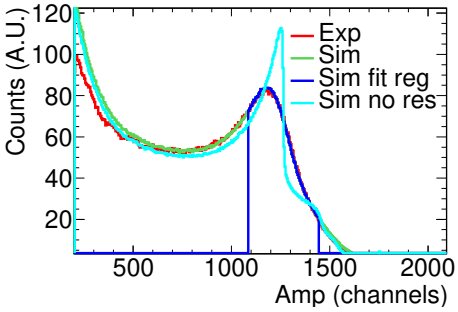

(b) ^{137}Cs

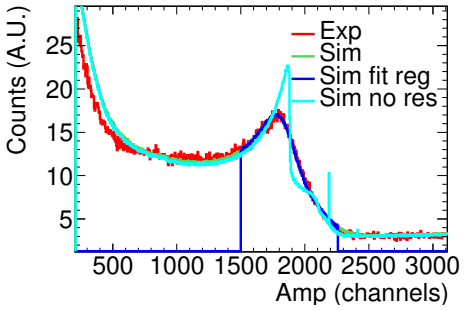

(c) ^{88}Y (0.898 MeV)

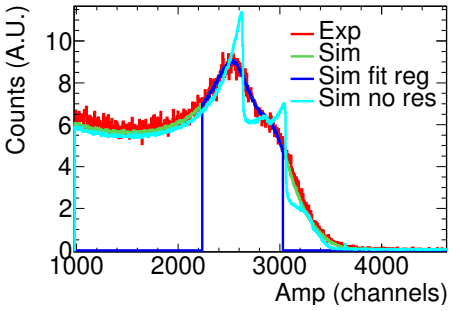

(d) ^{60}Co

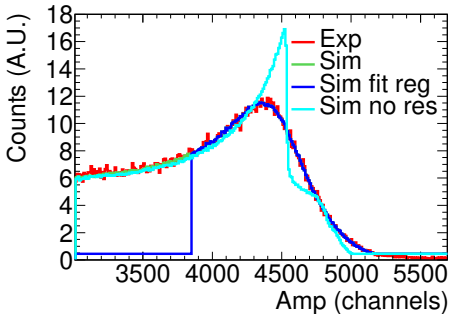

(e) ^{88}Y (1.836 MeV)

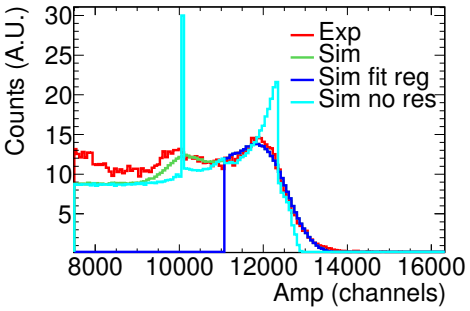

(f) Am-Be

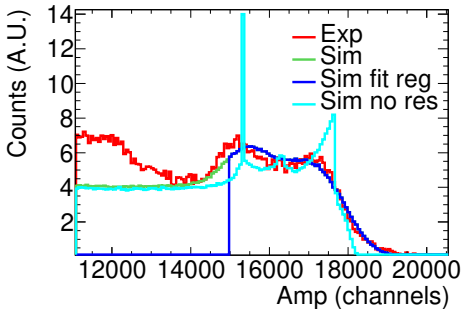

(g) Cm-C

Figure 5.2: Fit (energy calibration + energy resolution) of the different calibration γ-ray sources for detector 3. The experimental data (background subtracted), in red, are plotted together with the fitted simulated data, in green. The dark blue spectra shows the range used for the fit, and the cyan spectra corresponds to the results of the simulations without applying any resolution in the detector response.

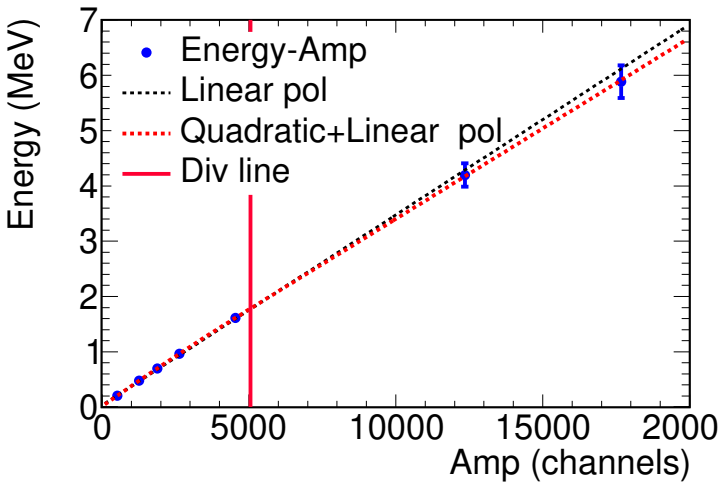

Figure 5.3: Energy calibration for detector 3, using the results obtained with the six γ-ray calibration sources (blue points). The values have been fitted to a first order polynomial (black dashed line) and to the function used in this work (red dashed line), described in Equation 5.2. The red vertical line corresponds to x_0, i.e. the border between the first and second order polynomials.

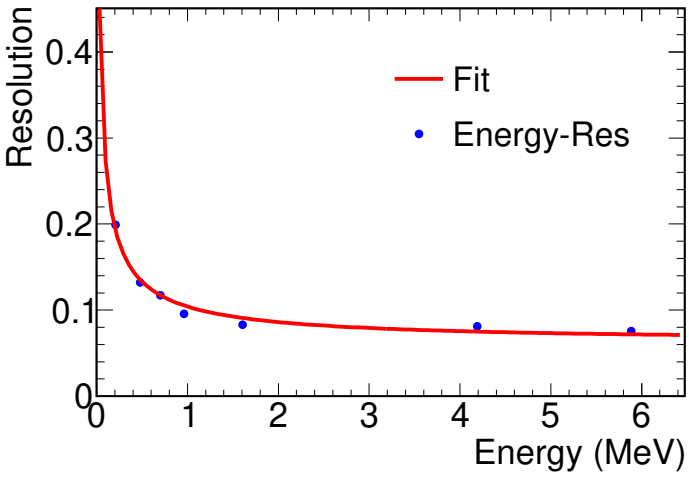

Figure 5.4: Energy resolution of detector 3 as a function of the deposited energy, obtained from the fit to the values obtained with the six γ-ray calibration sources. The experimental points, in blue, have been fitted to the function FWHM $= \sqrt{(\alpha \cdot E^2 + \beta \cdot E)}$.

5.2.2 Calculation of the active volume of the detectors

Before performing this measurement, a study of all the C_6D_6 detectors available at n_TOF was carried out. The high counting rates in EAR2 were found to cause gain changes in most detectors. Of all of them, this effect turned out to be less in the BICRON, which was the main reason for choosing these detectors. During the data collection, it was observed that the counting rates predicted by the Monte Carlo simulations when measuring calibration sources did not match the experimental values. After ruling out other options, the most reasonable hypothesis was thought to be that the detectors had leaked fluid. However, it was not possible to verify this in the middle of the experiment. At the end of data collection, the detectors were opened, and it was found that ∼30% of the liquid was indeed missing, these values coinciding with great accuracy with the predictions made by the simulations.

The real active volume of the detectors has been determined with precise Geant4 simulations. Different calibration sources were measured with known activities: ^{133}Ba ($3.67{\cdot}10^5$ Bq), ^{137}Cs ($3.61{\cdot}10^5$ Bq), ^{60}Co ($2.41{\cdot}10^4$ Bq) and ^{88}Y ($5.80{\cdot}10^4$ Bq). In Figure 5.5, the differences observed between the experimental results (blue line) and the simulations with the detectors full of C_6D_6 liquid (0.618 l) (green line) are illustrated.

The integrals of the experimental spectra are ∼30% lower than the simulations for detector 3. The amount of C_6D_6 liquid inside the detector has then been adjusted in the simulations to reproduce the measurements, resulting in 0.411 l instead of 0.618 l. The results of the simulations with the adjusted active volume is presented in red. In this case, the simulated response function of the detector reproduces with high accuracy the experimental results of the four γ-ray sources.

After the experiment, the BICRON detectors were opened at CIEMAT to measure the amount of C_6D_6 liquid in the detectors (Figure 5.6), and they were refilled afterwards. The amount of liquid in detector 3 found to be 0.422 l, i.e. compatible within 3% with the values obtained from the simulations.
The process explained in this section for detector 3 has been repeated for the rest of detectors. The values obtained for detectors 1 and 4 with the simulations are 0.465 and 0.399 l, and with the measurements opening the detectors 0.491 and 0.422 l. The two values obtained for detector 1 are compatible within 5% and the ones of detector 4 within 3%.

5.2.3 Corrections of the gain changes in the detectors

The stability of the gain of the detectors along the measurement can affect the calculation of the weighting factors, and increase or decrease the counts above the threshold. In reference [65], it is shown that the number of weighted counts varies approximately linearly with the variation of the detector gain (i.e. a 5% increase in the gain will mean 5% more counts in the weighted histograms).
This effect may not play an essential role in the normalisation of the measurement because the cascades of ^{240}Pu and ^{244,246,248}Cm are similar (Figure 3.10), and the effects may be cancelled. On the other hand, if the changes in gain varies between the runs, it can affect the dummy subtraction, and if the change in gain varies as a function of the neutron

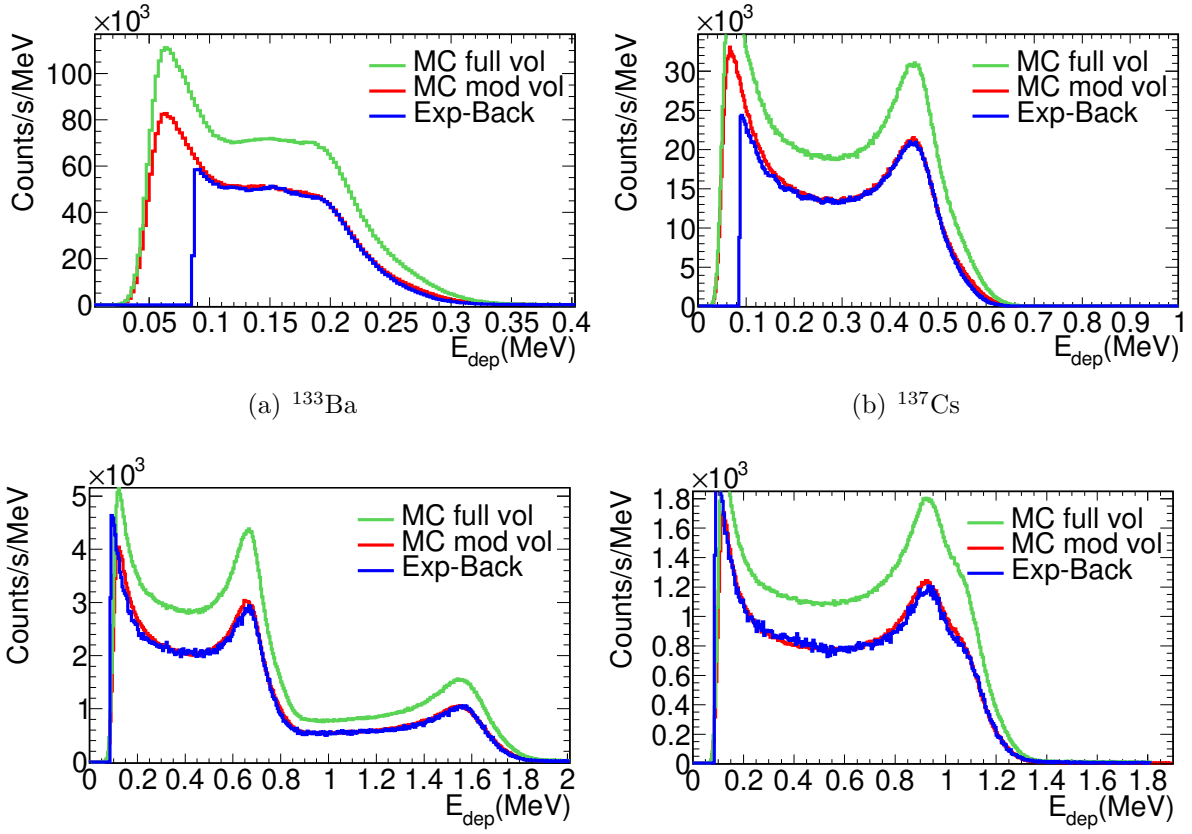

(a) ^{133}Ba (b) ^{137}Cs

(c) ^{88}Y (d) ^{60}Co

Figure 5.5: Geant4 simulations for different γ-ray calibration sources compared with the experimental results (background subtracted), in blue, of detector 3. The Monte Carlo simulations for different active volumes are presented in the green lines (0.618 l) and in the red lines (0.411 l).

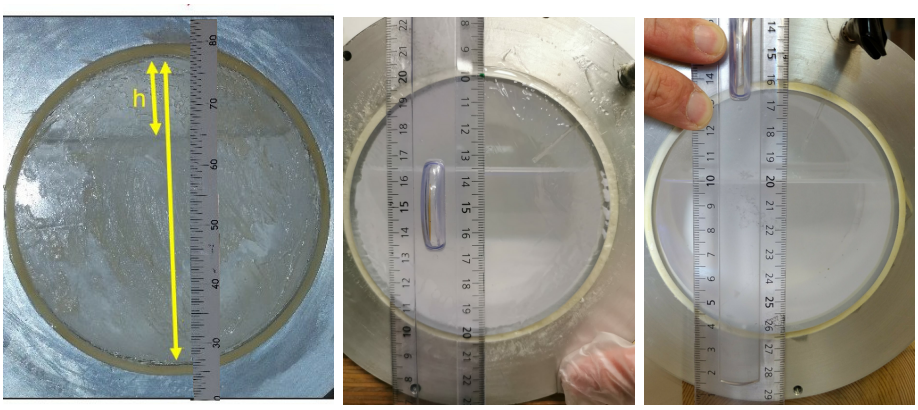

(a) Det 1 (b) Det 3 (c) Det 4

Figure 5.6: Photographs showing the amount of C_6D_6 liquid inside the three BICRON detectors.

energy (or the counting rate), it can affect strongly the value of the yield obtained for each capture resonance.

For this reason, an exhaustive work has been done to characterise the possible changes in the gain of the detectors. It has been observed that the C_6D_6 detectors at n_TOF may suffer from three different effects: changes in gain due to high constant counting rates (5.2.3.1), changes in gain due to the particle-flash (5.2.3.2) and changes in gain as a function of time throughout the measurement (5.2.3.3).

5.2.3.1 Characterisation of the gain as a function of the counting rate

Before the measurement, a precise work was performed to optimise the capture setup and characterise the C_6D_6 detectors; this process was done with measurements and Monte Carlo simulations.

The new C_6D_6 detectors manufactured at the Legnaro National Laboratory (LNL) made of carbon fibre (L_6D_6) [145, 146] were the first option considered to perform this measurement in EAR2. These detectors had been used to perform capture measurements in EAR1 [147, 148, 149, 150]. In the characterisation process, it was found that the gain of the L_6D_6 detectors changed with the counting rates [151]. In Figure 5.7 it is shown that for a ^{137}Cs+^{88}Y source located at 2.5 cm (∼50 counts/ms) and 40 cm (∼1 counts/ms) from a L_6D_6 detector, the gain changed by ∼12%. No gain changes were observed when the same test was performed with a BICRON detector (panel (b) of the figure).

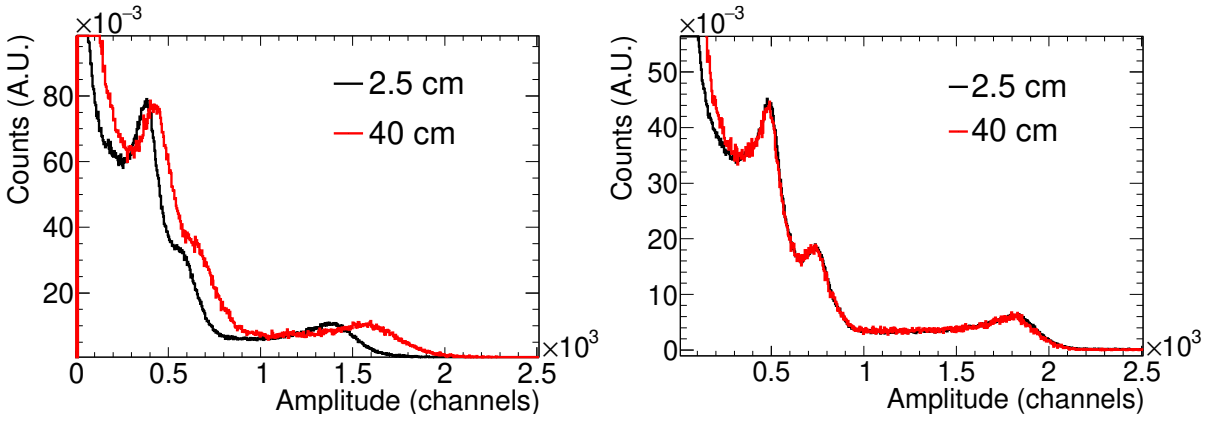

(a) L_6D_6 F (b) BICRON 3

Figure 5.7: Amplitude spectra of a ^{137}Cs and ^{88}Y calibration sources placed together at 2.5 cm and 40 cm from the L_6D_6 (left) and the BICRON (right) detectors. The spectra are normalised to the same area.

As presented in Figure 5.16, the counting rate in the Cm measurements with the BICRON detectors placed at 5 cm is of the order of 500 counts/ms. As previously mentioned, the L_6D_6 detectors suffer from considerable gain shifts with counting rates a factor of ten lower, so these detectors are not an option for this measurement. Any change of gain has been observed with the BICRON detectors and the calibration sources. The limitation of this test is that the highest counting rate obtained is one order of magnitude lower than the maximum counting rate in the Cm experiment. In order to verify that the BICRON detectors behave correctly with these high counting rates, the deposited

energy spectra for different counting rates in the ^{197}Au saturated resonance are compared in Figure 5.8. As shown in the figure, the spectra in the three regions with considerably different counting rates are identical and thus a solid proof of no gain modifications due to variations of the counting rate.

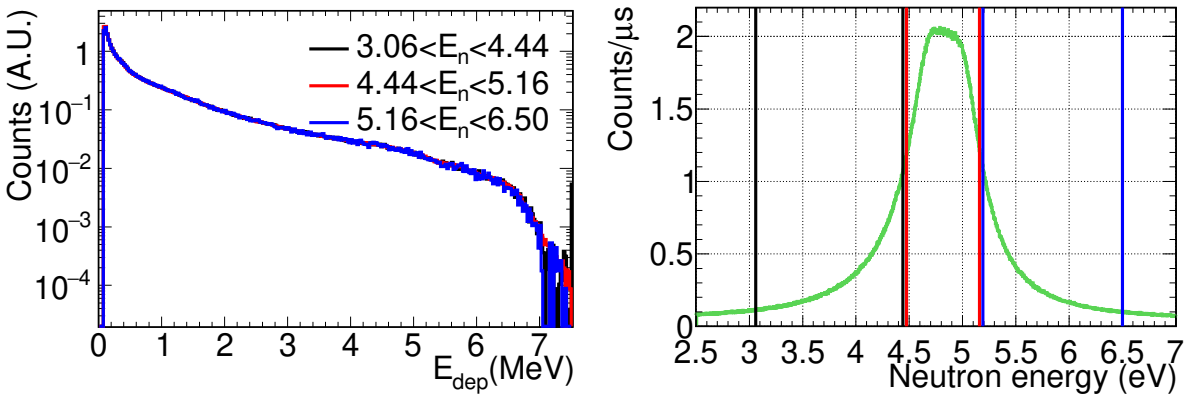

Figure 5.8: Deposited energy spectrum for ^{197}Au subtracting the background for different counting rates. The different spectra are presented in the left panel with different cuts in the energy of the neutrons. In the right panel, the cuts are presented.

5.2.3.2 Characterisation of the gain modifications for the particle-flash

These section aims to determine the effects of the particle-flash (relativistic charged particles and prompt γ-rays) arriving at the BICRON detectors in short TOFs (tens of ns). It was determined that the BICRON detectors suffer from a gain variation during $\sim$20 ms due to the particle-flash. The gain shift effect is characterised in this section as a function of the beam intensity and the neutron energy (time-of-flight) for each detector.

The differences in gain for different beam intensities can be seen in Figure 5.9, where the pulse height spectra is compared for the 4.9 eV resonance of ^{197}Au with three different proton beam intensities: $\sim 7{\cdot}10^{12}$ (Primary), $\sim 3{\cdot}10^{12}$ (Parasitic) and $\sim 7{\cdot}10^{11}$ (Low). The differences in gain for different neutron energy (time-of-flight) can be seen in Figure 5.10. The recorded energy spectra of the different ^{197}Au resonances have to be equal (as can be seen in the results obtained in panel (c) for BICRON 4), so the differences observed as a function of the neutron energy are due to the effect of the particle-flash.

The effect of the gain shift as a function of the neutron energy due to the particle flash is observed in the previous figures. In order to precisely characterise this effect, a dedicated measurement with an ^{88}Y source in the beam has been performed. The final gain shift corrections have been obtained by comparing the pulse height spectra obtained without beam for the ^{88}Y calibration source with the spectra obtained at different TOFs (neutron energies) when measuring the spectra with primary and parasitic pulses. The process is described in the following three steps:

1) A ^{88}Y γ-ray source with an activity of $6{\cdot}10^4$ Bq is placed close to the detectors in a

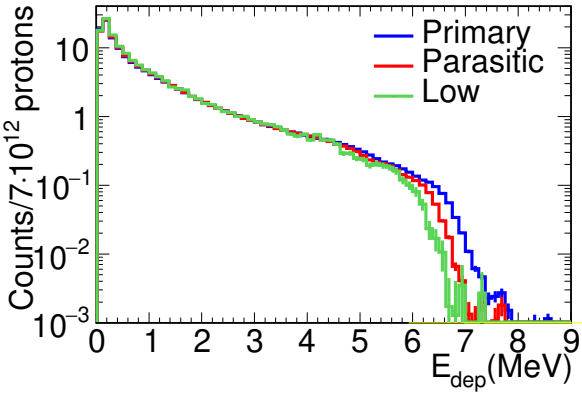

(a) Det 1

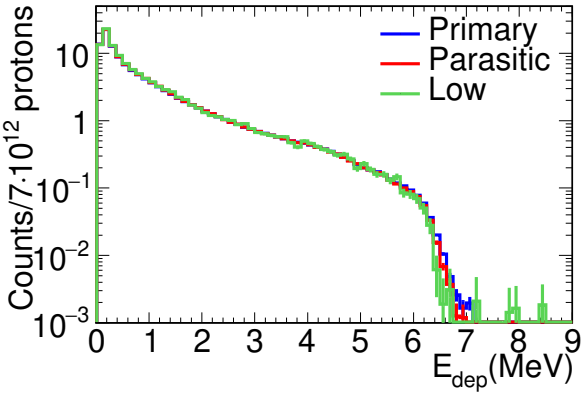

(b) Det 3

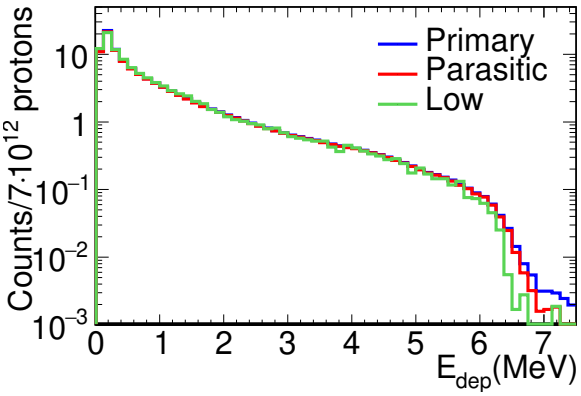

(c) Det 4

Figure 5.9: Energy deposited spectra for each detector with different beam intensities subtracting the background for the ^{197}Au cascade. The blue line corresponds to pulses with an average intensity of $7{\cdot}10^{12}$ (Primary), the red line $3{\cdot}10^{12}$ (Parasitic) and the green line $7{\cdot}10^{11}$ (Low) protons.

measurement of the ^{244}Cm Dummy with beam. The different backgrounds are subtracted, and the ^{88}Y spectra are obtained for different neutron energy ranges. The different spectra are compared for three neutron energy ranges 0.001-0.01 eV, 0.1-0.8 eV and 1-10 eV for each detector in Figure 5.11, as an example. In the same plot, the spectrum obtained for the ^{88}Y measured without beam is also plotted to observe if there are significant shifts in the gain. The ^{88}Y with beam spectra (green lines of Figure 5.11) are shifted to match the ^{88}Y spectrum measured without beam. Using this technique, the gains shifts are calculated for different neutron energy ranges.

2) The values of the different gain shifts obtained as a function of the neutron energy are fitted with a logarithmic function as can be observed in Figure 5.12. The energy calibration of the detectors is shifted as a function of the neutron energy with these functions.

3) The uncertainties associated with this process are presented in the green lines of Figure

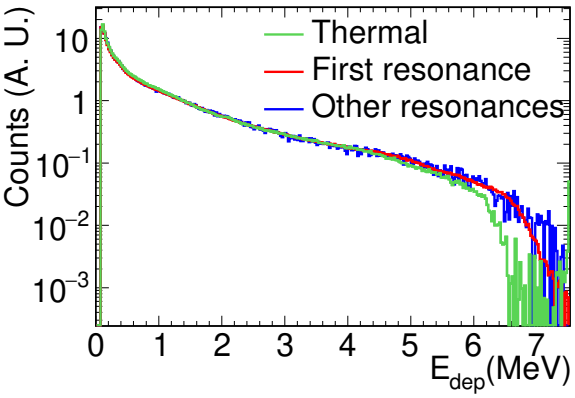

(a) Det 1

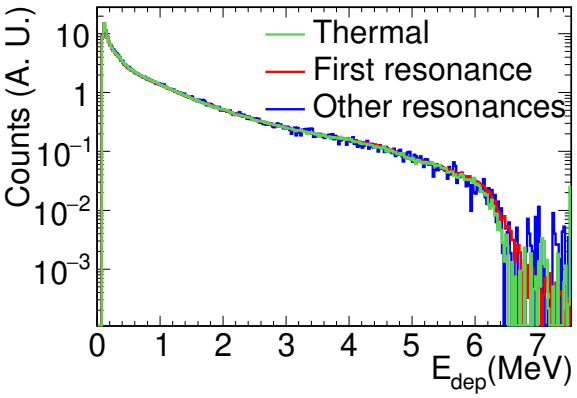

(b) Det 3

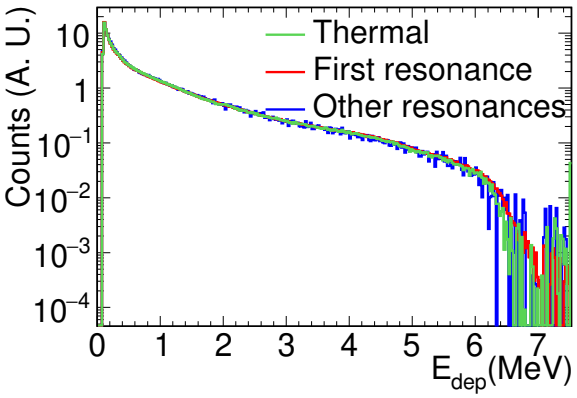

(c) Det 4

Figure 5.10: Energy deposited spectra for each detector for primary pulses subtracting the background for the ^{197}Au cascade. The green line corresponds to the thermal resonance (0.01-0.1 eV), the red line to the first resonance (4.5-5.5 eV) and the blue line to the sum of all the resonances between 50 and 150 eV.

5.12 and they are propagated in the yield and the resonance parameters calculations.

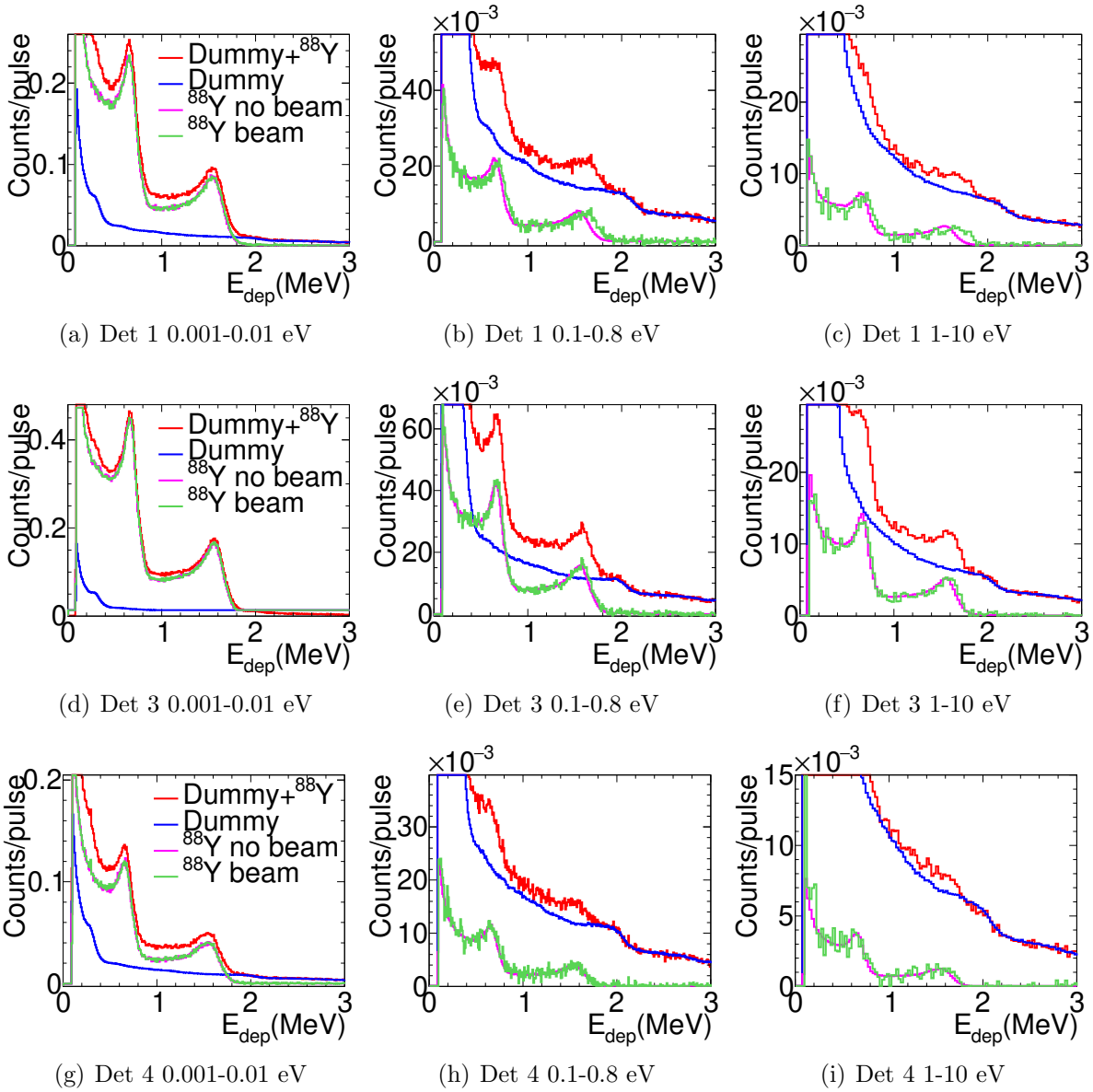

(a) Det 1 0.001-0.01 eV (b) Det 1 0.1-0.8 eV (c) Det 1 1-10 eV

(d) Det 3 0.001-0.01 eV (e) Det 3 0.1-0.8 eV (f) Det 3 1-10 eV

(g) Det 4 0.001-0.01 eV (h) Det 4 0.1-0.8 eV (i) Det 4 1-10 eV

Figure 5.11: ^{88}Y spectra obtained by measuring with primary beam for the different detectors and neutron energy cuts. The red line is the spectra obtained of the beam measurement with the ^{88}Y and the ^{244}Cm dummy in place. The blue line is the spectra obtained for the ^{244}Cm dummy. The green line is the red line subtracting the blue line; it corresponds to the counts associated with the ^{88}Y. The pink line is the ^{88}Y spectra obtained in the measurement without beam.

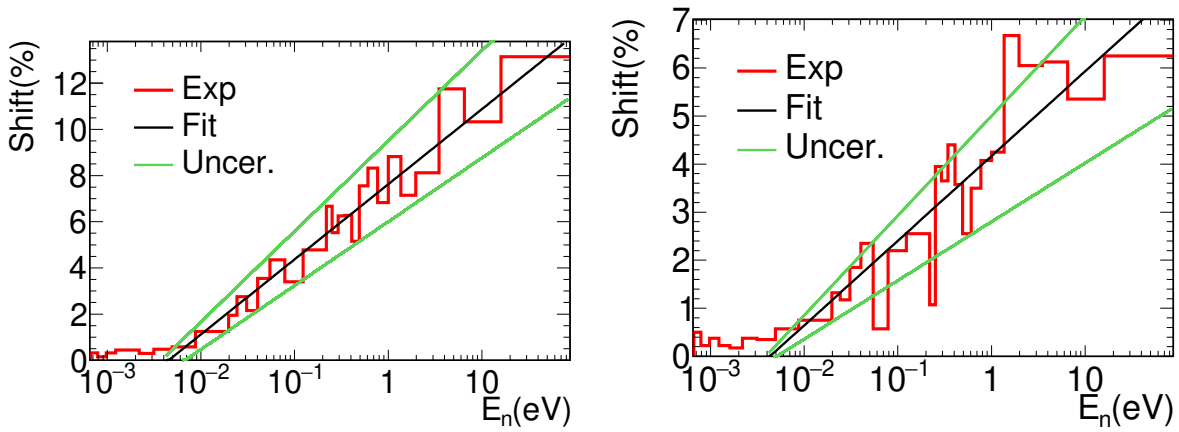

(a) Primary Det 1

(b) Parasitic Det 1

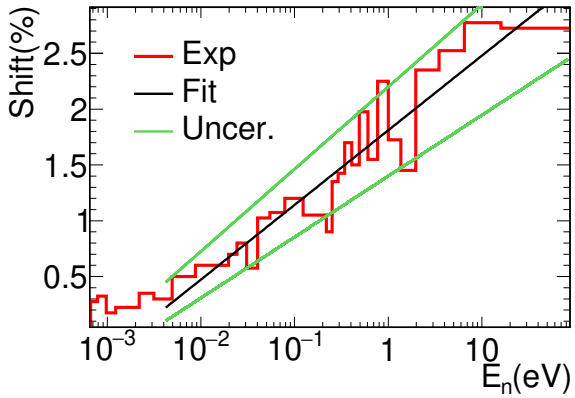

(c) Primary Det 3

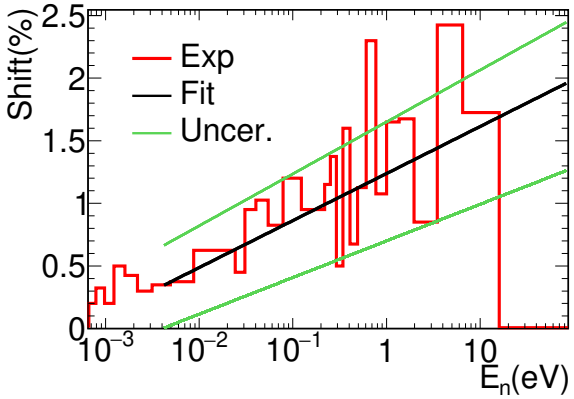

(d) Parasitic Det 3

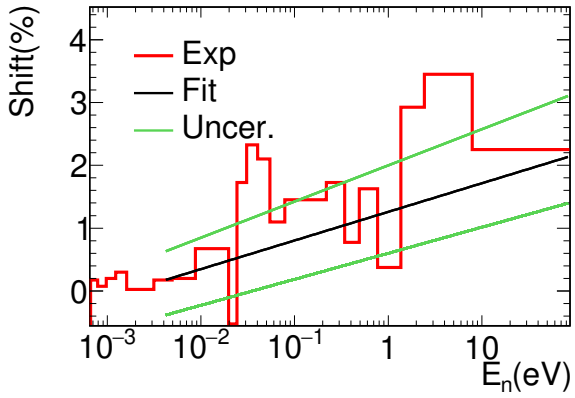

(e) Primary Det 4

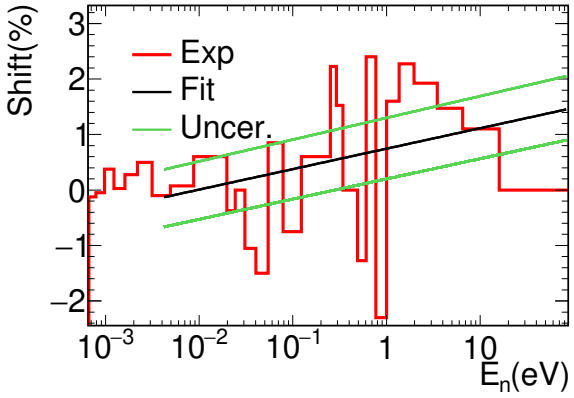

(f) Parasitic Det 4

Figure 5.12: Gain shift for each detector for primary and parasitic pulses obtained with the ^{88}Y measurement. The black lines are the fits with a logarithmic function of each detector's response. The green lines correspond to the uncertainty estimation.

5.2.3.3 Characterisation of the gain modifications during the measurement

The measurement lasted more than three months, and gain shifts were observed during this period. The dummy and the Cm samples were measured in different periods (Figure 5.19), so if the gain shifts during the measurement are not corrected, it can strongly affect the background subtraction.

In order to monitor the gain shifts, the position of the ^{137}Cs, ^{88}Y and Am-Be peaks are measured every week. In Figure 5.13 the changes in gain for the three detectors are presented.

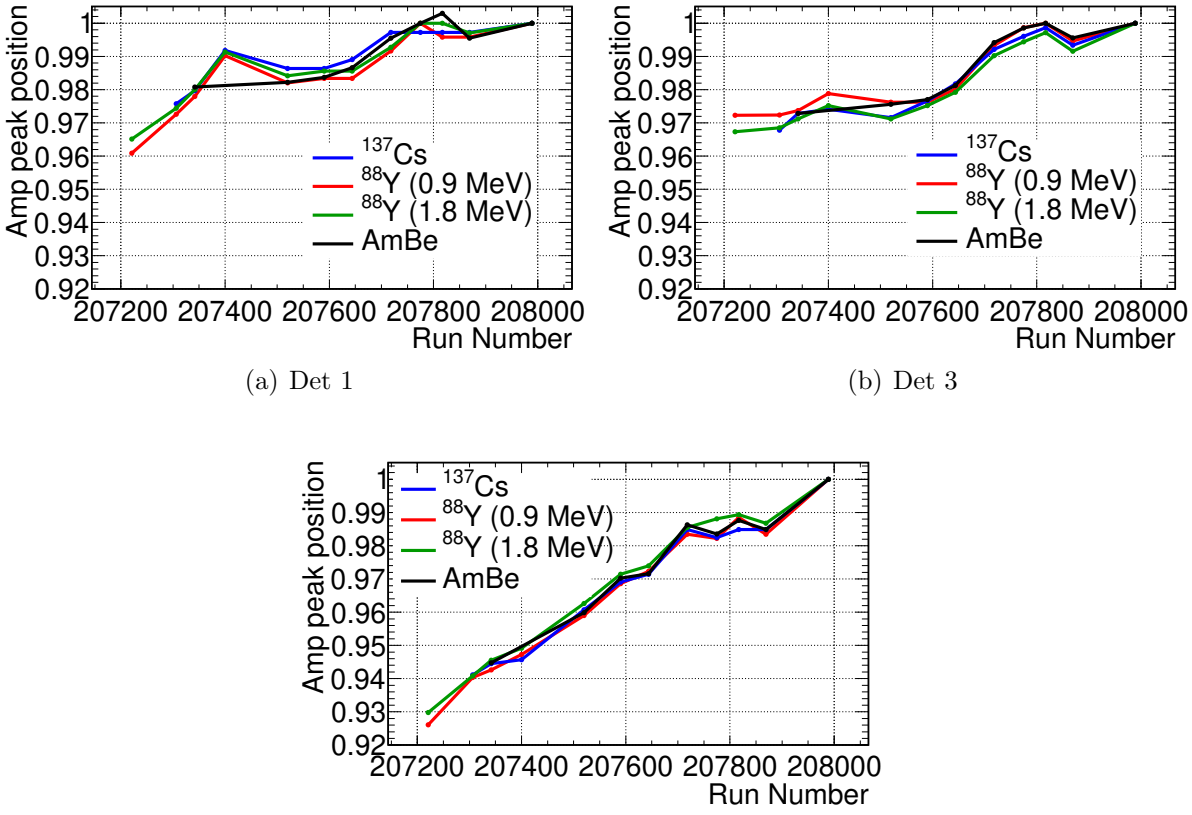

(a) Det 1

(b) Det 3

(c) Det 4

Figure 5.13: Modification of the position in amplitude of the peak of the γ-ray sources (^{137}Cs, ^{88}Y and Am-Be) respect to the value obtained for run 207989.

The gain shift for each run is calculated as the average of the shifts obtained for the four peaks of Figure 5.13. Interpolating these values the gain shift has been obtained for each run and this correction has been applied to the analysis. The maximum shifts for detectors 1 and 3 are less than 4%, whereas for detector 4 is 7%.

5.2.4 Time calibration

The coincidences between the three C_6D_6 detectors are applied to the analysis to find the γ-rays from the same cascade detected in more than one BICRON detector, including

also the possibility of one γ-ray depositing energy in more than one detector. When a γ-cascade deposited energy in more than one detector, randomly, only one of the signals of the detectors is considered. This is done to correctly calculate the uncertainty due to counting statistics, which is calculated as the square root of the number of cascades detected and not as the square root of the number of γ-rays detected. For this purpose, it is necessary to calibrate in time the detectors and to determine the time resolution to set the coincidence window.

The BICRON detectors have been synchronised by applying the same method used in the TAC analysis (Section 4.1.4), with an ^{88}Y source. In Figure 5.14, the coincides for the two γ-rays emitted from the ^{88}Y are presented, together with the fits. The offsets between detectors are independent of the TOF, and the values with respect to detector 1 are 2.2 and -2.9 ns for detectors 3 and 4, respectively.

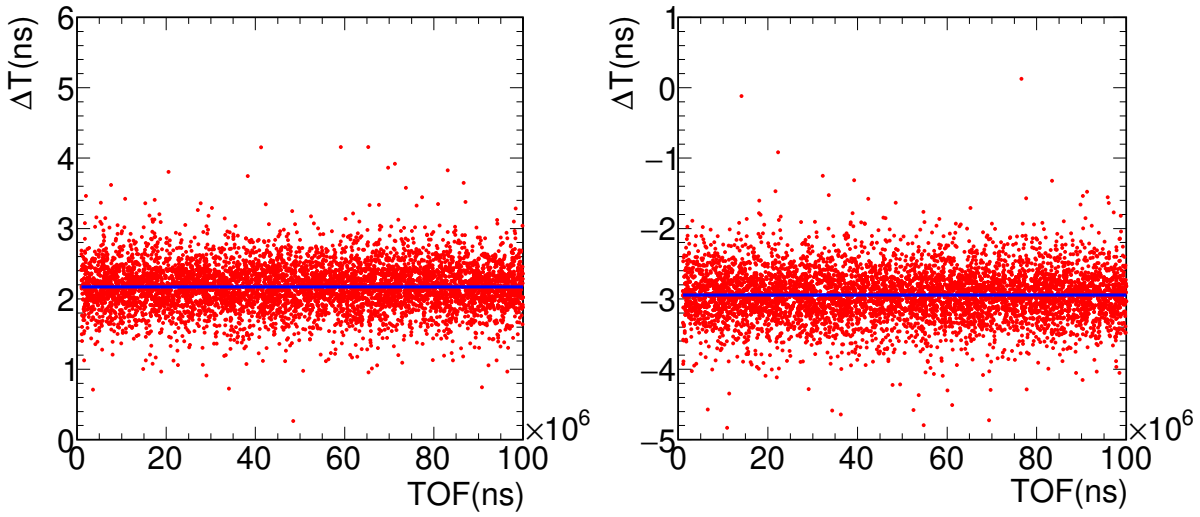

(a) Det 3 compare with Det 1

(b) Det 4 compare with Det 1

Figure 5.14: Time differences of detectors 3 and 4 respect to detector 1 for an ^{88}Y γ-ray source. The blue line is a linear fit of the data points.

The time coincidence window has been set to 3 ns considering the time resolution of the detectors presented in Figure 5.15.

5.2.5 Pile-up corrections

As previously mentioned in Section 4.1.5, the DAQ system used at n_TOF can record all the signals, and the PSA routine [83] has implemented techniques to distinguish the signals using pulse shape fitting. However, the routine may fail when fitting two consecutive pulses located very close one to the other. To correct for the pile-up effects the "standard" approach has been used with a dead-time (τ). In general, the dead-time of the detection systems can be classified into two models:

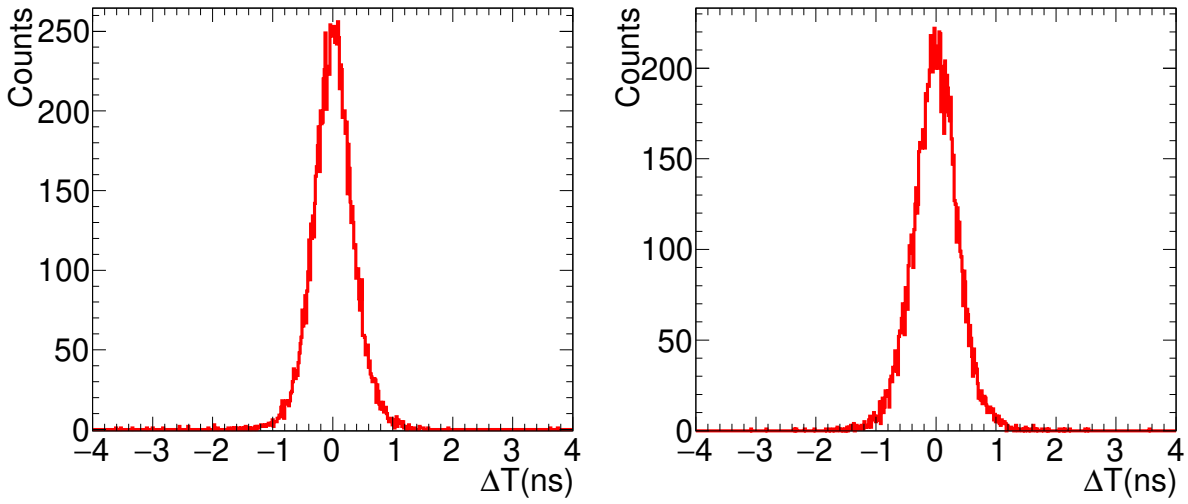

(a) Det 3 compare with Det 1

(b) Det 4 compare with Det 1

Figure 5.15: Time differences of detector 3 and 4 respect to detector 1 for an ^{88}Y γ-ray source applying the time correction factors, computed after the time calibrations.

- The paralyzable model: the second pulse expands the dead-time of the detector (τ).
- The non-paralyzable model: the true events that occur during the dead period are lost and assumed to have no effect on the detector's behaviour.

They are in some sense two extremes of idealized systems behaviour, and real experiments often display a behaviour that is intermediate between these two cases [132]. The two models have the same first-order losses and differ only when true event counting rates are high. The equation to correct the non-paralyzable dead-time and the first-order of the paralyzable is:

$$n = \frac{m}{1 - C\tau} \tag{5.3}$$

where n is the number of counts expected in a certain time interval, m is the number of counts measured for in that interval, and C is the counting rate. The counting rates in one of the detectors are presented in Figure 5.16. This equation is used to calculate the dead-time losses, and if the corrections are small enough, the second-order corrections of the paralyzable correction can be neglected. A complete explanation of these approximations are presented on page 123 of [132].

The time distribution between two consecutive pulses are shown in Figure 5.17 for different counting rates: background measurement without beam with a counting rate of $\sim$0.001 counts/μs (panel a) and the saturated resonance of ^{197}Au (panel b) with a counting rate of $\sim$2 counts/μs. The τ of this system is set to 20 ns as an intermediate value between the two extreme situations. The consecutive signals separated less than 20 ns are artificially removed. The counts lost due to the pile-up and the ones removed

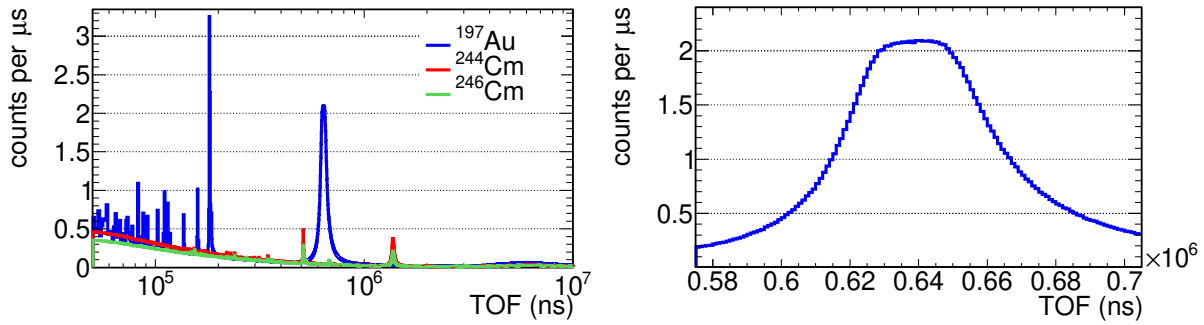

Figure 5.16: Counting rates of detector 1 as a function of the TOF for the primary pulses for the three samples measured, excluding measurements with dummy samples. The right panel is a zoom to the counting rate in the first ^{197}Au saturated resonance at 4.9 eV.

artificially are corrected by multiplying the obtained counting rate in an interval by the pile-up correction factor, calculated for each time interval as $1/(1 - C\tau)$.

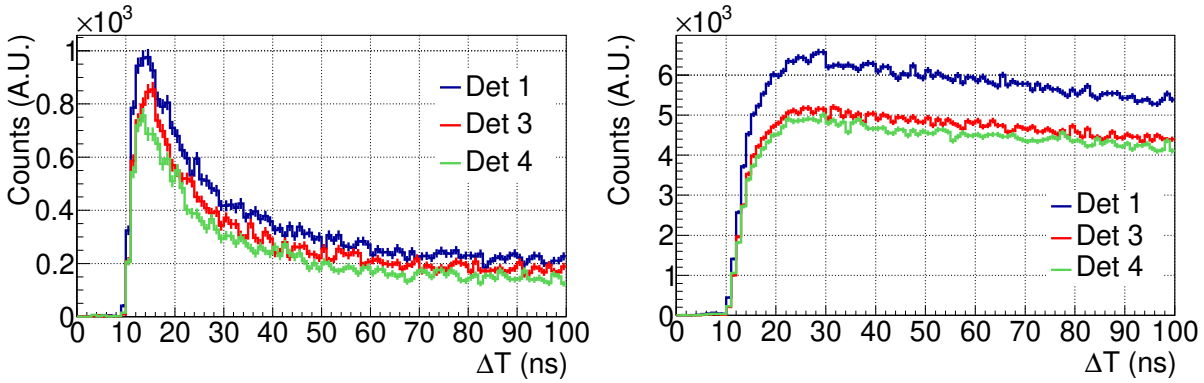

(a) Background measurement (without beam)

(b) First resonance of ^{197}Au (4.9 eV)

Figure 5.17: Time distribution of each two consecutive pulses for the background measurement without beam (panel (a)) and for the first saturated resonance of ^{197}Au at 4.9 eV (panel (b)).

In Figure 5.18 the pile-up correction factors applied are presented for detector 1. The corrections for the ^{244}Cm sample are less than 1.5%, and for the ^{246}Cm sample less than 0.8% for primary pulses in all the detectors. These corrections are less than 0.5% for parasitic pulses. These small corrections lend further confidence that the assumed approximation done is valid.

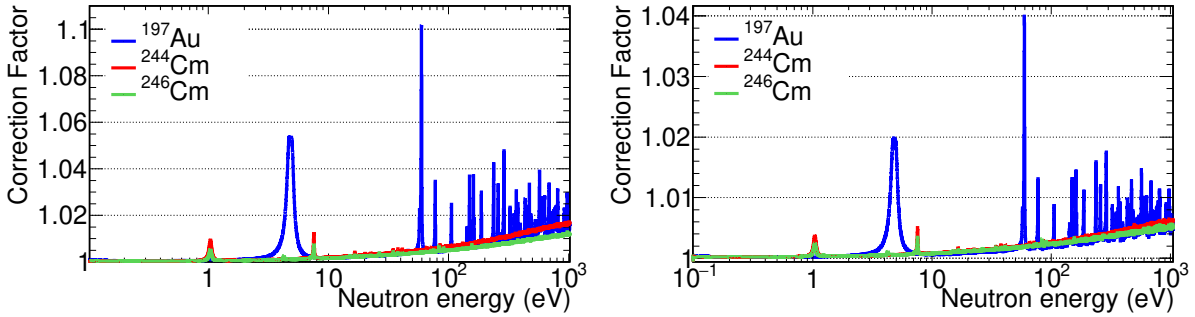

(a) Primary pulses

(b) Parasitic pulses

Figure 5.18: Pulse pile-up correction factors for detector 1 applied to the measured counting rates for different samples, and primary and parasitic pulses. The corrections applied to detectors 3 and 4 are lower than those applied for detector 1 because they have less active volume.

5.2.6 Determination of the deposited energy thresholds

Different conditions in the energy spectra can be applied to reduce the signal to background ratio in the capture yield calculations. In this analysis, a lower and a higher threshold have been set.

The lower threshold used for the detectors is 0.12 MeV. For signals below this threshold, the pulse shape routine starts to have problems differentiating signals from electronic noise, and as a consequence, the signal to background ratio is considerably increased. For values of the threshold higher than 0.12 MeV, the signal to background ratio is not considerably improved, and the efficiency decays. For example, for a threshold of 0.15 MeV, the efficiencies to detect the ^{244}Cm cascades are reduced $\sim$8% compared with a threshold of 0.12 MeV.

The neutron separation energy of ^{241}Pu, ^{245}Cm, ^{247}Cm and ^{249}Cm are 5.241, 5.520, 5.155 and 4.713 MeV respectively. For this reason, a high energy cut of 6 MeV is also set in the analysis.

5.2.7 Monitorisation of the counting rate

After the gain corrections and the energy calibration, the counting rate of the C_6D_6 detectors has been calculated for each run. In Figure 5.19 the sum of the counting rates for the three C_6D_6 detectors divided by the counts in the SiMon2 detector are compared. The ratios are constant for all the samples except for the ^{197}Au sample. This result is a strong indication of the measurement analysis precision, particularly the corrections of the gain of the detectors, the correct assessment of each run, and the stable configuration of the measurement. The counting rate differences in the ^{197}Au measurements are associated with a sample misalignment with respect to the centre of the beam.

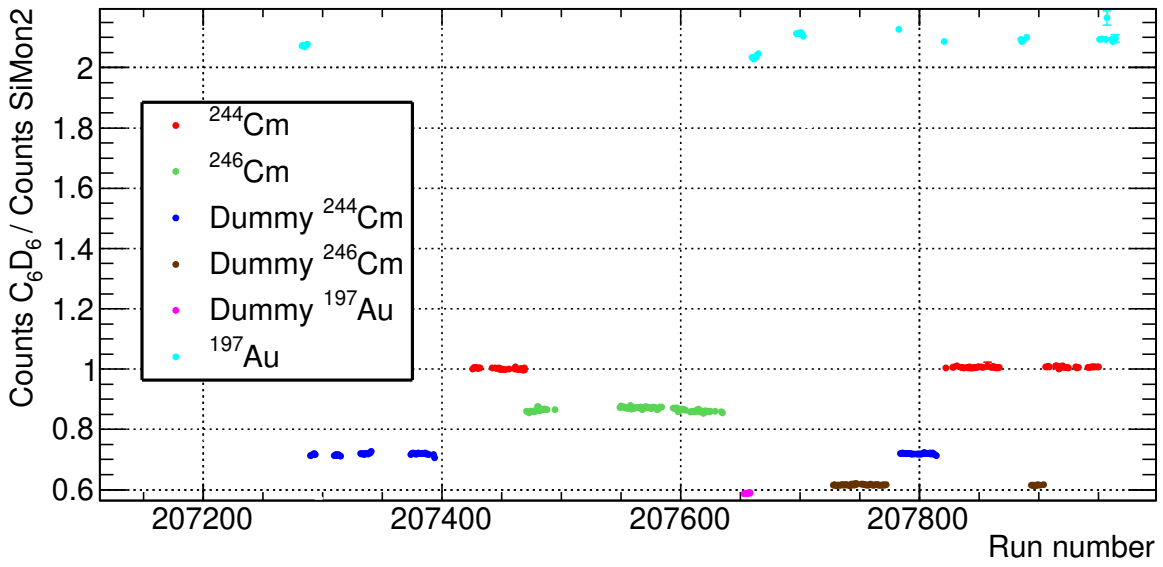

Figure 5.19: Number of counts in the three C_6D_6 detectors with energy between 0.12 and 6 MeV divided by the number of counts in the SiMon2 detector, for each run with beam. All the ratios have been normalised to the value obtained for run 207422.

5.3 The PHWT and TED technique

To obtain the capture yield is necessary to know the efficiency (ε_c) to detect the (n,γ) cascades, but this efficiency may depends on the de-excitation pattern of the compound nucleus. One possibility to avoid this dependency is to use the Total Energy Detection (TED) technique [65, 152]. The TED technique is based on these two principles:

1. The efficiency of detecting one γ-ray is very small ($\varepsilon_\gamma \ll 1$), so that at most only one of the γ-rays of the cascade is detected.

2. The efficiency of detecting one γ-ray (ε_γ) is proportional to his energy γ-ray (E_γ), $\varepsilon_\gamma = k \cdot E_\gamma$.

Under these conditions, the ε_c becomes proportional to the sum energy of the γ-rays of the cascade (E_c). The γ-ray j have an efficiency to be detected of $\varepsilon_{\gamma j}$:

$$\varepsilon_c = 1 - \prod_j (1 - \varepsilon_{\gamma j}) \approx \sum_j \varepsilon_{\gamma j} \approx kE_c \tag{5.4}$$

In consequence, ε_c is independent of the de-excitation pattern of the nucleus produced in the capture reaction. At low neutron energies, where the energy of the neutron is well below the neutron separation energy, $\varepsilon_c \cong S_n$.

These assumptions can not be fulfilled for real detectors with sufficient efficiency to achieve enough statistics in a reasonable time. To solve the problem that the efficiency of the detectors is not proportional to the energy of the incident gamma-ray, the Pulse

Height Weighting Technique (PHWT) is used [152], consisting in applying a pulse-height-dependent Weighting Factor (WF), such that the weighted sum of the response for a γ-ray becomes proportional to its energy. The experimental conditions deviates from this ideal situation. For this reason, the correction factors for the PHWT (F_{PHWT}) are calculated with Monte Carlo simulations for each isotope.

The use of the TED and PHWT techniques [65] with C_6D_6 detectors are well established and has been successfully applied in many n_TOF capture experiments with stable isotopes [107, 108, 153, 154] and radioactive isotopes, including several actinides [73, 109, 110, 111].

5.3.1 Calculation of the Weighting Functions (WFs)

Following the theoretical principles of the PHWT, the WFs are calculated to transform the detector's response to achieve the desired proportionality of the efficiency with the γ-ray energy. The WFs are calculated following Ref. [65], dividing the process in the following steps:

i) The response function to mono-energetic γ-rays has been obtained with Geant4 simulations (Section 5.1).

ii) A 5th-degree polynomial function is fitted to the results of the simulations to make the efficiency proportional to the energy of the γ-rays. This is done using the *Minuit* minimization code included in the ROOT analysis toolkit [155] and the previous simulations.

In Figure 5.20, the WFs calculated for the three BICRON detectors for the ^{244}Cm sample setup are presented. The differences observed between the three detectors are mainly due to the differences in the active volume (Section 5.2.2). The use of the calculated WFs

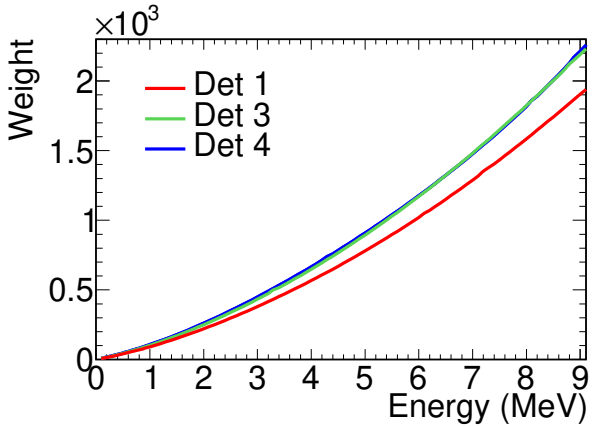

Figure 5.20: The WFs obtained for the BICRON detectors.

satisfy the proportionality between the efficiency and the γ-ray energy ($\varepsilon_\gamma = k \cdot E_\gamma$) with an average RMS better than than 0.6% (Figure 5.21).

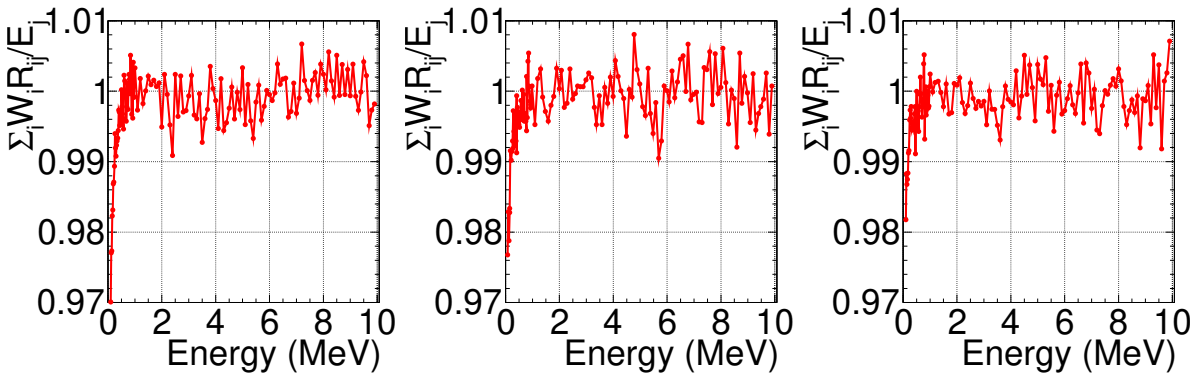

(a) Det 1 (b) Det 3 (c) Det 4

Figure 5.21: Proportionality check between the efficiency and the γ-ray energy for the WF with the ^{244}Cm sample setup.

The setup used for the measurement with the ^{244}Cm sample was different from the ^{246}Cm sample setup. The ^{244}Cm sample was compound of two pellets and the ^{246}Cm sample only of one, so the γ-rays are produced in different volumes. In principle, different WFs should be used, but the two configurations are very similar and as observed in Figure 5.22 the RMS obtained for the ^{246}Cm sample setup with the WFs obtained for the ^{244}Cm sample was smaller than 0.8%. This value was small enough, in order to use these WFs to perform the ^{246}Cm sample analysis.

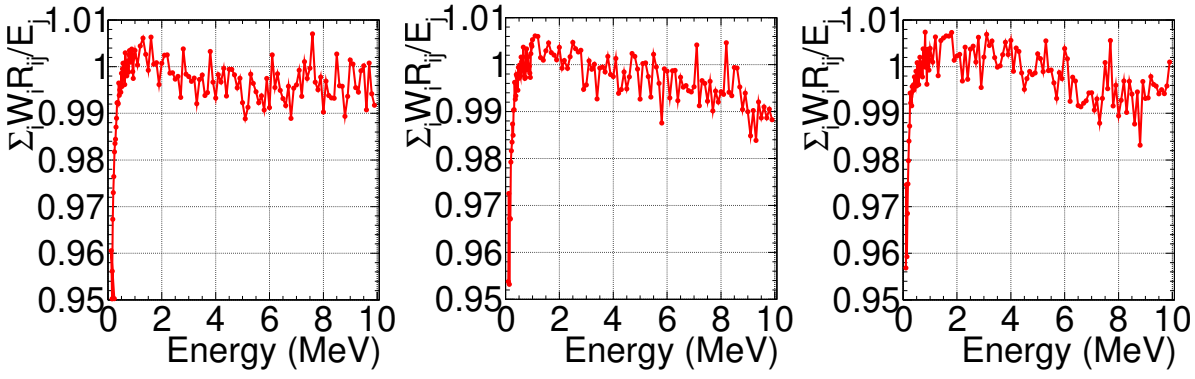

(a) Det 1 (b) Det 3 (c) Det 4

Figure 5.22: Proportionality check between the efficiency and the γ-ray energy for the WF with the ^{246}Cm sample setup.

As observed in Figures 5.21 and 5.22 the WFs does not reproduced perfectly the condition $\varepsilon_\gamma = k \cdot E_\gamma$. To calculate the propagation of these differences in the final calculation of the yield, the capture cascades of ^{240}Pu and ^{244,246,248}Cm are simulated applying the WFs. Then, the number of counts obtained in the simulations should be equal to the number of cascades simulated multiplied by the S_n of the isotope. All the differences obtained in these simulations are below 0.3% (Table 5.2), so this percentage is considered as the uncertainty in the calculation of the WFs.

	^{240}Pu	^{244}Cm	^{246}Cm	^{248}Cm
^{244}Cm sample	0.24 (3)	0.29 (3)	-	-
^{246}Cm sample	0.20 (3)	0.26 (3)	0.26 (3)	0.25 (3)

Table 5.2: Differences in percentage between the efficiency to detect the simulated cascade applying the WF and the S_n of each isotope. The cascades simulated to calculate these values are without isomers or conversion electrons.

5.3.2 Calculation of the PHWT correction factors (F_{PHWT})

The WF is obtained by simulating an ideal experiment, but the real experiment at n_TOF deviates from that situation. The different experimental corrections generating deviations between the PHWT theory and its experimental application are:

i) **The 0.12 MeV threshold set in each detector.** Thus, the counts that are missed below the threshold need to be accounted for.

ii) **The effect of double or triple counting.** There is a small probability ($\sim$6%) of detecting various γ-rays of the same cascade or the same γ-ray in more than one BICRON detector (5.2.4). In the analysis, when this happens, randomly only one of the signals is considered.

iii) **Effect of γ-ray summing.** When two or more γ-rays are detected in one BICRON detector simultaneously, the weights applied are not correctly calculated. This is because the WFs are not linear, so $W(E_1+E_2) \neq W(E_1)+W(E_2)$, therefore the weights given to the signals are not the same if they are detected simultaneously or separated.

The F_{PHWT} are calculated for each isotope with Monte Carlo simulations considering these experimental corrections and the precise de-excitation cascades obtained with NuDEX. These correction factors are calculated following these steps:

- The response to the cascades of each isotope are simulated using Geant4 (Section 5.1). As already mentioned in Section 3, the EM cascades used in the simulations are obtained with different procedures:
  - ^{240}Pu. The decay scheme was obtained from the TAC data after adjusting the de-excitation scheme with the evolutive algorithm described in Section 3.1
  - ^{244}Cm. The same procedure than in the ^{240}Pu has been followed.
  - ^{246}Cm. The decay scheme was obtained from the C_6D_6 data in Section 3.2.
  - ^{248}Cm. The EM cascades for ^{248}Cm were modelled with the default NuDEX cascades due to the lack of statistics in the pulse height spectra.
- The data from the detectors are analysed as in a real experiment: by applying the WFs and the energy threshold, the γ-rays of the cascades are simulated in coincidence and when more than two γ-ray are detected only one is considered.

- Since the number of cascades simulated are known, a correction factor $F_{PHWT} = number\ of\ simulated\ cascades\ *\ S_n\ /\ number\ of\ detected\ cascades$ is calculated for each isotope.

The PHWT correction factors (F_{PHWT}) for each detector and isotope are presented in Table 5.3.

	Det1	Det 3	Det 4	Average
$F_{PHWT}(^{240}Pu)$	1.0946 (6)	1.0991 (7)	1.0994 (7)	1.0977 (4)
$F_{PHWT}(^{244}Cm)$	1.1308 (7)	1.1337 (7)	1.1359 (7)	1.1335 (4)
$F_{PHWT}(^{246}Cm)$	1.1688 (7)	1.1705 (7)	1.1722 (8)	1.1705 (4)
$F_{PHWT}(^{248}Cm)$	1.0866 (6)	1.0895 (7)	1.0898 (7)	1.0886 (4)
$F_{PHWT}(^{240}Pu)/F_{PHWT}(^{244}Cm)$	0.9680 (9)	0.9694 (9)	0.9679 (9)	0.9685 (5)
$F_{PHWT}(^{240}Pu)/F_{PHWT}(^{246}Cm)$	0.9365 (9)	0.9390 (9)	0.9379 (9)	0.9378 (5)
$F_{PHWT}(^{240}Pu)/F_{PHWT}(^{248}Cm)$	1.0074 (8)	1.0088 (9)	1.0088 (9)	1.0084 (5)

Table 5.3: The F_{PHWT} to correct the deviations from the PHWT theory and the ratios between them. The uncertainties in the table are derived from the statistics in the Monte Carlo simulations.

As has been done for the calculation of the WFs the correction factors have been calculated for the ^{244}Cm sample setup. It has been found that the differences with the values calculated for the ^{246}Cm sample setup are smaller than the uncertainties due to counting statistics, that are below 0.05%. For this reason, the values for the ^{244}Cm sample setup correction factors have also been taken for the ^{246}Cm sample setup.
As expected, the differences in the F_{PHWT} ratios between the detectors are very small (less than 0.1%) and the average value (column on the right) has been used in the analysis.

Concerning the uncertainties in the F_{PHWT}, the Cm yields are calculated normalised to the first resonance of ^{240}Pu. For this reason, only the uncertainties in the $F_{PHWT}(^{240}Pu)$/ $F_{PHWT}(^{244,246,248}Cm)$ ratios have been considered in the analysis. The different sources of uncertainties are:

- **The uncertainties in the Geant4 simulations and the reconstruction process.** All the cascades are very similar, so the possible uncertainties are cancelled when the ratio is calculated.

- **The uncertainties in the threshold.** The F_{PHWT} have been calculated for several thresholds, and they are shown in Table 5.4. As expected since the cascades are similar, the differences in the ratios for 0.1, 0.12 and 0.15 MeV thresholds are smaller than 0.3%. This 0.3% has been used to estimate the uncertainty in the F_{PHWT} ratio due to the detector thresholds.

- **The uncertainties in the γ-ray cascades**. The cascades play an essential role in the calculation of the different F_{PHWT}. For this reason, in Chapter 3 a precise

	0.1 MeV	0.12 MeV	0.15 MeV	0.3 MeV	0.5 MeV
$F_{PHWT}(^{240}Pu)$	1.0925 (4)	1.0977 (4)	1.1056 (4)	1.1505 (4)	1.2327 (5)
$F_{PHWT}(^{244}Cm)$	1.1265 (4)	1.1335 (4)	1.1439 (4)	1.1927 (4)	1.2756 (5)
$F_{PHWT}(^{246}Cm)$	1.1641 (4)	1.1705 (4)	1.1805 (4)	1.2334 (4)	1.3293 (5)
$F_{PHWT}(^{248}Cm)$	1.0831 (4)	1.0886 (4)	1.0971 (4)	1.1446 (4)	1.2286 (5)
$F_{PHWT}(^{240}Pu)/F_{PHWT}(^{244}Cm)$	0.9698 (5)	0.9685 (5)	0.9665 (5)	0.9646 (5)	0.9664 (6)
$F_{PHWT}(^{240}Pu)/F_{PHWT}(^{246}Cm)$	0.9385 (5)	0.9378 (5)	0.9365 (5)	0.9327 (5)	0.9273 (6)
$F_{PHWT}(^{240}Pu)/F_{PHWT}(^{248}Cm)$	1.0087 (5)	1.0084 (5)	1.0078 (5)	1.0052 (5)	1.0033 (6)

Table 5.4: The F_{PHWT} to correct the deviations from the PHWT theory with different detection thresholds and the ratios between them. The uncertainties in the table are derived from the statistics in the Monte Carlo simulations.

work has been done to determine the cascades. In particular, the cascades of ^{240}Pu and ^{244,246}Cm that have been obtained from the experimental data measured at n_TOF. In Table 5.5 the F_{PHWT} calculated with these cascades (second column) are compared with the ones obtained with the default NuDEX cascades (third column).

	Fitted cascade	Def. NuDEX cascade	Cascade without EC
$F_{PHWT}(^{240}Pu)$	1.0977 (4)	1.0994 (4)	1.0844 (4)
$F_{PHWT}(^{244}Cm)$	1.1335 (4)	1.1342 (4)	1.1103 (4)
$F_{PHWT}(^{246}Cm)$	1.1641 (4)	1.1570 (4)	1.1452 (4)
$F_{PHWT}(^{248}Cm)$	-	1.0886 (4)	1.0793 (4)
$F_{PHWT}(^{240}Pu)/F_{PHWT}(^{244}Cm)$	0.9685 (5)	0.9671 (5)	0.9767 (5)
$F_{PHWT}(^{240}Pu)/F_{PHWT}(^{246}Cm)$	0.9378 (5)	0.9502 (5)	0.9470 (5)
$F_{PHWT}(^{240}Pu)/F_{PHWT}(^{248}Cm)$	-	1.0084 (5)	1.0048 (5)

Table 5.5: The F_{PHWT} to correct the deviations from the PHWT theory for various cascades and the ratios between them. The uncertainties in the table are derived from the statistics in the Monte Carlo simulations. A detailed description of each column can be found in the text.

The differences in the ratios comparing the fitted and the NuDEX default cascades are less than 0.2% for $F_{PHWT}(^{240}Pu)/F_{PHWT}(^{244}Cm)$ and 1% for $F_{PHWT}(^{240}Pu)/F_{PHWT}(^{246}Cm)$. These small values indicate the low impact of the cascade shape in the final correction factor and are considered as the uncertainties due to the cascade determination. The cascade of ^{248}Cm is directly taken from the default NuDEX PSF, so the comparison can not be performed, and 2% is considered as the uncertainty in the ratio $F_{PHWT}(^{240}Pu)/F_{PHWT}(^{248}Cm)$.

The internal conversion electron process is included in NuDEX taking the data from the RIPL-3 database [118]. If this process is omitted, then the F_{PHWT} drops by 0.9% for ^{240}Pu, by 1.5% for ^{244}Cm, by 1.7% for ^{246}Cm and by 0.9% for ^{248}Cm, as illustrated in the fifth column of Table 5.5.

The total uncertainties in the ratios of the F_{PHWT} are presented in Table 5.6, including the uncertainties in the threshold (0.3 %), in the cascades (0.3% for ^{244}Cm, 1.0% for ^{246}Cm and 2.0% for ^{246}Cm) and also the ones of the WFs (0.3%) calculated in Section 5.3.1.

$F_{PHWT}(^{240}Pu)/F_{PHWT}(^{244}Cm)$	$F_{PHWT}(^{240}Pu)/F_{PHWT}(^{246}Cm)$	$F_{PHWT}(^{240}Pu)/F_{PHWT}(^{248}Cm)$
0.968(5)	0.938(10)	1.008(20)

Table 5.6: Final values of the ratios of the F_{PHWT} and their total uncertainties.

5.4 Background

The different sources of background in the ^{244,246,248}Cm and ^{240}Pu measurements in EAR2 with the C_6D_6 detectors are the same as in EAR1 measurement (Section 4.3). However, the importance and the uncertainty in the determination is different for both areas. The components in EAR2 are:

i) **The environmental background.** This background has been estimated using the environmental background dedicated measurement performed with beam-off and without any sample. This contribution is presented in the blue lines (Env. bkg.) of Figures 5.23 and 5.24.

ii) **The activity of the Cm samples.** Mainly the γ-rays and neutrons emitted from the decay of the different actinide isotopes in the samples. The activity of the samples are measured in dedicated runs with beam-off. The results obtained are presented in the red line (Activity ^{244,246}Cm) of Figures 5.23 and 5.24. It can be seen in these figures that these and the previous components have a negligible impact in comparison with the rest of the background sources.

iii) **Background induced by the neutron beam, excluding the part related to the interaction with the actinides of the samples.** In order to obtain these backgrounds, dummy samples were created, including the aluminium canings, the Kapton foils, the Mylar foils and the aluminium rings shown in Figure 2.14. This contribution was measured in dedicated runs with these dummy samples and are shown in the green lines (Dummy ^{244,246}Cm) of Figures 5.23 and 5.24.

iv) **The interaction of the neutron beam with the actinides in the samples.** The backgrounds produced by the capture, fission and elastic scattering in the actinides of the samples, except the capture events in ^{244,246,248}Cm and ^{240}Pu. These components

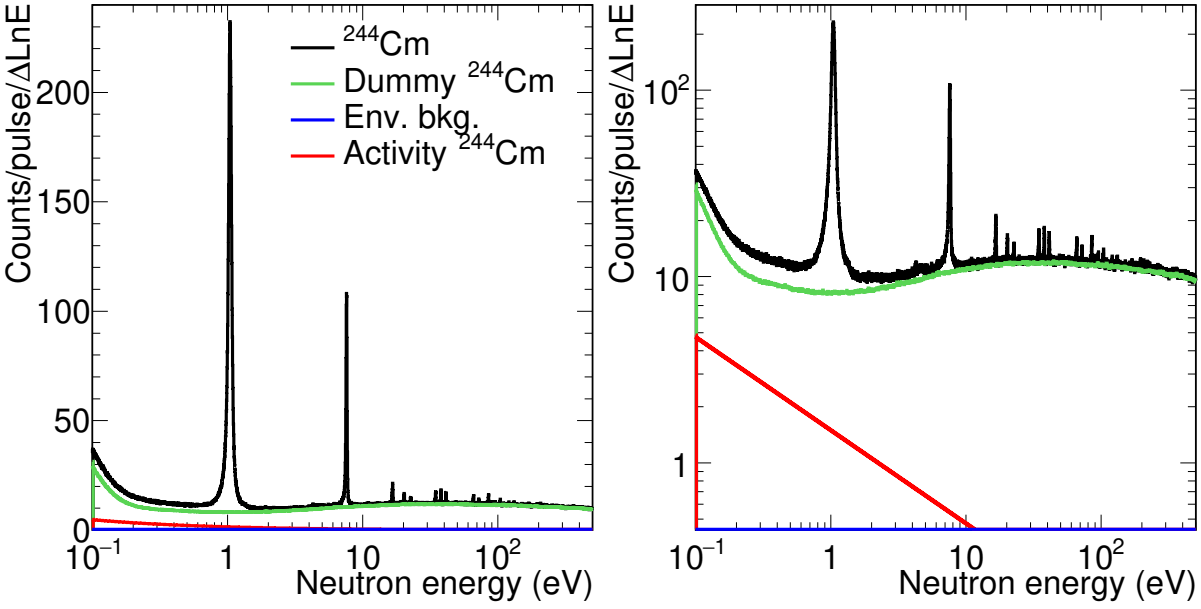

(a) ^{244}Cm $0.12 < E_{dep} < 6.0$ MeV (linear)

(b) ^{244}Cm $0.12 < E_{dep} < 6.0$ MeV (logarithmic)

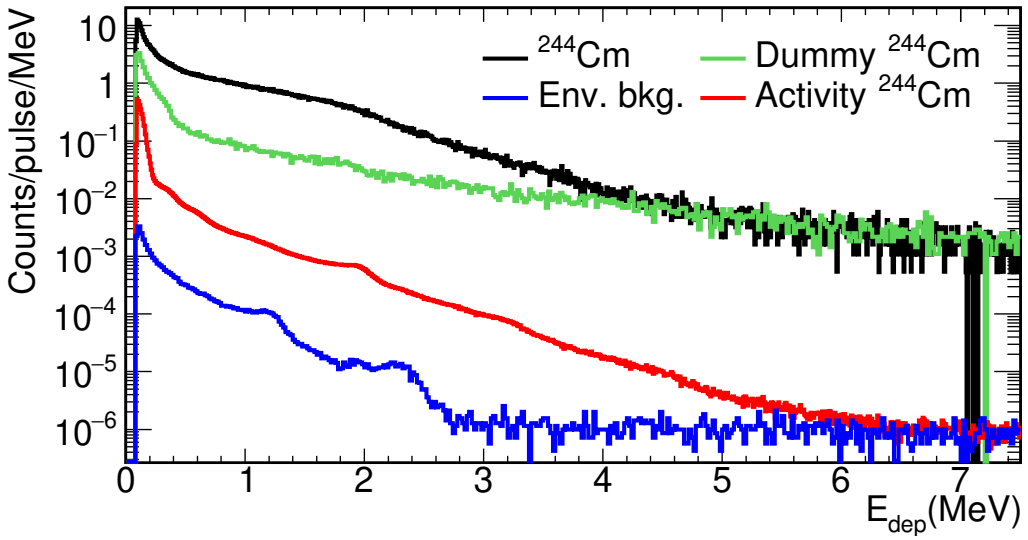

(c) ^{244}Cm ($7.4 < E_n < 7.7$ eV)

Figure 5.23: ^{244}Cm sample measurement (black) with the different background components of the measurement. A detailed description of the background components can be found in the text. The top panels indicate the number of counts as a function of the neutron energy with the analysis cuts, $0.12 < E_{dep} < 6$ MeV in linear and logarithmic scales. The bottom panel show the E_{dep} spectra contributions for the first ^{244}Cm resonance ($7.4 < E_n < 7.7$ MeV).

have not been determined experimentally but from the corresponding reaction yields and the associated detection efficiencies. The reaction yields were obtained with SAMMY, from the cross sections in JEFF-3.3 (or those adjusted in the resonance analysis) and from the different isotopic abundances (Table 2.2). The efficiency to detect a fission event is presented in Section 5.4.1, and finally, no corrections are

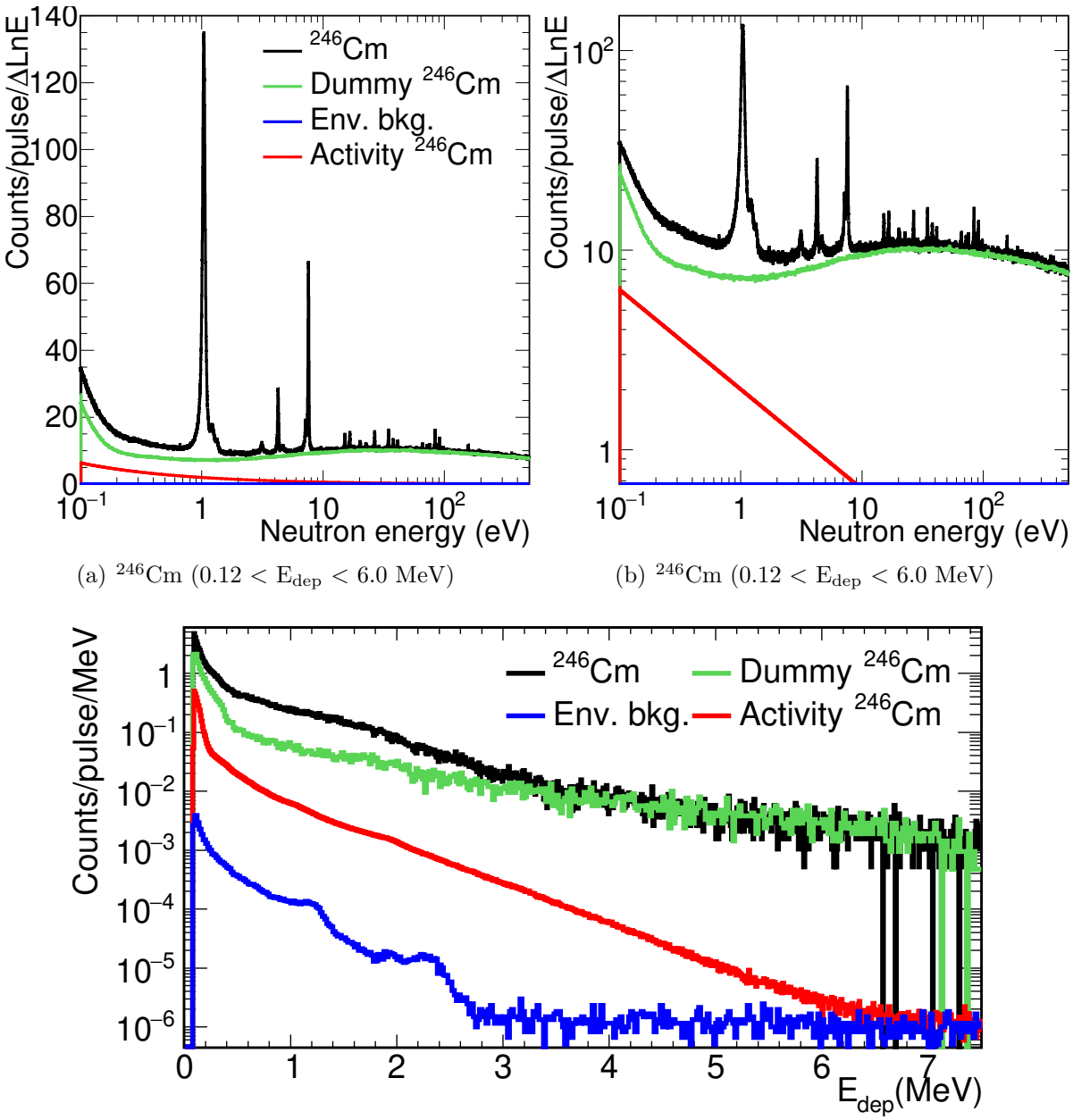

(a) ^{246}Cm ($0.12 < E_{dep} < 6.0$ MeV)

(b) ^{246}Cm ($0.12 < E_{dep} < 6.0$ MeV)

(c) ^{246}Cm ($4.20 < E_n < 4.35$ eV)

Figure 5.24: ^{246}Cm sample measurement (black) with the different background components of the measurement. A detailed description of the background components can be found in the text. The top panels indicate the number of counts as a function of the neutron energy with the analysis cuts, $0.12 < E_{dep} < 6$ MeV in linear and logarithmic scales. The bottom panel show the E_{dep} spectra contributions for the first ^{246}Cm resonance ($4.20 < E_n < 4.35$ MeV).

applied for the elastic scattering in the actinides of the samples (Section 5.4.2).

The background associated with the interaction of the neutron beam with the dead material (presented in iii) is the primary source of background in the measurement. For this reason, a precise work has been done to estimate these background components and the

main uncertainties associated with them, which can come from:

1. The differences between the Cm targets and the dummy targets created for the measurement. The dummy samples were prepared in Japan with exactly the same amount of Aluminium oxide. The mounting of the dummy samples inside the Mylar foils was done at CERN following the same techniques as the one used for the Cm samples.

2. The normalisation of the dummy measurements to the Cm measurements. The normalisation has been performed with the SiMon2 detector [90] and has an uncertainty estimated of 1% (Section 2.5.1).

3. The misalignment of the dummy sample respect to the Cm sample. It has been considered the possibility of having misalignments of up to 1 mm in the procedure of placing the sample in the beam.

4. The uncertainty due to counting statistics of the dummy measurement. In order to reduce the uncertainty due to counting statistics, the background has been rebinned by a factor of ten with respect to the binning used for the Cm samples. This has been done under the (reasonable) assumption that the background is smooth and does not contain resonant structures.

The effect of all of these uncertainties in the final background have been calculated comparing the Cm sample measurements and the dummies in the valley of the resonances. Since the Cm and Pu resonances are well separated from one to the others, the valleys between resonances should come from the background only. The dummy measurements have been compared with the Cm sample measurements in these valleys after subtracting the no beam contributions and taking into account the minimal contribution of the tails of the resonances of the actinides. The minor differences of less than 1% observed in these comparisons (Table 5.7) show the precision of the background calculations. Even though 1% is a small value for the background calculation, it can be reduced by re-normalising the dummy background by the values in Table 5.7 and then the uncertainties are directly the uncertainties in the table that are ∼0.5%.

	Sample ^{244}Cm	Sample^{246}Cm
Primary pulses	1.006(4)	1.005(5)
Parasitic pulses	1.008(5)	1.010(5)

Table 5.7: Dummy scale factors obtained comparing the valleys of the resonances of the Dummy samples and the Cm measurements of the ^{244}Cm and ^{246}Cm samples for primary and parasitic pulses. The uncertainties presented are due to counting statistics.

5.4.1 The fission efficiency in EAR2

The fission efficiency in the EAR2 setup, needed to obtain the background due to the fission reactions in the actinides present in the samples, has been calculated by comparing

the experimental yield for the ^{247}Cm first and second resonances and the evaluated fission cross section for this isotope.

It has been assumed that the fission cascades are similar for all the Cm isotopes in the sample and therefore, so are the efficiencies. Figure 5.25 shows the ^{247}Cm resonances located at 2.94 and 3.17 eV. For these resonances, the fission cross section is much higher than the capture cross section. The fission detection efficiency is then obtained from the fit to the experimental data. The value of $\varepsilon_{fission}$ obtained is 0.085(3), which is approximately three times higher than the one obtained for the capture of ^{240}Pu (Section 5.6).

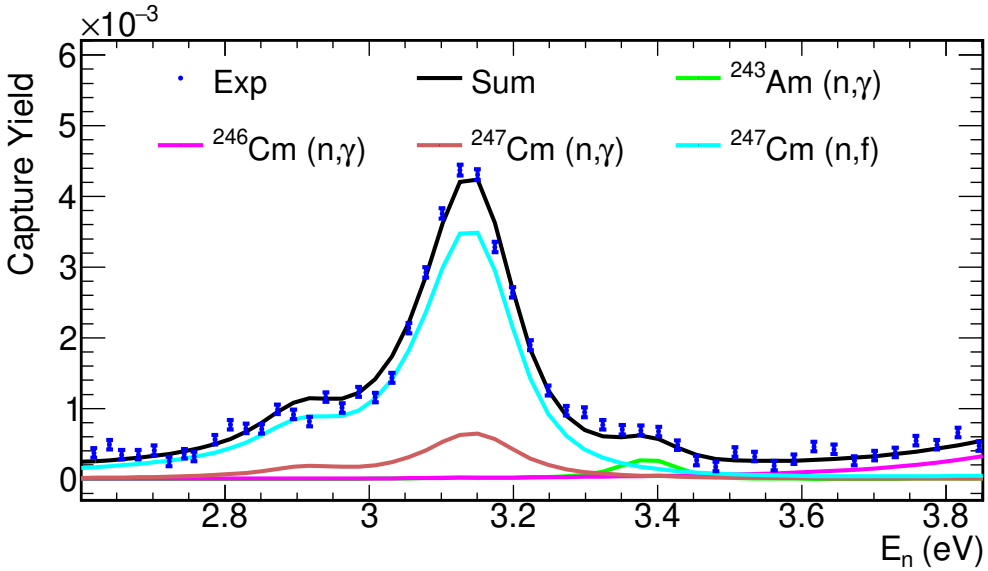

Figure 5.25: Experimental yield (Exp) of the ^{246}Cm sample together with the yield of the different isotopes calculated with SAMMY and JENDL-4.0. The contribution of the ^{247}Cm fission yield has been re-scaled to fit the experimental data, thus obtaining $\varepsilon_{fission}$. The black line (Sum) is the sum of the contributions of the different yields.

The uncertainty of the ^{247}Cm fission cross section in JENDL-4.0 in this energy region is 20%. The uncertainty in the abundance of ^{247}Cm in the sample is 15% (Table 2.2). Considering these two uncertainties, the total value of the uncertainty in the fission efficiency has been set to 30%.

5.4.2 Background due to elastic scattering

Neutrons scattered by the actinides in the sample can produce a background with the same resonant structure as the capture cross section: the elastically scattered neutron can be captured in the detector material (not just dead material), and subsequent γ-rays can be detected. The probability of detecting an elastic scattering compared with the one of detecting a capture event can be approximated by the expression (5.5) for each

resonance:

$$P^{ns} = (\frac{\varepsilon_n}{\varepsilon_c})\frac{\Gamma_n}{\Gamma_\gamma} \tag{5.5}$$

where ε_n is the efficiency to detect a neutron of the energy of the resonance, ε_c is the efficiency to detect a γ-ray cascade ($\sim$3% for the actinides of the measurement), and Γ_n and Γ_γ are the neutron and gamma widths of the resonance.

In previous works for the C_6D_6 detectors [71, 144, 156], the neutron sensitivity is defined as the ratio between ε_n and ε_c. This neutron sensitivity has been simulated with Geant4 and the results obtained for only one BICRON detector at 5 cm (black line of Figure 5.26) agree with the results obtained by R. Plag *et al.* [71]. In Figure 5.26 the neutron sensitivity is determined for each detector in the setup used for the Cm campaign, the neutron sensitivity is increased with respect to the one obtained for only one BICRON due to the interaction of the neutrons in the dead material of the configuration and also in the rest of detectors.

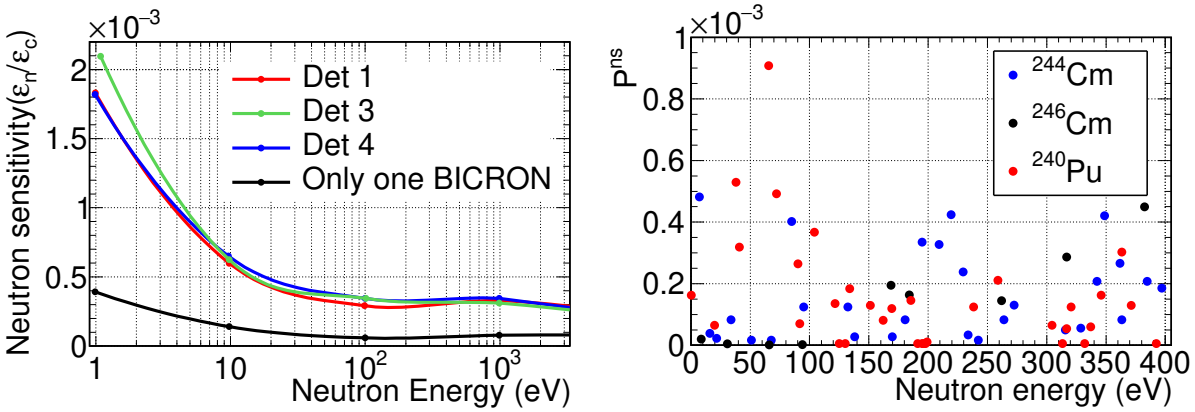

Figure 5.26: In the left panel, the neutron sensitivity of the three BICRON detectors (Det 1, Det 3 and Det 4) are presented. The black line (Only one BICRON) corresponds to the simulation performed with only one BICRON detector without any dead material. The right panel shows the P^{ns} values for the resonances in the energy range of the measurement calculated for ^{240}Pu, ^{244}Cm and ^{246}Cm.

The parameters P^{ns} are calculated for all the resonances of ^{240}Pu, ^{244}Cm and ^{246}Cm, and they are shown in the right panel of Figure 5.26 to see if it is necessary to apply corrections due to the elastic scattering in these actinides. The P^{ns} values obtained are below 0.001 for all the resonances, so these corrections are small enough not to be included in the EAR2 analysis. The resonances of ^{248}Cm are note included in Figure 5.26, but in this isotope, the values of P^{ns} are also below 0.001.

5.5 Normalisation of the experimental yield

The Cm capture cross section measurements are normalised to the well known first resonance of ^{240}Pu using the JEFF-3.3 [51] RP. Also, an estimation of the mass of ^{240}Pu

and the Cm isotopes are necessary to perform the shelf-shielding and multiple scattering corrections in the resonance analysis. The mass of ^{240}Pu has been obtained by normalising the yield to the first resonance at 1.056 eV in JEFF-3.3. The masses of the rest of the isotopes have been calculated with the value obtained for ^{240}Pu and the abundances of Table 2.2. The neutron fluence in the sample, necessary for this calculation, has been calculated by multiplying the neutron fluence for a sample covering all the beam (Section 2.5.3) with the Beam Interception Factor (BIF).

In order to calculate the BIF the same procedure, using the saturated resonance method, followed in EAR1 with the TAC (Section 4.4) has been used in EAR2 with the C_6D_6 detectors. In this case, equation 5.1 has been applied to obtain the yield considering $S_n(^{197}Au) = 6.512$ MeV and a PHWT correction factor ($F_{PHWT}(^{197}Au)$) of 1.10(2), these value has been obtained following the same procedure explained in Section 5.3.2 for the Pu and Cm isotopes. The precise fit of the BIF for the three detectors can be seen in Figure 5.27, and the result obtained is 3.14(7)%.

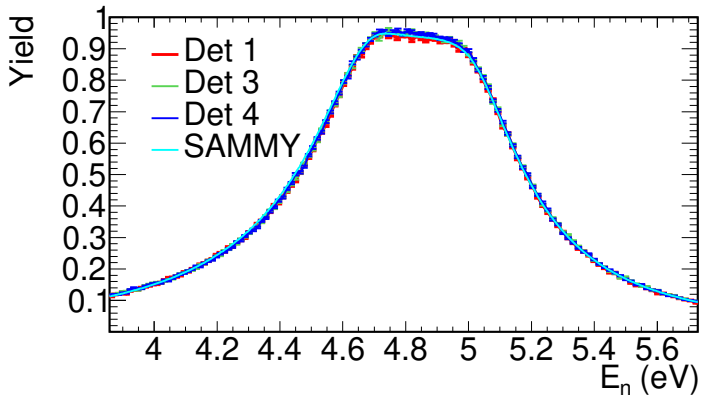

Figure 5.27: Capture yield of the 4.9 eV ^{197}Au saturated resonance to determine the fraction of the neutron beam intercepted by the sample.

5.6 Unweighted yield calculation

The application of the PHWT is used to obtain an efficiency to detect the γ-ray cascade proportional to the neutron separation energy (S_n). As an intrinsic consequence of the weighting procedure, the statistical fluctuations in the obtained yield are larger than with the standard counting technique, i.e. the uncertainties due to counting statistics are increased.

The PHWT and TED technique are necessary for cascades where the de-excitation pattern strongly depends on the resonance, for example, in the cascades of light nuclei. However, in the case of the actinides measured in the experiment, all of the isotopes are 0^+ heavy nuclei with more than a million levels below the neutron separation energy. Also, the incident neutrons' energy is at least four orders of magnitude lower than the neutron separation energy. Thus it can be expected that the γ-cascades do not vary significantly

from one resonance to another.

Under this assumption, the unweighted spectra can be used instead of the weighted spectra, as has been done in the analysis of ^{242}Pu by J. Lerendegui *et al.* [111, 157]. The unweighted yield for a given isotope is then normalised to the weighted yield. After the normalisation, it is necessary to demonstrate that both yields are compatible so then the unweighted yield with lower uncertainties due to counting statistics can be used for the resonance analysis. In order to calculate the unweighted yield, the following equation has been applied:

$$Y_{\gamma,exp,i} = \frac{(C - B)}{\varepsilon_{c,i} \cdot \phi_n} \tag{5.6}$$

where C is the total unweighted counting rate, B is the background unweighted counting rate, ϕ_n is the number of neutrons impinging in the sample by unit time and $\varepsilon_{c,i}$ is the efficiency in detecting the cascade of each isotope i.

The detection efficiency (ε_c) is obtained by comparing the integrals of the resonances obtained with the weighted yield, using the PHWT and TED technique, and the unweighted yield, i.e. normalizing the unweighted to weighted yield. The efficiency values obtained for each isotope are presented in Table 5.8.

	^{240}Pu	^{244}Cm	^{246}Cm	^{248}Cm
ε_c	0.03023(2)	0.03134(6)	0.02898(18)	0.02685(50)

Table 5.8: Efficiency to detect the capture cascades for the unweighted spectra. The uncertainties in the table are due to counting statistics in the experimental data.

The fact that the $\varepsilon_{c,i}$ of the four isotopes are comparable is a consequence of the similarity of the S_n and the γ-ray cascades. The uncertainty values given in Table 5.8 are the uncertainties due to counting statistics. They are higher for ^{246}Cm and ^{248}Cm due to the smaller cross section and masses of these isotopes in the samples.

The unweighted capture yield can be calculated with equation 5.6 and the efficiencies presented in Table 5.8. As previously mentioned, the validation of the method is done by comparing the weighted and unweighted yields obtained for various resonances (Figure 5.28) and the Γ_n values (Figure 5.29) obtained following the techniques described in Chapter 6. The differences observed are compatible with the uncertainties due to counting statistics, validating the method.

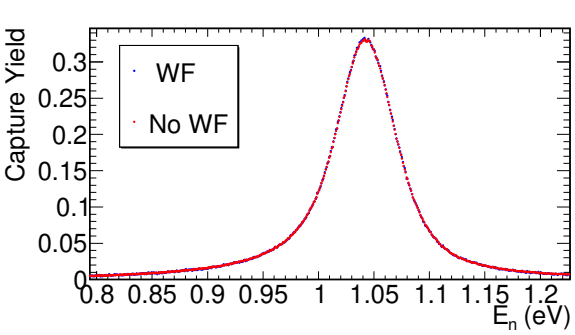

(a) ^{240}Pu first resonance

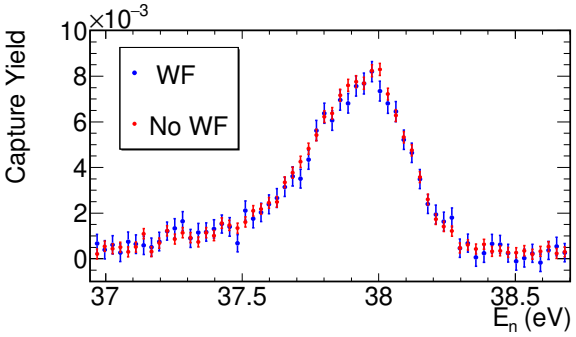

(b) ^{240}Pu second resonance

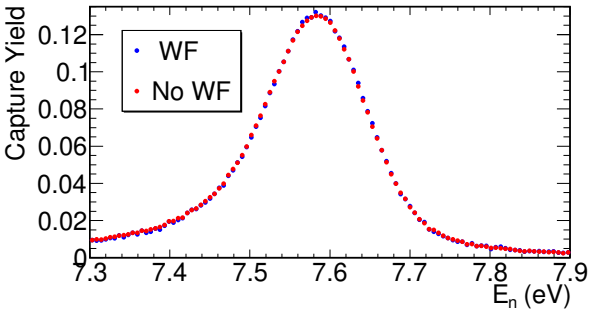

(c) ^{244}Cm first resonance

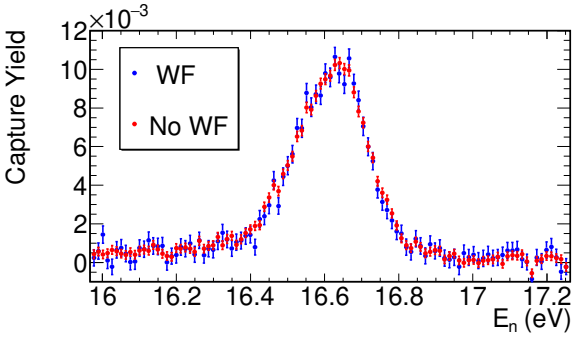

(d) ^{244}Cm second resonance

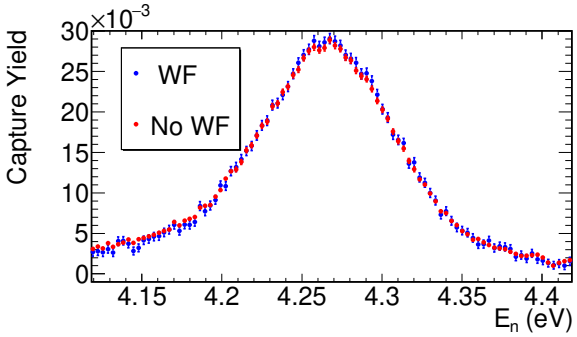

(e) ^{246}Cm first resonance

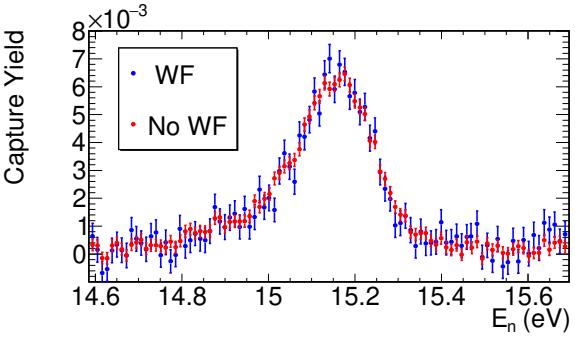

(f) ^{246}Cm second resonance

Figure 5.28: Comparison of the weighted and the unweighted yield for various resonances.

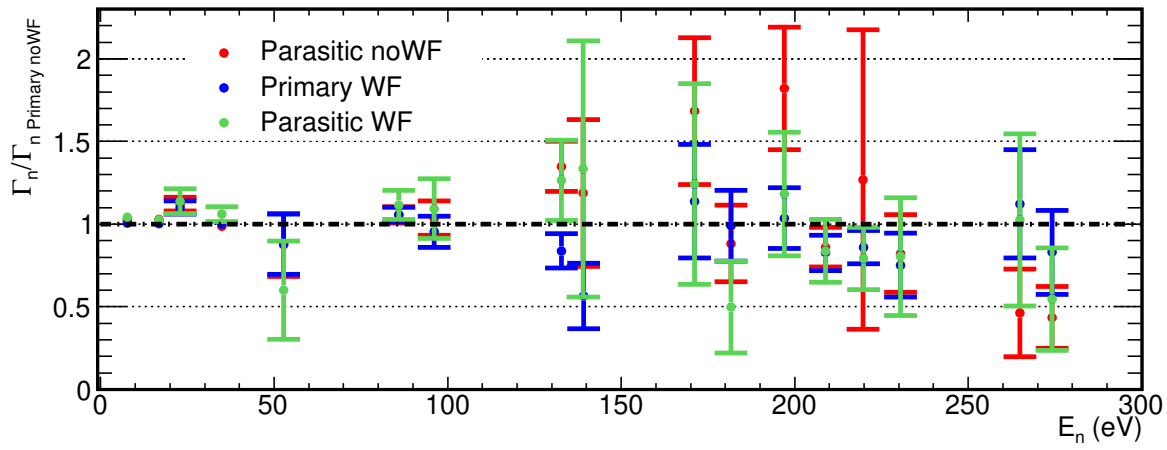

(a) ^{244}Cm sample ^{244}Cm

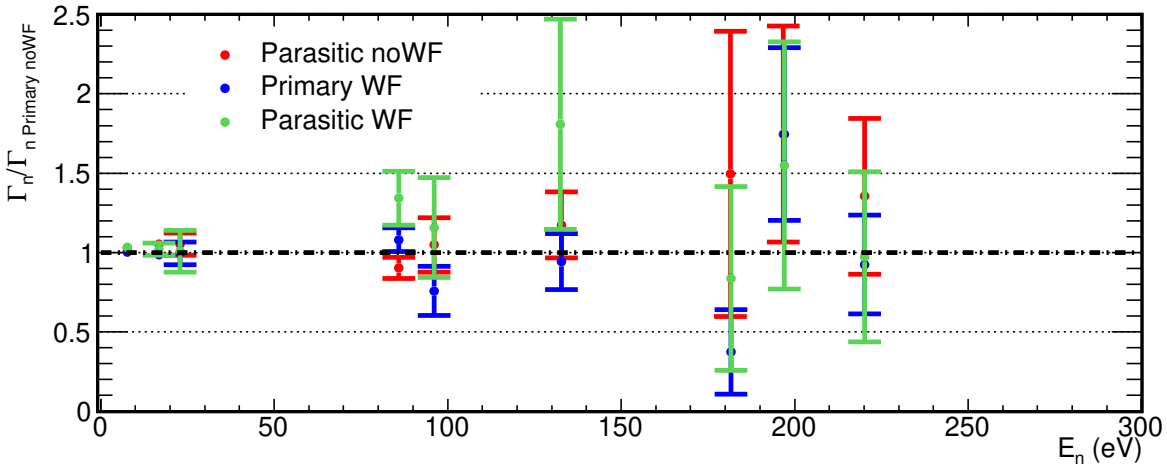

(b) ^{244}Cm sample ^{246}Cm

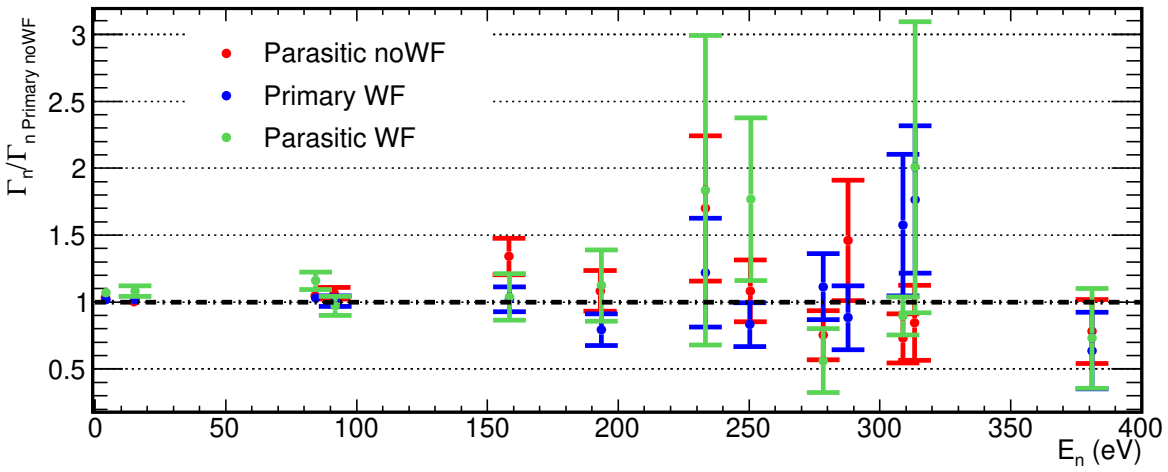

(c) ^{246}Cm sample ^{246}Cm

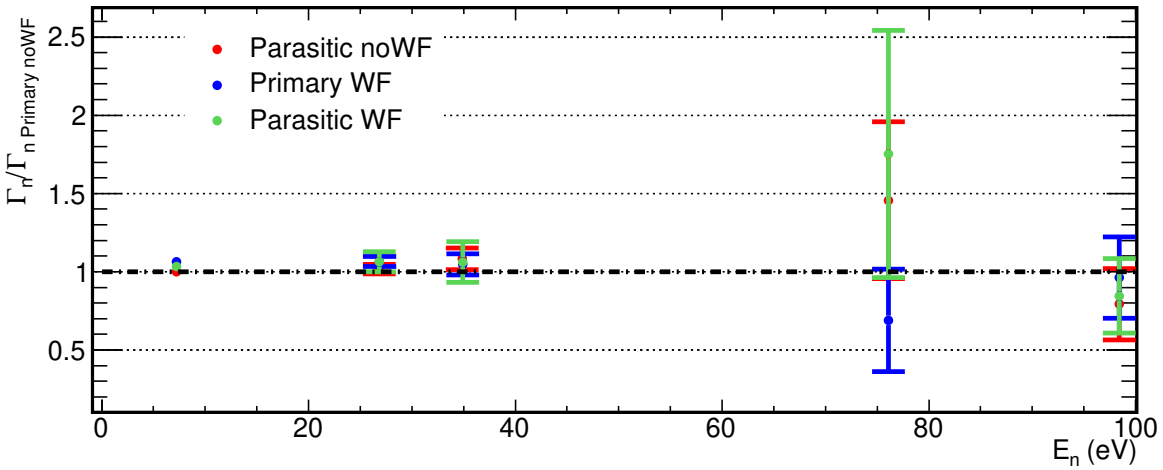

(d) ^{248}Cm sample ^{246}Cm

Figure 5.29: Comparison of the E_n and Γ_n parameters for ^{244}Cm obtained with the ^{244}Cm and ^{246}Cm samples in EAR2, with and without applying the WF technique for primary and parasitic pulses. The error bars correspond to the uncertainties due to counting statistics.

5.7 Final uncertainties in the capture yield

The final yield for isotope i is obtained with the unweighted spectra using Equation 5.6 with the efficiency ($\varepsilon_{c,i}$) determined in Section 5.6, to calculate this factor, the PHWT and TED technique are applied. The uncertainties considered in the yield calculation, in addition to those due to counting statistics, are the following:

i) **Uncertainty in the normalisation**. The Cm yields have been normalised with respect to the first resonance of ^{240}Pu. The uncertainties associated with the normalisation process are:

- The uncertainty in the capture cross section of ^{240}Pu, which is 2.75% (Section 6.2).
- The uncertainty in the calculation of the ratio between the ^{240}Pu and the ^{244,246,248}Cm masses in the ^{244}Cm and ^{246}Cm samples (Table 2.2).
- The uncertainties in the ratios $F_{PHWT,240Pu}/F_{PHWT,^{244,246,248}Cm}$ presented in Section 5.3.2.
- The uncertainties in the detection of the cascaded ratios for the unweighted spectra $\varepsilon_{c,^{244,246,248}Cm}/\varepsilon_{c,^{240}Pu}$ presented in Section 5.6.

The different normalisation uncertainties are summarised for the Cm isotopes of each sample in Table 5.9. In the penultimate row, all the uncertainties have been added quadratically except the uncertainty in the nuclear data of ^{240}Pu. Finally, in the last row, all the uncertainties have been added quadratically.

Uncertainty	^{244}Cm sample	^{246}Cm sample		
	^{244}Cm	^{244}Cm	^{246}Cm	^{248}Cm
Nuclear data of ^{240}Pu	2.75	2.75	2.75	2.75
Abundance ^{240}Pu/Cm in the sample	2.8	2.6	2.7	3.3
$F_{PHWT,^{240}Pu}/F_{PHWT,Cm}$	0.5	0.5	1.1	2.0
$\varepsilon_{c,Cm}/\varepsilon_{c,^{240}Pu}$	0.2	0.2	0.5	1.8
Total quadratic sum without the uncertainty in the nuclear data of ^{240}Pu	2.9	2.7	3.0	4.3
Total quadratic sum	4.0	3.8	4.3	5.1

Table 5.9: Uncertainties (%) in the normalisation. In the last row the uncertainties are added quadratically to obtain the total normalisation uncertainty and in the penultimate row all the uncertainties except the one of the nuclear data of ^{240}Pu are added.

The ^{240}Pu yield has been normalised to the first resonance at 1.056 eV, so the only uncertainty is the one due to the capture cross section of this resonance (2.75%).

ii) **Uncertainty in the energy dependence of the neutron fluence**. Described in Section 2.5.3, which is 1%.

iii) **Uncertainty in the background subtraction (excluding the background related with the interaction of the neutron beam with the actinides in the sample)**. The different background sources are presented in Section 5.4. The uncertainties in the background determination are 0.4% for the ^{244}Cm and 0.5% for the ^{246}Cm sample.

iv) **The uncertainty in the fission background produced by the actinides in the sample**. These background components are presented in Section 6. The uncertainty in the efficiency to detect a fission cascade is 30%.

v) **Uncertainties in the masses**. The ^{244,246,248}Cm and ^{240}Pu capture cross sections have been normalised to the first resonance of ^{240}Pu, so the uncertainties in the total values of the different masses, which have been estimated in 5% (Section 6.2) have only a small impact in the calculation of the self shielding and multiple scattering effects.

Chapter 6

Resonance analysis of the capture yields

The three capture yields presented in Sections 4 and 5 have been analysed to obtain the Resonance Parameters (RP) of the ^{244,246,248}Cm and ^{240}Pu isotopes in the Resolved Resonance Region (RRR).

The resonances have been fitted with SAMMY [104], a code widely used in the nuclear data community, applying the R-matrix formalism and the Reich-Moore approximation [158], and considering all the isotopes present in the samples. The reader is referred to [25] for a detailed description of the formalism and the different approximations.

The resonance parameters of ^{244}Cm and ^{240}Pu have been obtained separately in the measurement at EAR1 and in the two measurements at EAR2 with the ^{244}Cm and ^{246}Cm samples. The RP values of the three measurements are combined for the first time in a capture experiment at n_TOF to obtain the final values of the cross section considering the various correlations between the measurements. The RP of ^{246,248}Cm have been obtained in the measurement performed in EAR2 with the ^{246}Cm sample. Also in this chapter, the RP obtained for each isotope are discussed and compared with previous measurements and evaluations.

6.1 Methodology

The multi-level multichannel R-matrix code SAMMY [104] used in the analysis was developed by Nancy Larson to be used in the analysis of neutron-induced cross section data, although it is now widely used to analyse a great variety of cross section data. To make the fit with Bayes' method, SAMMY compares the yield obtained from the cross sections, the dimensions of the measured sample, and different experimental effects with the yield measured experimentally. The most important experimental effects in the yield modelled by SAMMY are the following:

- The Doppler broadening, which is caused by the thermal motion of the target nuclei. The different models available in SAMMY are:

i) The Free Gas Model (FGM), which assumes that the nuclei have the same velocity distribution as the atoms of an ideal gas, following the Maxwell-Boltzmann distribution. The distribution can be approximate with a Gaussian broadening of the reaction rate on the energy scale with a width provided by the so-called Doppler width (Δ) [25].

$$\Delta = \sqrt{\frac{4EkT}{M/m}} \tag{6.1}$$

In this formula, used by default in SAMMY, M is the mass of the target nucleus, kT is the temperature of the gas, and m is the neutron mass. The temperatures in the areas were measured during all the campaigns with thermometers. At EAR1 the average temperature was $24.8^{\underline{o}}$ C, and in EAR2 was $21.5^{\underline{o}}$ C. The fluctuations were $\pm 1^{\underline{o}}$ C in both areas.

ii) The Crystal Lattice Model (CLM) [159], assumes that the nucleus is part of the atom, which is bound to the rest of the atoms of the solid. This material has a phonon spectrum, which is considered to simulate the nuclei's velocity distribution. When using the CLM in this work, several phonon spectra of UO_2 were used, available in SAMMY example file 124, instead of the phonon spectrum of CmO_2, since it has not been possible to find the latter.

- The multiple scattering effect, which takes into account that the neutrons can be captured after one or more elastic scatterings. SAMMY calculates this effect by performing dedicated Monte Carlo simulations, considering the dimensions of the sample and its isotopic composition.

- The resolution broadening caused by the different TOF of the neutrons of the same energy arriving at the sample. The time-energy distribution of the neutrons is given by the resolution function (RF), which is described in sections 2.5.4 and 2.5.5.

The resonance analysis performed for the different samples is complex because the samples have many isotopes with different reaction channels (capture, fission and elastic scattering). In the SAMMY input, the RP, the abundance and the capture efficiency to detect each isotope are included. A total of more than 300 resonances are included in the analysis from nine different isotopes. The different resonances can be divided into three main groups:

i) The resonances that are fitted. The parameters E_0 and Γ_n of these resonances are fitted in the capture yield. These resonances are the majority of the ^{244}Cm and ^{240}Pu resonances in the ^{244}Cm sample and the resonances of ^{244,246,248}Cm and ^{240}Pu in the ^{246}Cm sample.

ii) The resonances included in the calculation of the capture yield, but not fitted. These resonances are considered as background in the capture yield. They are the non-fitted resonances of ^{244,246,248}Cm and ^{240}Pu and other impurities such as other Cm isotopes or ^{243}Am (Section 2.4).

iii) The resonances of aluminium and oxygen in the sample (i.e. their cross sections). The contributions to the capture yield of the neutrons captured or elastically scattered in the aluminium and oxygen atoms in the sample have been already subtracted from the yield. However, they must be included in the resonance analysis to consider the self-shielding and multiple scattering effects correctly. Then, the aluminium and oxygen isotopes are included in the SAMMY input but with a detection efficiency equal to zero.

Unfortunately, the contribution due to fission reactions can not be directly included in the SAMMY input as has been done for the contribution due to capture reactions. SAMMY calculates either the capture or the fission yield, and different efficiencies can be set for the different isotopes, but it is not possible to compute a yield which is a mix between capture and fission. For this reason, the background due to fission reactions is calculated before the fit and subtracted to the capture yield.

The fitting procedure in this analysis has been different from the ones done in previous measurements [9, 122, 144, 156, 157]. The reason is that the backgrounds due to fission reactions are determined from the fission cross sections and the fission detection efficiencies, but the fission cross sections depend on the RP which are being fitted. Thus, the background depends on the fitted parameters, so the following recursive process has been followed:

i) The first step is the normalisation to the strongest resonance of ^{240}Pu at 1.056 eV in JEFF-3.3. The normalisation is done by fitting the mass of ^{240}Pu in the sample, and the mass of the rest of the isotopes are calculated according to their relative abundances (Table 2.2).

ii) The fission backgrounds are calculated using the initial resonance parameters to obtain a fission yield, together with the efficiencies of detecting a fission reaction (Sections 4.3.1 and 5.4.1).

iii) The fit of the resonance parameters is performed, taking into account the background calculated in (ii). In most of the cases, the RP which are fitted are E_0 and Γ_n. The value of the Γ_γ parameters are fixed to a constant value (Section 6.3), and the Γ_f parameters are taken from JENDL-4.0.

iv) The parameters obtained in the fit are taken as the initial parameters of ii), and the process is repeated until it converges.

The background related with the elastic scattered neutrons in the actinides present in the sample have been calculated in a similar way as the background due to fission reactions: from an *elastic scattering* yield, obtained from evaluated cross sections and the actinides content, and a detection efficiency (Section 4.3.1). This contribution has been calculated only for the measurement performed in EAR1, since it has been neglected for the measurements in EAR2 (Section 5.4.2). However, unlike for fission, SAMMY cannot calculate *elastic scattering* yields, so MCNP [100] calculations have been used instead.

The uncertainties due to counting statistics in the experimental yields are propagated to the resonance parameters by SAMMY. The uncertainties due to systematic effects have been propagated from the uncertainties in the experimental yields (Sections 4.5 and 5.7) to the RP in the following way. For each type of uncertainty, two new yields have been created. If the nominal yield is described with a set of data points (E_i,Y_i), with E_i the neutron energy and Y_i the capture yield at the point i, then the two new yields are constructed as (E_i,Y_i+$\sigma_{k,i}$) and (E_i,Y_i-$\sigma_{k,i}$), where $\sigma_{k,i}$ is the uncertainty due to the k-type of uncertainty at point i. The fitting process described with steps (i) to (iv) are repeated for both yields, and two new sets of RP are then obtained. The uncertainties in the RP are then computed from the differences in the fitted RP. In particular, they were estimated as half of the difference, in absolute value, between the two values obtained in these two fits.

The uncertainties considered by this technique in EAR1 are (the words between the brackets are abbreviations of the uncertainty type, which are used later):

1. The uncertainty in the fission background (Fis), which has been estimated at 30% (Section 4.3.1). As indicated above, two new fits were performed to propagate this uncertainty to the RP: one using a fission background 30% lower and the other 30% higher. The differences in the two new sets of RP were then used to estimate the uncertainties in the RP due to the uncertainty in the fission background subtraction.

2. The uncertainty in the background due to neutrons scattered in the Pu and Cm isotopes (Section 4.3.1) (Elas). The uncertainties in the yield have been obtained by propagating the uncertainties in the efficiency of detecting elastic scattered neutrons (Figure 4.15).

3. The uncertainty in the subtraction of the background related with the interaction of the neutron beam with all but the Pu and Cm isotopes (Dummy). The background is measured with the dummy sample, which has been estimated to have a 1% uncertainty.

4. The uncertainty in the temperature (Temp). The temperature in EAR1 was 298±1 K during the experiment. The uncertainty for the temperature variation is calculated in a similar procedure to the previous ones. In this case, the yield used to fit is the same, but the SAMMY fits have been performed with a temperature one Kelvin higher (299) and one Kelvin lower (297). The differences obtained in these RP have been used to estimate the RP uncertainties due to the temperature variations.

5. The uncertainty in the abundances ratio (Mass). The uncertainty in the ratio ^{240}Pu/^{244}Cm is 2.8% (Table 2.2).

6. The uncertainty in the ratio of the ^{244}Cm(n,γ) and ^{240}Pu(n,γ) detection efficiencies (Nor), which is 1.7% (Section 4.2).

7. The uncertainty in the capture cross section of the first resonance of ^{240}Pu (^{240}Pu), which is 2.75% according to JEFF-3.3 (Section 6.2). This uncertainty is somehow independent of the measurement, and may be reduced with future measurements

and evaluations of ^{240}Pu

The uncertainties considered in EAR2 are:

1. The uncertainty in the fission background (Fis), which has been estimated in 30% (Section 5.4.1).

2. The changes in the gain as a function of the neutron energy (Gain). The uncertainty in the calculation of the changes of gain are estimated for each detector and presented in Figure 5.12.

3. The uncertainty in the subtraction of the background related with the interaction of the neutron beam with all but the Pu and Cm isotopes (Dummy). Which are measured with the dummy sample with 0.4-0.5% uncertainty (Section 5.4).

4. The uncertainty in the temperature (Temp). The temperature in EAR2 was 294.3±1 K during the experiment. The uncertainties in the temperature were propagated with the same procedure followed for the analysis of the EAR1.

5. The uncertainty in the abundances ratio (Mass). The uncertainty in the ratio ^{240}Pu/^{244}Cm is 2.8% in the ^{244}Cm sample and 2.6% in the ^{246}Cm sample. The uncertainty in the ratio ^{240}Pu/^{246}Cm is 2.9% and in the ^{240}Pu/^{248}Cm is 3.3% for the ^{246}Cm sample (Table 2.2).

6. The uncertainties in the correction factors (F_{PHWT}) of the PHWT and in the capture efficiencies (ε_c) calculated for the unweighted yields propagated to the normalisation (Nor). The uncertainty in the ratios $F_{PHWT,240Pu}/F_{PHWT,^{244,246,248}Cm}$ which is 0.5% for ^{244}Cm and ^{246}Cm. The uncertainty increase to 2% in ^{248}Cm (Section 5.3.2). The uncertainty in the ratios $\varepsilon_{c,^{240}Pu}/\varepsilon_{c,^{244,246,248}Cm}$ are 0.2% for the ^{244}Cm, 0.5% for the ^{246}Cm and 1.8% for the ^{248}Cm (Section 5.6). Then, the total experimental uncertainties in the normalisation are 0.5% in ^{244}Cm, 0.7% in ^{246}Cm and 2.7% in ^{248}Cm.

7. The uncertainty in the capture cross section of the first resonance of ^{240}Pu (^{240}Pu), which is 2.75% (Section 6.2).

6.2 Normalisation to the first resonance of ^{240}Pu

The first step to obtain the resonance parameters is the normalisation to the resonance of ^{240}Pu located at 1.056 eV, referred to as the first resonance of ^{240}Pu in this work. From this normalisation and the relative abundances, the masses of the isotopes in the samples are calculated. The absolute values of the masses are important to perform accurate shelf-shielding and multiple scattering corrections.

The first resonance of ^{240}Pu is relatively well known with an uncertainty in the capture cross section of 2.75% in JEFF-3.3 [160]. The ratio between the fission and the capture cross sections is below ∼0.0003. In Table 6.1, the RP for this resonance in JEFF-3.3

[51] and JENDL-4.0 [20] are presented. The only difference between them is in the Γ_n parameter, leading to a difference of 0.04% (-0.23%) in the integrated capture (total) cross section between 0.8 and 1.3 eV. The values in ENDF/B-VIII.0 [52] are the same than in JEFF-3.3.

	E_0 (eV)	Γ_γ (meV)	Γ_n (meV)	Γ_f (meV)
JEFF-3.3	1.056	2.4544	29.148	0.0081415
JENDL-4.0	1.056	2.4544	30.0	0.0081415

Table 6.1: Parameters of the first ^{240}Pu resonance in JEFF-3.3 and JENDL-4.0.

The masses of ^{240}Pu in the two samples has been calculated by comparing the experimental yield for the first resonance with the yield calculated with SAMMY using JEFF-3.3. The results of the mass together with the resulting areal density are presented in Table 6.2. The values obtained for the ^{244}Cm sample mass in EAR1 and EAR2 are compatible. This indicates a strong consistency between the analysis, since for both mass values to be compatible it is necessary, in addition to many other things, that the efficiencies of both detection systems are consistent, not only for ^{240}Pu(n,γ) cascades but also for ^{197}Au(n,γ), which is used to normalise the neutron fluence. In Section 6.7, the resonance parameters of ^{240}Pu for the rest of the resonances are presented. These parameters are compatible between the three measurements, and also with JEFF-3.3. This result gives more confidence in the normalisation done to the first resonance.

Sample	Area	Mass (mg)	Areal density (atoms/b)
^{244}Cm	EAR1	0.310(6)	$3.97(8)\cdot10^{-6}$
	EAR2	0.312(7)	$3.99(10)\cdot10^{-6}$
^{246}Cm	EAR2	0.159(4)	$2.03(5)\cdot10^{-6}$

Table 6.2: Masses of ^{240}Pu in the samples calculated from the fits to JEFF-3.3. The uncertainties between brackets included all the uncertainties presented in Table 6.3 but the 2.75% uncertainty in the nuclear data of ^{240}Pu.

The three fits of the resonances are illustrated in Figure 6.1. In addition, Figure 6.2 shows the fits obtained using two different Doppler broadening models (FGM and CLM). At the view of the residuals in Figures 6.1 and 6.2, it is observed that the shapes of the resonances are reproduced considerably well, but there is some room for improvement. This is discussed in more detail in Section 6.2.1, but these small differences do not have a significant impact on the normalisation.

The different sources of uncertainties in the total masses have been calculated and are presented in Table 6.3. The principal sources of uncertainty in the mass calculation in EAR1 and EAR2 are the uncertainties in the nuclear data of ^{240}Pu (2.75%) and the ^{197}Au normalisation (2%). It is important to note that the uncertainties in the masses are not

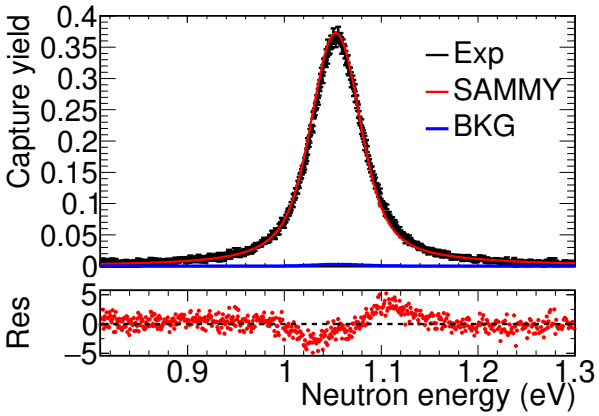

(a) ^{244}Cm sample EAR1

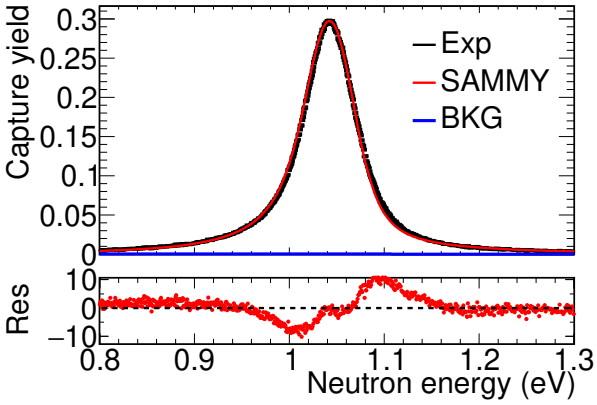

(b) ^{244}Cm sample EAR2

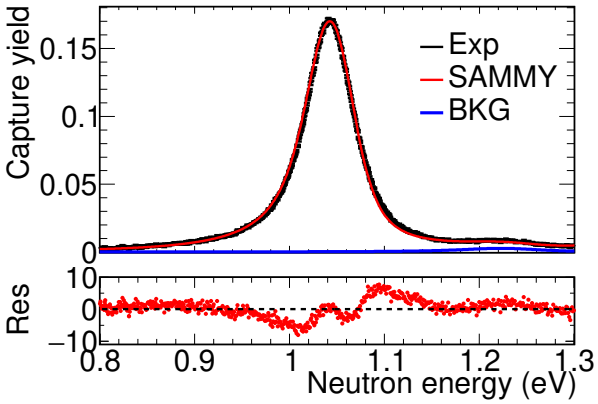

(c) ^{246}Cm sample EAR2

Figure 6.1: Experimental capture yields (Exp) in the energy range of the strongest ^{240}Pu resonance fitted to JEFF-3.3 (SAMMY). The background (BKG) in the resonance is very small.

Sample	Area	Uncertainties (%)									
		Sta	Gain	Elas	Fis	Dummy	Temp	Au Nor	RF	ND	Tot
^{244}Cm	EAR1	0.21	-	0.23	0.02	0.02	0.01	2	-	2.75	3.40
	EAR2	0.06	1.30	-	0.03	0.09	0.01	2	0.3	2.75	3.65
^{246}Cm	EAR2	0.08	1.35	-	0.7	0.19	0.01	2	0.23	2.75	3.73

Table 6.3: Partial and total (Tot) uncertainties in the calculation of the ^{240}Pu masses. The column *Au Nor* is the uncertainties associated to the normalisation to the Au measurement (Sections 4.4 and 4.4). The column *ND* (*Nuclear Data*) is the uncertainty in the cross section of ^{240}Pu in JEFF-3.3.

propagated directly to the cross sections. For example, the normalisation to the ^{197}Au measurement does not affect the normalisation of the Cm cross sections. The absolute value of the sample masses is only relevant to model the self-shielding and multiple scat-

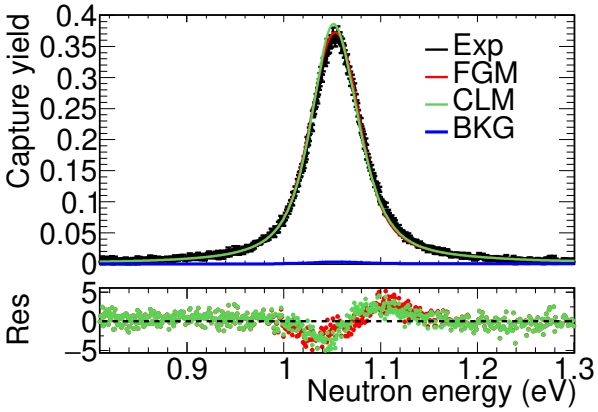

Figure 6.2: Experimental capture yields (Exp) in the energy range of the strongest ^{240}Pu resonance compared to the yield obtained with the JEFF-3.3 RP using two Doppler models: the FGM (FGM) and the CLM (CLM). The background (BKG) in the resonance is very small.

tering effects.

6.2.1 Calculation of the E_n and Γ_γ parameters of the first resonance of ^{240}Pu

The first resonance of ^{240}Pu is used to normalise the measurement, so no information concerning the area of the resonance can be obtained. This area is in good approximation proportional to Γ_n, and the width of the resonance is related with the Γ_γ parameter. Thus, the E_0 and Γ_γ of the resonance has been fitted using a fixed value of Γ_n (the one in JEFF-3.3). Only the yield measured in EAR1 has been fitted since in EAR2 the uncertainty in Γ_γ due to the RF is too big (∼20%). The result of the fit, presented in Figure 6.3, gives an energy (E_0) of the resonance of 1.0570 ± 0.0005 eV. This value is less than 0.1% lower than the evaluated value of JEFF-3.3 and JENDL-4.0 (1.0560 eV).

The value of Γ_γ obtained in the fit is 31.7 ± 1.6 meV, whereas the evaluated values are 29.148 meV for JEFF-3.3 and 30.00 meV for JENDL-4.0. The uncertainty in Γ_γ includes systematic and counting statistics and is dominated by the Doppler broadening contribution. Figure 6.3 also shows, that after fitting E_0 and Γ_γ, the shape of the resonance is reproduced significantly better, although not perfectly, as observed in the residuals. These kinds of discrepancies have also been observed in other similar analyses [9, 157] and are attributed to the Doppler broadening model or to sample inhomogeneities [161].

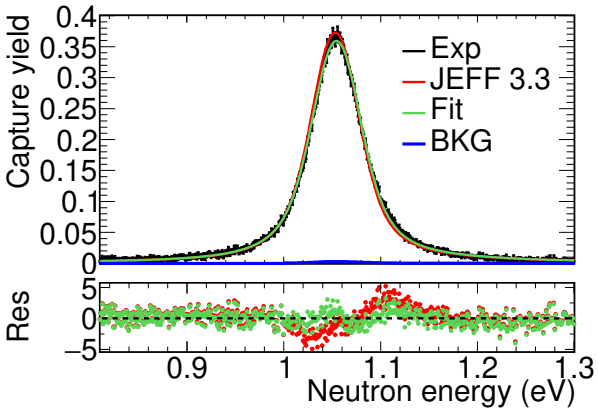

Figure 6.3: Experimental capture yield (Exp) in the energy range of the strongest ^{240}Pu compared with the yield obtained using the FGM with the JEFF-3.3 parameters (JEFF-3.3) and fitting the E_0 and Γ_γ parameters (Fit). The background (BKG) in the resonance is very small.

6.3 Resonance analysis of the experimental yields

The experimental yields have been fitted with SAMMY to obtain the resonance parameters of ^{244,246,248}Cm and ^{240}Pu following the methodology explained in Section 6.1. The analysis of each of the three measurements has been done independently. The energy of the resonances fitted for each sample in the measurement performed in each area are summarised in Table 6.4.

Sample	Area	Isotope	E_0 (eV)
^{244}Cm	EAR1	^{244}Cm	7.7, 16.8, 22.9, 35.0, 52.8, 86.0, 96.1
		^{240}Pu	20.4, 38.3, 41.7, 66.6, 72.8, 90.8
	EAR2	^{244}Cm	7.7, 16.8, 22.9, 35.0, 52.8, 86.0, 96.1, 132.8, 139.1 171.2, 181.6, 197.0, 209.8, 220.1, 230.5, 264.9, 274.1
		^{240}Pu	20.4, 38.3, 41.7, 66.6, 72.8, 90.8, 92.5,105.0, 121.6,135.4, 152.1, 162.6, 170.2, 185.9
^{246}Cm	EAR2	^{244}Cm	7.7, 16.8, 22.9, 86.0, 96.1, 132.8, 181.6, 197.0, 220.1
		^{246}Cm	4.3, 15.3, 84.4, 91.8, 158.4, 193.5,232.8, 250.7, 278.3, 288.2, 313.4, 316, 362, 381
		^{248}Cm	7.2, 26.9, 35.0, 76.1, 98.8
		^{240}Pu	20.4, 38.3, 41.7, 66.6, 72.8, 90.8, 92.5,105.0,121.6,135.4, 152.1

Table 6.4: Energy of the resonances fitted in the ^{244}Cm sample in EAR1 and in the ^{244}Cm and ^{246}Cm samples in EAR2.

The RP that describe the resonances are E_0, Γ_n, Γ_γ and Γ_f. At n_TOF thanks to the two long flight paths of 20 and 180 meters the energy of the resonances (E_0) can be measured with high precision. On the other hand, due to the Doppler broadening effect and the neutron resolution broadening the measurements are more sensitive to the capture resonance area than to the resonances' width. In addition, the small statistics obtained for most of the resonances makes it even more difficult to obtain precise information on the widths of the resonances. The area of the resonances (A_r) is proportional to $g\Gamma_n\Gamma_\gamma/\Gamma = R_K$ (Section 1.3.2). In most of the resonances of the analysis $\Gamma_\gamma \gg \Gamma_n, \Gamma_f$ and then $A_r \approx \Gamma_n$. It is expected that the values of Γ_γ for the different resonances of the same isotope fluctuate only a bit between them [25]. In addition, this parameter is mainly related to the width of the resonances, that are measured with considerable high uncertainty. For this reason, the Γ_γ parameter is fixed in the fits, and the Γ_n is fitted.

For the first resonance of ^{244}Cm measured in EAR1, the resolution broadening is very small, and there is enough statistics to obtain the value of Γ_γ (Section 6.4.1) with low uncertainty. Then the rest of the ^{244}Cm resonances are fitted with the radiative width obtained in this fit, 39.0 meV. For the rest of isotopes (^{246,248}Cm and ^{240}Pu) the Γ_γ are taken from JENDL-4.0 to perform the fits. The measurement is not sensible to Γ_f. In consequence, the values of Γ_f to perform the fits are taken from JENDL-4.0. The resonances are s-wave, since the p-wave resonances start to be relevant at higher neutron energies. The spin is 1/2 for all the resonances, since the ground states of ^{240}Pu and ^{244,246,248}Cm is 0+. To summarise, the Γ_γ and Γ_f are fixed in the analysis of the ^{244,246,248}Cm resonances whereas E_0 and Γ_n are fitted.

A total of 7 resonances of ^{244}Cm have been fitted in the capture yield analysis of the ^{244}Cm sample in EAR1, as illustrated in Figure 6.4. More detailed figures are exhibited in Appendix C.1. In previous measurements (Cote, Moore, Berreth and Belanova), a resonance at 67.99 eV has been observed, but the statistics and capture to background ratios in this measurement are not good enough to distinguish it (Figure C.3). Resonances above 100 eV are observed, but the uncertainties in the fitted RP due to counting statistics are too large to perform a resonance analysis. Also, 7 resonances of ^{240}Pu are fitted only up to 100 eV for the same reason as the ^{244}Cm resonances.

In the measurement at EAR2 with the ^{244}Cm sample, a total of 17 resonances of ^{244}Cm have been fitted. The fits are illustrated in Figure 6.5. According to Moore and other previous measurements, three tiny resonances are located at 67.99, 234.9 and 242.7 eV, but the statistics and capture to background ratios in this measurement are not good enough to distinguish them (Figures C.3 and C.6). Above 300 eV uncertainties due to counting statistics and background subtraction are too large, and the resonances have not been fitted. A total of 14 resonances of ^{240}Pu are fitted in the sample up to 200 eV. At higher energies, the uncertainties are too high to perform resonance analysis.

As presented in table 6.4, a total of 9, 14, 5 and 11 resonances of ^{244}Cm, ^{246}Cm, ^{248}Cm and ^{240}Pu have been fitted, respectively, in the yield of the ^{246}Cm sample. The fits are illustrated in Figure 6.6.

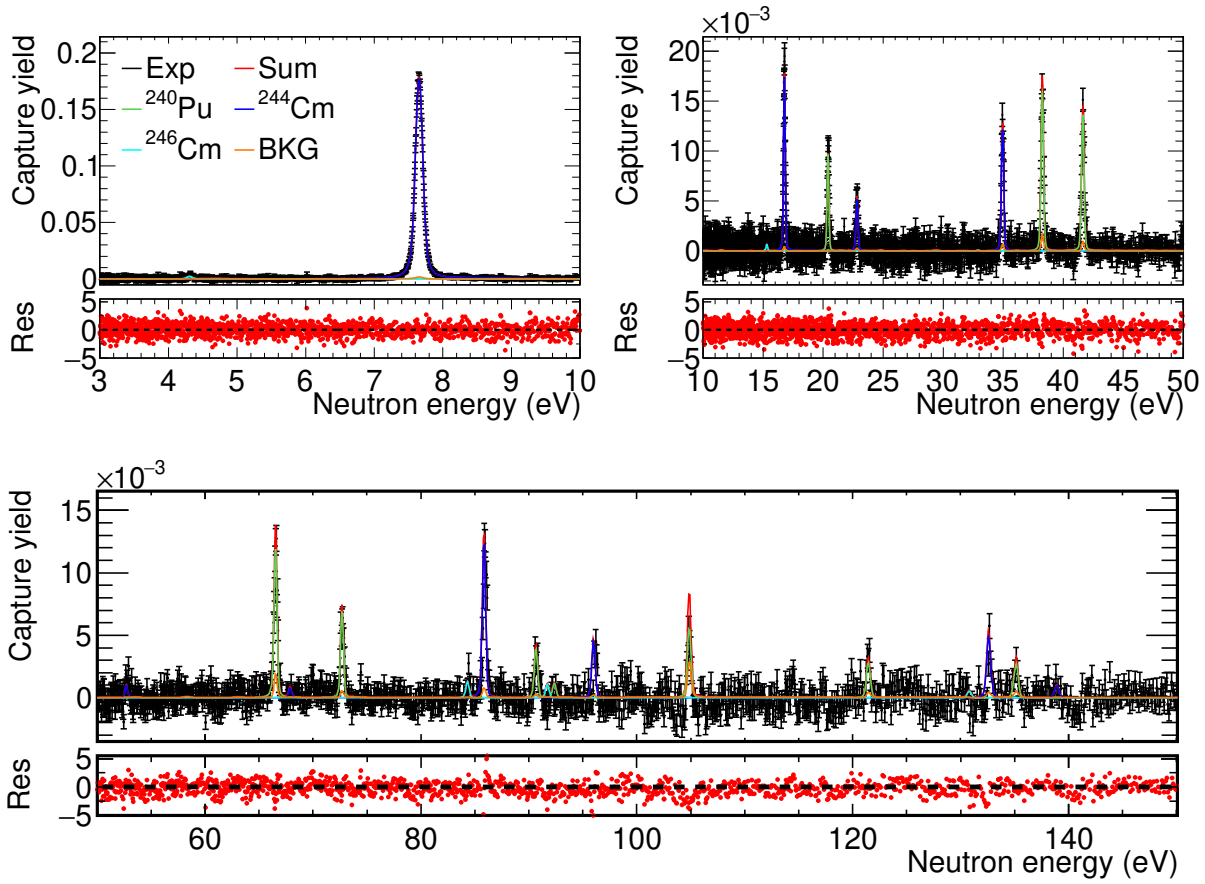

Figure 6.4: Experimental capture yield measured in EAR1 for the ^{244}Cm sample compared with the fitted yields obtained with SAMMY. The experimental capture yield (Exp) is in black including only the uncertainties due to counting statistics. The green, blue and cyan lines correspond to the SAMMY capture yield for each isotope. The orange line (BKG) corresponds to the background due to fission and elastic scattering events in the actinides. The red line (Sum) corresponds to the sum of all the capture yields plus the mentioned background.

The RP of ^{244}Cm are fitted until 230 eV in the ^{246}Cm sample, since at higher energies the uncertainties due to counting statistics and background subtraction are too large. In addition, the ^{244}Cm resonance at 35.0 eV has not been fitted because there is a resonance of ^{248}Cm at the same energy. The values of the ^{244}Cm RP which have not been fitted have been taken from the values obtained in the analysis of the ^{244}Cm sample measurement in EAR2.

A total of 14 resonances of ^{246}Cm are fitted in the analysis of the ^{246}Cm sample. More detailed figures concerning the fits performed to the ^{246}Cm resonances are illustrated in Appendix C.2. The resonance at 306.8 eV presented in panel (d) of Figure C.9 has never been observed in any previous measurement. This resonance can not be assigned to ^{244}Cm because it is not observed in the measurement performed with the ^{244}Cm sample, which has a higher content in ^{244}Cm. On the other hand, the resonance can be assigned to ^{246}Cm or ^{248}Cm. The decision has been made by considering the results of previous

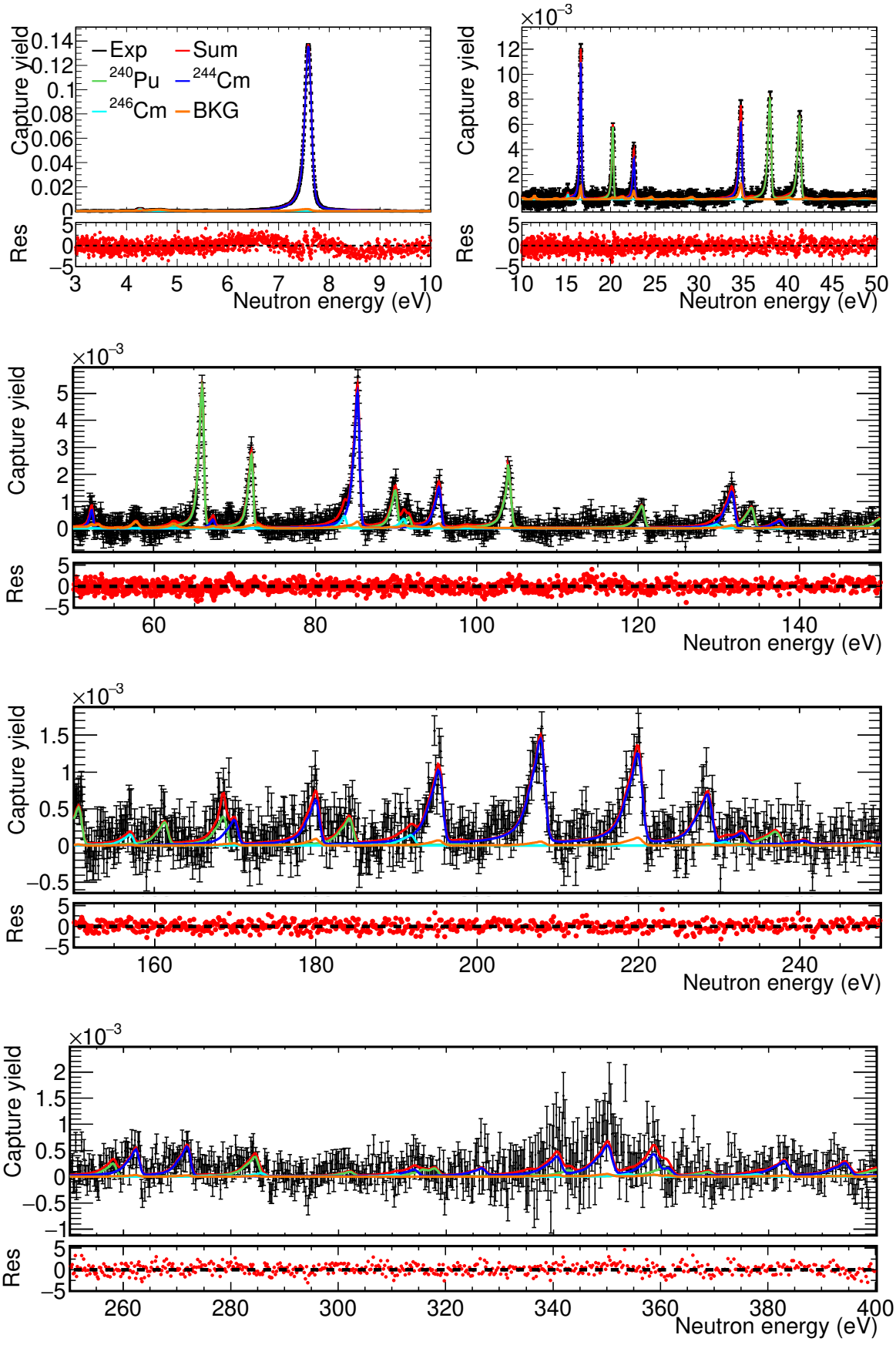

Figure 6.5: Same as Figure 6.4 but with the ^{244}Cm sample in EAR2

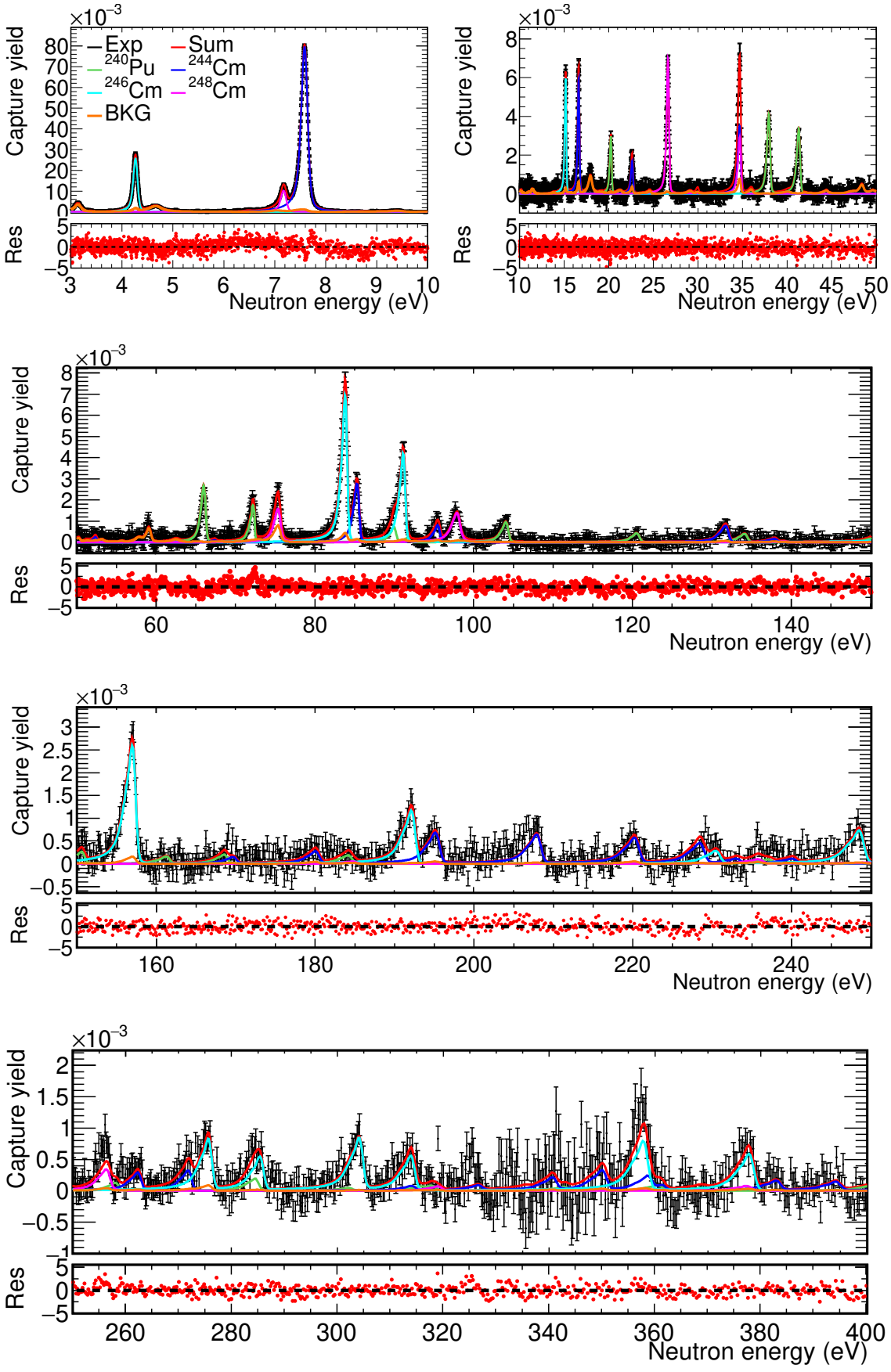

Figure 6.6: Same as Figure 6.4 but with the ^{246}Cm sample in EAR2

measurements of these two isotopes. In this energy region, the only previous capture or transmission measurement of ^{246}Cm has been done by Moore with a capture sample with five times more ^{244}Cm than ^{246}Cm. The process of finding new resonances of ^{246}Cm is based on the fission measurement performed with a high purity sample, so it can not be discarded that some small ^{246}Cm resonances were not founded, in particular resonances with small fission cross section. In the case of ^{248}Cm, there is only one measurement at this energy region, the transmission experiment done by Benjamin [7] with a high purity sample. This experiment was very sensitive to resonances of ^{248}Cm. For these reasons, the resonance has been assigned to ^{246}Cm. This resonance has also been observed and assign to ^{246}Cm in the posterior Kawase measurement. The resonance of ^{246}Cm at 360.8 eV was considered as a doublet in the previous measurement of Moore. As observed in Figure C.9, the resonance is not correctly fitted with a radiative width of 34.7 meV (green line), whereas it is precisely fitted with a radiative width of 62 meV (cyan line). The value of 62 meV for the radiative width is too large, so the resonance is also considered as a doublet in this analysis.

The JENDL-4.0 evaluation of ^{246}Cm takes the RP from the Maslov *et al.* evaluation [59]. In it, three weak resonances at 32.95, 47 and 131 eV were added without being observed in any capture, fission, or transmission measurement. These three resonances have not been observed in this measurement neither (Figure C.10).

A total of 5 resonances of ^{248}Cm are fitted in the analysis of the ^{246}Cm sample. More detailed figures concerning the fits performed to the ^{248}Cm resonances are illustrated in Appendix C.3. The transmission measurement performed by Benjamin *et al.* [7] with a ^{248}Cm sample of 13 mg was sensible to many resonances in the energy range from 100 to 300 eV. Due to the capture background size, the resonances at 140.3 eV, 186.4, 237.9, 321.8 and 380.6 eV are not observed at the n_TOF experiment. The resonance at 258.7 eV (panel (f) of Figure C.11) is observed, but the uncertainties due to counting statistics and background subtraction are too large to fit the resonance.

In addition to the Cm resonances, the RP of 11 ^{240}Pu resonances are obtained in the ^{246}Cm sample analysis. The resonances fitted were between 20 to 150 eV because, at higher energies, the uncertainties of the fits are too large to perform resonance fits.

6.4 ^{244}Cm resonance parameters

The resonance parameters of ^{244}Cm have been obtained in the three measurements performed (one in EAR1 and two in EAR2). The fits have been done with a fixed radiative width (Section 6.4.1), so the parameters fitted in each resonance are E_0 and Γ_n (Sections 6.4.2 and 6.4.3). The results obtained in the three fits have been combined to obtain the final results at n_TOF (6.4.4), and in Section 6.4.5 these results are compared with previous measurements and evaluations.

6.4.1 Calculation of the radiative width (Γ_γ)

The radiative width has been obtained from the measurement of the first resonance at 7.66 eV in EAR1, with a 4% uncertainty. The two subsequent resonances are located at 16.77 and 22.85 eV, and the uncertainties in the radiative widths are 20% and 33%, respectively, mainly due to the uncertainties due to counting statistics. The large uncertainty in the RF at EAR2 has made it impossible to obtain the radiative widths with uncertainties lower than 20%. For these reasons, the radiative width of ^{244}Cm obtained with the fit to the first resonance in the measurement at EAR1 has been used to perform the fit of the rest of the ^{244}Cm resonances in this work. The value of the Γ_γ obtained with the fit to the first resonance in Figure 6.7 is 39.0 ± 1.5 meV.

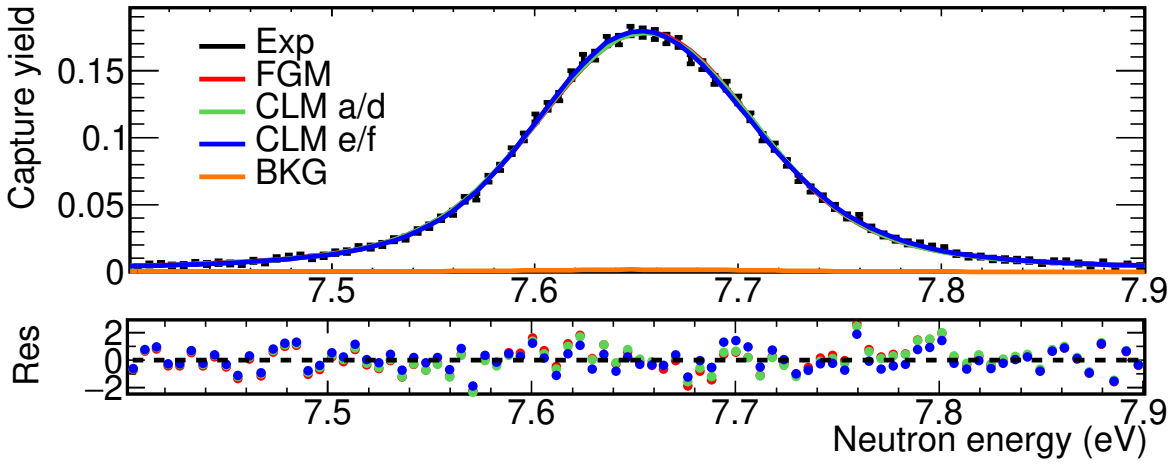

Figure 6.7: SAMMY fits and residuals for the first ^{244}Cm resonance in EAR1, using the Free Gas (FGM) and the Crystal Lattice (CLM) models for the treatment of the Doppler broadening.

The main source of uncertainty in the calculation is the one related to the treatment of the Doppler effect, which has been estimated by performing fits with different models: the FGM and the CLM with two different phonon spectra, named here as a/d and e/f. In Table 6.5, the values of the RP obtained with the different models are given.

	E_0 (eV)	Γ_γ (meV)	Γ_n (meV)	R_k (meV)
FGM	7.664	39.0	9.19	7.42
CLM a/d	7.664	37.7	9.34	7.47
CLM e/f	7.665	37.4	9.27	7.41

Table 6.5: Resonance parameters obtained for the first ^{244}Cm resonance measured in EAR1 using the Free Gas (FGM) and the Crystal Lattice (CLM) models for the treatment of the Doppler broadening.

The uncertainty determined from the dispersion of these values is 1.3 meV (4%). Similar values were found in previous works [9, 157]. The rest of the uncertainties are calculated according to the description given in Section 6.1, and they are presented in Table 6.6.

Value (meV)	Uncertainties						
	Sta	Fis	Dummy	Elas	Temp	Doppler	Sum
39.0	0.6	0.1	0.1	0.1	0.1	1.3	1.5

Table 6.6: Partial and total (Sum) uncertainties of the radiative width obtained in the fit of the first resonance of ^{244}Cm in EAR1. The description of the different names: Sta, Fis, Dummy, Elas, Temp and Doppler are given in Section 6.1.

There are only four previous measurements of the radiative width of ^{244}Cm, and they are presented in Table 6.7. The result obtained in this work is compatible with all the previous measurements, except with the most recent value of Kawase.

JENDL-4.0	Coté [29]	Berreth [8]	Kimura [32]	Kawase [33]	This work
37.00	37.5 ± 2.1	35 ± 2	38.1 ± 2.9	36.1 ± 0.5	39.0 ± 1.5

Table 6.7: Different values of the radiative width (meV) of ^{244}Cm obtained in the previous transmission and capture measurements.

6.4.2 Measurement in EAR1 with the ^{244}Cm sample

The RP of a total of 7 resonances have been obtained from the yield of EAR1 between 7 and 100 eV. The results are presented in Table 6.8. For each resonance, the values of E_0 and Γ_n are fitted with the rest of the parameters fixed. The Γ_γ is fixed to 39.0 meV and the Γ_f to the JENDL-4.0 values.

The uncertainties of the different resonances measured can be correlated. In this work, the uncertainties are considered or totally uncorrelated or totally uncorrelated between the resonances, for simplicity. The uncertainties considered as totally uncorrelated are the uncertainty due to counting statistics and the uncertainty due to the subtraction of the elastic scattering background. The rest of the uncertainties (Fis, Dummy, Temp, Norm, Mass and ^{240}Pu) are considered as totally correlated. The values of the uncertainty associated with the temperature (Temp) are always below 0.1% for the Γ_n parameters. For this reason, they are not given in any of the resonances of this work. The most significant uncertainties for the first two resonances are the mass (2.8%) and the uncertainty in the nuclear data of ^{240}Pu (2.75%) (Figure 6.8). For the rest of the resonances, the main uncertainty is the one due to counting statistics.

E_0 (eV)	
Value	Uncertainty (Sta)
7.664	0.001
16.793	0.002
22.849	0.007
34.999	0.005
52.886	0.038
86.073	0.009
96.318	0.031

Γ_n (meV)											
E_0 (eV)	Value	Uncertainty									
		Sta (UU)	Fis (CU)	Dummy (CU)	Elas (UU)	Nor (CU)	Mass (CU)	^{240}Pu (CU)	Sum (CU)	Sum (UU)	Sum Total
7.7	9.19	0.04	0.02	-	0.03	0.16	0.26	0.25	0.39	0.06	0.40
16.8	2.02	0.05	0.01	-	-	0.03	0.06	0.06	0.09	0.05	0.10
22.8	0.94	0.06	0.01	-	-	0.02	0.03	0.03	0.04	0.06	0.07
35.0	4.40	0.17	0.07	0.03	0.01	0.07	0.12	0.12	0.20	0.17	0.26
52.9	0.77	0.16	0.01	0.03	-	0.01	0.02	0.02	0.04	0.16	0.17
86.1	22.70	1.54	0.13	0.40	0.41	0.39	0.64	0.62	1.06	1.60	1.92
96.3	5.15	0.78	0.05	0.26	0.03	0.09	0.14	0.14	0.35	0.78	0.85

Table 6.8: Resonance parameters of ^{244}Cm obtained in EAR1 with the ^{244}Cm sample. Uncertainties lower than 0.01 are not reported. The different uncertainties are correlated (UC) or uncorrelated (UU) between the resonances.

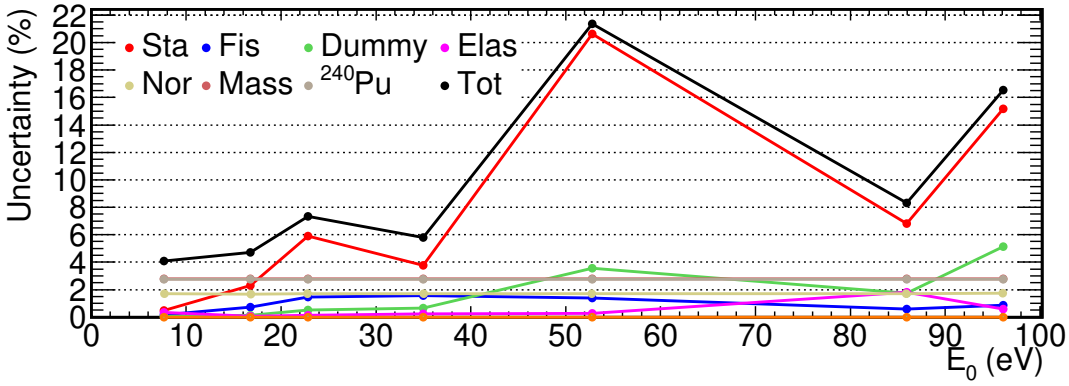

Figure 6.8: Uncertainties of the Γ_n parameters of ^{244}Cm measured in EAR1. The graphs have been obtained from the data of Table 6.8.

6.4.3 Measurement in EAR2 with the ^{244}Cm and ^{246}Cm samples

A total of 17 and 9 resonances of ^{244}Cm are fitted, respectively, in the yields of the ^{244}Cm and the ^{246}Cm samples in EAR2. In Tables 6.9 and 6.10 the fitted RP are presented with their uncertainties, and the same values are plotted in Figure 6.9.

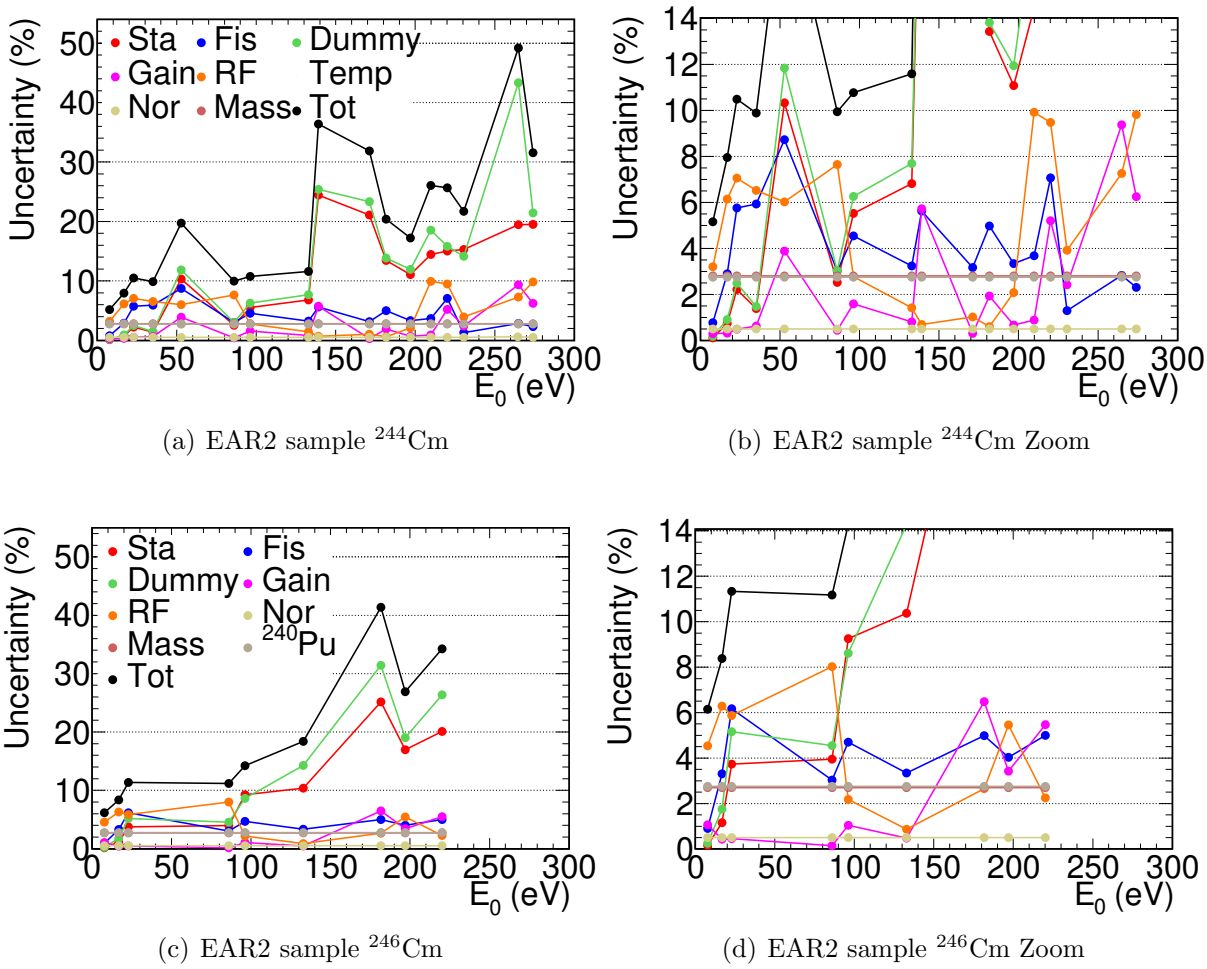

(a) EAR2 sample ^{244}Cm

(b) EAR2 sample ^{244}Cm Zoom

(c) EAR2 sample ^{246}Cm

(d) EAR2 sample ^{246}Cm Zoom

Figure 6.9: Uncertainties of the Γ_n parameters of ^{244}Cm measured in EAR2 with the ^{244}Cm (top) and the ^{246}Cm (bottom) samples. The graphs have been obtained from the data of Tables 6.9 and 6.10.

The uncertainties considered as totally uncorrelated between the resonances for all the isotopes measured in EAR2 are: the uncertainty due to counting statistics (Sta), the uncertainty associated with the RF (RF) and the uncertainty of the gain shifts (Gain). The rest of the uncertainties (Fis, Dummy, Temp, Nor, ^{240}Pu and Mass) are considered as totally correlated. The largest source of uncertainty at low energies is the RF, whereas at energies higher than 100 eV are the dummy subtraction and the uncertainty due to counting statistics.

E_0 (eV)			
Value	Uncertainty		
	Sta	RF	Sum
7.664	0.001	0.003	0.003
16.792	0.001	0.002	0.002
22.835	0.004	0.002	0.004
35.002	0.003	0.001	0.003
52.81	0.03	0.01	0.03
86.06	0.01	0.01	0.01
96.25	0.02	0.01	0.03
132.89	0.04	0.02	0.04
138.88	0.15	0.04	0.16
171.43	0.15	0.18	0.24
181.62	0.10	0.03	0.10
197.01	0.06	0.05	0.08
209.76	0.05	0.08	0.10
221.92	0.06	0.11	0.12
230.62	0.11	0.11	0.16
264.61	0.16	0.20	0.26
274.23	0.14	0.22	0.26

Γ_n (meV)												
E_0 (eV)	Value	Uncertainty										
		Sta (UU)	Fis (CU)	Dummy (CU)	Gain (UU)	RF (UU)	Nor (CU)	Mass (CU)	^{240}Pu (CU)	Sum (CU)	Sum (UU)	Sum Total
7.67	8.85	0.01	0.07	0.02	0.03	0.28	0.09	0.25	0.24	0.37	0.28	0.46
16.77	1.92	0.01	0.06	0.02	0.01	0.12	0.02	0.05	0.05	0.10	0.12	0.15
22.85	0.96	0.02	0.06	0.02	-	0.07	0.01	0.03	0.03	0.07	0.07	0.10
34.99	4.13	0.06	0.24	0.06	0.03	0.27	0.04	0.12	0.11	0.30	0.28	0.41
52.78	0.85	0.09	0.07	0.10	0.03	0.05	0.01	0.02	0.02	0.13	0.11	0.17
85.96	26.2	0.7	0.8	0.8	0.1	2.0	0.3	0.7	0.7	1.5	2.1	2.6
96.12	7.0	0.4	0.3	0.4	0.1	0.2	0.1	0.2	0.2	0.6	0.4	0.8
132.80	13.6	0.9	0.4	1.0	0.1	0.2	0.1	0.4	0.4	1.3	1.0	1.6
139.10	2.5	0.6	0.1	0.6	0.1	-	-	0.1	0.1	0.7	0.6	0.9
171.20	4.6	1.0	0.1	1.1	0.1	-	-	0.1	0.1	1.1	1.0	1.5
181.60	10.8	1.5	0.5	1.5	0.2	0.1	0.1	0.3	0.3	1.7	1.5	2.2
197.00	27.3	3.0	0.9	3.3	0.2	0.6	0.3	0.8	0.7	3.6	3.1	4.7
209.80	79.3	11.5	2.9	14.7	0.7	7.9	-	2.2	2.2	15.3	13.9	20.7
220.10	70.2	10.6	5.0	11.1	3.7	6.7	-	2.0	1.9	12.5	13.0	18.0
230.50	22.0	3.4	0.3	3.1	0.5	0.9	0.2	0.6	0.6	3.2	3.5	4.8
264.90	20.9	4.1	0.6	9.1	2.0	1.5	0.2	0.6	0.6	9.1	4.8	10.3
274.10	29.7	5.8	0.7	6.4	1.9	2.9	0.3	0.8	0.8	6.5	6.7	9.4

Table 6.9: Resonance parameters of ^{244}Cm obtained in EAR2 with the ^{244}Cm sample. Uncertainties lower than 0.01 are not reported. The different uncertainties are correlated (UC) or uncorrelated (UU) between the resonances.

E_0 (eV)			
Value	Uncertainty		
	Sta	RF	Sum
7.663	0.001	0.003	0.003
16.788	0.002	0.002	0.002
22.836	0.006	0.003	0.007
86.09	0.01	0.00	0.01
96.33	0.04	0.01	0.04
132.92	0.06	0.03	0.06
181.69	0.20	0.03	0.21
196.92	0.09	0.06	0.11
222.24	0.12	0.06	0.14

Γ_n (meV)												
E_0 (eV)	Value	Uncertainty										
		Sta (UU)	Fis (CU)	Dummy (CU)	Gain (UU)	RF (UU)	Nor (CU)	Mass (CU)	^{240}Pu (CU)	Sum (CU)	Sum (UU)	Sum Total
7.67	8.68	0.01	0.08	0.02	0.09	0.39	0.09	0.23	0.24	0.36	0.41	0.54
16.77	1.81	0.02	0.06	0.03	0.01	0.11	0.02	0.05	0.05	0.10	0.12	0.15
22.85	0.87	0.03	0.05	0.05	-	0.05	0.01	0.02	0.02	0.08	0.06	0.10
85.96	24.5	1.0	0.7	1.1	0.1	2.0	0.1	0.6	0.7	1.6	2.2	2.7
96.12	6.4	0.6	0.3	0.5	0.1	0.1	-	0.2	0.2	0.7	0.6	0.9
132.80	13.8	1.4	0.5	2.0	0.1	0.1	0.1	0.4	0.4	2.1	1.4	2.5
181.60	7.6	1.9	0.4	2.4	0.5	0.2	0.0	0.2	0.2	2.4	2.0	3.2
197.00	35.1	6.0	1.4	6.7	1.2	1.9	0.2	1.0	1.0	7.0	6.4	9.4
220.10	36.5	7.3	1.8	9.6	2.0	0.8	0.2	1.0	1.0	9.9	7.6	12.5

Table 6.10: Resonance parameters of ^{244}Cm obtained in EAR2 with the ^{246}Cm sample. Uncertainties lower than 0.01 are not reported. The different uncertainties are correlated (UC) or uncorrelated (UU) between the resonances.

6.4.4 Comparison of the three ^{244}Cm measurements and the final results

This section aims to combine the information of three measurements to obtain the final values of the ^{244}Cm RP at n_TOF and their uncertainties. There are uncertainties correlated between the measurements performed in EAR2 with two different samples, for example, the uncertainty in the resolution broadening (RF). There are also correlations between the measurements performed in the two different areas with the same ^{244}Cm sample, for example, the uncertainty in the abundance of ^{244}Cm in the sample (Mass). There are also correlations between the uncertainties of the resonance parameters of the different resonances of the same measurement, for example, the uncertainty in the normalisation (Nor).

The complexity of the problem and the considerable number of resonances and uncertainties made it very difficult and inefficient to apply a direct analytical solution without any approximation. The difficulties and paradoxes found in these methods have to be also considered, for example, the "Peelle's Pertinent Puzzle" [162, 163]. To simplify the calculations, the process of obtaining the final values of the resonances used in this section is based on approximating the uncertainties as completely correlated or uncorrelated. The weighted mean is calculated, making this approximation to obtain the final value of the energies of the resonances (E_0) and the Γ_n. The weighted mean ($\hat{\mu}$) and the total uncertainty ($\sigma(\hat{\mu})$) for a set of parameters x_i with uncertainties totally uncorrelated ($\sigma_{unco,i}$) between the measurements and with a uncertainty totally correlated (σ_{corr}) are:

$$\hat{\mu} = \frac{\sum_i x_i/\sigma^2_{unco,i}}{\sum_i 1/\sigma^2_{unco,i}} \tag{6.2}$$

$$\sigma(\hat{\mu}) = \sqrt{\sigma^2_{corr} + 1/\sum_i 1/\sigma^2_{unco,i}}$$

The final value of the energies of the resonances (E_0) has been obtained in two steps. In the first step, the energy of the resonances obtained in the measurements performed in EAR2 with the ^{244}Cm and ^{246}Cm samples are combined, calculating the weighted mean of the two values. In order to calculate the weighted means with Equation 6.2, the uncertainties due to counting statistics have been considered as totally uncorrelated and the RF uncertainties as totally correlated. In the second step, the weighted mean of the values obtained in the first step and the values obtained in the measurement at EAR1 are combined. The weights used in the mean calculations are taken from the total uncertainties of each value considering them, as totally uncorrelated.

The final E_0 values are presented in Table 6.11, and in Figure 6.10 the comparison of the final values and the values of the three measurements are presented. The values of E_0 obtained in the three measurements are compatible between them, and also with the final values, and the differences are less than 0.1%.

E_0 (eV)		Γ_n (meV)			
Value	Uncer. Total	Value	Uncertainty		
			Total	(UU)	(CU)
7.6645	0.0003	9.06	0.32	0.05	0.32
16.792	0.002	1.983	0.083	0.043	0.071
22.839	0.003	0.929	0.058	0.046	0.036
35.001	0.003	4.30	0.22	0.15	0.17
52.84	0.03	0.80	0.12	0.11	0.05
86.07	0.01	23.5	1.6	1.2	1.0
96.29	0.02	6.10	0.56	0.42	0.36
132.90	0.04	13.6	1.5	0.8	1.2
138.88	0.18	2.48	0.91	0.63	0.66
171.43	0.25	4.5	1.5	1.0	1.1
181.64	0.10	9.6	2.0	1.2	1.6
196.98	0.10	28.7	4.5	2.8	3.5
209.76	0.10	78	21	14	15
221.99	0.12	47	15	9	12
230.62	0.16	21.8	4.8	3.5	3.2
264.61	0.27	21	10	5	9
274.22	0.27	29	9	7	6

Table 6.11: Final resonance parameters values of ^{244}Cm obtained from the combination of the three measurements at n_TOF. The total uncertainties are divided in the correlated (UC) and uncorrelated (UU) components.

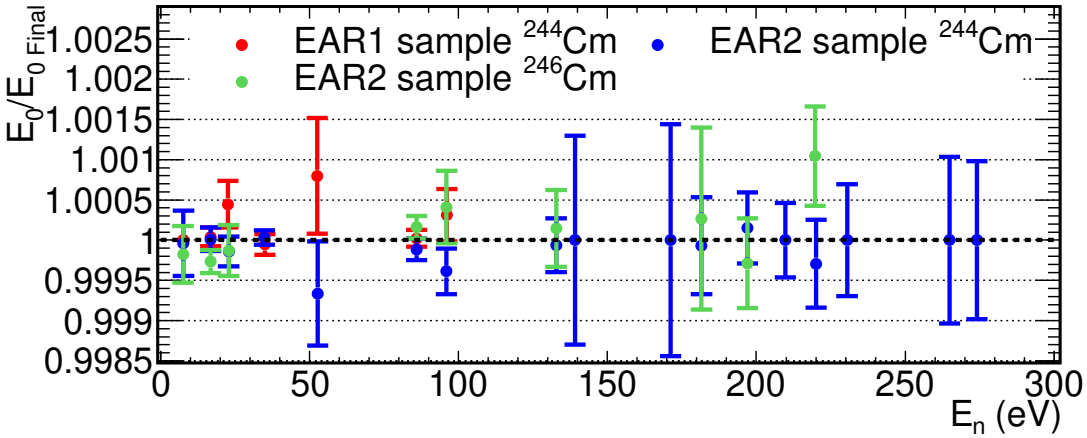

Figure 6.10: E_0 values obtained in the three measurements of ^{244}Cm (Table 6.8, 6.9 and 6.10) with their uncertainties divided by the final E_0 value (Table 6.11) presented in this section.

The calculation of the final Γ_n values is more complex than the calculation of the E_0, due to the considerable amount of uncertainties and the different correlations between

them. The calculation is done in three steps, and always under the assumption that the uncertainties are totally correlated or totally uncorrelated between the measurements:

i) The uncertainty related to the mass of ^{244}Cm (Mass) is reduced by comparing the two measurements in EAR2. The uncertainty in the mass of ^{244}Cm in the ^{244}Cm sample is 2.8%, whereas the uncertainty in the ^{246}Cm sample is 2.6%. These uncertainties are totally uncorrelated, since they come from counting statistics in the measurement process [32]. The weighted mean of the Γ_n parameter is calculated for the strong first resonance considering as totally uncorrelated the mass uncertainty. The rest of the uncertainties are totally correlated or are small enough to be neglected. The Γ_n parameters obtained for the first resonance are 8.85 and 8.68 meV for the ^{244}Cm and the ^{246}Cm samples, respectively (Tables 6.9 and 6.10). The weighted average obtained value has been 8.76 meV reducing the mass uncertainty to 1.9%. The new value obtained is 1% lower than the value obtained for the ^{244}Cm sample and 1% higher than the ^{246}Cm sample value. The mass uncertainties are directly correlated to all of the resonances measured with these samples, so the Γ_n values obtained with the ^{244}Cm samples have been decreased 1% and the ^{246}Cm have been increased 1%.

ii) After scaling the Γ_n parameters with the values obtained in the previous step. The weighted mean of the parameters obtained in the two measurements of ^{244}Cm in EAR2 with the ^{244}Cm sample and the ^{246}Cm sample have been calculated with Equation 6.2. The uncertainties considered as totally uncorrelated are the uncertainties due to counting statistics and the gain uncertainty. As an approximation, the rest of the uncertainties are considered as totally correlated between the two measurements.

iii) The weighted mean of the Γ_n parameters of step ii) and the values obtained in EAR1 are combined. The Γ_n parameters obtained in the EAR1 with the ^{244}Cm sample have been decreased 1% due to the mass correction calculated in step i). The weighted mean have been calculated between the two sets of data with Equation 6.2 and considering all the uncertainties as totally uncorrelated except the uncertainties related to the mass (1.9%) and the one related to the ^{240}Pu nuclear data (2.75%). Performing this calculation, the final Γ_n values and their uncertainties are calculated. It is interesting to divide the uncertainties in the Γ_n values between the component that are correlated (CU) between all the resonances and the uncorrelated (UU) component as have been done for the the previous Γ_n parameters (Tables 6.8, 6.9 and 6.10). These divisions are made taking the ratio CU/UU from the EAR1 measurement for the resonances measured in this area and from the EAR2 measurement with the ^{244}Cm sample for the rest of the resonances.

Following these three steps the final values of Γ_n are obtained and presented in Table 6.11. These final values of Γ_n and the values of the three measurements are compatible, as presented in Figure 6.11.

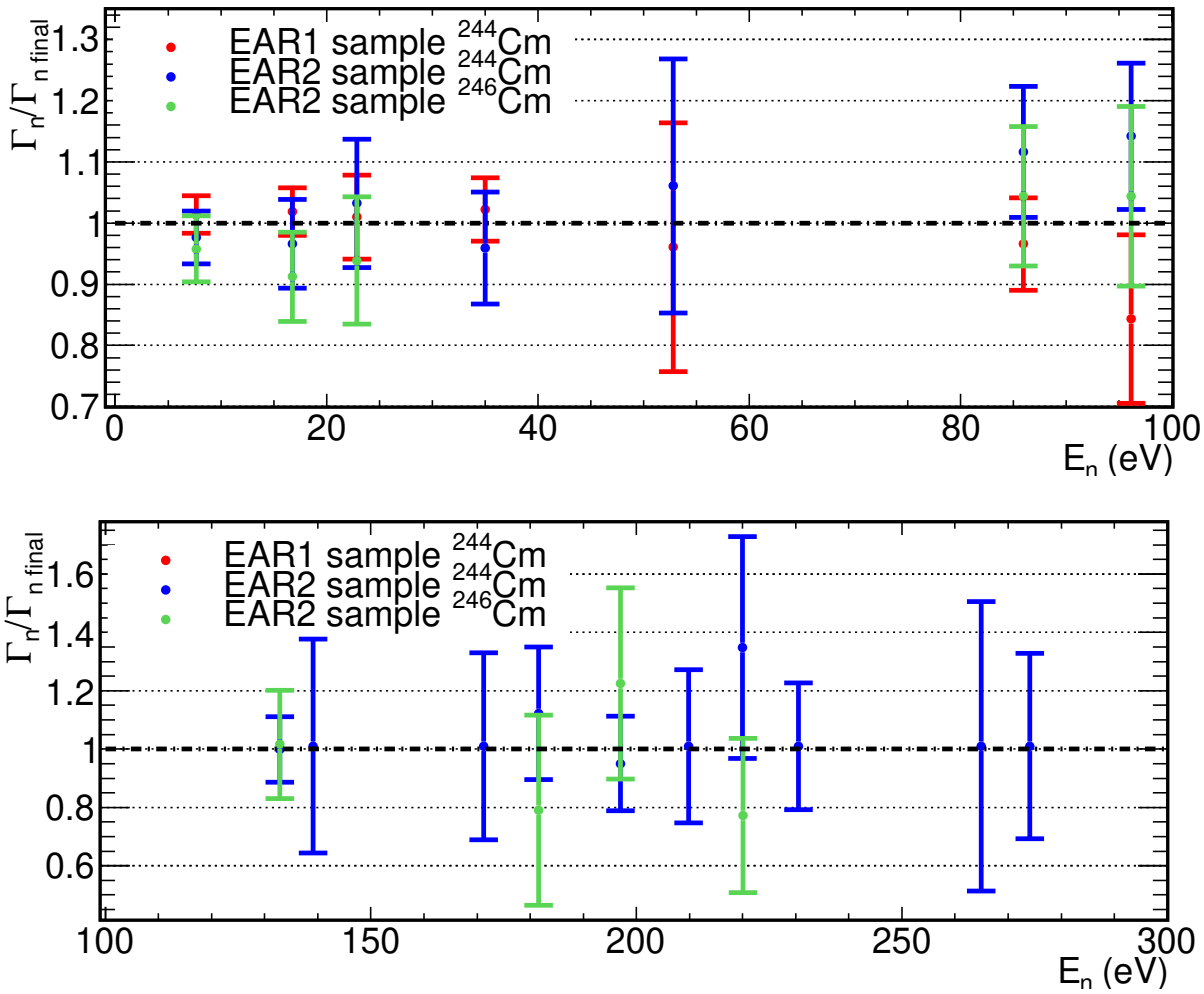

Figure 6.11: Γ_n values obtained in the three measurements of ^{244}Cm (Tables 6.8, 6.9 and 6.10) compare with the final value combining these measurements (Table 6.11). The uncertainties in the values consider all the sources of uncertainties except the uncertainty of the nuclear data of ^{240}Pu (2.75%), that is totally correlated in all the measurements.

6.4.5 Comparison with previous measurements

In this section, the final ^{244}Cm RP obtained at n_TOF are compared with the previous transmission and captures measurements. The energy of the resonances deviates less than 0.2% from the evaluated data of JENDL-4.0, as presented in Figure 6.12, except for the resonance located at 222.0 eV, where the difference is below 1%.

The radiative kernel (R_K) of the resonances are compared with previous measurements and evaluations in Figure 6.13 and Table 6.12. The n_TOF measurement is the first capture measurement performed in the extended range from 7 to 280 eV. The other two previous capture measurements were done between 7 to 22 eV (Kimura) and 22 to 1000 eV (Moore). After the n_TOF measurement, the Kawase experiment was done between 7 to 430 eV. There are three previous transmission measurements, but the three fit fewer resonances than this measurement.

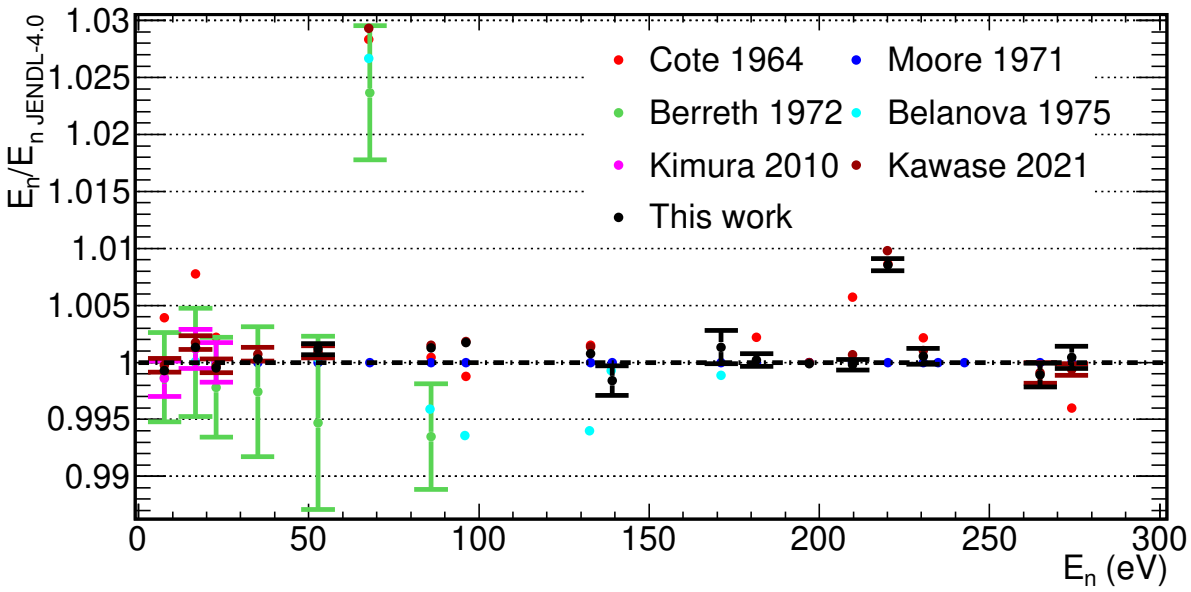

Figure 6.12: Ratio between the ^{244}Cm E_0 values obtained in different experiments, including this work, and JENDL-4.0.

The R_K values obtained at n_TOF are compatible with the JENDL-4.0 values for most of the resonances. The exceptions are the resonances at 52.78 and 209.8 eV, whose R_K are 40% and 30% larger than the JENDL-4.0 evaluation. The R_K values obtained in this work are compatible with the values obtained by Moore *et al.* in 1971. The R_K values obtained in the new Kawase measurement at energies higher than 50 eV are below the Moore and the n_TOF values for the majority of the resonances.

Finally, the uncertainties in the R_K obtained are compared with the ones in previous measurements in Figure 6.14. The uncertainties obtained at n_TOF are similar to the smallest ones previously reported for energies below 135 eV. At higher energies, the measurements of Cote and Kawase have lower uncertainties.

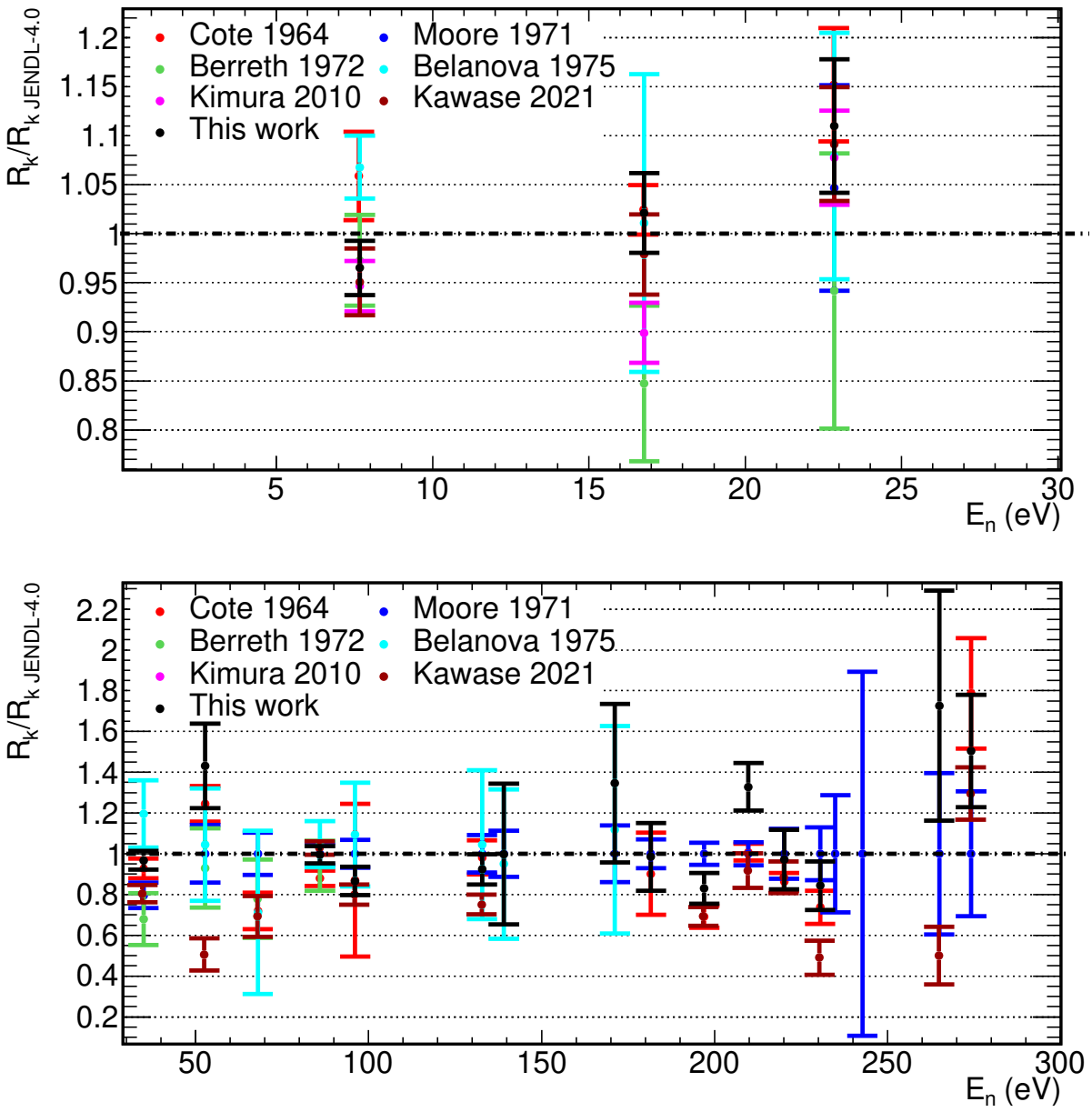

Figure 6.13: Ratio between the ^{244}Cm R_K values obtained in different experiments, including this work, and JENDL-4.0.

E_0 (eV)	Cote	Moore	Berreth	Belanova	Kimura	Kawase	This work	JENDL-4
7.67	8.05±0.34		7.40±0.35	8.12±0.24	7.20±0.19	7.25±0.26	7.33±0.21	7.60
16.77	1.83±0.05		1.51±0.15	1.81±0.27	1.61±0.05	1.81±0.07	1.83±0.07	1.79
22.85	0.88±0.04	0.80±0.08	0.71±0.11	0.82±0.10	0.82±0.04	0.89±0.05	0.84±0.05	0.76
34.99	3.48±0.18	2.98±0.24	2.55±0.47	4.48±0.62	-	3.31±0.15	3.63±0.17	3.75
52.78	0.66±0.05	0.53±0.07	0.49±0.10	0.55±0.15	-	0.28±0.04	0.75±0.11	0.53
67.99	0.44±0.05	0.61±0.06	0.47±0.11	0.43±0.24	-	0.45±0.07	-	0.61
85.96	12.84±0.54	14.59±0.83	13.72±1.80	15.27±1.66	-	15.12±0.48	14.51±0.61	14.59
96.12	5.13±2.21	5.89±0.41	-	6.44±1.50	-	4.85±0.30	5.10±0.41	5.89
132.8	10.49±0.90	10.69±0.98	-	11.17±3.90	-	8.20±0.53	9.87±0.80	10.69
139.1	-	2.19±0.25	-	2.08±0.80	-	-	2.18±0.76	2.19
171.2	-	2.94±0.41	-	3.28±1.49	-	-	3.95±1.14	2.94
181.6	6.80±1.51	7.54±0.54	-	-	-	-	7.42±1.25	7.54
197.0	13.57±1.05	19.64±1.07	-	-	-	13.76±0.91	16.29±1.48	19.64
209.8	19.69±0.82	19.54±1.10	-	-	-	17.99±1.66	25.95±2.29	19.54
220.1	18.68±0.95	21.66±2.66	-	-	-	19.45±1.69	21.05±3.15	21.66
230.5	12.16±1.34	16.47±2.13	-	-	-	8.12±1.39	13.89±1.96	16.47
234.9	-	3.37±0.97	-	-	-	-	-	3.37
242.7	-	1.19±1.06	-	-	-	-	-	1.19
264.9	-	7.72±3.06	-	-	-	3.85±1.09	13.33±4.36	7.72
274.1	19.74±3.00	11.04±3.39	-	-	-	14.26±1.42	16.60±3.04	11.04

Table 6.12: R_K (meV) values obtained in this work and in previous measurements and evaluations for the ^{244}Cm resonances below 300 eV.

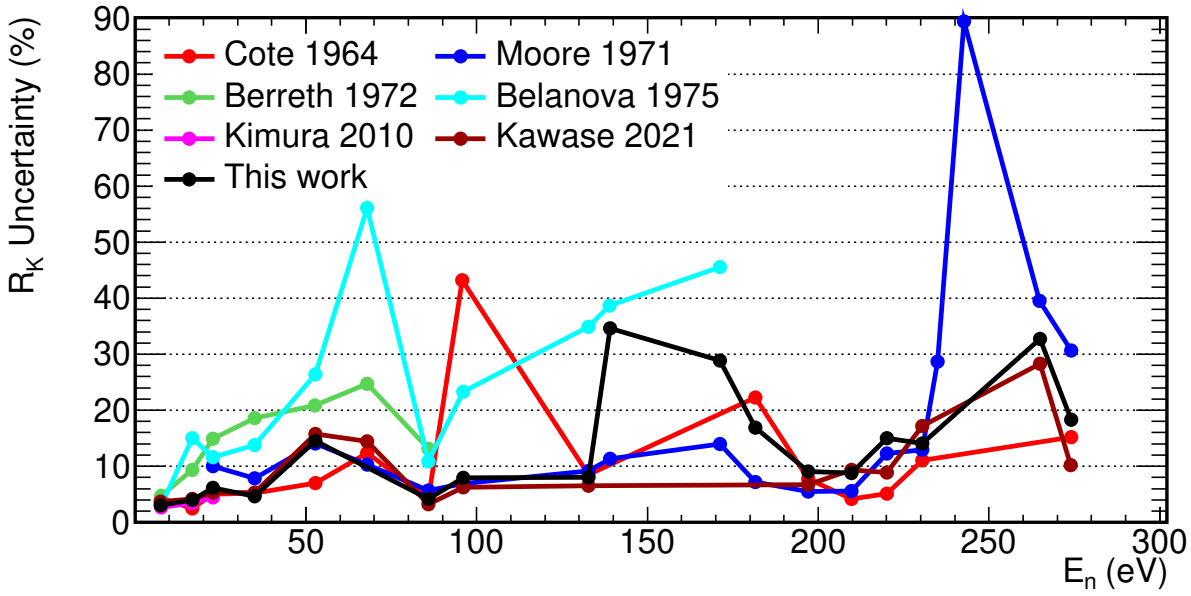

Figure 6.14: Comparison between the uncertainties in the R_K values measured in this work and the data of previous measurements for the resonances of ^{244}Cm below 300 eV.

6.5 ^{246}Cm resonance parameters

The resonance parameters of ^{246}Cm have been obtained in the measurement performed in EAR2 with the ^{246}Cm sample. Section 6.5.1 presents the calculation of the Γ_γ parameter, and Section 6.5.2 the calculation of E_0, Γ_n and R_K, and also the comparison with previous results.

6.5.1 Calculation of the radiative width (Γ_γ)

The uncertainties obtained in Γ_γ at EAR2, mainly due to RF, are pretty significant. In the case of the strongest resonance of ^{246}Cm, at 4.3 eV, the uncertainty in the Γ_γ is ~20%, and the value obtained for this resonance for the radiative width is compatible with JENDL-4.0. For this reason, the resonance analysis has been performed by taking the Γ_γ values from JENDL-4.0 and adjusting only Γ_n and E_0.

The main uncertainty is the one due to the RF, in order to estimate these uncertainty the adjustment of the resonance has been performed with two different RF in Figure 6.15.

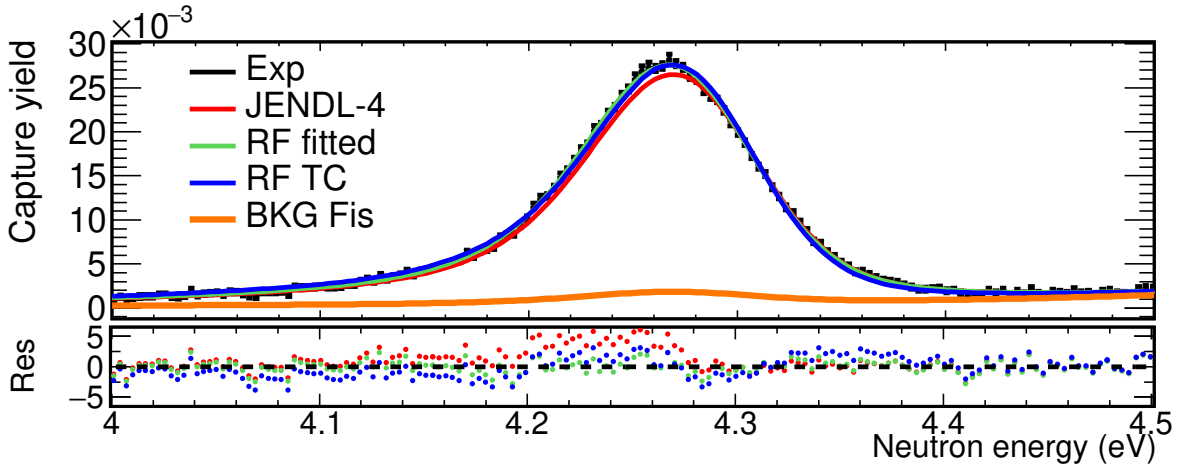

Figure 6.15: SAMMY yields and residuals for the strongest ^{246}Cm resonance at 4.3 eV to calculate the radiative width. The yield with the JENDL-4.0 (red) RP is compared with the fits obtained with SAMMY using the RF obtained by fitting ^{197}Au resonances (green) and the RF calculated with the TC (blue).

This uncertainty and the rest are present in Table 6.13, together with the final value obtained for the radiative width. The main sources of uncertainty are the RF (18%) and the one related with the subtraction of the background measured with the dummy sample (8%). The value obtained is compatible with all the previous measurements, see Table 6.14, mainly due to the large uncertainty.

Value (meV)	Uncertainties							
	Sta	Fis	Dummy	Elas	Temp	Doppler	Sum	
28.4	0.4	2.0	2.3	0.3	5.1	0.1	1.7	6.1

Table 6.13: Uncertainties of the radiative width of the strongest resonance of ^{246}Cm. The description of the different partial uncertainties can be found in Section 6.1. The last column (Sum) presents the quadratic sum of all the uncertainties.

JENDL-4.0 [20]	Coté [29]	Berreth [8]	Benjamin [7]	Kimura [32]	Kawase [33]	This work
28.0	35 ± 5	35 ± 2	31 ± 6	28.1 ± 2	27.3 ± 0.5	28 ± 6

Table 6.14: Radiative width (meV) of the strongest resonance of ^{246}Cm obtained in this work and in previous transmission and capture measurements.

6.5.2 Calculation of the resonances parameters E_0, Γ_n and R_K

A total of 14 resonances of ^{246}Cm have been fitted from the yield of the ^{246}Cm sample. In Table 6.15 the resonance parameters fitted (E_0 and Γ_n) are presented together with all their uncertainties. These uncertainties are plotted in Figure 6.16. The correlations between the uncertainties of the resonances are the same than in the ^{244}Cm resonances (Section 6.4.3), i.e. the assignment of UU or CU to each type of uncertainty.

The total uncertainty for the first four resonances is 5-6% due to the sum of the Mass, ^{240}Pu, Fis and RF uncertainties. At higher energies, the main uncertainties are the subtraction of the background (Dummy) and the uncertainty due to counting statistics (Sta).

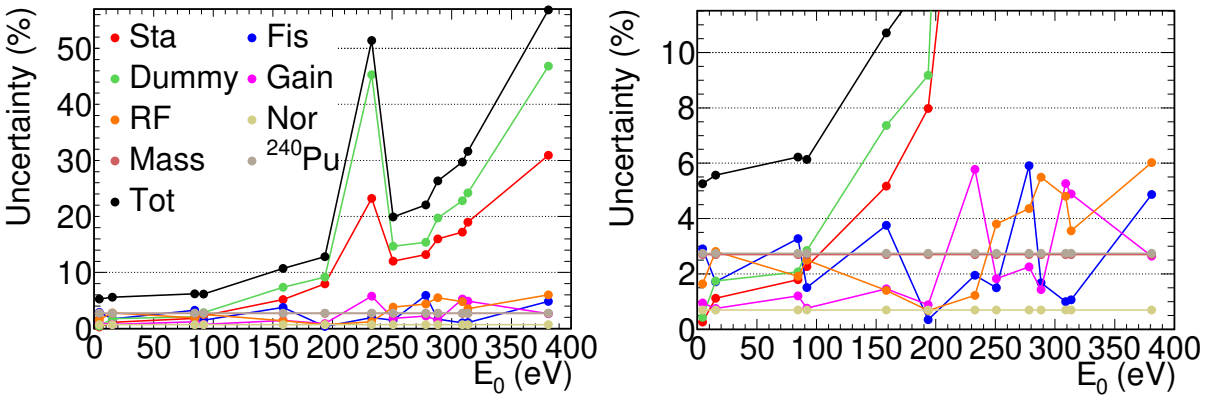

Figure 6.16: Uncertainties of the Γ_n parameters of ^{246}Cm measured in EAR2. The plots correspond to the data in Table 6.15. Both panels show the same graphs, but with a different range in the Y axis.

E_0 (eV)			
Value	Uncertainty		
	Sta	RF	Sum
4.3129	0.0002	0.0001	0.0002
15.3104	0.0014	0.0001	0.0014
84.5757	0.0050	0.0001	0.0050
91.9446	0.0082	0.0001	0.0082
158.414	0.020	0.010	0.023
193.855	0.053	0.017	0.056
232.50	0.24	0.01	0.24
250.76	0.10	0.03	0.10
278.08	0.10	0.06	0.11
287.91	0.15	0.01	0.15
306.79	0.11	0.01	0.11
316.64	0.17	0.01	0.17
360.88	0.16	0.10	0.19
381.10	0.20	0.03	0.21

Γ_n (meV)												
E_0 (eV)	Value	Uncertainty										
		Sta (UU)	Fis (CU)	Dummy (CU)	Gain (UU)	RF (UU)	Nor (CU)	Mass (CU)	^{240}Pu (CU)	Sum (CU)	Sum (UU)	Sum Total
4.31	0.324	0.001	0.009	0.001	0.003	0.005	0.002	0.009	0.009	0.016	0.006	0.017
15.31	0.541	0.006	0.009	0.009	0.004	0.015	0.004	0.015	0.015	0.025	0.017	0.030
84.58	23.4	0.4	0.8	0.5	0.3	0.4	0.2	0.6	0.6	1.3	0.7	1.5
91.94	13.6	0.3	0.2	0.4	0.1	0.3	0.1	0.4	0.4	0.7	0.5	0.8
158.4	39.9	2.1	1.5	2.9	0.6	0.6	0.3	1.1	1.1	3.6	2.2	4.3
193.9	17.7	1.4	0.1	1.6	0.2	0.1	0.1	0.5	0.5	1.8	1.4	2.3
232.5	4.3	1.0	0.1	1.9	0.2	0.1	0.1	0.1	0.1	2.0	1.0	2.2
250.8	18.4	2.2	0.3	2.7	0.3	0.7	0.1	0.5	0.5	2.8	2.3	3.7
278.1	31.6	4.2	1.9	4.9	0.7	1.4	0.2	0.9	0.9	5.3	4.4	7.0
287.9	17.0	2.7	0.3	3.3	0.2	0.9	0.1	0.5	0.5	3.4	2.9	4.5
306.8	49.1	8.5	0.5	11.2	2.6	2.4	0.3	1.3	1.4	11.4	9.1	14.6
316.6	24.2	4.6	0.3	5.9	1.2	0.9	0.2	0.7	0.7	5.9	4.8	7.7
381.1	59.9	18.5	2.9	28.0	1.6	3.6	0.4	1.6	1.6	28.3	18.9	34.0

Table 6.15: Resonance parameters values of ^{246}Cm obtained in EAR2 with the ^{246}Cm sample. A detailed explanation of the uncertainties and the methodology applied is given in the text. The different uncertainties are correlated (UC) or uncorrelated (UU) between the resonances.

The E_0 of each resonance is compared with JENDL-4.0 and with previous measurements in Figure 6.17. The resonance energies deviate less than 0.2% from JENDL-4.0, except for the resonance located at 316 eV.

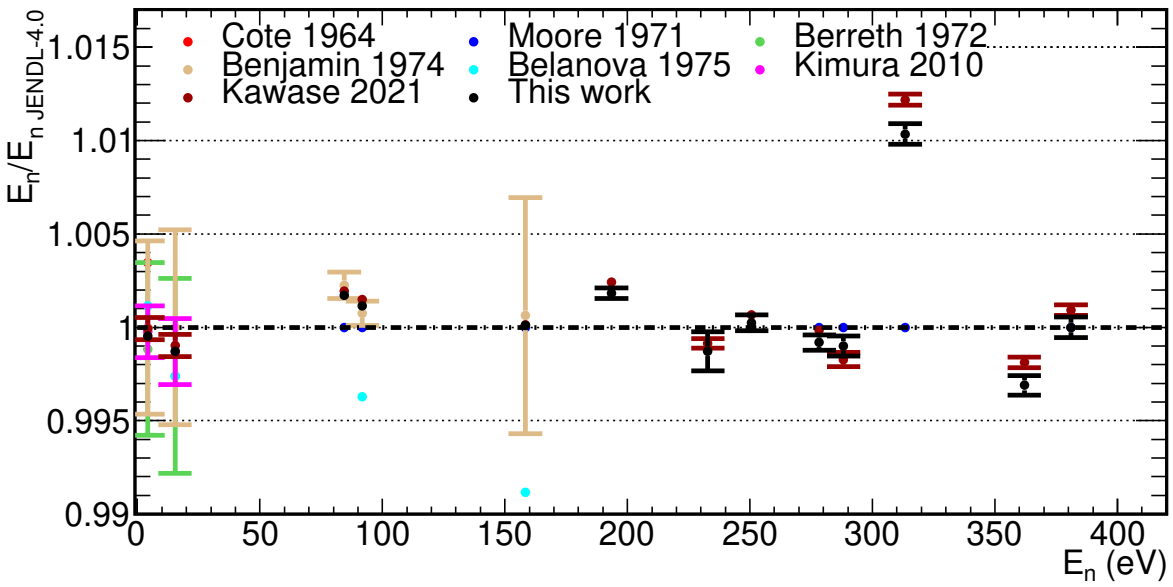

Figure 6.17: Ratio between the ^{246}Cm E_0 values obtained in different experiments, including this work, and JENDL-4.0.

The n_TOF experiment has measured more resonances than any other previous transmission or capture measurement, as can be seen in Table 6.16 and Figure 6.18, and also in Table 1.3. The posterior Kawase experiment has obtained the resonances parameters in a more extensive energy range from 4 to 650 eV.

E_0 (eV)	Cote	Moore	Berreth	Benjamin	Belanova	Kimura	Kawase	This work	JENDL-4
4.31	0.38±0.01	-	0.32±0.30	0.30±0.02	0.33±0.01	0.28±0.01	0.30±0.01	0.32±0.02	0.30
15.31	-	-	0.53±0.07	0.53±0.11	0.51±0.01	0.49±0.04	0.52±0.03	0.52±0.03	0.53
84.58	-	13.64±1.96	-	14.18±0.80	-	-	13.79±0.49	13.82±0.52	13.66
91.94	-	12.52±0.87	-	7.29±1.67	7.78±1.55	-	9.62±0.43	9.72±0.43	12.59
158.41	-	16.09±1.57	-	14.10±2.56	17.58±2.06	-	16.74±0.63	18.39±0.93	16.06
193.85	-	-	-	-	-	-	10.06±0.62	11.70±0.99	23.12
232.50	-	-	-	-	-	-	4.2±0.5	3.8±1.7	10.74
250.76	-	7.2±3.9	-	-	-	-	13.4±0.9	11.9±1.6	7.12
278.08	-	5.7±4.1	-	-	-	-	15.4±1.0	16.2±1.9	5.45
287.91	-	22.7±5.7	-	-	-	-	11.6±1.1	11.3±2.0	22.8
306.79	-	-	-	-	-	-	17.3±1.2	20.3±2.5	-
316.64	-	14.9±2.8	-	-	-	-	-	14.2±2.6	15.1
360.88					Doublet				
381.10	-	28.1±3.3	-	-	-	-	22.8±1.8	21.9±4.6	28.25

Table 6.16: R_K (meV) values obtained in this work, in previous measurements and evaluations for the ^{246}Cm resonances below 400 eV. The resonance at 360.88 eV is considered as a double as explained in Section 6.3.

The R_K obtained for the three first resonances (4.31, 15.31 and 84.58 eV) and the two last ones (316.64 and 381.10 eV) are compatible with the previous measurements and JENDL-4.0. The rest of the resonances are not compatible with the JENDL-4.0 values. On the other hand, the values are compatible with the measurement performed by Kawase

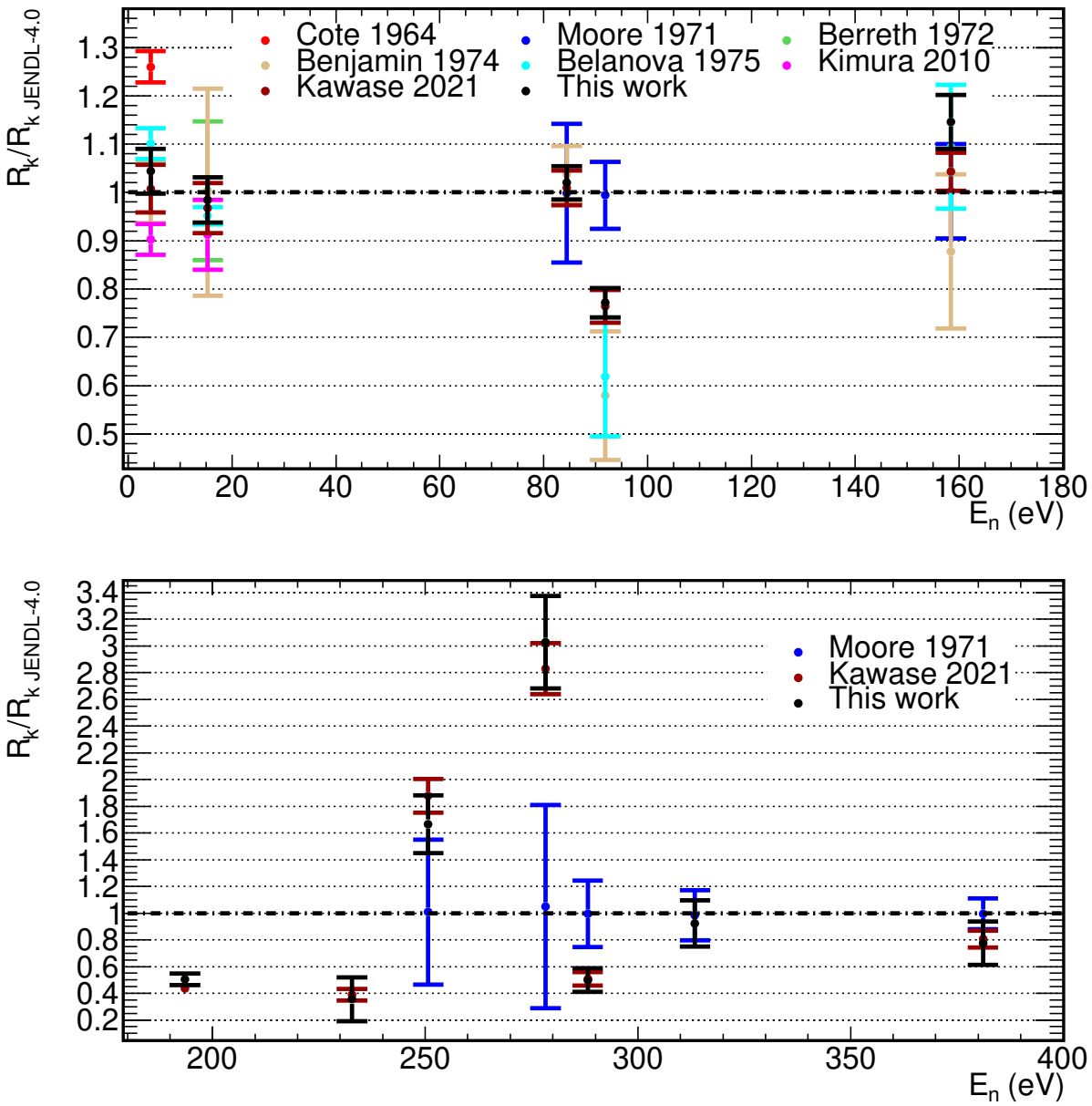

Figure 6.18: Ratio between the ^{246}Cm R_K values obtained in different experiments, including this work, and JENDL-4.0.

for the majority of the resonances.

The measurement performed at n_TOF have uncertainties in the R_K considerably smaller than any other previous transmission or capture measurement, as shown in Figure 6.19. The uncertainties at energies below 150 eV are similar to the ones of the posterior experiment of Kawase, whereas, at higher energies, the uncertainties in the Kawase experiment are smaller.

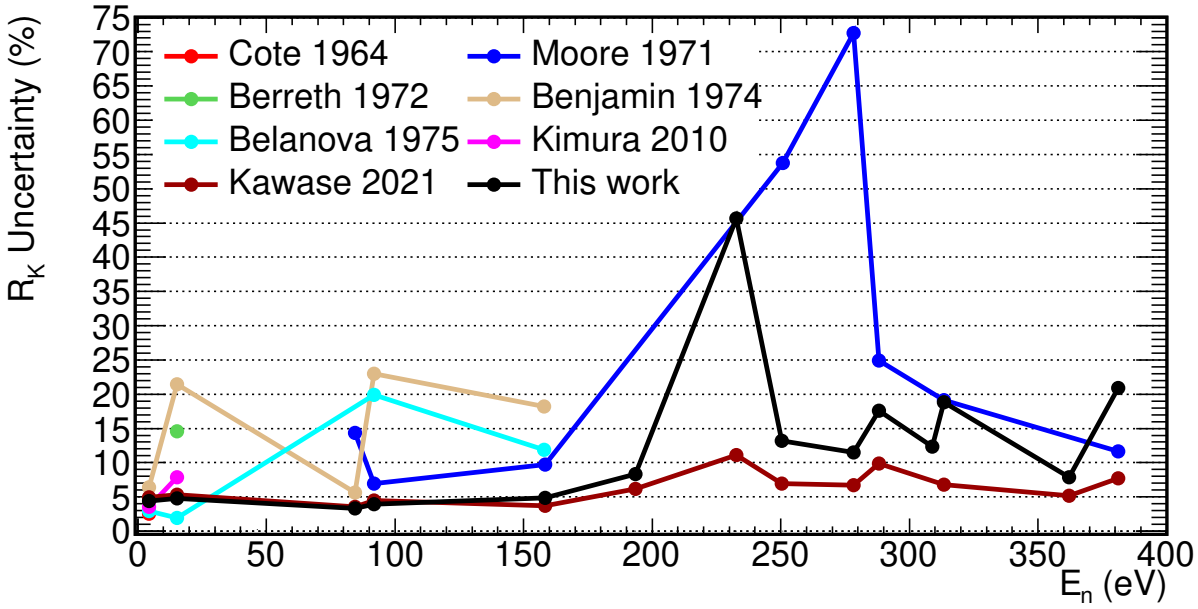

Figure 6.19: Comparison between the uncertainties in the R_K values measured in this work and the data of previous measurements for the resonances of ^{246}Cm.

6.6 ^{248}Cm resonance parameters

A total of five resonances of ^{248}Cm are fitted from the yield of the ^{246}Cm sample. In Table 6.17 the resonance parameters fitted (E_0 and Γ_n) are presented together with all their uncertainties. The correlations between the resonances, i.e. the assignment of UU or CU to each type of uncertainty, are the same as in the ^{244}Cm and ^{246}Cm analysis in EAR2. The Γ_γ values were fixed to those of JENDL-4.0 since the uncertainties in the Γ_γ parameters resulting from the analysis of the n_TOF data are too large.

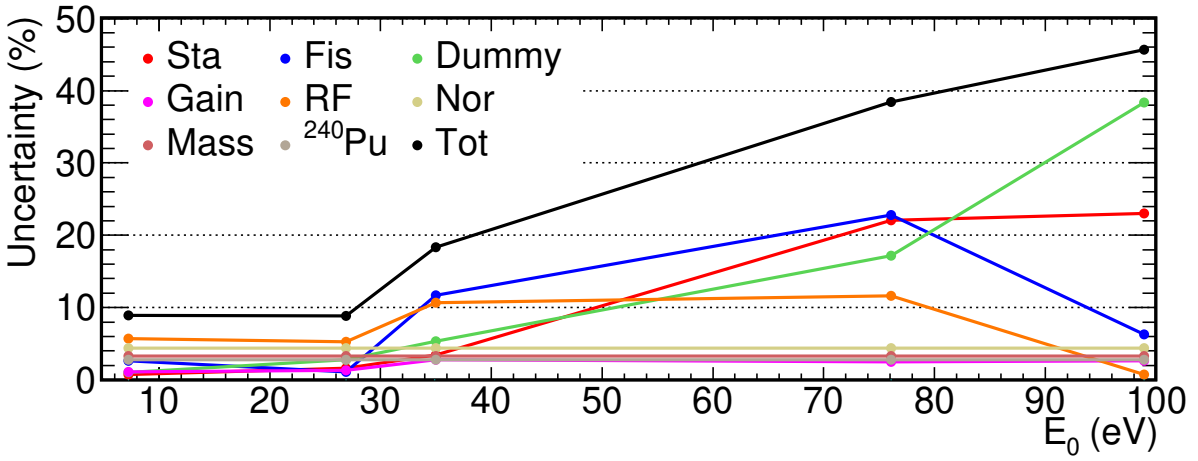

Figure 6.20: Uncertainties of the Γ_n parameters of ^{248}Cm measured in EAR2. The graphs have been obtained from the data of Table 6.17.

E_0 (meV)			
Value	Uncertainty		
	Sta	RF	Sum
7.2466	0.0005	0.0008	0.0010
26.899	0.002	0.001	0.002
35.011	0.006	0.001	0.006
76.075	0.022	0.013	0.025
98.841	0.032	0.015	0.035

Γ_n (meV)												
E_0 (eV)	Value	Uncertainty										
		Sta (UU)	Fis (CU)	Dummy (CU)	Gain (UU)	RF (UU)	Nor (CU)	Mass (CU)	^{240}Pu (CU)	Sum (CU)	Sum (UU)	Sum Total
7.25	1.94	0.01	0.05	0.02	0.02	0.11	0.05	0.06	0.05	0.11	0.11	0.16
26.90	18.2	0.3	0.2	0.5	0.2	1.0	0.5	0.6	0.5	1.1	1.0	1.5
35.01	9.8	0.3	1.2	0.5	0.3	1.0	0.3	0.3	0.3	1.4	1.1	1.8
76.07	268	59	61	46	7	31	7	9	7	78	67	103
98.84	371	85	23	142	10	3	10	12	10	145	86	169

Table 6.17: Resonance parameters of ^{248}Cm obtained in EAR2 with the ^{246}Cm sample. The different uncertainties are correlated (UC) or uncorrelated (UU) between the resonances. A detailed explanation of the uncertainties and the methodology applied is given in the text.

The E_0 of each resonance is compared with JENDL-4.0 and with previous measurements in Figure 6.21. The energy of the resonances deviates less than 0.1% from JENDL-4.0 for all the cases.

Concerning the R_K, the values are compared with previous experiments and with JENDL-4.0 in Table 6.18 and Figure 6.22. The resonances at 35, 76 and 98.8 eV have been measured in a capture measurement for the first time at n_TOF. The R_K obtained for the three first resonances are compatible with JENDL-4.0 and with other measurements. The R_K obtained for the resonances at 76 and 98.8 eV are 20% and 65% larger than JENDL-4.0, and are not compatible with any other measurement.

The uncertainties in the radiative kernel for this work and the previous measurements are compared in Figure 6.23. The uncertainties in this work are below 15% but are considerably larger than the values reported by Benjamin, which are most probaby underestimated.

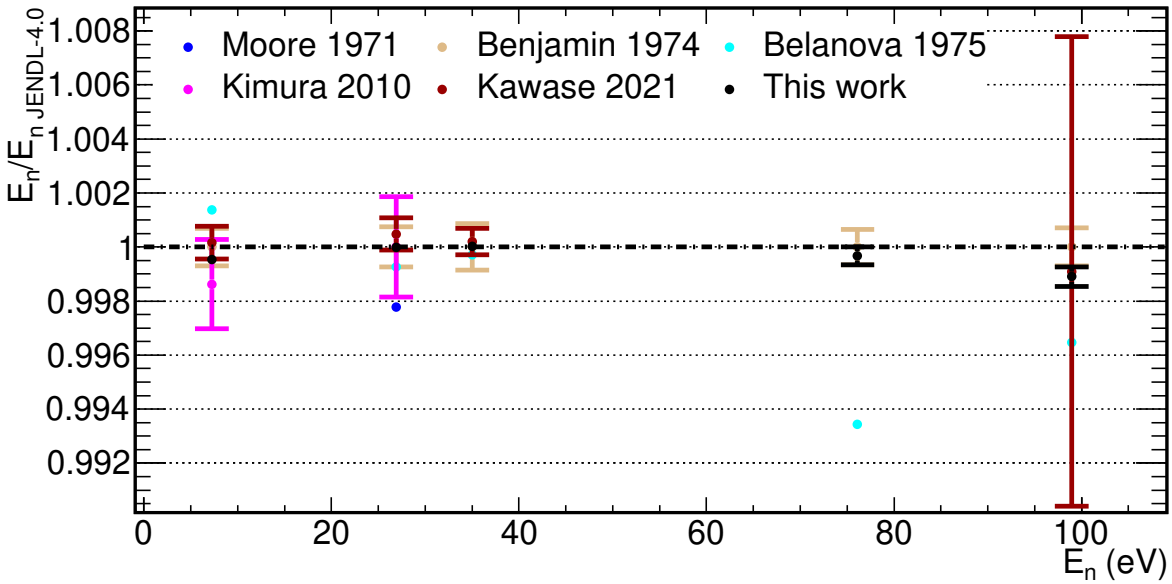

Figure 6.21: Ratio between the ^{248}Cm E_0 values obtained in different experiments, including this work, and JENDL-4.0.

E_0	Moore	Benjamin	Belanova	Kimura	Kawase	This work	JENDL-4
7.25	-	1.65±0.05	1.81±0.04	1.66±0.09	1.57±0.08	1.79±0.14	1.74
26.90	14.89±1.07	12.11±0.55	14.04±2.94	11.54±1.19	10.27±0.90	11.56±0.60	11.97
35.01	-	8.4±0.3	7.7±1.3	-	7.77±0.67	7.4±1.0	8.31
76.07	-	19.8±0.2	27.9±1.1	-	-	23.4±0.9	19.73
98.84	-	22.1±0.1	32.3±0.7	-	28.06±1.02	36.1±1.6	22.03

Table 6.18: R_K (meV) values obtained in this work, in previous measurements and evaluations for the ^{248}Cm resonances below 100 eV.

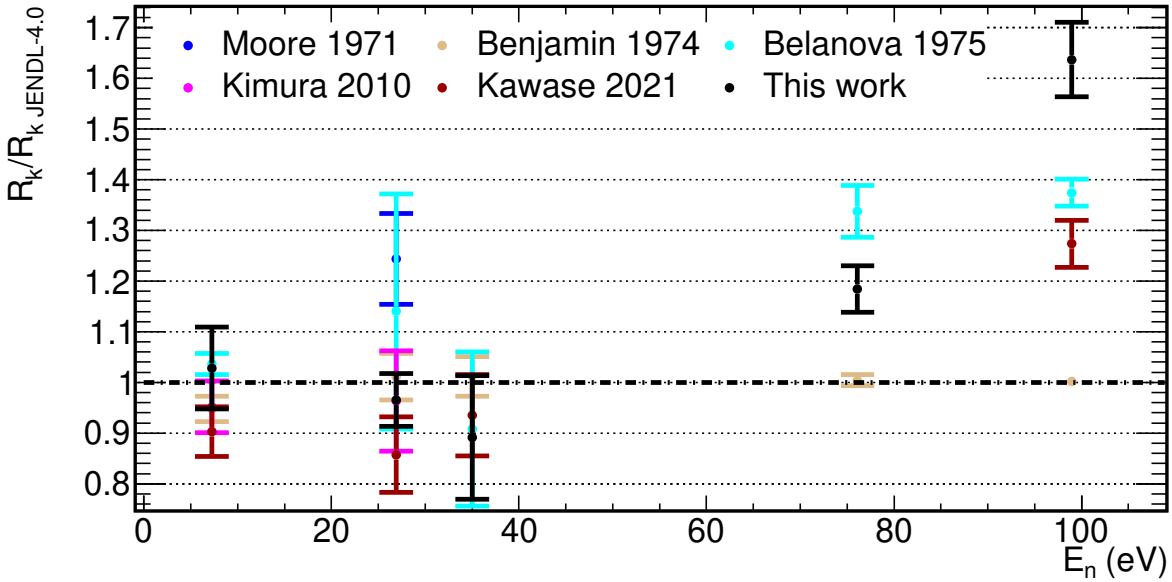

Figure 6.22: Ratio between the ^{248}Cm R_K values obtained in different experiments, including this work, and JENDL-4.0.

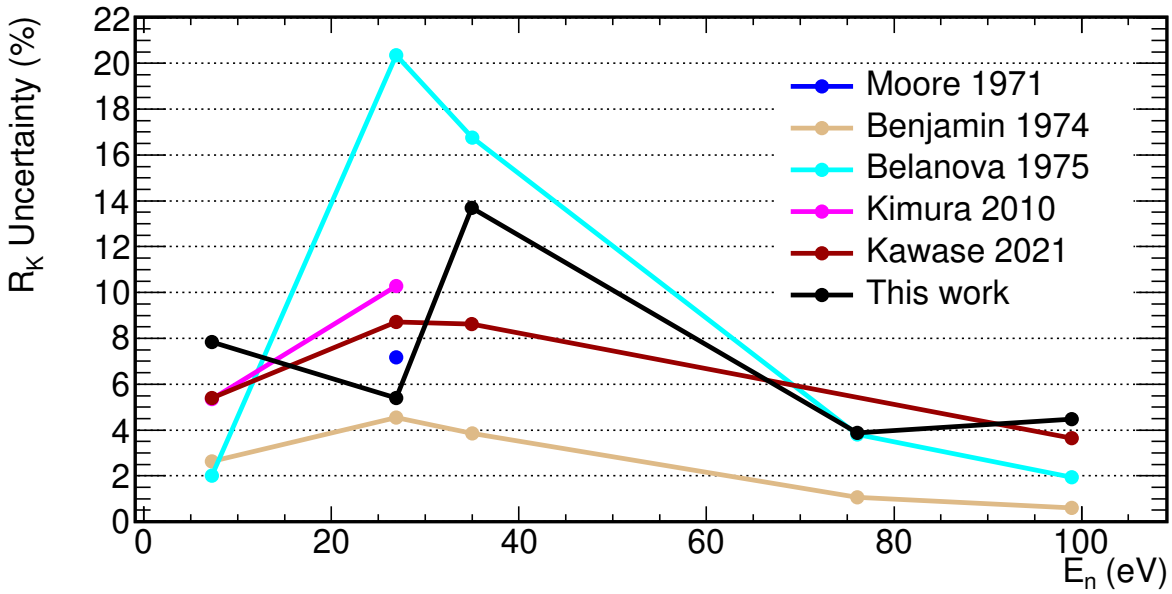

Figure 6.23: Comparison between the uncertainties in the R_K values in this work and the values reported in previous measurements for the resonances of ^{248}Cm.

6.7 ^{240}Pu resonance parameters

The resonance parameters of ^{240}Pu have been obtained in the three measurements performed (one in EAR1 and two in EAR2) between 20 and 170 eV. The RP have been normalised to the first resonance of this isotope at 1.056 eV, and the normalisation process is presented in Section 6.2, and also in this section, the Γ_n and E_0 are obtained for this strong resonance.

The resonance parameters obtained in the three measurements are presented in Tables 6.19, 6.20 and 6.21 with their uncertainties. The uncertainties are the same as for the Cm isotopes. The only exceptions are the Normalisation (Nor) and the isotopic abundance (Mass) uncertainties, which are zero because the normalisation has been performed to a resonance of the same isotope.

E_0 (eV)	
Value	Uncertainty (Sta)
20.450	0.003
38.328	0.004
41.716	0.005
66.639	0.007
72.82	0.01
90.84	0.03

Γ_n (meV)									
E_0 (eV)	Value	Uncertainty							
		Sta (UU)	Fis (CU)	Dummy (CU)	Elas (UU)	^{240}Pu (CU)	Sum (CU)	Sum (UU)	Sum Total
20.4	2.84	0.11	0.01	0.01	0.01	0.08	0.08	0.11	0.13
38.3	17.9	1.0	-	0.2	0.8	0.5	0.5	1.2	1.3
41.7	15.7	0.9	-	0.1	0.4	0.4	0.5	1.0	1.1
66.6	38.5	3.6	-	0.8	4.6	1.1	1.3	5.9	6.0
72.8	18.5	2.0	0.1	0.3	0.7	0.5	0.6	2.1	2.2
90.8	9.9	1.7	-	0.6	0.2	0.3	0.6	1.8	1.9

Table 6.19: Resonance parameters of ^{240}Pu obtained in EAR1 with the ^{244}Cm sample. The different uncertainties are correlated (UC) or uncorrelated (UU) between the resonances. Uncertainties lower than 0.1 are not reported.

The final RP of ^{240}Pu (Table 6.22) have been obtained from the combination of the three measurements approximating the uncertainties as totally correlated or uncorrelated, following the same procedure as in the analysis of ^{244}Cm (Section 6.4.4).

E_0 (eV)			
Value	Uncertainty		
	Sta	RF	Sum
20.449	0.002	0.002	0.003
38.321	0.002	0.001	0.002
41.719	0.003	0.001	0.003
66.64	0.01	0.01	0.01
72.81	0.01	0.01	0.01
90.77	0.02	0.01	0.03
92.49	0.07	0.02	0.08
105.03	0.02	0.01	0.02
121.60	0.07	0.02	0.07
135.36	0.07	0.03	0.08
152.06	0.08	0.05	0.09
162.63	0.19	0.02	0.19
170.20	0.12	0.10	0.16
185.94	0.14	0.08	0.16

Γ_n (meV)										
E_0 (eV)	Value	Uncertainty								
		Sta (UU)	Fis (CU)	Dummy (CU)	Gain (UU)	RF (UU)	^{240}Pu (CU)	Sum (CU)	Sum (UU)	Sum Total
20.4	2.53	0.04	0.03	0.11	0.01	0.17	0.07	0.13	0.17	0.22
38.3	20.7	0.4	0.1	0.5	0.2	2.4	0.6	0.8	2.4	2.5
41.7	17.5	0.3	0.1	0.5	0.1	2.1	0.5	0.7	2.1	2.2
66.6	46.5	1.9	0.5	2.2	0.4	7.4	1.3	2.6	7.6	8.1
72.8	23.4	1.2	0.9	3.2	0.2	2.7	0.6	3.4	2.9	4.5
90.8	14.9	1.1	0.2	1.1	0.4	0.1	0.4	1.2	1.2	1.7
92.5	3.8	0.6	0.3	1.2	0.1	0.3	0.1	1.3	0.7	1.4
105.0	64.4	8	1	12	2	4	2	12	9	15
121.6	11.7	1.5	0.1	1.7	0.1	0.2	0.3	1.7	1.5	2.3
135.4	16.4	2.3	0.1	2.2	0.6	0.2	0.5	2.3	2.4	3.3
152.1	21.5	3.1	0.3	3.9	0.2	0.6	0.6	3.9	3.2	5.1
162.6	8.1	2.2	0.1	2.6	0.4	0.1	0.2	2.6	2.3	3.4
170.2	22.6	5.3	0.2	3.9	0.6	0.2	0.6	3.9	5.4	6.6
185.9	21.7	5.2	0.1	5.2	0.4	0.5	0.6	5.3	5.3	7.4

Table 6.20: Resonance parameters of ^{240}Pu obtained in EAR2 with the ^{244}Cm sample. The different uncertainties are correlated (UC) or uncorrelated (UU) between the resonances.

The E_0 values obtained in the three measurements are compatible between them, and also with the final E_0 values, as observed in Figure 6.24. In Figure 6.25 the final E_0 values are compared to JENDL-4.0 and other previous measurements, finding that they

E_0 (eV)			
Value	Uncertainty		
	Sta	RF	Sum
20.447	0.004	0.002	0.004
38.322	0.004	0.001	0.004
41.712	0.006	0.001	0.006
66.64	0.01	0.01	0.01
90.78	0.05	0.22	0.23
105.03	0.04	0.02	0.04
121.73	0.15	0.01	0.15
135.17	0.11	0.02	0.11
152.12	0.14	0.06	0.15

Γ_n (meV)										
E_0 (eV)	Value	Uncertainty								
		Sta (UU)	Fis (CU)	Dummy (CU)	Gain (UU)	RF (UU)	^{240}Pu (CU)	Sum (CU)	Sum (UU)	Sum Total
20.4	2.53	0.04	0.03	0.11	0.01	0.17	0.07	0.13	0.17	0.22
38.3	20.7	0.4	0.1	0.5	0.2	2.4	0.6	0.8	2.4	2.5
41.7	17.5	0.3	0.1	0.5	0.1	2.1	0.5	0.7	2.1	2.2
66.6	46.5	1.9	0.5	2.2	0.4	7.4	1.3	2.6	7.6	8.1
72.8	23.4	1.2	0.9	3.2	0.2	2.7	0.6	3.4	2.9	4.5
90.8	14.9	1.1	0.2	1.1	0.4	0.1	0.4	1.2	1.2	1.7
92.5	3.8	0.6	0.3	1.2	0.1	0.3	0.1	1.3	0.7	1.4
105.0	64.4	8	1	12	2	4	2	12	9	15
121.6	11.7	1.5	0.1	1.7	0.1	0.2	0.3	1.7	1.5	2.3
135.4	16.4	2.3	0.1	2.2	0.6	0.2	0.5	2.3	2.4	3.3
152.1	21.5	3.1	0.3	3.9	0.2	0.6	0.6	3.9	3.2	5.1
162.6	8.1	2.2	0.1	2.6	0.4	0.1	0.2	2.6	2.3	3.4
170.2	22.6	5.3	0.2	3.9	0.6	0.2	0.6	3.9	5.4	6.6
185.9	21.7	5.2	0.1	5.2	0.4	0.5	0.6	5.3	5.3	7.4

Table 6.21: Resonance parameters of ^{240}Pu obtained in EAR2 with the ^{246}Cm sample. The different uncertainties are correlated (UC) or uncorrelated (UU) between the resonances.

are compatible with JENDL-4.0, except for the resonance at 20.449 eV.

The final values of the Γ_n parameters obtained in the three measurements are compatible between them, and also with the final value, as presented in Figure 6.26. The radiative kernels (R_K) of the resonances are compared with previous measurements and evaluations in Figure 6.27 and Table 6.23.

Five previous measurements report the RP for this isotope. The first transmission

E_0 (eV)		Γ_n (meV)			
Value	Uncer. Total	Value	Uncertainty		
			Total	(UU)	(CU)
20.449	0.002	2.77	0.13	0.10	0.09
38.323	0.002	18.3	1.3	1.0	0.8
41.718	0.003	16.0	1.0	0.8	0.6
66.641	0.005	41.3	4.9	4.0	2.8
72.815	0.009	24.3	2.1	1.7	1.2
90.80	0.02	12.8	1.3	1.0	0.8
92.49	0.08	3.8	1.4	0.7	1.3
105.03	0.02	63	15	8	12
121.60	0.07	11.7	2.3	1.5	1.8
135.30	0.07	17.1	3.1	2.1	2.3
152.06	0.09	21.5	5.1	3.2	4.0
162.59	0.18	8.1	3.4	2.3	2.6
170.20	0.16	22.6	6.6	5.4	3.9
185.94	0.16	21.7	7.5	5.3	5.3

Table 6.22: Final resonance parameters values of ^{240}Pu obtained from the combination of the three measurements at n_TOF. The total uncertainties are divided in the correlated (UC) and uncorrelated (UU) components.

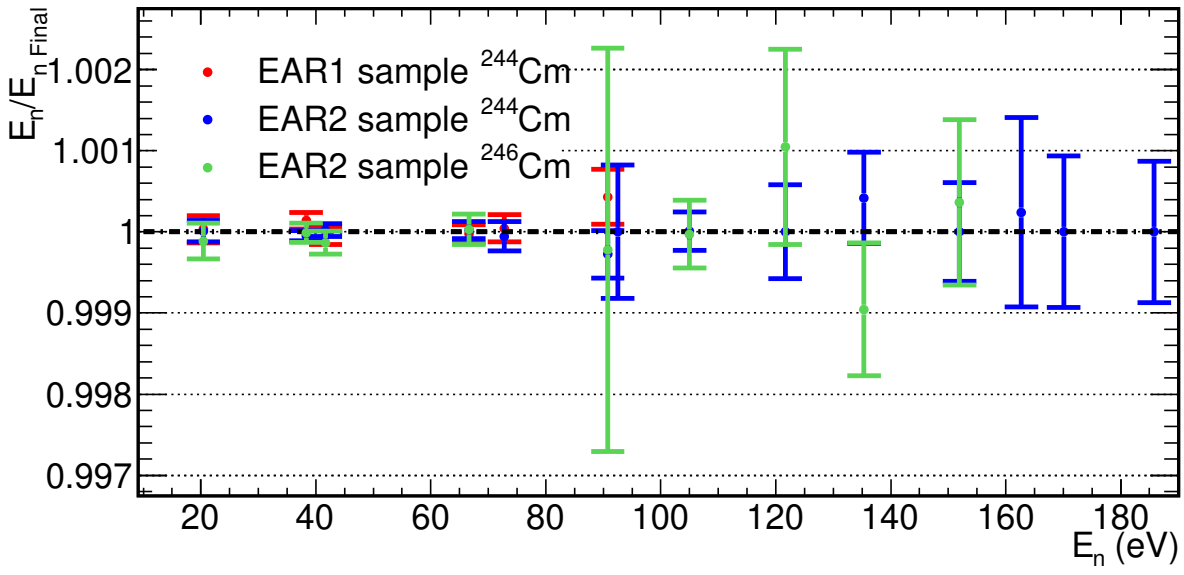

Figure 6.24: The E_0 values obtained in the three measurements of ^{240}Pu (Table 6.19, 6.20 and 6.21) with their uncertainties divided by the final E_0 value (Table 6.22) presented in this section.

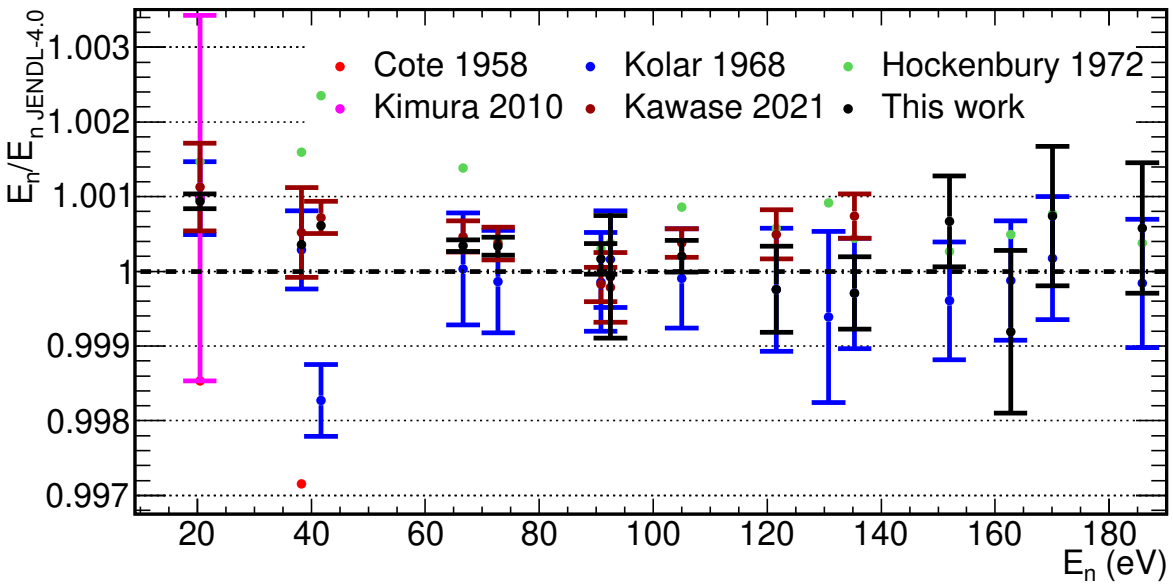

Figure 6.25: Ratio between the ^{240}Pu E_0 values obtained in different experiments, including this work, and JENDL-4.0.

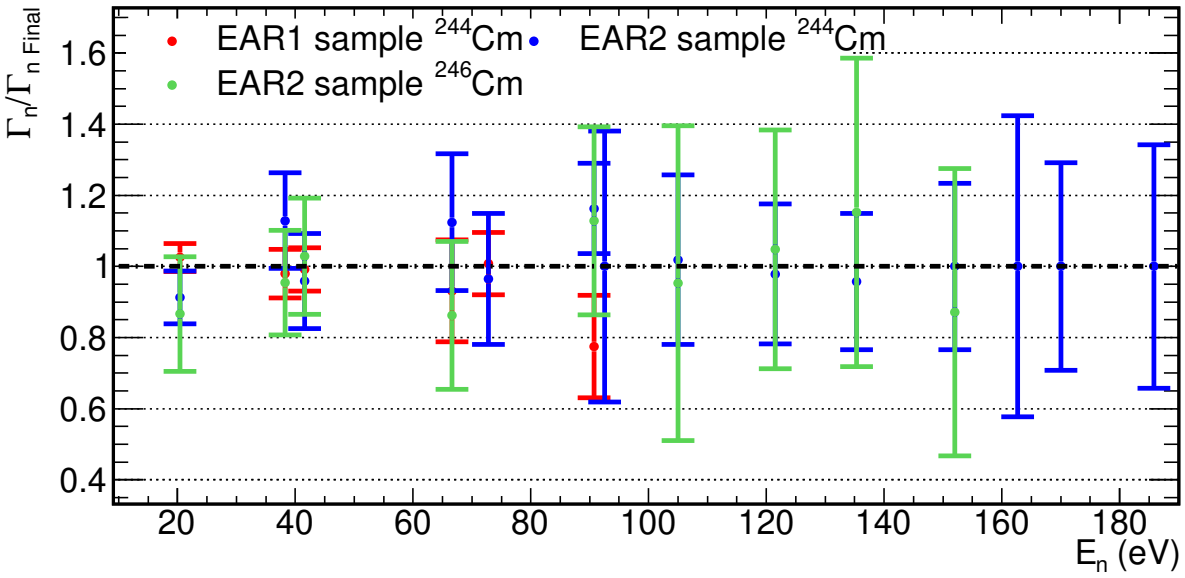

Figure 6.26: Γ_n values obtained in the three measurements of ^{240}Pu (Tables 6.19, 6.20 and 6.21) compare with the final value combining these measurements (Table 6.22). The uncertainties in the values consider all the sources of uncertainties except the uncertainty of the nuclear data of ^{240}Pu (2.75%).

measurement was performed in 1958 at the Argonne fast chopper [38] by Cote *et al.* The second set of parameters were obtained by Kolar *et al.* [164] with a combination of the transmission and capture measurements performed in 1968 in the 60 MeV electron linear accelerator of the CBNM [165]. The work done by Hockenbury *et al.* [166] has obtained the RP combining the results of a fission, a capture and a transmission measurement

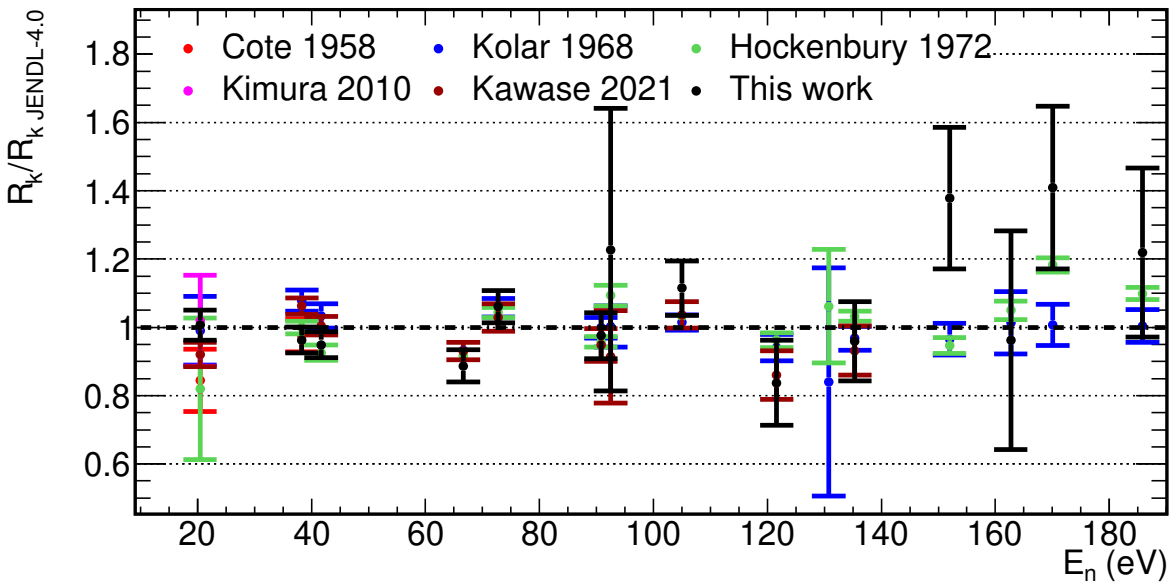

Figure 6.27: Ratio between the ^{240}Pu R_K values obtained in different experiments, including this work, and JENDL-4.0.

E_0 (eV)	Cote	Kolar	Hockenbury	Kimura	Kawase	This work	JENDL-4
1.056	2.23±0.05	-	-	2.26±0.02	2.26±0.07	-	2.27
20.43	2.12±0.23	2.49±0.25	2.06±0.52	2.56±0.33	2.31±0.09	2.53±0.11	2.51
38.309	10.53±0.52	11.63±0.33	10.78±0.20	-	11.46±0.26	10.38±0.41	10.78
41.692	-	10.70±0.37	9.59±0.23	-	10.40±0.28	9.83±0.39	10.36
66.618	-	19.30±0.26	18.97±0.13	-	19.25±0.54	18.35±0.98	20.69
72.79	-	12.58±0.33	12.41±0.17	-	12.24±0.48	12.62±0.57	11.90
90.783	-	9.26±0.28	8.88±0.15	-	8.79±0.44	9.05±0.63	9.28
92.495	-	2.7±0.2	3.0±0.1	-	2.5±0.4	3.3±1.1	2.72
105.01	-	17.9±0.4	18.2±0.2	-	18.3±0.7	19.7±1.4	17.6
121.63	-	9.7±0.4	9.9±0.2	-	8.9±0.7	8.6±1.3	10.3
125.7	-	-	-	-	-	-	0.1
130.78	-	0.1±0.1	0.2±0.0	-	-	-	0.2
135.34	-	11.4±0.4	12.1±0.2	-	10.9±0.8	11.3±1.4	11.7
151.96	-	9.5±0.5	9.3±0.2	-	-	13.6±2.0	9.9
162.72	-	6.7±0.6	6.9±0.2	-	-	6.3±2.1	6.6
170.07	-	9.4±0.6	11.0±0.2	-	-	13.1±2.2	9.3
185.83	-	10.5±0.5	11.5±0.2	-	-	12.7±2.6	10.5

Table 6.23: R_K (meV) values obtained in this work, and in previous measurements and evaluations for the ^{240}Pu resonances below 200 eV.

at the Rensselaer facility [167] in 1972. The most recent measurements are the ones of Kimura *et al.* in 2010 [32] and Kawase *et al.* in 2018 [33] using the same sample than in the n_TOF measurement. The radiative kernel values obtained at n_TOF are compatible with the previous measurements and evaluations.

The uncertainties of the R_K obtained at n_TOF are similar to the ones of the previous

measurements for the resonances below 50 eV as presented in Figure 6.28. At higher energies, the R_K of the measurements of Kolar, Hockenbury and Kawase have uncertainties considerable smaller than the n_TOF values.

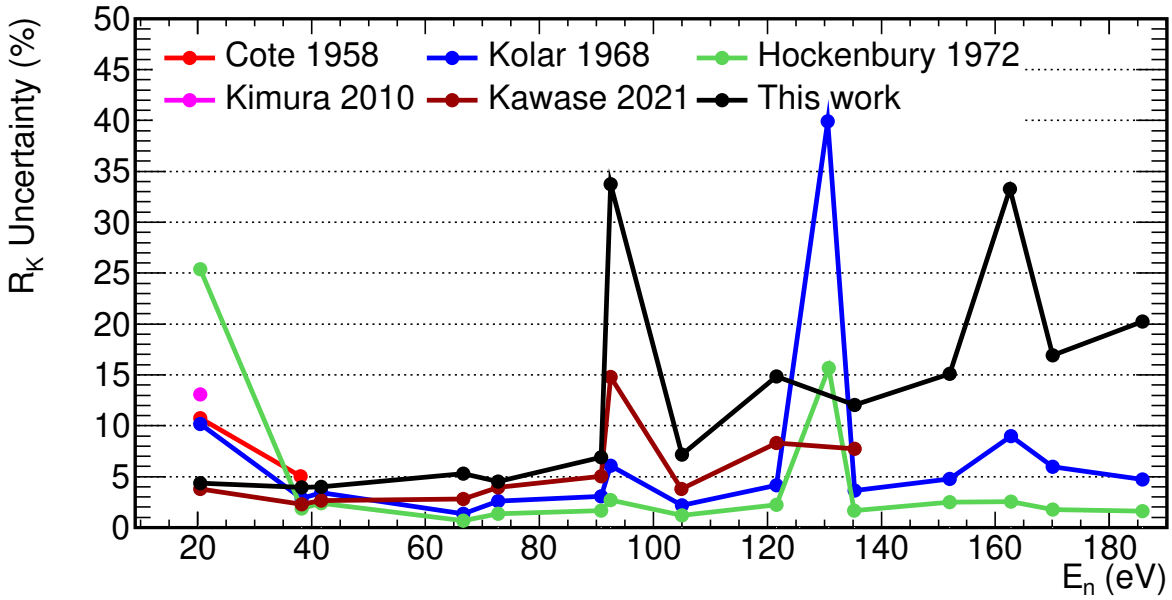

Figure 6.28: Comparison between the uncertainties in the R_K values measured in this work and the data of previous measurements for the resonances of ^{240}Pu below 200 eV.

The compatibility of the values obtained at n_TOF and the previous measurements for the resonances of ^{240}Pu is a strong validation of the full analysis process, giving a higher confidence in the results provided for the Cm isotopes.

Chapter 7

Summary and conclusions

Accurate neutron capture cross section data for minor actinides (MAs) are required to estimate the production and transmutation rates of MAs in light water reactors, critical fast reactors like Gen-IV systems and other innovative reactor systems such as accelerator driven systems (ADS) [14, 168]. In particular, capture reactions in ^{244}Cm, ^{246}Cm and ^{248}Cm (^{244,246,248}Cm) are in the path for the formation of other Cm isotopes and heavier elements such as Bk and Cf. In addition, ^{244}Cm shares $\sim$40% of the total actinide decay heat in irradiated reactor fuels with a high burnup, even after fifteen years of cooling. Finally, the Cm isotopes are the main neutron emitters in the irradiated fuels, producing more than half of the neutrons emitted in the first 10000 years. There are only two capture measurements of the ^{244,246,248}Cm capture cross sections before this work. The first measurement was done in 1969, using the neutrons produced in an underground nuclear explosion [31], and the second one was done in 2010 by Kimura *et al.* at J-PARC [32]. After the n_TOF experiment, a new measurement was performed by Kawase *et al.* also in J-PARC [33].

This work provides new experimental data on the ^{244,246,248}Cm capture cross sections to improve the present evaluations. The measurements have been performed at the n_TOF facility at CERN with two different samples, one prepared to measure the cross section of ^{244}Cm and the other to measure the cross sections of ^{246,248}Cm. The two samples were the same as the ones used in the Cm capture measurements at J-PARC by Kimura [32] and Kawase [33].

The cross section of ^{244}Cm has been measured in the first experimental area of n_TOF (EAR1) with the Total Absorption Calorimeter (TAC), and in the second experimental area (EAR2) with C_6D_6 detectors. The cross sections of ^{246}Cm and ^{248}Cm have been measured only in EAR2. In addition, the resonances of ^{240}Pu, present in the samples due to the decay of ^{244}Cm, have been analysed as well. The ^{244,246,248}Cm and ^{240}Pu cross sections have been normalised to the first resonance of ^{240}Pu.

This manuscript aims to describe the performance and analysis of these measurements, including the data reduction, the relevant simulations and the resonance analysis. A rigorous calculation of all types of uncertainties has been carried out in all the steps. For the first time, a capture cross section analysis has been performed at both n_TOF experimen-

tal areas, with different detection setups, and the results obtained are compatible. The capture yields of the measurements will be delivered to the EXFOR database, as well as the results of the resonance analysis.

7.1 Comparison with evaluated data and previous measurements

A summary of the results obtained for the three Cm isotopes and ^{240}Pu are presented in the following list, comparing the RP obtained in this work with the JENDL-4.0 evaluation [20], which has been adopted by JEFF-3.3 [51] and ENDF/B-VIII.0 [52] for all the Cm isotopes involved in this work:

- ^{244}**Cm**. A total of 17 resonances have been analysed in the energy range between 7 and 300 eV. The majority of the radiative kernel values (i.e. resonance areas) obtained in this work are compatible with the JENDL-4.0 values (Figure 7.1). The uncertainties obtained at n_TOF for the resonances below 135 eV are as small as those obtained in the best previous measurements.

- ^{246}**Cm**. A total of 14 resonances have been analysed with the SAMMY code in the energy range between 4 and 400 eV. A new resonance was found at 306.8 eV, two resonances (193.5 and 235.8 eV) have been measured for the first time in a transmission or capture experiment, and the resonance at 361 eV is considered as an unresolved doublet. The detailed uncertainties obtained in the analysis are smaller than those obtained in any previous capture or transmission measurement. The uncertainties at energies below 150 eV are similar to the ones of the posterior experiment of Kawase, whereas, at higher energies, the uncertainties in the Kawase experiment are smaller. The radiative kernel values at energies below 80 eV are compatible with JENDL-4.0. At higher energies, the values obtained at n_TOF for most of the resonances are not compatible with the JENDL-4.0 (Figure 7.1).

- ^{248}**Cm**. Five resonances have been analysed in the energy range between 7 and 100 eV. Three of these resonances (35.0, 76.1 and 99.0 eV) have been measured for the first time in a capture experiment. The radiative kernel of the first three resonances are compatible with JENDL-4.0 and with the values reported in other experiments. The values obtained for the resonances located at 76.1 and 99.0 eV are considerably larger than the those of JENDL-4.0.

- ^{240}**Pu**. A total of 14 resonances have been analysed in the energy range between 20 and 200 eV. The resonance parameters are compatible with the evaluations as presented in Figure 7.1. The cross section obtained was normalised to the first resonance of ^{240}Pu. The excellent agreement between these values measured at n_TOF and JENDL-4.0 serves, to a great extent, as a validation of the results obtained for the Cm isotopes.

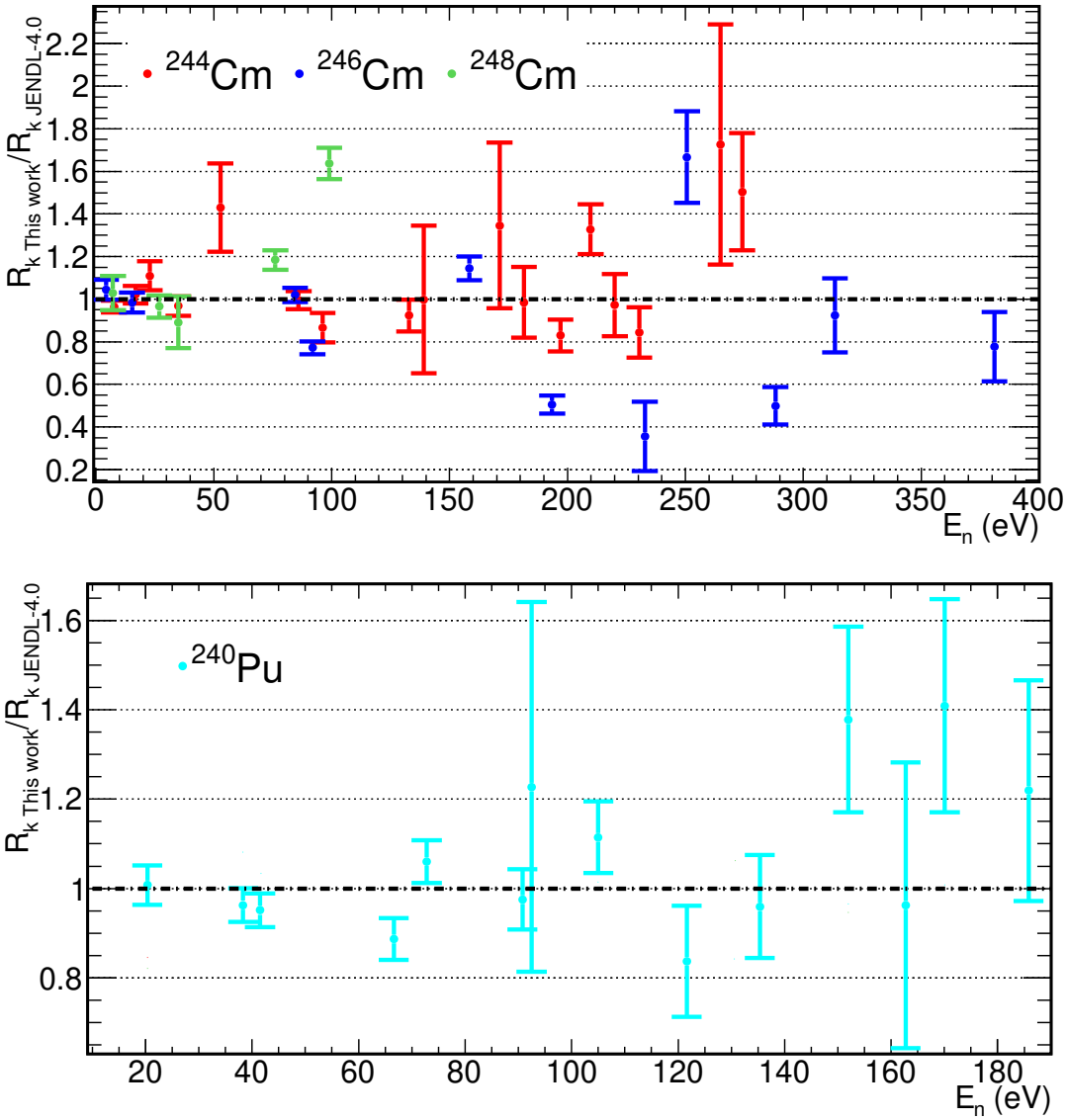

Figure 7.1: Ratio between the radiative kernels of ^{244,246,248}Cm and ^{240}Pu obtained in this work and the JENDL-4.0 values.

7.2 Other achievements of this work

In addition to the cross sections presented in the previous section, there are other achievements that have been made during this work. The most relevant ones are the following::

- The discovery of a considerable alteration of the neutron fluence in EAR2 by a minor modification of the impinging position of the proton beam in the target. Throughout the entire data taking, the counting rates of all the detectors were monitored carefully: the proton beam detectors (BCT and PKUP) were constantly compared with those of the neutron detectors (SiMon and SiMon2) and the γ-ray detectors (TAC and C_6D_6). Thanks to this monitoring work, it was found for the first time at n_TOF that a slight change in the impinging position of the proton beam in the lead target can modify the neutron fluence in EAR2. This effect was

taken into account during all subsequent measurements performed at EAR2, and a special device has been installed in the new n_TOF spallation target to monitor the impinging position of the proton beam.

- In addition to the cross sections, information about the γ-ray cascades emitted after the neutron capture in ^{240}Pu and ^{244}Cm have been obtained. The experimental data obtained with the TAC have been fitted with an evolutive algorithm to obtain this information. In previous works, this procedure has been done by adjusting the parameters *by hand*. The γ-ray cascades, which reproduce the experimental data obtained in EAR1 with the TAC data, also reproduce with high accuracy the experimental data obtained with C_6D_6 detectors in EAR2.

- A new methodology has been developed in this work to characterise the resolution broadening in EAR2, parameterised in the so-called Resolution Function (RF). This is the effect that occurs because not all neutrons of a certain energy reach the sample at the same time. For the first time, it has been found that the RF differs strongly for small radius samples compared with samples covering the full beam. This new methodology, based on fitting the RF to the experimental data, was needed since the standard one, based on Monte Carlo simulations, was not able to reproduce the experimental results for small radius samples.

- It was observed for the first time at n_TOF that many of the C_6D_6 type detectors suffer changes in their gain with high counting rates. Two new types of effects were observed. The first effect is the change in gain with high constant counting rates, observed when measuring with calibration sources located at different distances from the detector. The second effect is the change in gain as a function of the time-of-flight (TOF) due to very high counting rates in a very short period, produced by the particle-flash. This second change in gain has affected the ^{240}Pu and ^{244,246,248}Cm measurements, and a new methodology has been developed to correct it. These results have had consequences in subsequent measurements at n_TOF carried out with C_6D_6, since they have tried to keep the counting rates during the calibration low enough to not have changes in the gain of the detectors. In addition, new detectors able to support the high counting rates at EAR2 have been developed.

- For the first time at n_TOF, the resonance parameters of four different actinides have been obtained in the analysis of the same sample. The analysis has been performed, including the capture and fission contributions of each isotope, the fitted ones and the ones considered as background. The fission components of the isotopes have been subtracted in both areas using an iterative process. The process consists of calculating the backgrounds with the initial RP obtained in the previous fit until the RP obtained in the fit are equal to the initial parameters, i.e. the process has converged.

- For the first time at n_TOF the capture cross section of an isotope has been obtained by combining three different measurements, whose results are correlated in a very complex way. The resonance parameters of ^{244}Cm and ^{240}Pu have been obtained in EAR2 with the two samples, and in EAR1 with one of those samples, using a different detector (the TAC). The results obtained in the three measurements are

compatible, and have been combined considering the different uncertainties and their correlations to obtain the final n_TOF results.

7.3 Improvements for future capture measurements in EAR2

The measurement of the Cm isotopes has been the first capture campaign performed in EAR2. From the experience acquired during this work, the following lines of improvement for future capture measurements in EAR2 are proposed:

- The spallation target used in the Cm campaign was not built to optimise the capture measurements in EAR2. A new target has been constructed, improving the RF in EAR2 significantly.
- The strong particle-flash of the EAR2 can cause modifications in the gain of the C_6D_6 detectors as a function of the time of flight. The BICRON detectors used for the Cm experiment were the best available option at that moment to measure in EAR2, even though these detectors suffer minor gain modification due to the particle-flash (Section 5.2.3). In order to mitigate this effect, for future measurements, there are two different approaches. The first one is the use of new PMTs more optimised for high counting rates. The second approach consists on using segmented detectors (i.e. smaller detectors) with less active volume that will suffer less from the particle-flash. Both approaches are at this moment under development at n_TOF.
- The scattering of neutrons and particles coming with the beam producing counts in the C_6D_6 detectors are one of the primary sources of background in the capture measurements performed in EAR2. In the case of the Cm measurement, this component contributes to approximately to 60% of the Dummy background. New measurements have been performed in the experimental EAR2 to obtain more information about the origin of this background, in an attempt to reduce it.

Appendices

Appendix A

BICRON C_6D_6 drawing

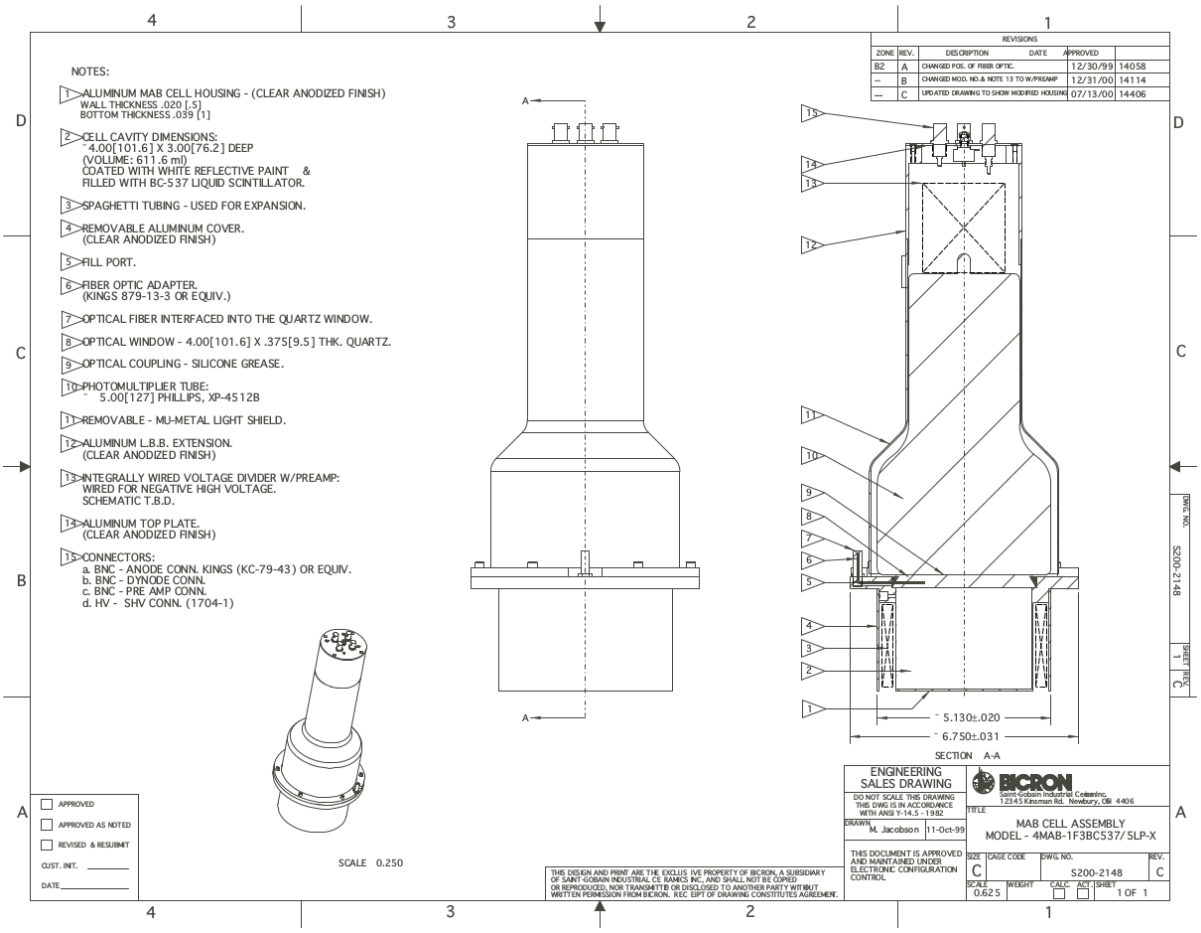

Figure A.1: BICRON Drawing

Appendix B

Transport Code (TC)

The Transport Code [87, 169] is a tool developed at n_TOF aimed to simulate the optical transport of particles from the target to the experimental areas. It outputs various histograms indicating the energy, time of flight and the resolution function of the particles. The TC uses as an input the different Monte Carlo simulations of the particle production in the spallation target performed with FLUKA [64, 99] + MCNPx [100]. These simulations have been performed until a scoring plane located at 37.2 cm from the target. The information of all the particles reaching this plane are stored and optically transported to the sample. If there is any obstacle in the particle trajectory, like collimators or beam pipes, the particles are discarded. A schema of the TC is presented in Figure B.1.

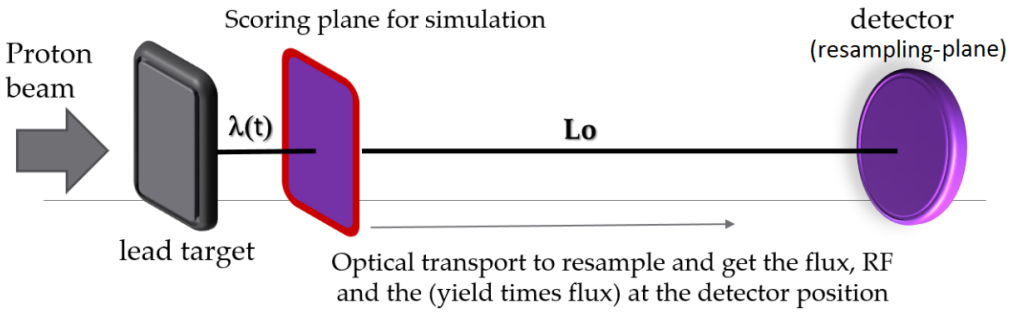

Figure B.1: Scheme of the neutron transport principle from the scoring plane to the final surface. Figure extracted from M. Sabaté-Gilarte thesis [87]

The information that has to be provided to the program are: the Monte Carlo simulation inputs, the experimental area, the collimator, the RMS of the beam, the time-of-flight distance, the particle (neutron or γ), the dimensions of the sample and the possible misalignment of the sample. The TC provides ROOT [155] histograms with the following information:

- The particle energy or time-of-flight spectra reaching to the sample.
- The interaction yield, in the case the properties of a sample and the cross sections are provided to the program.

- A bidimensional histogram comparing time-of-flight (s) vs energy (eV).
- A bidimensional histogram comparing λ (moderation length) (m) vs energy (eV).
- The beam profile.

Appendix C

Fits of the resonances of ^{244,246,248}Cm and ^{240}Pu

C.1 Fits of the ^{244}Cm resonances

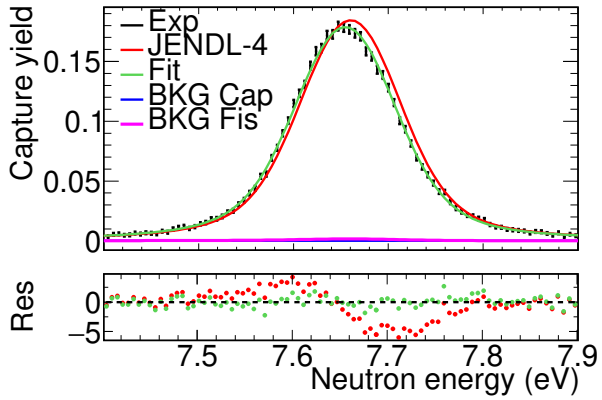

(a) Resonance 1: EAR1, ^{244}Cm sample

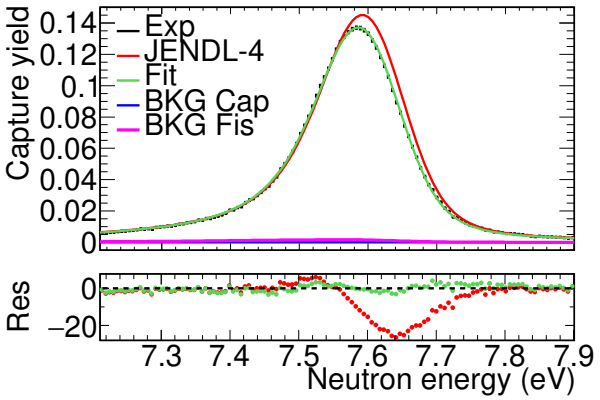

(b) Resonance 1: EAR2, ^{244}Cm sample

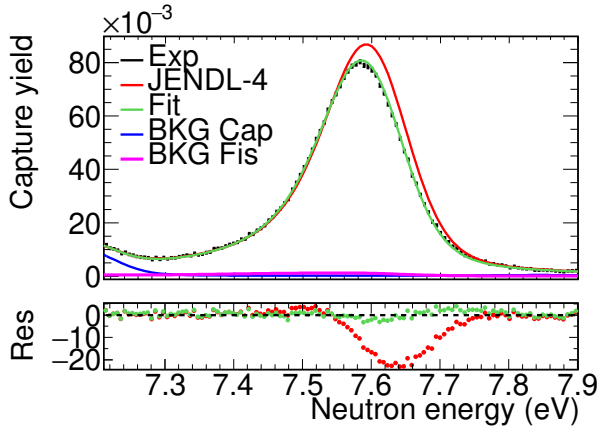

(c) Resonance 1: EAR2, ^{246}Cm sample

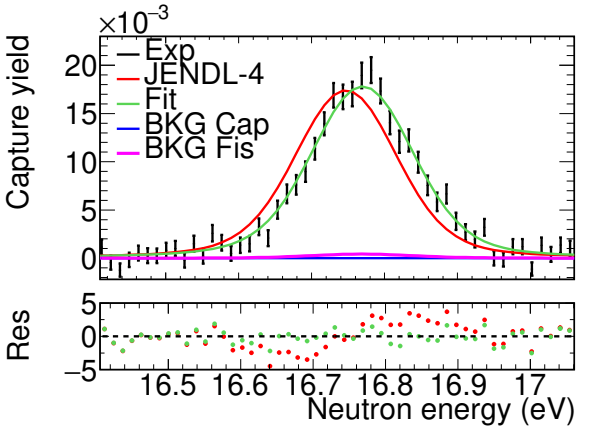

(d) Resonance 2: EAR1, ^{244}Cm sample

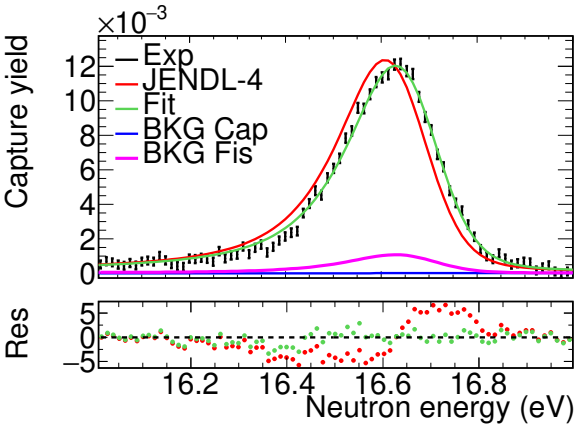

(e) Resonance 2: EAR2, ^{244}Cm sample

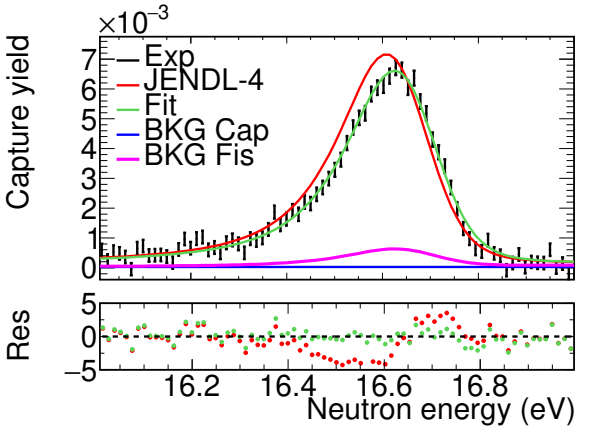

(f) Resonance 2: EAR2, ^{246}Cm sample

Figure C.1: Experimental ^{244}Cm capture yields close to the resonances at 7.67 and 16.8 eV (black) compared with the yield obtained with the JENDL-4.0 data (red) and with the yield obtained with the fit (green). In blue, the calculation of the background due to the other actinides and in pink the fission background.

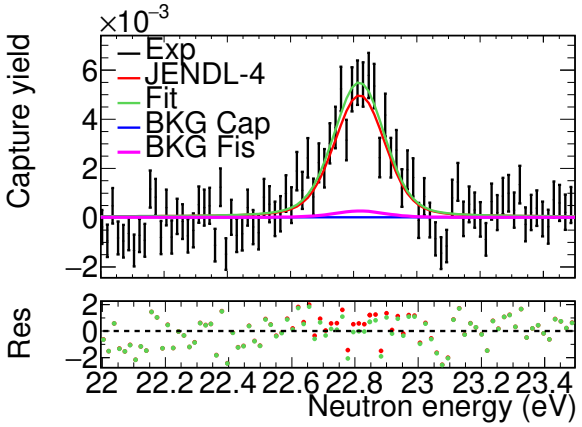

(a) Resonance 3: EAR1, ^{244}Cm sample

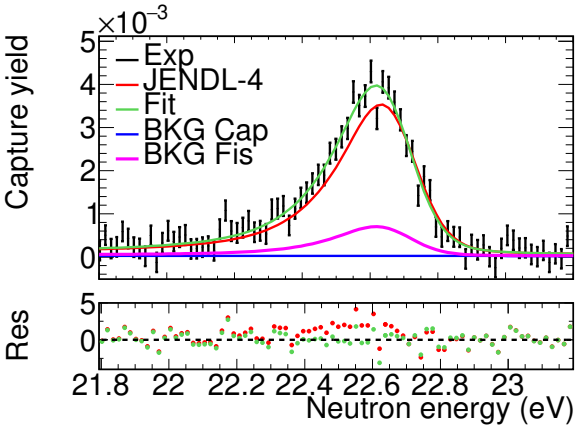

(b) Resonance 3: EAR2, ^{244}Cm sample

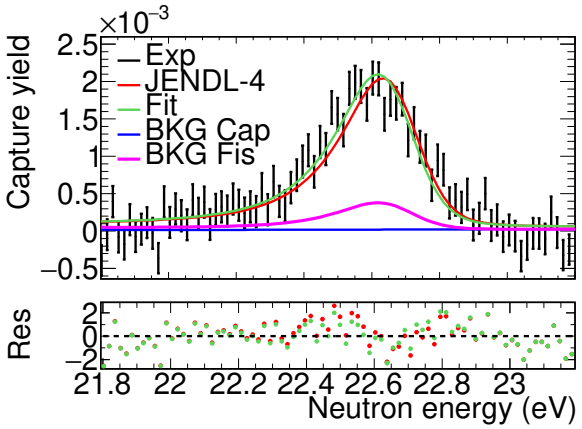

(c) Resonance 4: EAR2, ^{246}Cm sample

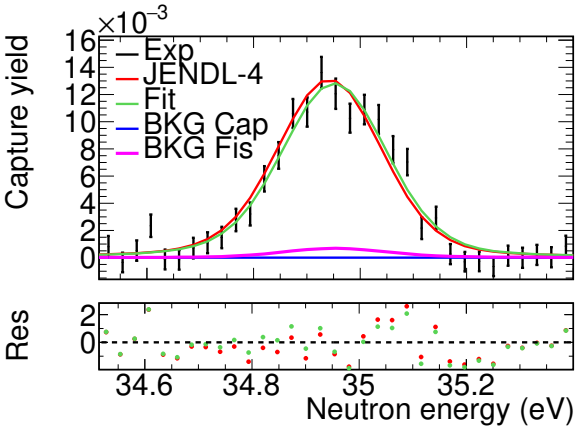

(d) Resonance 4: EAR1, ^{244}Cm sample

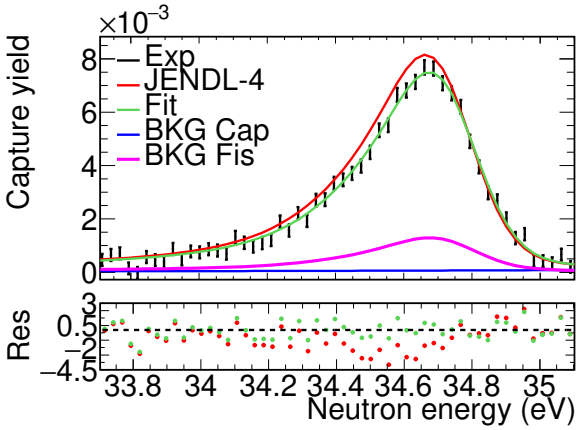

(e) Resonance 4: EAR2, ^{244}Cm sample

Figure C.2: Experimental ^{244}Cm capture yields close to the resonances at 22.85 and 34.99 (black) compared with the yield obtained with the JENDL-4.0 data (red) and with the yield obtained with the fit (green). In blue, the calculation of the background due to the other actinides and in pink the fission background.

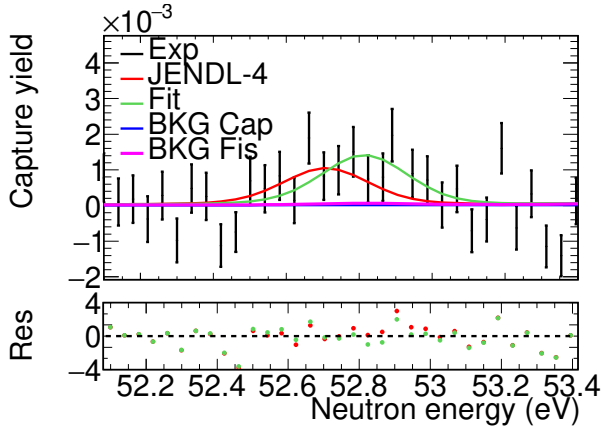

(a) Resonance 5: EAR1, ^{244}Cm sample

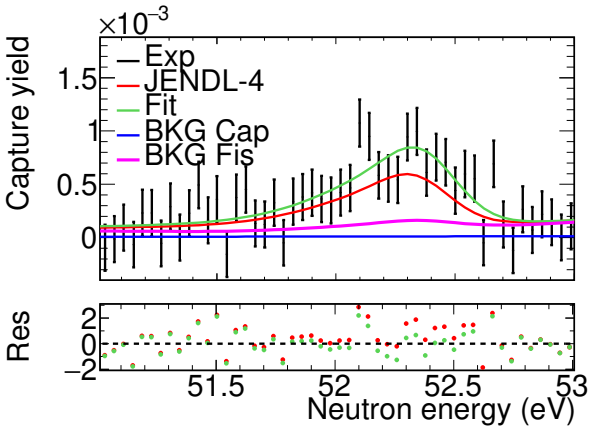

(b) Resonance 5: EAR2, ^{244}Cm sample

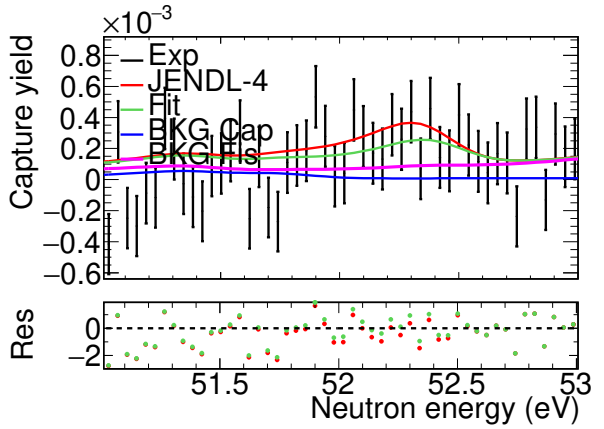

(c) Resonance 5: EAR2, ^{246}Cm sample

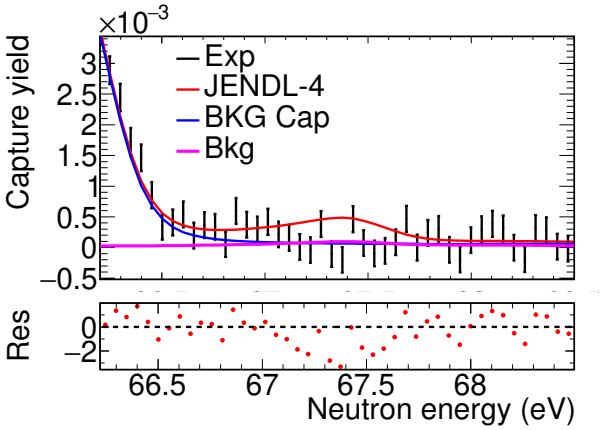

(d) No fitted: EAR2, ^{244}Cm sample

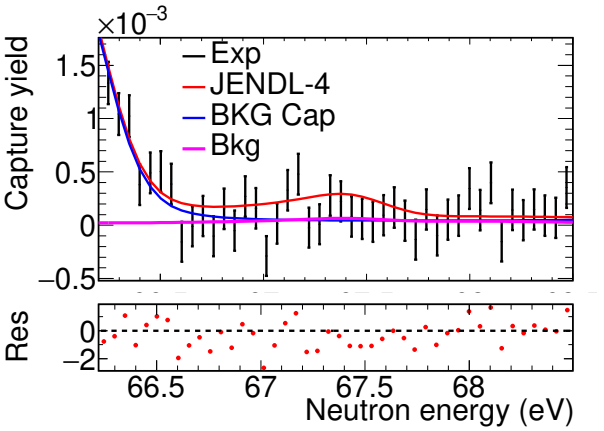

(e) No fitted: EAR2, ^{246}Cm sample

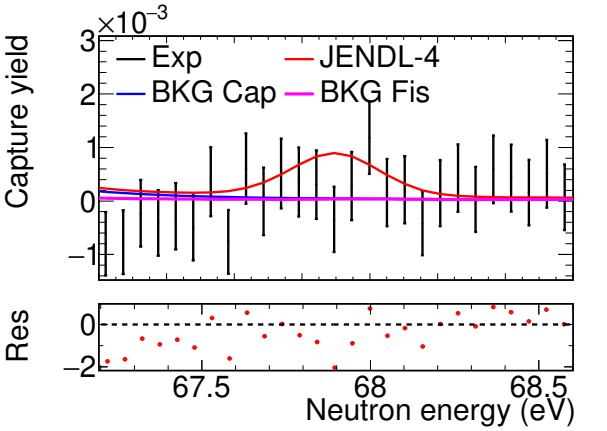

(f) No fitted: EAR1, ^{244}Cm sample

Figure C.3: Experimental ^{244}Cm capture yields close to the resonances at 52.78 and 67.99 eV (black) compared with the yield obtained with the JENDL-4.0 data (red) and with the yield obtained with the fit (green). The resonance at 67.99 eV has not been fitted. In blue, the calculation of the background due to the other actinides and in pink the fission background.

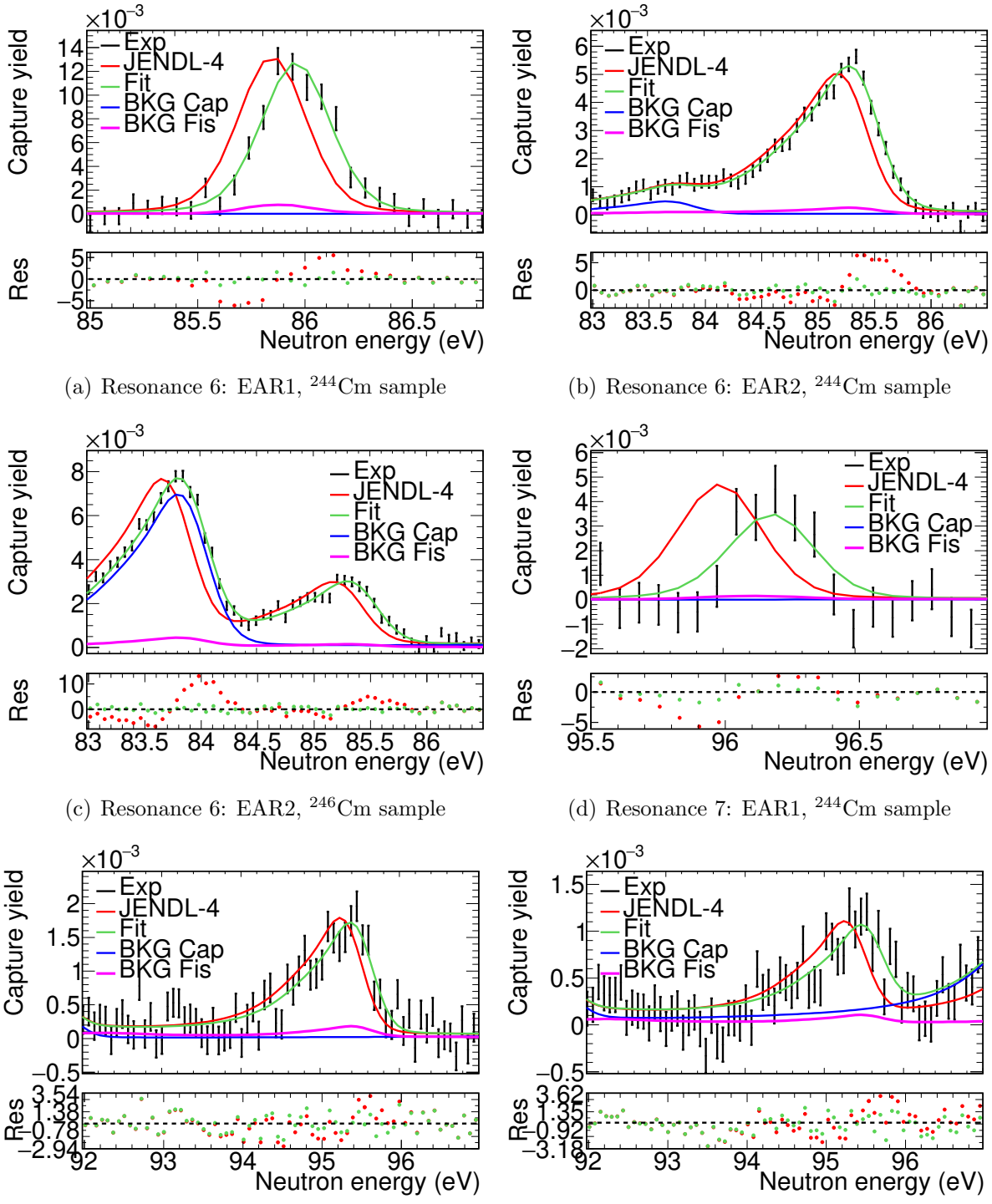

(a) Resonance 6: EAR1, ^{244}Cm sample

(b) Resonance 6: EAR2, ^{244}Cm sample

(c) Resonance 6: EAR2, ^{246}Cm sample

(d) Resonance 7: EAR1, ^{244}Cm sample

(e) Resonance 7: EAR2, ^{244}Cm sample

(f) Resonance 7: EAR2, ^{246}Cm sample

Figure C.4: Experimental ^{244}Cm capture yields close to the resonances at 85.96 and 96.12 eV (black) compared with the yield obtained with the JENDL-4.0 data (red) and with the yield obtained with the fit (green). In blue, the calculation of the background due to the other actinides and in pink the fission background.

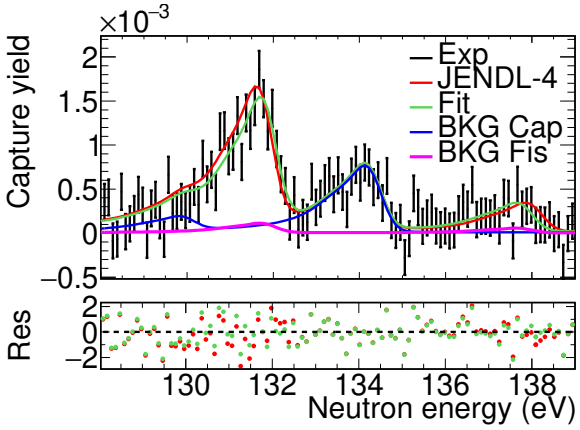

(a) Resonance 8 and 9: EAR2, ^{244}Cm sample

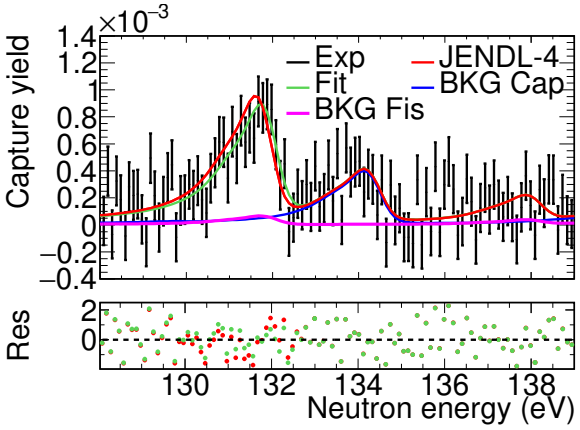

(b) Resonance 8: EAR2, ^{246}Cm sample

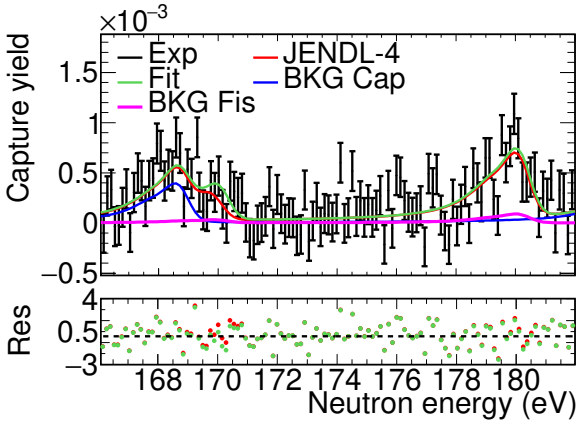

(c) Resonance 10 and 11: EAR2, ^{244}Cm sample

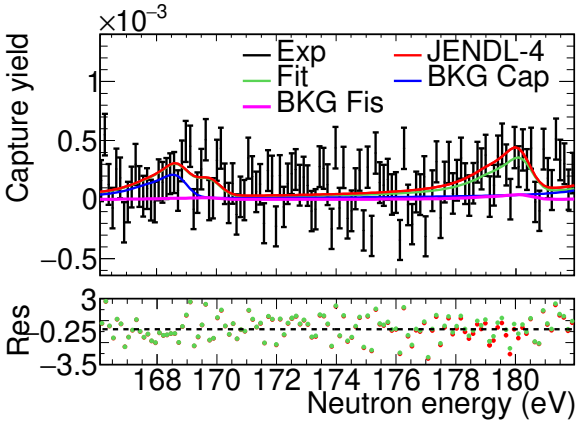

(d) Resonance 11: EAR2, ^{246}Cm sample

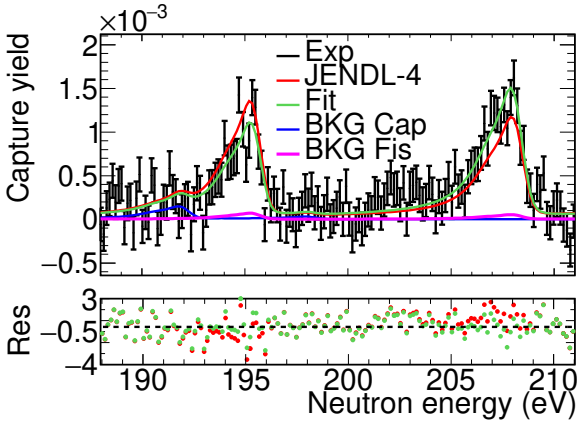

(e) Resonance 12 and 13: EAR2, ^{244}Cm sample

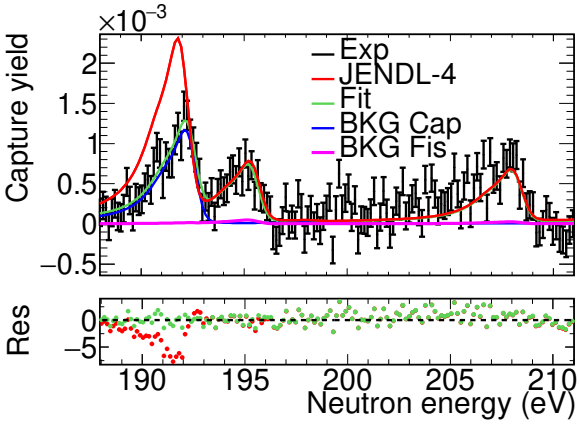

(f) Resonance 12: EAR2, ^{246}Cm sample

Figure C.5: Experimental ^{244}Cm capture yields close to the resonances at 132.80, 139.10, 171.20, 181.60, 197.0 and 209 eV (black) compared with the yield obtained with the JENDL-4.0 data (red) and with the yield obtained with the fit (green). In the data of the ^{244}Cm sample all the resonances were fitted and in the data of ^{246}Cm sample only the resonances at 132.80, 181.60 and 197.0 eV were fitted. In blue, the calculation of the background due to the other actinides and in pink the fission background.

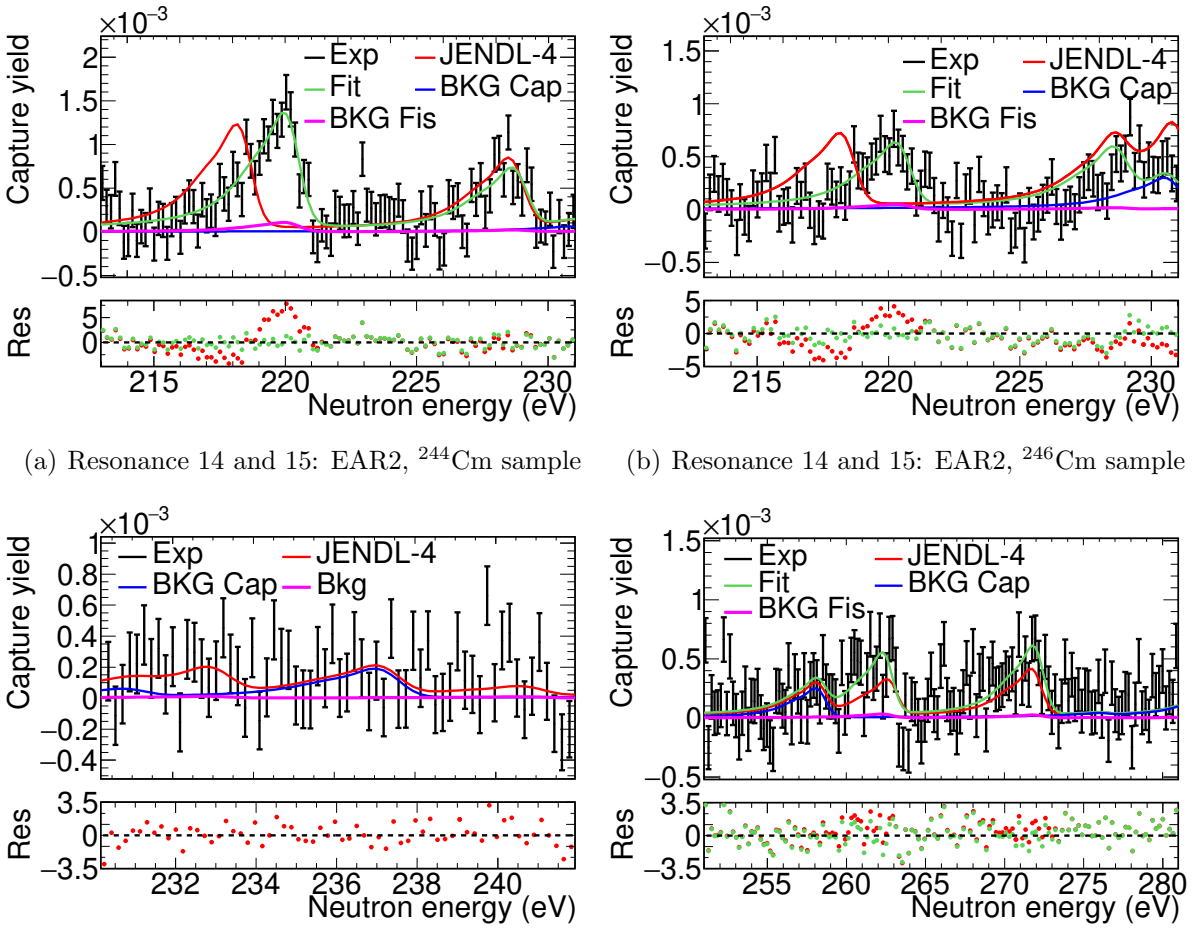

(a) Resonance 14 and 15: EAR2, ^{244}Cm sample

(b) Resonance 14 and 15: EAR2, ^{246}Cm sample

(c) Resonances at 234.90 and 242.70 eV: EAR2, ^{244}Cm sample

(d) Resonance 16 and 17: EAR2, ^{244}Cm sample

Figure C.6: Experimental ^{244}Cm capture yields close to the resonances at 220.10, 230.5, 234.9, 242.7, 264.9 and 274.10 eV (black) compared with the yield obtained with the JENDL-4.0 data (red) and with the yield obtained with the fit (green). The resonances at 234.9 and 242.7 eV are not fitted. In blue, the calculation of the background due to the other actinides and in pink the fission background.

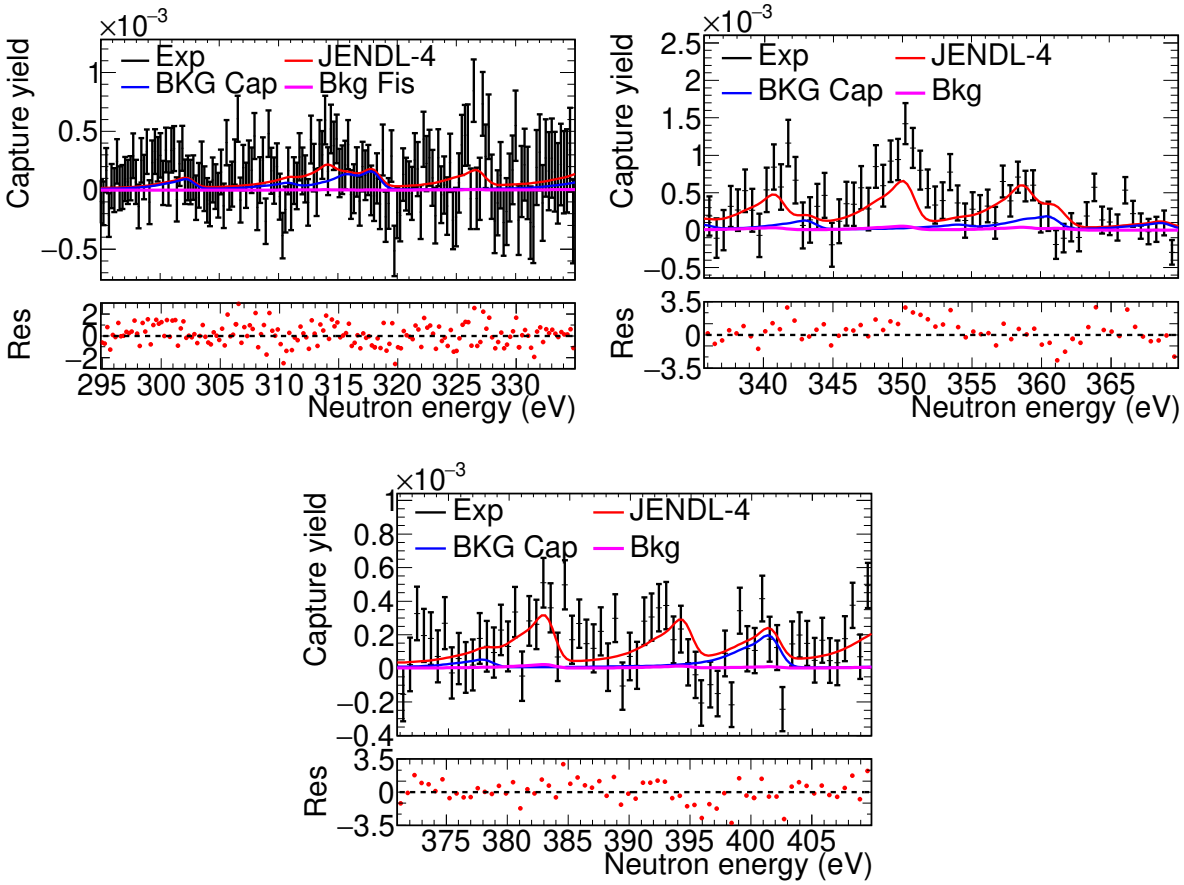

Figure C.7: Experimental yield of ^{244}Cm (black) from 300 to 410 eV compared with the yield obtained with the JENDL-4.0 data (red), the only measurement of the RP at this neutron energy is the one done by Moore so the JENDL-4.0 values are directly taken from this measurement. In blue, the calculation of the background due to the other actinides and in pink the fission background.

C.2 Fits of the ^{246}Cm resonances

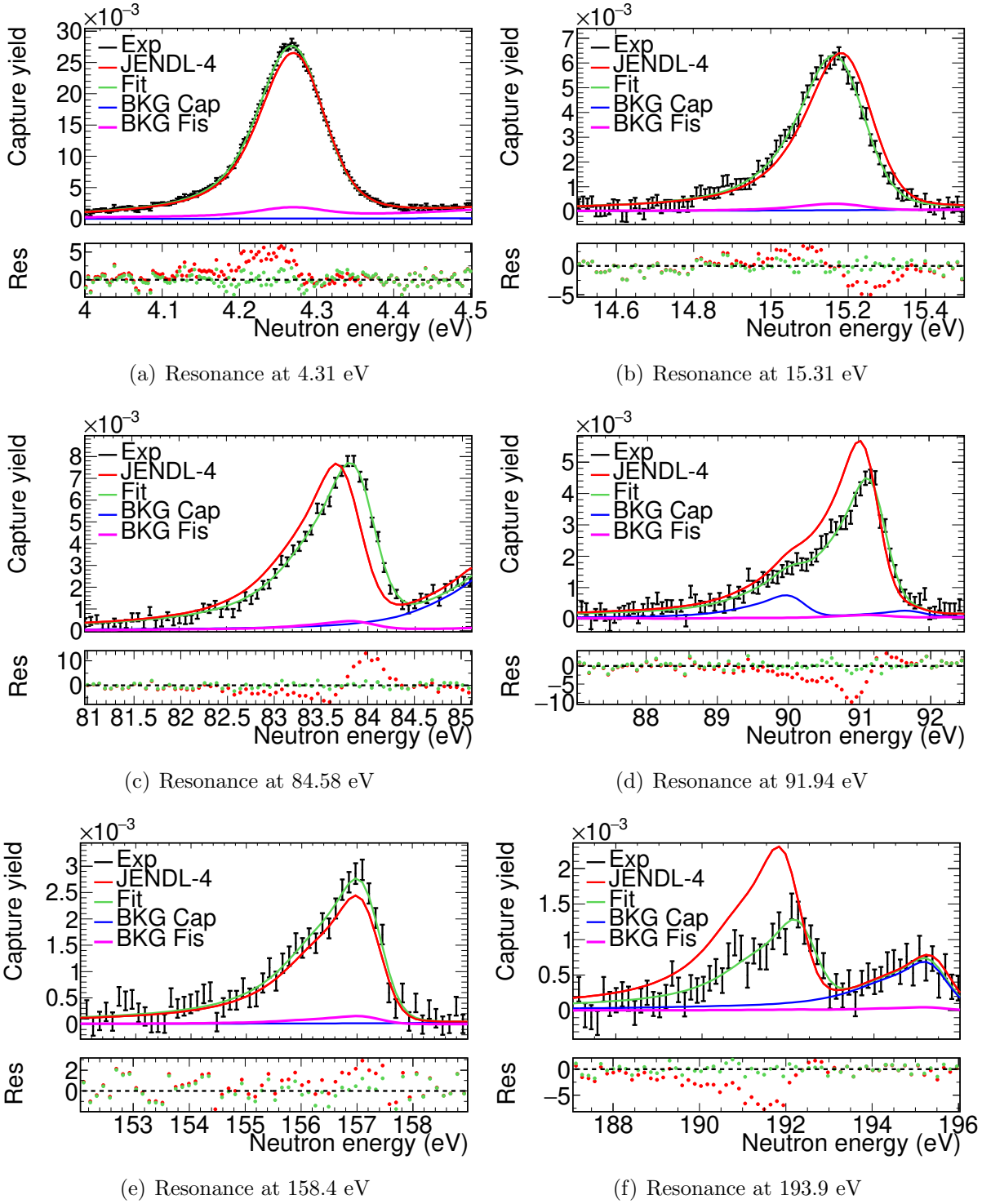

(a) Resonance at 4.31 eV

(b) Resonance at 15.31 eV

(c) Resonance at 84.58 eV

(d) Resonance at 91.94 eV

(e) Resonance at 158.4 eV

(f) Resonance at 193.9 eV

Figure C.8: Experimental ^{246}Cm capture yields close to the first six resonances (black) compared with the yield obtained with the JENDL-4.0 data (red) and with the yield obtained with the fit (green). In blue, the calculation of the background due to the other actinides and in pink the fission background.

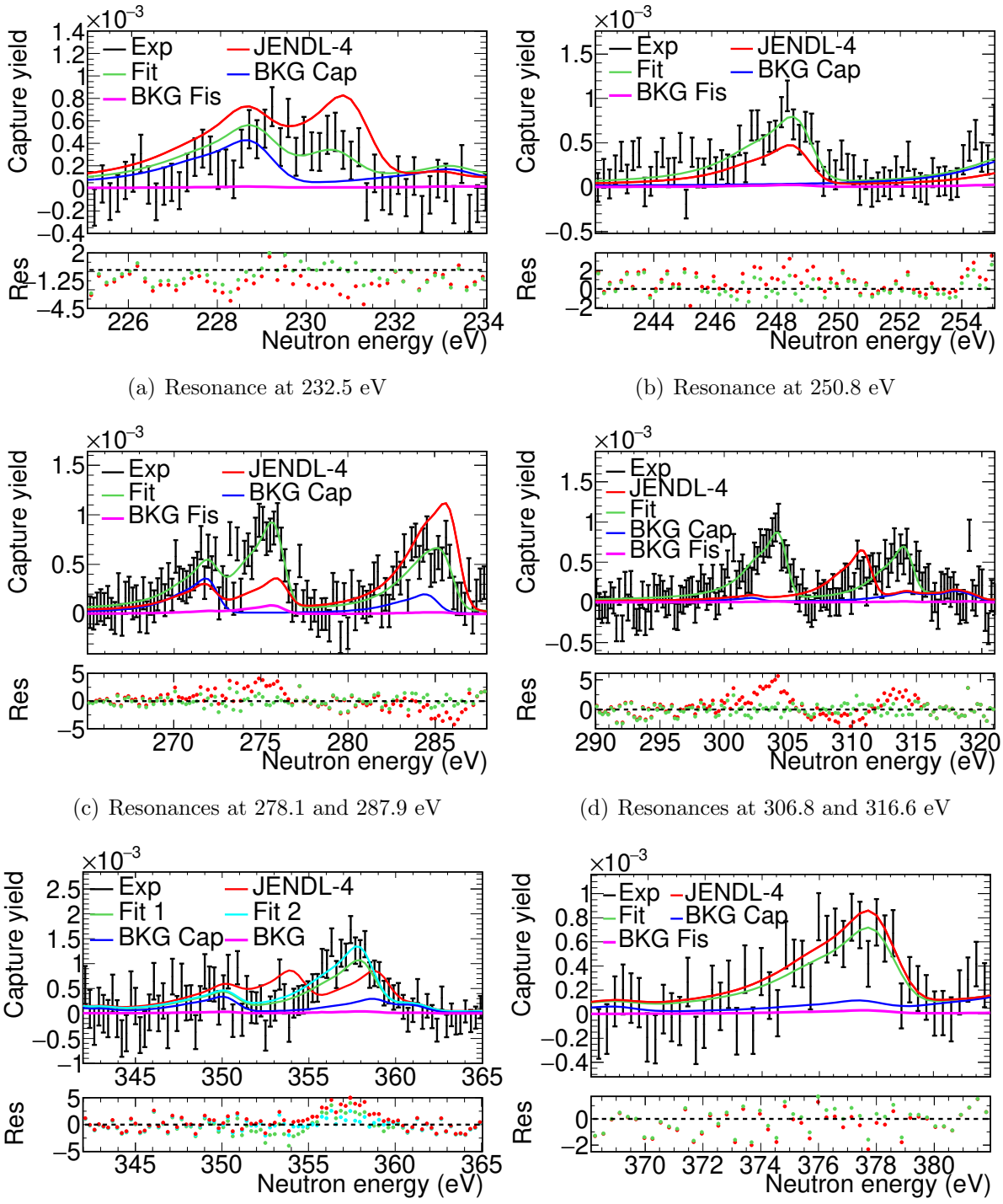

(a) Resonance at 232.5 eV

(b) Resonance at 250.8 eV

(c) Resonances at 278.1 and 287.9 eV

(d) Resonances at 306.8 and 316.6 eV

(e) Resonance at 361 eV

(f) Resonance at 381.1 eV

Figure C.9: Experimental ^{246}Cm capture yields close to the resonances between 230 and 400 eV (black) compared with the yield obtained with the JENDL-4.0 data (red) and with the yield obtained with the fit (green). In blue, the calculation of the background due to the other actinides and in pink the fission background.

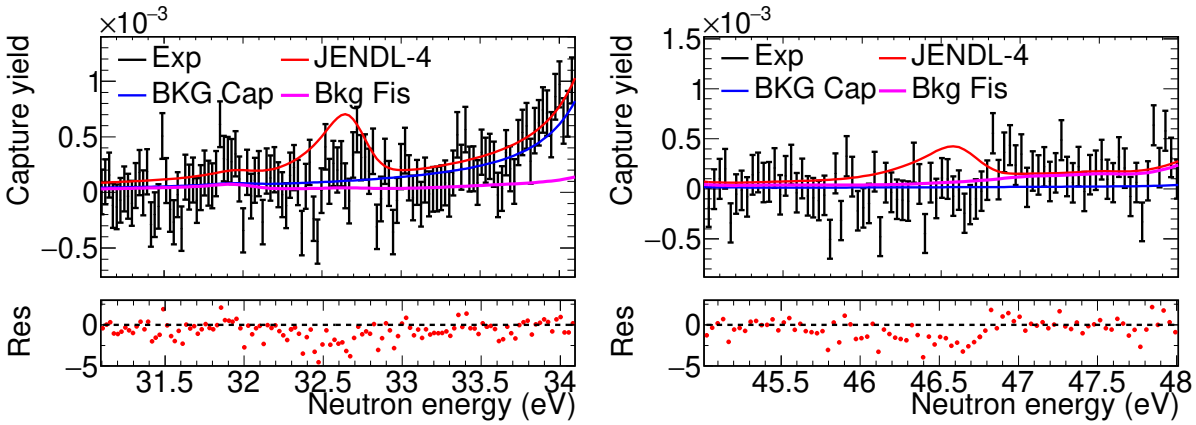

(a)

(b)

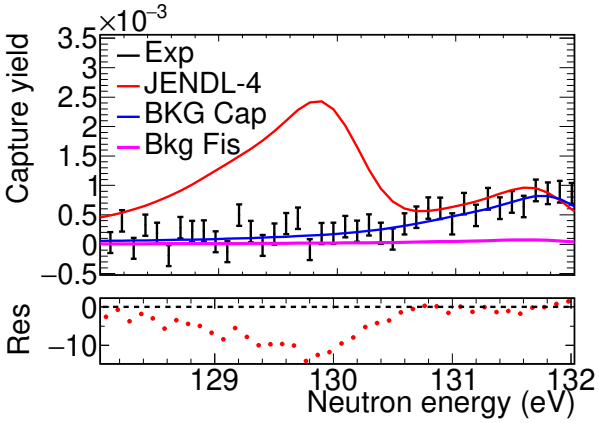

(c)

Figure C.10: Experimental ^{246}Cm capture yields close to the resonances at 32.95, 47 and 131 eV (black) compared with the yield obtained with the JENDL-4.0 data. In blue, the calculation of the background due to the other actinides and in pink the fission background.

C.3 Fits of the ^{248}Cm resonances

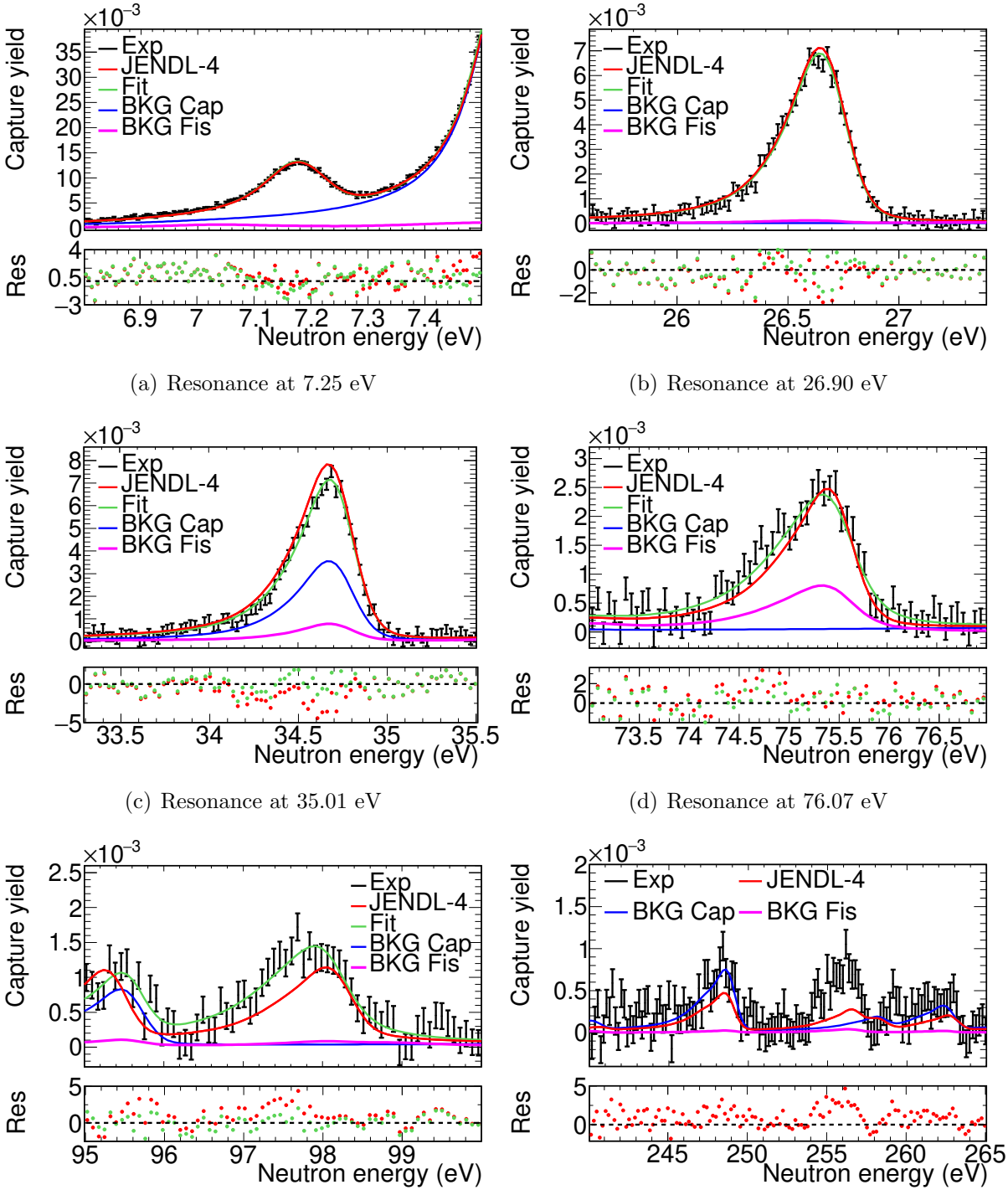

(a) Resonance at 7.25 eV

(b) Resonance at 26.90 eV

(c) Resonance at 35.01 eV

(d) Resonance at 76.07 eV

(e) Resonance at 98.84 eV

(f) Resonance at 260

Figure C.11: Experimental capture yields close to the resonances of ^{248}Cm (black) compared with the yield obtained with the JENDL-4.0 data (red) and with the yield obtained with the fit (green). In blue, the calculation of the background due to the other actinides and in pink the fission background.

C.4 Fits of the ^{240}Pu resonances

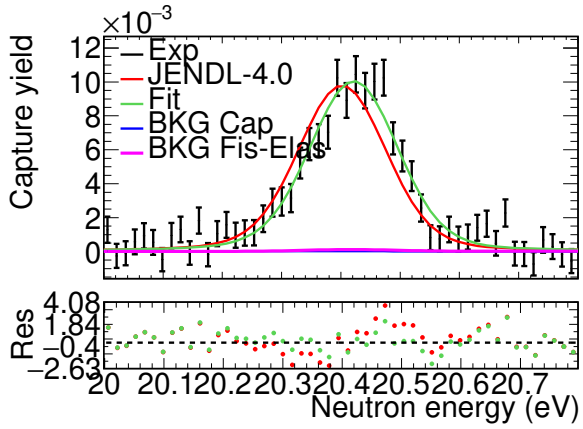

(a) Resonance at 20.4 eV. EAR1, ^{244}Cm sample

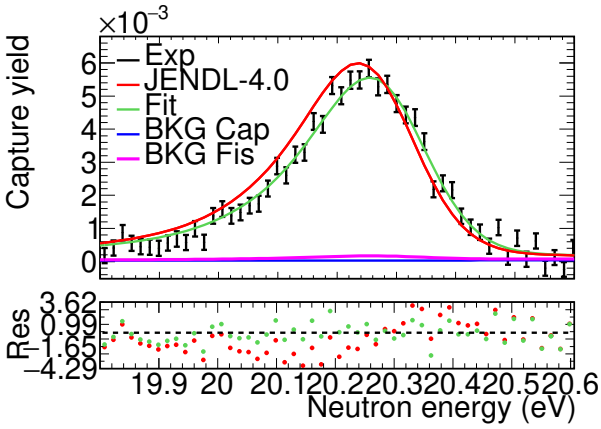

(b) Resonance at 20.4 eV. EAR2, ^{244}Cm sample

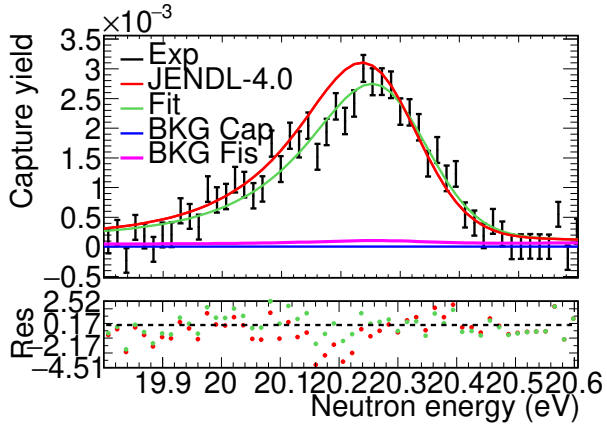

(c) Resonance at 20.4 eV. EAR2, ^{246}Cm sample

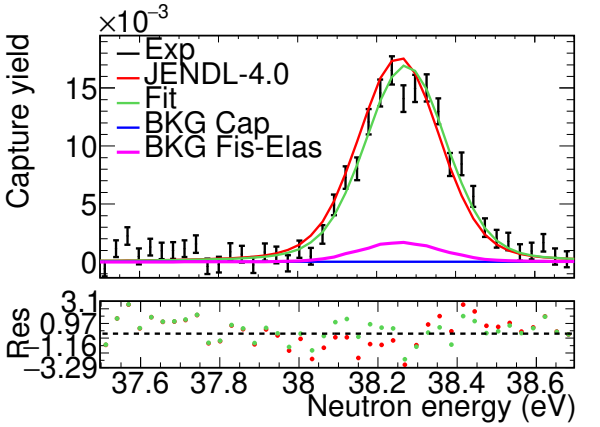

(d) Resonance at 38.3 eV. EAR1, ^{244}Cm sample

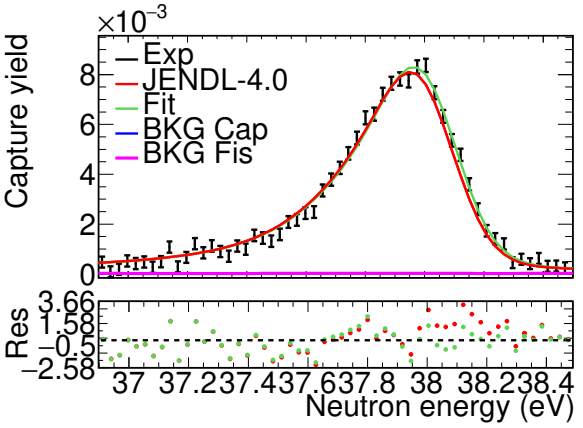

(e) Resonance at 38.3 eV. EAR2, ^{244}Cm sample

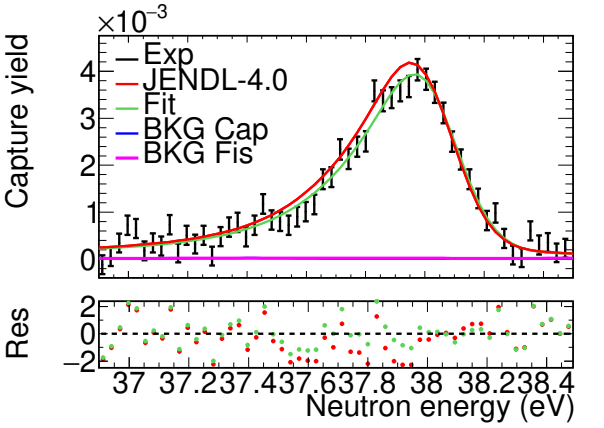

(f) Resonance at 38.3 eV. EAR2, ^{246}Cm sample

Figure C.12: Experimental ^{240}Pu capture yields close to the resonances at 20.4 and 38.3 eV compared (black) compared with the yield obtained with the JENDL-4.0 data (red) and with the yield obtained with the fit (green). In blue, the calculation of the background due to the other actinides and in pink the fission background.

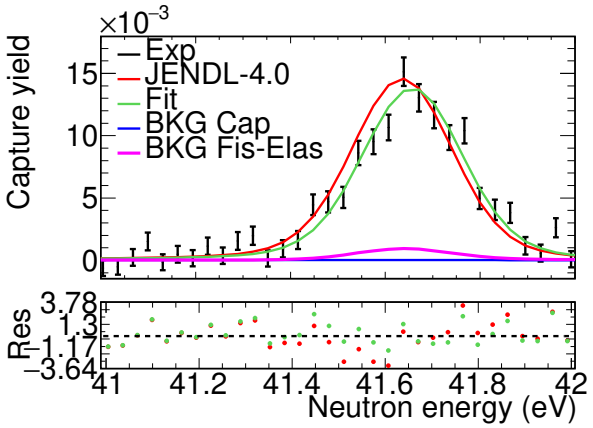

(a) Resonance at 41.7 eV. EAR1, ^{244}Cm sample

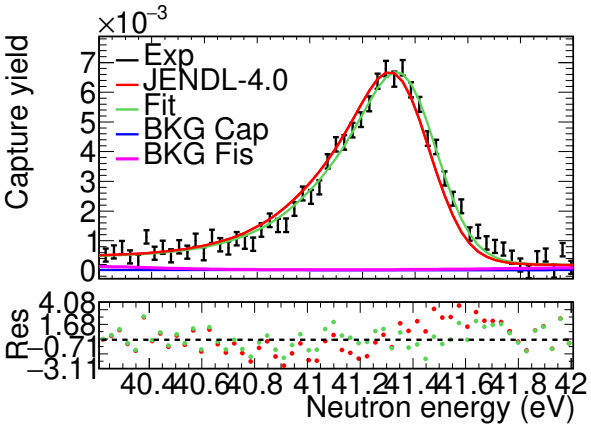

(b) Resonance at 41.7 eV. EAR2, ^{244}Cm sample

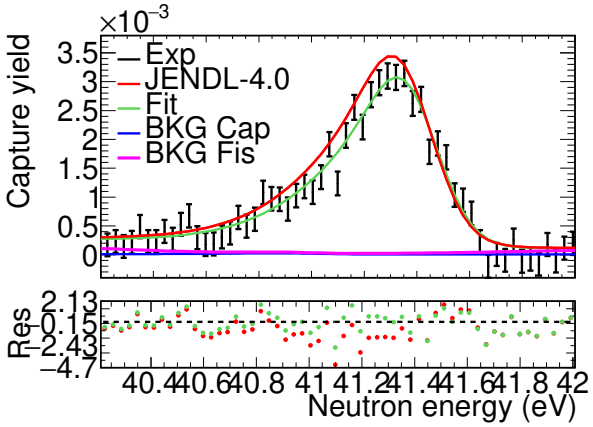

(c) Resonance at 41.7 eV. EAR2, ^{246}Cm sample

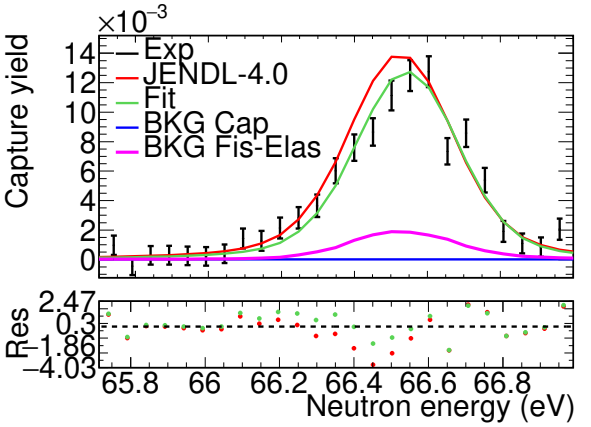

(d) Resonance at 66.6 eV. EAR1, ^{244}Cm sample

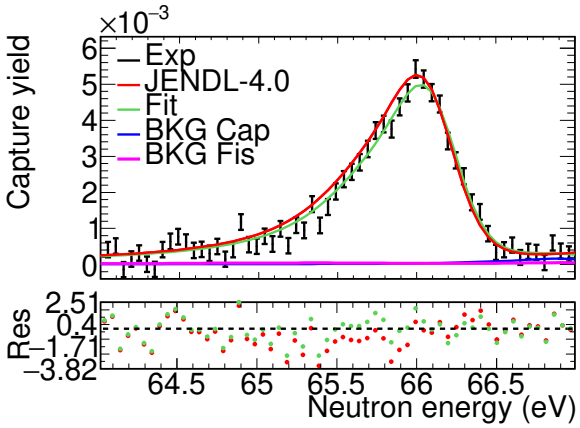

(e) Resonance at 66.6 eV. EAR2, ^{244}Cm sample

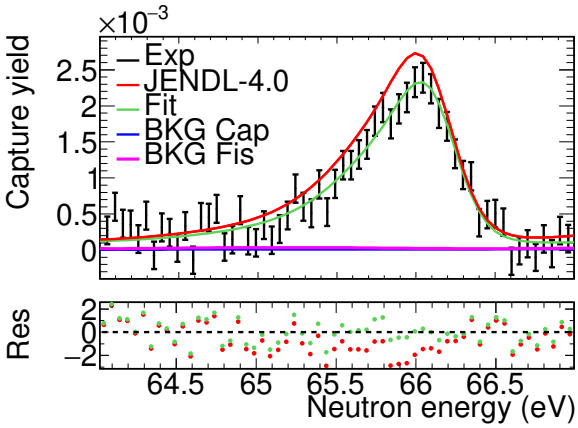

(f) Resonance at 66.6 eV. EAR2, ^{246}Cm sample

Figure C.13: Experimental ^{240}Pu capture yields close to the resonances at 41.7 and 66.6 eV (black) compared with the yield obtained with the JENDL-4.0 data (red) and with the yield obtained with the fit (green). In blue, the calculation of the background due to the other actinides and in pink the fission background.

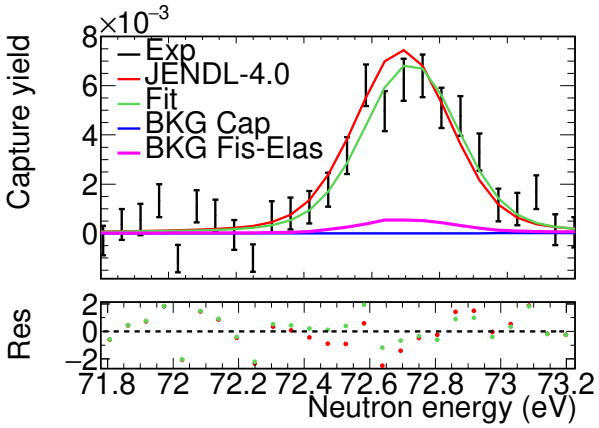

(a) Resonance at 72.8 eV. EAR1, ^{244}Cm sample

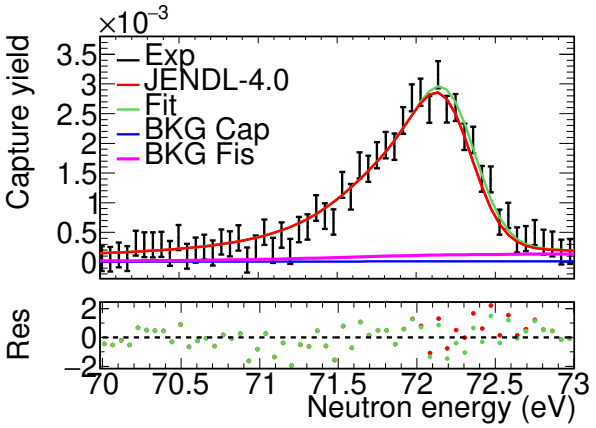

(b) Resonance at 72.8 eV. EAR2, ^{244}Cm sample

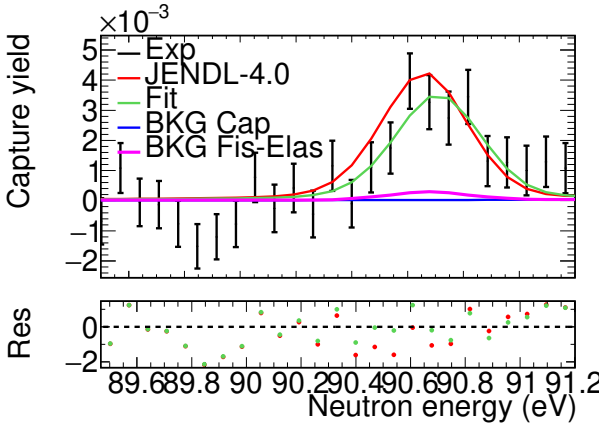

(c) Resonance at 90.8 eV. EAR1, ^{244}Cm sample

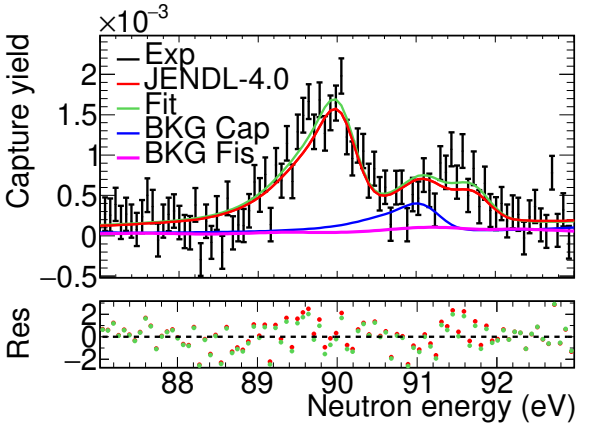

(d) Resonance at 90.8 and 92.4 eV. EAR2, ^{244}Cm sample

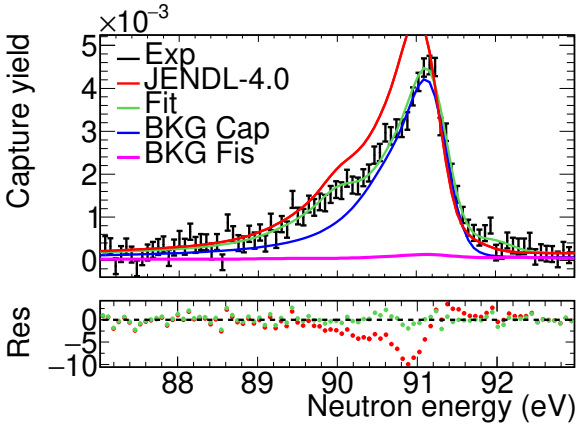

(e) Resonance at 90.8 eV. EAR2, ^{246}Cm sample

Figure C.14: Experimental ^{240}Pu capture yields close to the resonances at 2.8 and the 90.8 eV (black) compared with the yield obtained with the JENDL-4.0 data (red) and with the yield obtained with the fit (green). In blue, the calculation of the background due to the other actinides and in pink the fission background.

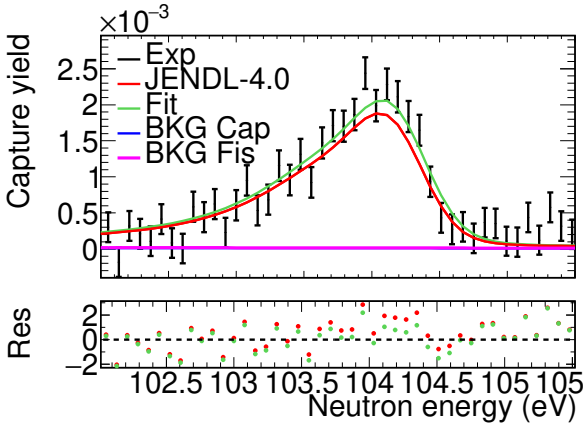

(a) Resonance at 105.0 eV. EAR2, ^{244}Cm sample

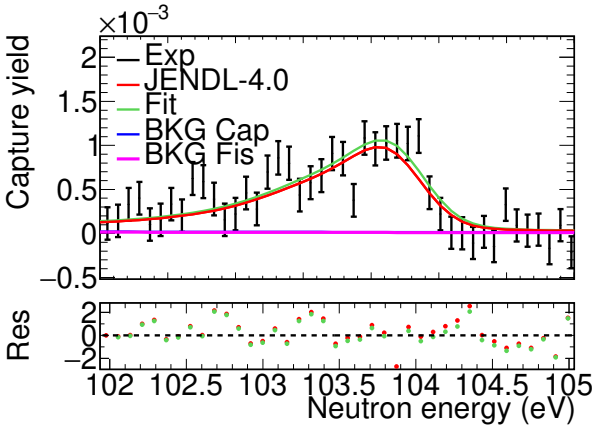

(b) Resonance at 105.0 eV. EAR2, ^{246}Cm sample

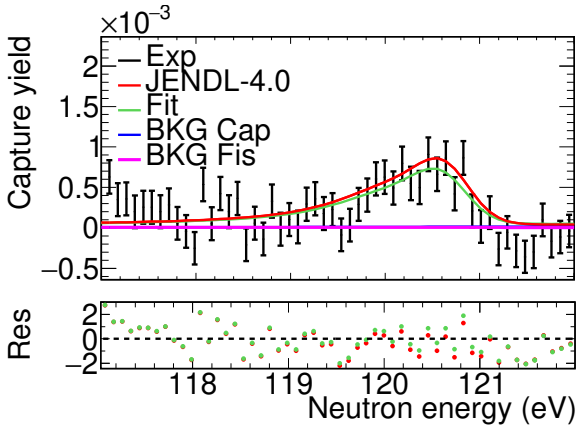

(c) Resonance at 121.6 eV. EAR2, ^{244}Cm sample

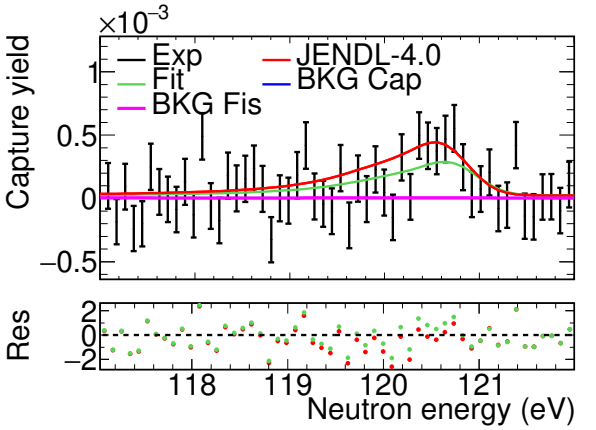

(d) Resonance at 121.6 eV. EAR2, ^{246}Cm sample

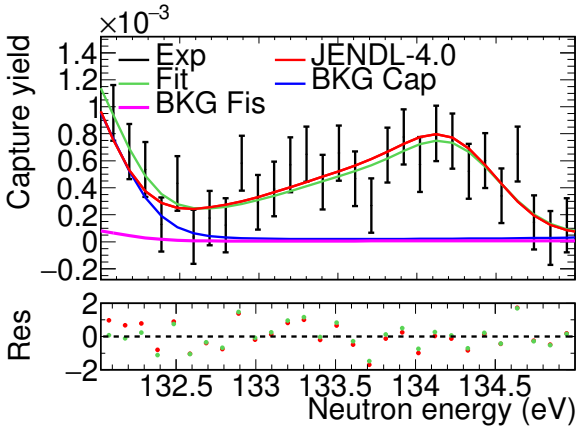

(e) Resonance at 135.3 eV. EAR2, ^{244}Cm sample

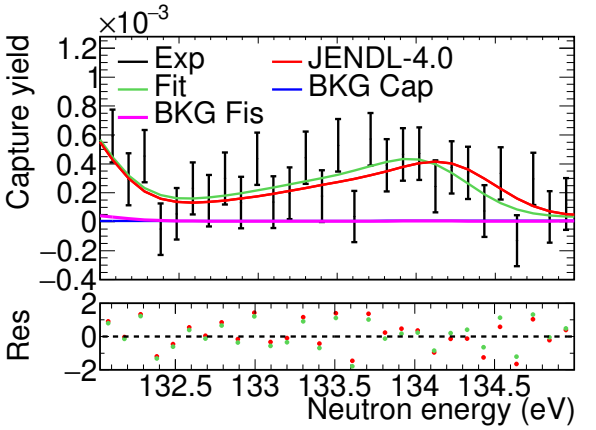

(f) Resonance at 135.3 eV. EAR2, ^{246}Cm sample

Figure C.15: Experimental ^{240}Pu capture yields close to the resonances at 105.0, 121.6 and 135.3 eV (black) compared with the yield obtained with the JENDL-4.0 data (red) and with the yield obtained with the fit (green). In blue, the calculation of the background due to the other actinides and in pink the fission background.

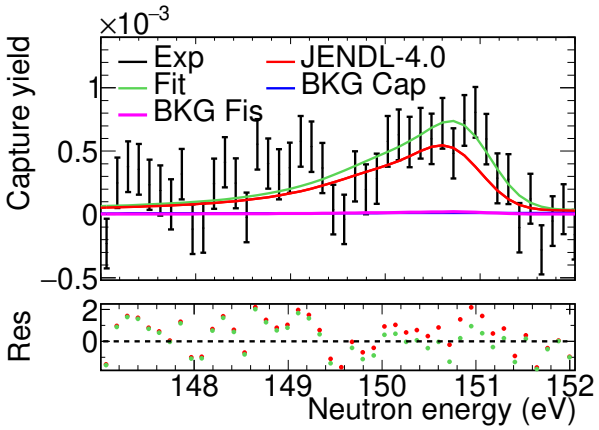

(a) Resonance at 152.0 eV. EAR2, ^{244}Cm sample

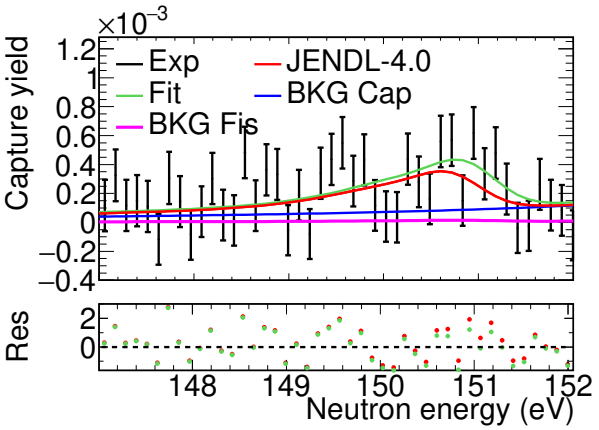

(b) Resonance at 152.0 eV. EAR2, ^{246}Cm sample

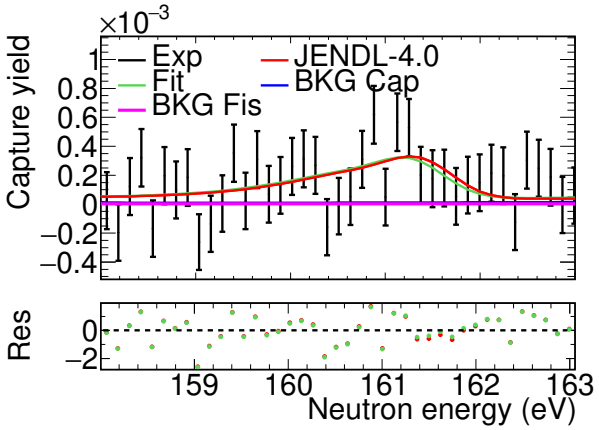

(c) Resonance at 162.7 eV. EAR2, ^{244}Cm sample

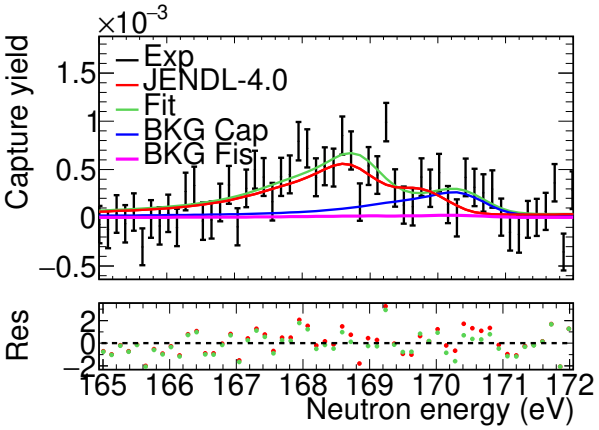

(d) Resonance at 170.1 eV. EAR2, ^{244}Cm sample

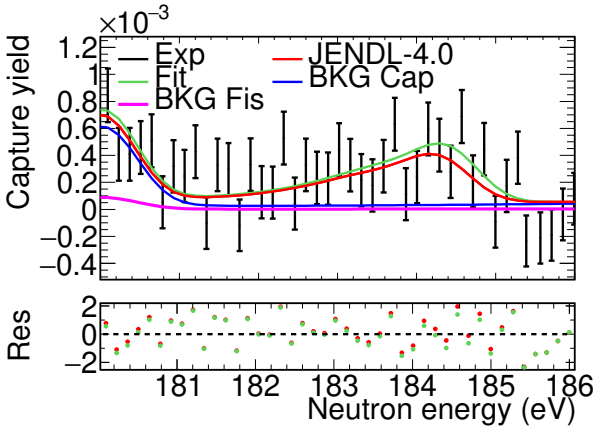

(e) Resonance at 185.8 eV. EAR2, ^{244}Cm sample

Figure C.16: Experimental ^{240}Pu capture yields close to the resonances at 152.0, 162.7, 170.1 eV (black) compared with the yield obtained with the JENDL-4.0 data (red) and with the yield obtained with the fit (green). In blue, the calculation of the background due to the other actinides and in pink the fission background.

List of Figures

.

List of Tables

Bibliography

[1] Key world energy statistics, 2020. *IEA Publications, International Energy Agency*, 2020. (15, 16, 17)

[2] U.S. Energy Information Administration. International Energy Outlook 2019 with projections to 2050. URL https://www.eia.gov/ieo. (15, 16)

[3] Enrico Fermi. Experimental Production of a Divergent Chain Reaction. *American Journal of Physics*, 20(9):536–558, 1952. DOI link: 10.1119/1.1933322. (16)

[4] Nuclear Share of Electricity Generation in 2019. Retrieved 28 June 2020. *IAEA 27 June 2020.* URL https://pris.iaea.org/PRIS/WorldStatistics/NuclearShareofElectricityGeneration.aspx. (16, 18, 19)

[5] Organisation Economic for Co-Operation and 75 . Paris (France) Development - Nuclear Energy Agency. *Physics and safety of transmutation systems A status report.* Organisation for Economic Co-Operation and Development - Nuclear Energy Agency, Nuclear Energy Agency of the OECD (NEA), 2006. ISBN 92-64-01082-3. URL http://inis.iaea.org/search/search.aspx?orig_q=RN:37021771. MANAGEMENT OF RADIOACTIVE WASTES, AND NON-RADIOACTIVE WASTES FROM NUCLEAR FACILITIES. (19, 22)

[6] John Wagner, Donald Mueller, Jess Gehin, et al. Categorization of Used Nuclear Fuel Inventory in Support of a Comprehensive National Nuclear Fuel Cycle Strategy. 10 2013. URL https://inis.iaea.org/search/search.aspx?orig_q=RN:44068822. (19)

[7] R. W. Benjamin, C. E. Ahlfeld, J. A. Harvey, and N. W. Hill. Neutron Total Cross Section of Curium-248. *Nuclear Science and Engineering*, 55(4):440–449, 1974. (20, 26, 28, 143, 158)

[8] J. R. Berreth, F. B. Simpson, and B. C. Rusche. The Total Neutron Cross Sections of the Curium Isotopes from 0.01 to 30 eV. *Nuclear Science and Engineering*, 49 (2):145–152, 1972. (20, 26, 145, 158)

[9] E. Mendoza. *Measurement of the ^{243}Am capture cross section at the n_TOF facility.* PhD thesis, 2014. (20, 61, 62, 73, 76, 81, 83, 84, 85, 132, 137, 145)

[10] *Classification of Radioactive Waste.* Number GSG-1 in General Safety Guides. INTERNATIONAL ATOMIC ENERGY AGENCY, Vienna, 2009. ISBN 978-92-0-109209-0. URL https://www.iaea.org/publications/8154/classification-of-radioactive-waste. (20)

[11] Geological disposal of radioactive wastes: national commitment, local and regional involvement A Collective Statement of the OECD Nuclear Energy Agency Radioactive Waste Management Committee, adopted March 2011. Technical report, Nuclear Energy Agency of the OECD (NEA), Apr 2012. URL http://inis.iaea.org/search/search.aspx?orig_q=RN:48099152. NEA-RWM–2011-16. (20)

[12] ICRP. Age-dependent Doses to the Members of the Public from Intake of Radionuclides - Part 5 Compilation of Ingestion and Inhalation Coefficients. *ICRP Publication 72. Ann. ICRP 26 (1).*, 1995. (20)

[13] A. G. Croff. ORIGEN2: A versatile computer code for calculating the nuclide compositions and characteristics of nuclear materials. *Nuclear Technology*, 62(3): 335–352, 1983. ISSN 0029-5450. URL http://inis.iaea.org/search/search.aspx?orig_q=RN:15034357. (21)

[14] Gerardo Aliberti, G. Palmiotti, Massimo Salvatores, et al. Nuclear data sensitivity, uncertainty and target accuracy assessment for future nuclear systems. *Annals of Nuclear Energy*, 33:700–733, 05 2006. DOI link: 10.1016/j.anucene.2006.02.003. (22, 25, 173)

[15] F. Carminati, R. Klapisch, J. P. Revol, C. Roche, J. A. Rubio, and C. Rubbia. An Energy amplifier for cleaner and inexhaustible nuclear energy production driven by a particle beam accelerator. 11 1993. URL https://cds.cern.ch/record/256520/files/at-93-047.pdf. (22)

[16] Organisation Economic for Co-Operation and Nuclear Energy Agency 75 . Paris (France) Development. *Accelerator-driven systems (ADS) and fast reactors (FR) in advanced nuclear fuel cycles.* Organisation for Economic Co-Operation and Development - Nuclear Energy Agency, Nuclear Energy Agency of the OECD (NEA), 2002. ISBN 92-64-18482-1. URL http://inis.iaea.org/search/search.aspx?orig_q=RN:33039274. MANAGEMENT OF RADIOACTIVE WASTES, AND NON-RADIOACTIVE WASTES FROM NUCLEAR FACILITIES. (22)

[17] The Generation IV International Forum. (July 1, 2021). . URL https://www.gen-4.org/gif/. (22)

[18] Technology Roadmap for Generation IV Nuclear Energy Systems. Technical report, . URL https://www.gen-4.org/gif/jcms/c_40481/technology-roadmap. (22)

[19] Multi purpose hYbrid Research Reactor for High-tech Applications. (July , 2021). URL http://myrrha.sckcen.be/. (22)

[20] K. Shibatai, O. Iwamoto, T. Nakagawa, et al. JENDL-4.0: A New Library for Nuclear Science and Engineering. *Journal of Nuclear Science and Technology*, 48 (1):1–30, 2011. DOI link: 10.1080/18811248.2011.9711675. (23, 29, 41, 135, 158, 174)

[21] Niels Bohr and John Archibald Wheeler. The Mechanism of Nuclear Fission. *Phys. Rev.*, 56:426–450, Sep 1939. DOI link: 10.1103/PhysRev.56.426. (24)

[22] E. P. Wigner and L. Eisenbud. Higher Angular Momenta and Long Range Interaction in Resonance Reactions. *Phys. Rev.*, 72:29–41, Jul 1947. DOI link: 10.1103/PhysRev.72.29. (24)

[23] G. Breit and E. Wigner. Capture of Slow Neutrons. *Phys. Rev.*, 49:519–531, Apr 1936. DOI link: 10.1103/PhysRev.49.519. (24)

[24] A. M. Lane and R. G. Thomas. R-Matrix Theory of Nuclear Reactions. *Rev. Mod. Phys.*, 30:257–353, Apr 1958. DOI link: 10.1103/RevModPhys.30.257. (24)

[25] F. H. Frohner. *Evaluation and analysis of nuclear resonance data*. Evaluation et analyse des donnees relatives aux resonances nucleaires. Organisation for Economic Co-Operation and Development, Nuclear Energy Agency of the OECD (NEA), 2000. ISBN 92-64-18272-1. URL http://inis.iaea.org/search/search.aspx?orig_q=RN:32011631. NUCLEAR PHYSICS AND RADIATION PHYSICS. (25, 130, 131, 139)

[26] N. Otuka, E. Dupont, V. Semkova, et al. Towards a More Complete and Accurate Experimental Nuclear Reaction Data Library (EXFOR): International Collaboration Between Nuclear Reaction Data Centres (NRDC). *Nuclear Data Sheets*, pages 272–276. ISSN 0090-3752. DOI link: 10.1016/j.nds.2014.07.065. (25)

[27] others. URL http://www-nds.iaea.org/exfor/exfor.htm. (25)

[28] V.V. Zerkin and B. Pritychenko. The experimental nuclear reaction data (EXFOR): Extended computer database and Web retrieval system. *Nuclear Instruments and Methods in Physics Research Section A: Accelerators, Spectrometers, Detectors and Associated Equipment*, pages 31–43. ISSN 0168-9002. DOI link: 10.1016/j.nima.2018.01.045. (25)

[29] R. E. Coté, R. F. Barnes, and H. Diamond. Total Neutron Cross Section of Cm^{244}. *Phys. Rev.*, 134:B1281–B1284, Jun 1964. DOI link: 10.1103/PhysRev.134.B1281. (26, 145, 158)

[30] T. S. Belanova, Yu. S. Zamyatnin, A. G. Kolesov, et al. Neutron resonances in 244Cm,245Cm,246Cm, and248Cm. *Soviet Atomic Energy*, 39(5):1020–1021, Nov 1975. ISSN 1573-8205. DOI link: 10.1007/BF01126376. (26, 28)

[31] M.S. Moore and G.A. Keyworth. Analysis of the Fission and Capture Cross Sections of the Curium Isotopes. *Phys. Rev. C*, 3:1656–1667, 1971. DOI link: 10.1103/PhysRevC.3.1656. (26, 173)

[32] Atsushi Kimura, Toshiyuki Fujii, Satoshi Fukutani, et al. Neutron-capture cross-sections of 244Cm and 246Cm measured with an array of large germanium detectors in the ANNRI at J-PARC/MLF. *Journal of Nuclear Science and Technology*, 49 (7):708–724, 2012. DOI link: 10.1080/00223131.2012.693887. (26, 28, 40, 41, 145, 152, 158, 171, 173)

[33] Shoichiro Kawase, Atsushi Kimura, Hideo Harada, et al. Neutron capture cross sections of curium isotopes measured with ANNRI at J-PARC. *Journal of Nuclear Science and Technology*, 58(7):764–786, 2021. DOI link: 10.1080/00223131.2020.1864492. (26, 28, 145, 158, 171, 173)

[34] Jr. Harold T. Maguire, Carlos R. S. Stopa, Robert C. Block, et al. Neutron-Induced Fission Cross-Section Measurements of 244Cm, 246Cm, and 248Cm. *Nuclear Science and Engineering*, 89(4):293–304, 1985. (26, 28)

[35] A. A. Alekseev, A. A. Bergman, A. I. Berlev, et al. Cross section for the subbarrier fission of 244Cm. *Physics of Atomic Nuclei*, 73(9):1487–1498, Sep 2010. ISSN 1562-692X. DOI link: 10.1134/S1063778810090036. (26, 28)

[36] A. A. Alekseev, A. A. Bergman, A. I. Berlev, et al. Cross section for 246Cm subbarrier fission. *Physics of Atomic Nuclei*, 73(10):1645–1655, Oct 2010. ISSN 1562-692X. DOI link: 10.1134/S1063778810100029. (26, 28)

[37] A. A. Alekseev, A. A. Bergman, A. I. Berlev, et al. 246–248Cm Neutron fission cross sections and resonance integrals. *Atomic Energy*, 109(6):408, Apr 2011. ISSN 1573-8205. DOI link: 10.1007/s10512-011-9376-6. (26, 28)

[38] L. Bollinger, R. E. Coté, and G. E. Thomas. A critical analysis of the design and application of neutron choppers. In *Proceedings of the Second International Conference on Peaceful Uses of Atomic Energy, Geneva*, volume 14, page 239, 1959. (26, 170)

[39] M. S. Moore, W. K. Brown, M. E. Ennis, et al. *Fission and capture cross-sections of curium*. IAEA, International Atomic Energy Agency (IAEA), 1970. URL http://inis.iaea.org/search/search.aspx?orig_q=RN:43040578. NUCLEAR PHYSICS AND RADIATION PHYSICS. (26)

[40] B C Diven. Nuclear Explosions as a Nuclear Physics Tool. *Annual Review of Nuclear Science*, 20(1):79–104, 1970. DOI link: 10.1146/annurev.ns.20.120170.000455. (26)

[41] A. Hemmendinger, M. G. Silbert, and A. Moat. Transient Response of Solid State Detectors. *IEEE Transactions on Nuclear Science*, 12(1):304–307, 1965. DOI link: 10.1109/TNS.1965.4323527. (26)

[42] A. N. Ellis, W. K. Brown, J. A. Farrell, and R. R. Fullwood. A Method of Calibration of Moxon-Rae Detectors. *IEEE Transactions on Nuclear Science*, 18(1):205–207, 1971. DOI link: 10.1109/TNS.1971.4325865. (26)

[43] R. G. Fluharty, F. B. Simpson, and O. D. Simpson. Neutron Resonance Measurements of Ag, Ta, and U^{238}. *Phys. Rev.*, 103:1778–1786, Sep 1956. DOI link: 10.1103/PhysRev.103.1778. (28)

[44] R.L. Macklin. Gamma flash suppression for the ORELA pulsed neutron source. *Nuclear Instruments and Methods*, 91(1):79–84, 1971. ISSN 0029-554X. DOI link: 10.1016/0029-554X(71)90641-0. (28)

[45] S.M. Kalebin et al. Proceedings of conference on neutron physics, Kiev. 103:267, 1972. (28)

[46] R. E. Slovacek, D. S. Cramer, E. B. Bean, J. R. Valentine, R. W. Hockenbury, and R. C. Block. 238U(n, f) Measurements Below 100 keV. *Nuclear Science and Engineering*, 62(3):455–462, 1977. (28)

[47] Masayuki Igashira, Yoshiaki Kiyanagi, and Masumi Oshima. Nuclear data study at J-PARC BL04. *Nuclear Instruments & Methods in Physics Research Section A-accelerators Spectrometers Detectors and Associated Equipment - NUCL INSTRUM METH PHYS RES A*, 600:332–334, 02 2009. DOI link: 10.1016/j.nima.2008.11.085. (28)

[48] T. Kin, K. Furutaka, S. Goko, et al. Development of a 4 germanium spectrometer for nuclear data measurements at J-PARC. In *2009 IEEE Nuclear Science Symposium Conference Record (NSS/MIC)*, pages 1194–1197, 2009. DOI link: 10.1109/NSSMIC.2009.5402387. (28)

[49] A. A. Alekseev, A. A. Bergman, O. N. Goncharenko, et al. *Investigations of the neutron-fission processes on the lead neutron slowing-down spectrometer of INR RAS*. JINR, Joint Institute for Nuclear Research (JINR), 2004. ISBN 5-9530-0066-9. URL http://inis.iaea.org/search/search.aspx?orig_q=RN:39069836. NUCLEAR PHYSICS AND RADIATION PHYSICS. (28)

[50] Nakao, T., Terada, K., Kimura, A., et al. Developments of a new data acquisition system at ANNRI. *EPJ Web Conf.*, 146:03021, 2017. DOI link: 10.1051/epjconf/201714603021. (29)

[51] Data Bank. JEFF-3.3. Technical report, OECD/NEA, 2017. (29, 40, 46, 93, 123, 135, 174)

[52] D.A. Brown, M.B. Chadwick, R. Capote, et al. ENDF/B-VIII.0: The 8th Major Release of the Nuclear Reaction Data Library with CIELO-project Cross Sections, New Standards and Thermal Scattering Data. *Nuclear Data Sheets*, 148:1–142, 2018. ISSN 0090-3752. DOI link: 10.1016/j.nds.2018.02.001. Special Issue on Nuclear Reaction Data. (29, 135, 174)

[53] Blokhin A.I., Gai E.V, Ignatyuk A.V., Koba I.I, et al. NEW VERSION OF NEUTRON EVALUATED DATA LIBRARY BROND-3.1. In Russian. *Probl.At.Sci.Technol.Series Nucl.React.Constants 62*, 2016. (29)

[54] Ge, Zhigang, Xu, Ruirui, Wu, Haicheng, et al. CENDL-3.2: The new version of Chinese general purpose evaluated nuclear data library. *EPJ Web Conf.*, 239:09001, 2020. DOI link: 10.1051/epjconf/202023909001. (29)

[55] Tsuneo .. Nakagawa. Evaluation of neutron nuclear data for curium isotopes. Technical report, Japan, 1990. URL http://inis.iaea.org/search/search.aspx?orig_q=RN:21092438. JAERI-M–90-101. (29)

[56] Tsuneo NAKAGAWA, Keiichi SHIBATA, Satoshi CHIBA, et al. Japanese Evaluated Nuclear Data Library Version 3 Revision-2: JENDL-3.2. *Journal of Nuclear Science and Technology*, 32(12):1259–1271, 1995. DOI link: 10.1080/18811248.1995.9731849. (29)

[57] *BROND-2.2 Russian evaluated neutron reaction data library Summary documentation*, International Atomic Energy Agency (IAEA), 1994. URL http://inis.iaea.org/search/search.aspx?orig_q=RN:30022845. IAEA-NDS–90(rev8). (29)

[58] A. B. Klepatskij, A. M. Kolesov, V. M. Maslov, Yu.V. Porodzinskij, and E.Sh. Sukhovitskij. Evaluated neutron nuclear data for curium-244. Technical report, International Atomic Energy Agency (IAEA), 1991. URL http://inis.iaea.org/search/search.aspx?orig_q=RN:23015568. INDC(CCP)–316/L. (29)

[59] V.M. Maslov, E.Sh. Sukhovitskij, Yu.V. Porodzinsldj, A.B. Klepatskij, and G.B. Morogovskij. EVALUATION OF NEUTRON DATA FOR CURIUM-246. *INDC(BLR)-004/L*, 1996. URL https://inis.iaea.org/collection/NCLCollectionStore/_Public/27/078/27078190.pdf. (29, 143)

[60] Keiichi SHIBATA, Toshihiko KAWANO, Tsuneo NAKAGAWA, et al. Japanese Evaluated Nuclear Data Library Version 3 Revision-3: JENDL-3.3. *Journal of Nuclear Science and Technology*, 39(11):1125–1136, 2002. DOI link: 10.1080/18811248.2002.9715303. (29)

[61] Yasuyuki KIKUCHI and Tsuneo NAKAGAWA. EVALUATION OF NEUTRON DATA FOR 248Cm AND 249Cm . Technical report, Japan, 1984. URL https://www-nds.iaea.org/publications/indc/indc-jpn-0087. JAERI-M–84-116. (29)

[62] C. Rubbia et al. A High resolution spallation driven facility at the CERN PS to measure neutron cross-sections in the interval from 1-eV to 250-MeV: A Relative performance asses. 6 1998. URL https://inspirehep.net/literature/474568. (30)

[63] C. Guerrero, A. Tsinganis, et al. Performance of the neutron time-of-flight facility n_TOF at CERN. *The European Physical Journal A*, 49:27, 2013. DOI link: 10.1140/epja/i2013-13027-6. (30, 31, 46, 49)

[64] C. Weiss, E. Chiaveri, S. Girod, et al. The new vertical neutron beam line at the CERN n_TOF facility design and outlook on the performance. *Nuclear Instruments and Methods in Physics Research Section A: Accelerators, Spectrometers, Detectors and Associated Equipment*, 799:90–98, 2015. DOI link: 10.1016/j.nima.2015.07.027. (30, 32, 180)

[65] U Abbondanno et al. New experimental validation of the pulse height weighting technique for capture cross-section measurements. *Nuclear Instruments and Methods in Physics Research Section A: Accelerators, Spectrometers, Detectors and Associated Equipment*, 521:454–467, 2004. DOI link: 10.1016/j.nima.2003.09.066. (30, 32, 99, 112, 113)

[66] C. Guerrero et al. The n_TOF Total Absorption Calorimeter for neutron capture measurements at CERN. *Nuclear Instruments and Methods in Physics Research Section A: Accelerators, Spectrometers, Detectors and Associated Equipment*, 608: 424–433, 09 2009. DOI link: 10.1016/j.nima.2009.07.025. (30, 32, 34)

[67] N. Colonna. Neutron cross-section measurements at the n_TOF facility at CERN. *Nuclear Instruments and Methods in Physics Research Section B: Beam Interactions with Materials and Atoms*, 213:49–54, 01 2004. DOI link: 10.1016/S0168-583X(03)01532-5. (30)

[68] E. Chiaveri et al. The CERN n_TOF Facility: Neutron Beams Performances for Cross Section Measurements. *Nuclear Data Sheets*, 119:1–4, 2014. DOI link: 10.1016/j.nds.2014.08.003. (30)

[69] S. Barros, I. Bergström, V. Vlachoudis, C. Weiss, et al. Optimization of n_TOF-EAR2 using FLUKA. *Journal of Instrumentation*, 10(09):P09003–P09003, sep 2015. DOI link: 10.1088/1748-0221/10/09/p09003. (32)

[70] Nicola Colonna, Frank Gunsing, and Enrico Chiaveri. The Second Beam-Line and Experimental Area at n_TOF: A New Opportunity for Challenging Neutron Measurements at CERN. *Nuclear Physics News*, 25:19–23, 10 2015. DOI link: 10.1080/10619127.2015.1035930. (32)

[71] R. Plag, M. Heil, F. Käppeler, et al. An optimized C6D6 detector for studies of resonance-dominated (n,gamma) cross-sections. *Nuclear Instruments and Methods in Physics Research Section A: Accelerators, Spectrometers, Detectors and Associated Equipment*, 496:425–436, 2003. DOI link: 10.1016/s0168-9002(02)01749-7. (32, 36, 37, 123)

[72] E. Mendoza, Daniel Ott, Altstadt, et al. Measurement and analysis of the 241Am neutron capture cross section at the n_TOF facility at CERN. *Physical Review C*, 97, 05 2018. DOI link: 10.1103/PhysRevC.97.054616. (32, 73, 79, 80)

[73] K. Fraval, Gunsing, et al. Measurement and analysis of the ^{241}Am(n,γ) cross section with liquid scintillator detectors using time-of-flight spectroscopy at the n_TOF facility at CERN. *Phys. Rev. C*, 89:044609, Apr 2014. DOI link: 10.1103/PhysRevC.89.044609. (32, 60, 113)

[74] Oprea, A., Gunsing, F., Schillebeeckx, P., et al. Neutron capture cross section measurements of 241Am at the n_TOF facility. *EPJ Web Conf.*, 239:01009, 2020. DOI link: 10.1051/epjconf/202023901009. (32)

[75] M. Calviani, J. Praena, et al. High-accuracy ^{233}U(n, f) cross-section measurement at the white-neutron source n_TOF from near-thermal to 1 MeV neutron energy. *Phys. Rev. C*, 80:044604, Oct 2009. DOI link: 10.1103/PhysRevC.80.044604. (32)

[76] D. Tarrío, L.S. Leong, Audouin, et al. Measurement of the angular distribution of fission fragments using a PPAC assembly at CERN n_TOF. *Nuclear Instruments and Methods in Physics Research Section A: Accelerators, Spectrometers, Detectors*

and Associated Equipment, 743:79–85, 2014. DOI link: 10.1016/j.nima.2013.12.056. (32, 46, 51)

[77] F. Belloni, F. Gunsing, and T. Papaevangelou. Micromegas for neutron detection and imaging. *Modern Physics Letters A*, 28:1340023, 04 2013. DOI link: 10.1142/S0217732313400233. (32, 46)

[78] J. Balibrea-Correa, E. Mendoza, D. Cano-Ott, E. González, R. Capote, Krtička, et al. Measurement of the α ratio and (n, γ) cross section of ^{235}U from 0.2 to 200 eV at n_TOF. *Phys. Rev. C*, 102:044615, Oct 2020. DOI link: 10.1103/PhysRevC.102.044615. (32, 60, 61, 73, 79, 80, 87)

[79] Bacak, M. et al. Preliminary results on the 233U capture cross section and alpha ratio measured at n_TOF (CERN) with the fission tagging technique. *EPJ Web Conf.*, 211:03007, 2019. DOI link: 10.1051/epjconf/201921103007. (32, 60, 61)

[80] N. Colonna, A. Tsinganis, R. Vlastou, et al. The fission experimental programme at the CERN n_TOF facility: status and perspectives. *The European Physical Journal A*, 56(2):48, Feb 2020. ISSN 1434-601X. DOI link: 10.1140/epja/s10050-020-00037-8. (33)

[81] A. Masi et al. The CERN nTOF Facility Data Acquisition System. In *Proc. of International Conference on Accelerator and Large Experimental Control Systems (ICALEPCS'17), Barcelona, Spain, 8-13 October 2017*, number 16 in International Conference on Accelerator and Large Experimental Control Systems, pages 1900–1905, Geneva, Switzerland, Jan. 2018. JACoW. (33)

[82] CERN Advanced STORage manager. 2020. (33)

[83] P. Žugec, C. Weiss, C. Guerrero, F. Gunsing, et al. Pulse processing routines for neutron time-of-flight data. *Nuclear Instruments and Methods in Physics Research Section A: Accelerators, Spectrometers, Detectors and Associated Equipment*, 812: 134–144, 2016. DOI link: 10.1016/j.nima.2015.12.054. (33, 38, 108)

[84] The SP Devices website. December 2020. URL `https://www.spdevices.com`. (33)

[85] P. Zugec and Collaboration n_TOF. User's guide through Pulse Shape Analysis routines. 2014. (33)

[86] S. Marrone, E. Berthomieux, Becvar, et al. Pulse shape analysis of signals from BaF2 and CeF3 scintillators for neutron capture experiments. *Nuclear Instruments and Methods in Physics Research Section A: Accelerators, Spectrometers, Detectors and Associated Equipment*, 568(2):904–911, 2006. DOI link: 10.1016/j.nima.2006.08.064. (33, 73)

[87] M. Sabate-Gilarte. *The n_TOF-EAR2 facility at CERN: neutron flux determination and the ^{33}s (N,alpha)^{30}si cross section measurement; implications in BNCT.* PhD thesis, Universidad de Sevilla. Departamento de Física Atómica, Molecular y Nuclear, 2017. URL `https://idus.us.es/handle/11441/61303`. (33, 47, 180)

[88] C. Guerrero, D. Cano-Ott, M. Fernández-Ordóñez, et al. Analysis of the BC501A neutron detector signals using the true pulse shape. *Nuclear Instruments and Methods in Physics Research Section A: Accelerators, Spectrometers, Detectors and Associated Equipment*, 597(2):212–218, 2008. DOI link: 10.1016/j.nima.2008.09.017. (34)

[89] S. Marrone, P.F. Mastinu, Abbondanno, et al. A low background neutron flux monitor for the n_TOF facility at CERN. *Nuclear Instruments and Methods in Physics Research Section A: Accelerators, Spectrometers, Detectors and Associated Equipment*, 517(1):389–398, 2004. DOI link: 10.1016/j.nima.2003.09.060. (34, 36)

[90] L. Cosentino, A. Musumarra, M. Barbagallo, N. Colonna, L. Damone, A. Pappalardo, M. Piscopo, and P. Finocchiaro. Silicon detectors for monitoring neutron beams in n-TOF beamlines. *Review of Scientific Instruments*, 86:073509, 2015. DOI link: 10.1063/1.4927073. (36, 39, 46, 121)

[91] V. P. Chechev. Evaluation of 242Cm and 244Cm decay data. *Physics of Atomic Nuclei*, 69(7):1188, Jul 2006. DOI link: 10.1134/S1063778806070155. (40)

[92] T. FUJII. Study on Nuclear Data by using a High Intensity Pulsed Neutron Source for Advanced Nuclear System (4) Analysis of Components of the Samples for Nuclear Data. *Conference record of 2010 Annual Meeting of AESJ, Mito, Japan, 26-28 March 2010*, 95, 2010. URL https://ci.nii.ac.jp/naid/10030702569/en/. (40)

[93] M. Barbagallo, C. Guerrero, et al. High-accuracy determination of the neutron flux at n_TOF. *The European Physical Journal A*, 49(12):156, Dec 2013. DOI link: 10.1140/epja/i2013-13156-x. (45, 46)

[94] Pancin et al. Measurement of the n_TOF beam profile with a micromegas detector. *Nuclear Instruments and Methods in Physics Research Section A: Accelerators, Spectrometers, Detectors and Associated Equipment*, 524(1):102–114, 2004. DOI link: 10.1016/j.nima.2004.01.055. (46)

[95] M. Sabaté-Gilarte, M. Barbagallo, Colonna, et al. High-accuracy determination of the neutron flux in the new experimental area n_TOF-EAR2 at CERN. *The European Physical Journal A*, 53:210, 2017. DOI link: 10.1140/epja/i2017-12392-4. (46, 47)

[96] G. Lorusso, N. Colonna, Marrone, et al. Time–energy relation of the n_TOF neutron beam: energy standards revisited. *Nuclear Instruments and Methods in Physics Research Section A: Accelerators, Spectrometers, Detectors and Associated Equipment*, 532(3):622–630, 2004. DOI link: 10.1016/j.nima.2004.04.247. (49)

[97] S. Lo Meo, M. A. Cortés-Giraldo, C. Massimi, et al. GEANT4 simulations of the nTOF spallation source and their benchmarking. *The European Physical Journal A*, (12):160, Dec 2015. DOI link: 10.1140/epja/i2015-15160-6. (49)

[98] V. Vlachoudis et al. EAR2 Resolution Function. Update on FLUKA+MCNPx simulations. Technical report, CERN, 10 2019. URL https://indico.cern.

ch/event/844622/contributions/3546550/attachments/1918258/3172487/Resolution_Function_2019-10.pdf. (49)

[99] Alfredo Ferrari, Paola R. Sala, Alberto Fasso, and Johannes Ranft. FLUKA: A multi-particle transport code (Program version 2005). 10 2005. DOI link: 10.2172/877507. (49, 180)

[100] D. B. Pelowitz et al. *MCNPX User's Manual, Version 2.7.0*, la-cp-11-00438 edition, 2011. (49, 132, 180)

[101] S. Agostinelli et al. Geant4—a simulation toolkit. *Nucl. Instrum. Methods A*, 506 (3):250–303, 2003. DOI link: 10.1016/S0168-9002(03)01368-8. (49, 60, 83)

[102] J. Lerendegui-Marco, S. Lo Meo, C. Guerrero, et al. Geant4 simulation of the n_TOF-EAR2 neutron beam: Characteristics and prospects. *The European Physical Journal A*, 52(4):100, Apr 2016. DOI link: 10.1140/epja/i2016-16100-8. (49)

[103] A. Stamatopoulos. *Study of the 240Pu(n,f) and 237Np(n,f) reaction cross sections at the new experimental area (EAR2) of the CERN n _TOF facility.* PhD thesis, National Technical University of Athens, 2020. (50)

[104] N.M. Larsson. Updated User's Guide for SAMMY: Multilevel R-matrix Fits to Neutron Data Using Bayes Equations. Technical report, ORNL, 2006. (50, 130)

[105] C. Guerrero, Daniel Ott, E. Mendoza, et al. Measurement and resonance analysis of the 237Np neutron capture cross section. *Phys. Rev. C*, 85, 04 2012. DOI link: 10.1103/PhysRevC.85.044616. (60, 61, 73, 79, 80, 83, 84, 85)

[106] E. Mendoza, D. Cano-Ott, C. Guerrero, et al. Measurement and analysis of the ^{243}Am neutron capture cross section at the n_TOF facility at CERN. *Phys. Rev. C*, 90:034608, Sep 2014. DOI link: 10.1103/PhysRevC.90.034608. (60, 61, 73, 79, 80)

[107] C. Domingo-Pardo et al. New measurement of neutron capture resonances in Bi-209. *Physical Review C*, 74:025807, 2006. DOI link: 10.1103/PhysRevC.74.025807. (60, 94, 113)

[108] S. Marrone, U. Abbondanno, G. Aerts, et al. Measurement of the 151Sm(n,gamma) cross section from 0.6 eV to 1 MeV via the neutron time-of-flight technique at the CERN n_TOF facility. *Physical Review C*, 73:034604, 2006. DOI link: 10.1103/PhysRevC.73.034604. (60, 113)

[109] M. Mastromarco, M. Barbagallo, M.J. Vermeulen, et al. The U-236 neutron capture cross-section measured at the n_TOF CERN facility. *EPJ Web of Conferences*, 146: 11054, 2017. DOI link: 10.1051/epjconf/201714611054. (60, 113)

[110] F. Mingrone, C. Massimi, G. Vannini, et al. Neutron capture cross section measurement of U-238 at the CERN n_TOF facility in the energy region from 1 eV to 700 keV. *Physical Review C*, 95:034604, 2017. DOI link: 10.1103/PhysRevC.95.034604. (60, 94, 113)

[111] J. Lerendegui-Marco, C. Guerrero, E. Mendoza, et al. Radiative neutron capture on Pu-242 in the resonance region at the CERN n_TOF-EAR1 facility. *Physical Review C*, 97:024605, 2018. DOI link: 10.1103/PhysRevC.97.024605. (60, 113, 125)

[112] M. Jandel, T. A. Bredeweg, E. M. Bond, et al. Neutron capture cross section of ^{241}Am. *Phys. Rev. C*, 78:034609, Sep 2008. DOI link: 10.1103/PhysRevC.78.034609. (61)

[113] M. Q. Buckner, C. Y. Wu, and R. A. Henderson. Absolute measurement of the ^{242}Pu neutron-capture cross section. *Phys. Rev. C*, 93:044613, Apr 2016. DOI link: 10.1103/PhysRevC.93.044613. (61)

[114] Tomoyuki Tanaka, Kaito Hagiwara, Enrico Gazzola, et al. Gamma-ray spectra from thermal neutron capture on gadolinium-155 and natural gadolinium. *Progress of Theoretical and Experimental Physics*, 2020(4), 04 2020. ISSN 2050-3911. DOI link: 10.1093/ptep/ptaa015. 043D02. (61)

[115] Mendoza, E., Cano-Ott, D., Jordan, D., et al. NuDEX: A new nuclear cascades generator. *EPJ Web Conf.*, 239:17006, 2020. DOI link: 10.1051/epjconf/202023917006. (61, 95)

[116] F. Bečvář. Simulation of cascades in complex nuclei with emphasis on assessment of uncertainties of cascade-related quantities. *Nuclear Instruments and Methods in Physics Research Section A: Accelerators, Spectrometers, Detectors and Associated Equipment*, 417(2):434–449, 1998. DOI link: 10.1016/S0168-9002(98)00787-6. (61)

[117] D. Jordan, A. Algora, and J.L. Tain. An event generator for simulations of complex -decay experiments. *Nuclear Instruments and Methods in Physics Research Section A: Accelerators, Spectrometers, Detectors and Associated Equipment*, 828:52–57, 2016. DOI link: 10.1016/j.nima.2016.05.034. (61)

[118] R. Capote et al. RIPL – Reference Input Parameter Library for Calculation of Nuclear Reactions and Nuclear Data Evaluations. *Nuclear Data Sheets*, 110(12): 3107–3214, 2009. DOI link: 10.1016/j.nds.2009.10.004. Special Issue on Nuclear Reaction Data. (61, 118)

[119] C. H. Johnson. Statistical model radiation widths for 75<A<130 and the enhancement of P-wave neutron capture for A≈90. *Phys. Rev. C*, 16:2238–2248, Dec 1977. DOI link: 10.1103/PhysRevC.16.2238. (61)

[120] J. Kopecky and M. Uhl. Test of gamma-ray strength functions in nuclear reaction model calculations. *Phys. Rev. C*, 41:1941–1955, May 1990. DOI link: 10.1103/PhysRevC.41.1941. (61)

[121] S. Goriely, P. Dimitriou, M. Wiedeking, et al. Reference database for photon strength functions. *The European Physical Journal A*, 55(10):172, Oct 2019. ISSN 1434-601X. DOI link: 10.1140/epja/i2019-12840-1. (61, 63)

[122] Guerrero C. et al. *Measurements of the 237Np and 240Pu neutron capture cross sections at the n_TOF facility at CERN*. PhD thesis, 2008. (61, 62, 88, 132)

[123] Mendoza, E., Alcayne, V., Cano-Ott, D, et al. Study of photon strength functions of 241Pu and 245Cm from neutron capture measurements. *EPJ Web Conf.*, 239: 01015, 2020. DOI link: 10.1051/epjconf/202023901015. (62)

[124] Rainer Storn and Kenneth Price. Differential Evolution - A Simple and Efficient Heuristic for Global Optimization over Continuous Spaces. *Journal of Global Optimization*, 11:341–359, 01 1997. DOI link: 10.1023/A:1008202821328. (63)

[125] Swagatam Das, Sankha Mullick, and Ponnuthurai Suganthan. Recent Advances in Differential Evolution – An Updated Survey. *Swarm and Evolutionary Computation*, 27, 02 2016. DOI link: 10.1016/j.swevo.2016.01.004. (63)

[126] C. Guerrero, U. Abbondanno, and G. Aerts. Application of Photon Strength Functions to (n, γ) measurements with the n_TOF TAC. *PoS*, PSF07:6, 2008. (67)

[127] C. Guerrero et al. Study of Photon Strength Function of Actinides: the Case of 235U, 238Np and 241Pu. *Journal of the Korean Physical Society*, 59(1510), 2011. (67)

[128] J. Kroll, B. Baramsai, and G. Mitchell. Photon strength functions in Gd isotopes studied from radiative capture of resonance neutrons. *EPJ Web of Conferences*, 69, 03 2014. DOI link: 10.1051/epjconf/20136900018. (67)

[129] B. Baramsai, Frantisek Becvar, T.A. Bredeweg, et al. Scissors Mode of 162 Dy Studied from Resonance Neutron Capture. *EPJ Web of Conferences*, 93:01037, 01 2015. DOI link: 10.1051/epjconf/20159301037. (67)

[130] J. L. Ullmann, T. Kawano, and B. Baramsai. Constraining the calculation of $^{234,236,238}\mathrm{U}(n,\gamma)$ cross sections with measurements of the γ-ray spectra at the DANCE facility. *Phys. Rev. C*, 96:024627, Aug 2017. DOI link: 10.1103/PhysRevC.96.024627. (67)

[131] Moreno-Soto, J., Berthoumieux, E, Dupont, E, et al. Study of the photon strength functions and level density in the gamma decay of the n + 234U reaction. *EPJ Web Conf.*, 211:02002, 2019. DOI link: 10.1051/epjconf/201921102002. (67)

[132] G. Knoll. *Radiation Detection and Measurement*. Wiley, third edition, 2000. (76, 109)

[133] Balibrea J. *Measurement of the neutron capture cross section of the ^{23}U at the n_TOF facility*. PhD thesis, CIEMAT, 2018. (76, 83, 84, 85, 88)

[134] E. Mendoza, D. Cano-Ott, C. Guerrero, et al. Pulse pile-up and dead time corrections for digitized signals from a BaF2 calorimeter. *Nuclear Instruments and Methods in Physics Research Section A: Accelerators, Spectrometers, Detectors and Associated Equipment*, 768:55–61, 2014. DOI link: 10.1016/j.nima.2014.09.010. (81)

[135] C. Guerrero, D. Cano-Ott, E. Mendoza, et al. Correction of dead-time and pile-up in a detector array for constant and rapidly varying counting rates. *Nuclear Instruments and Methods in Physics Research Section A: Accelerators, Spectrometers, Detectors and Associated Equipment*, 777:63–69, 2015. DOI link: 10.1016/j.nima.2014.12.008. (81)

[136] H. Burkhardt, V. M. Grichine, P. Gumplinger, et al. Geant4 standard electromagnetic package for HEP applications. In *IEEE Symposium Conference Record Nuclear Science 2004.*, volume 3, pages 1907–1910 Vol. 3, 2004. DOI link: 10.1109/NSSMIC.2004.1462617. (83)

[137] C. Guerrero, D. Cano-Ott, E. Mendoza, et al. Monte Carlo simulation of the n_TOF Total Absorption Calorimeter. *Nuclear Instruments and Methods in Physics Research Section A: Accelerators, Spectrometers, Detectors and Associated Equipment*, 671:108–117, 2012. DOI link: 10.1016/j.nima.2011.12.046. (83, 84, 85)

[138] M. Bacak. *Development of a detector for the simultaneous measurement and for the study of uranium-233 capture and fission yields at the CERN n_TOF neutron source* . PhD thesis, Technische Universität Wien, 2019. URL https://tel.archives-ouvertes.fr/tel-02358659/document. (83, 84, 85)

[139] Richard L. Macklin, Joseph Halperin, and Ronald R. Winters. Absolute neutron capture yield calibration. *Nuclear Instruments and Methods*, 164(1):213–214, 1979. DOI link: 10.1016/0029-554X(79)90457-9. (88)

[140] A. Borella, G. Aerts, F. Gunsing, M. Moxon, P. Schillebeeckx, and R. Wynants. The use of C6D6 detectors for neutron induced capture cross-section measurements in the resonance region. *Nuclear Instruments and Methods in Physics Research Section A: Accelerators, Spectrometers, Detectors and Associated Equipment*, 577 (3):626–640, 2007. ISSN 0168-9002. DOI link: 10.1016/j.nima.2007.03.034. (88)

[141] C. Lederer, C. Massimi, E. Berthoumieux, et al. ^{62}Ni(n,γ) and ^{63}Ni(n,γ) cross sections measured at the n_TOF facility at CERN. *Phys. Rev. C*, 89:025810, Feb 2014. DOI link: 10.1103/PhysRevC.89.025810. (94)

[142] J. Lerendegui-Marco, C. Guerrero, M. A. Cortés-Giraldo, and J. M. Quesada. Geant4 Simulations for the Analysis of (n, gamma) Measurements at n_TOF. In *Basic Concepts in Nuclear Physics: Theory, Experiments and Applications*, pages 209–210, Cham, 2016. Springer International Publishing. (94)

[143] A Casanovas, A E Tarifeño-Saldivia, Domingo-Pardo, et al. Neutron capture measurement at the n TOF facility of the 204Tl and 205Tl s-process branching points. *Journal of Physics: Conference Series*, 1668:012005, oct 2020. DOI link: 10.1088/1742-6596/1668/1/012005. (94)

[144] C. Domingo-Pardo. *New radiative neutron capture measurement of 207Pb and 209Bi*. PhD thesis, 2005. (96, 123, 132)

[145] P F Mastinu, R. Baccomi, E. Berthoumieux, et al. New C6D6 detectors: reduced neutron sensitivity and improved safety. Technical report, CERN-, 2013. URL http://cds.cern.ch/record/1558147/files/n_TOF-PUB-2013-002.pdf?subformat=pdfa&version=1. (101)

[146] Jorge Lerendegui Marco. Implementation of the L6D6´s Geant4 geometry and Simulations of Response to Gammas and Neutrons . Technical report, Aug 2013. URL http://cds.cern.ch/record/1749924. (101)

[147] A. Mazzone, Cristallo, et al. Measurement of the 154Gd(n,) cross section and its astrophysical implications. *Physics Letters B*, 804:135405, 2020. ISSN 0370-2693. DOI link: 10.1016/j.physletb.2020.135405. (101)

[148] M. Mastromarco, Manna, et al. Cross section measurements of 155,157Gd(n,gamma) induced by thermal and epithermal neutrons. *The European Physical Journal A*, 55(1):9, Jan 2019. ISSN 1434-601X. DOI link: 10.1140/epja/i2019-12692-7. (101)

[149] V. Babiano-Suarez, O. Aberle, V. Alcayne, et al. 80Se(n,gamma) cross-section measurement at CERN n_TOF. *Journal of Physics: Conference Series*, 1668:012001, oct 2020. DOI link: 10.1088/1742-6596/1668/1/012001. (101)

[150] Simone Amaducci, Nicola Colonna, Luigi Cosentino, et al. First Results of the 140Ce(n,)141Ce Cross-Section Measurement at n_TOF. *Universe*, 7(6):200, Jun 2021. ISSN 2218-1997. DOI link: 10.3390/universe7060200. (101)

[151] V. Alcayne, E. Mendoza, et al. The Change of Gain of the L6D6. Technical report, CERN, 2017. URL `https://indico.cern.ch/event/639918/contributions/2594721/attachments/1472532/2279759/C6D6_Tests_2017_v04.pdf`. (101)

[152] R. L. Macklin and J. H. Gibbons. Capture-Cross-Section Studies for 30—220-keV Neutrons Using a New Technique. *Physical Review C*, 159(4):1007, 1967. DOI link: 10.1103/PhysRev.159.1007. (112, 113)

[153] U. Abbondanno et al. Neutron Capture Cross Section Measurement of ^{151}Sm at the CERN Neutron Time of Flight Facility (n_TOF). *Phys. Rev. Lett.*, 93:161103, Oct 2004. DOI link: 10.1103/PhysRevLett.93.161103. (113)

[154] G. Tagliente et al. Measurements of the 90,91,92,94,96Zr(n,) cross-sections at n_TOF. *Nuclear Physics A*, 758:573–576, 2005. ISSN 0375-9474. DOI link: 10.1016/j.nuclphysa.2005.05.184. Nuclei in the Cosmos VIII. (113)

[155] R. Brun and F. Rademakers. ROOT: An object oriented data analysis framework. *Nucl. Instrum. Meth. A*, 389:81–86, 1997. DOI link: 10.1016/S0168-9002(97)00048-X. (113, 180)

[156] F. Mingrone. *Radiative neutron capture cross section on 238 U at the n_TOF CERN facility: a high precision measurement*. PhD thesis, Alma Mater Studiorum - Universitá di Bologna, 2015. (123, 132)

[157] J. Lerendegui-Marco. *Neutron radiative capture on 242Pu: addressing the target accuracies for innovative nuclear systems*. PhD thesis, 2018. (125, 132, 137, 145)

[158] C. W. Reich and M. S. Moore. Multilevel Formula for the Fission Process. *Phys. Rev.*, 111:929–933, Aug 1958. DOI link: 10.1103/PhysRev.111.929. (130)

[159] Dimitri G. Naberejnev, Claude Mounier, and Richard Sanchez. The Influence of Crystalline Binding on Resonant Absorption and Reaction Rates. *Nuclear Science and Engineering*, 131(2):222–229, 1999. (131)

[160] N. Soppera, M. Bossant, and E. Dupont. JANIS 4: An Improved Version of the NEA Java-based Nuclear Data Information System. *Nuclear Data Sheets*, 120:294–296, 2014. ISSN 0090-3752. DOI link: 10.1016/j.nds.2014.07.071. (134)

[161] S. Kopecky, P. Siegler, and A. Moens. Low energy transmission measurements of 240,242Pu at GELINA and their impact on the capture width. *EPJ Web Conf.*, 116:4, 2007. DOI link: 10.1051/ndata:07391. (137)

[162] Satoshi, Tokai Ibaraki, and D. L. Smith. A suggested procedure for resolving an anomaly in least-squares data analysis known as "Peelle's Pertinent Puzzle" and the general implications for nuclear data evaluation. Technical report, United States, 1991. Research Org.: Argonne National Lab., IL (United States). (150)

[163] Rudolf Frühwirth, D. Neudecker, and Helmut Leeb. Peelle's Pertinent Puzzle and its Solution. *EPJ Web of Conferences*, 27:00008–, 05 2012. DOI link: 10.1051/epjconf/20122700008. (150)

[164] W. Kolar and K.H. Böckhoff. Resonance parameters of 240Pu: Part I—Neutron widths. *Journal of Nuclear Energy*, 22(5):299–315, 1968. ISSN 0022-3107. DOI link: 10.1016/0022-3107(68)90003-8. (170)

[165] Andrée Lamberty and Hendrik Emons. Reference materials: from CBNM to IRMM. *Accreditation and Quality Assurance*, 16:393–398, 08 2011. DOI link: 10.1007/s00769-011-0781-2. (170)

[166] R. W. Hockenbury, W. R. Moyer, and R. C. Block. Neutron Capture, Fission, and Total Cross Sections of Plutonium-240 from 20 eV to 30 keV. *Nuclear Science and Engineering*, 49(2):153–161, 1972. (170)

[167] R. W. Hockenbury, Z. M. Bartolome, J. R. Tatarckuz, W. R. Moyer, and R. C. Block. Neutron Radiative Capture in Na, Al, Fe, and Ni from 1 to 200 keV. *Phys. Rev.*, 178:1746–1769, Feb 1969. DOI link: 10.1103/PhysRev.178.1746. (171)

[168] Gerardo Aliberti, Giuseppe Palmiotti, Massimo Salvatores, and C. Stenberg. Impact of Nuclear Data Uncertainties on Transmutation of Actinides in Accelerator-Driven Assemblies. *Nuclear Science and Engineering - NUCL SCI ENG*, 146, 01 2004. (173)

[169] Collaboration n_TOF. Transport Simulation GUI- User Manual. 2018. URL `https://twiki.cern.ch/twiki/pub/NTOF/TransportCode/user_manual.pdf`. (180)